



HAL
open science

Physics of pore closure in polar firn, and its implications for the understanding of past feedbacks between climate and carbon cycle

Kévin Fourteau

► To cite this version:

Kévin Fourteau. Physics of pore closure in polar firn, and its implications for the understanding of past feedbacks between climate and carbon cycle. Climatology. Université Grenoble Alpes, 2019. English. NNT : 2019GREAU018 . tel-02338731

HAL Id: tel-02338731

<https://theses.hal.science/tel-02338731>

Submitted on 30 Oct 2019

HAL is a multi-disciplinary open access archive for the deposit and dissemination of scientific research documents, whether they are published or not. The documents may come from teaching and research institutions in France or abroad, or from public or private research centers.

L'archive ouverte pluridisciplinaire **HAL**, est destinée au dépôt et à la diffusion de documents scientifiques de niveau recherche, publiés ou non, émanant des établissements d'enseignement et de recherche français ou étrangers, des laboratoires publics ou privés.



THÈSE

Pour obtenir le grade de

DOCTEUR DE LA COMMUNAUTÉ UNIVERSITÉ GRENOBLE ALPES

Spécialité : Sciences de la Terre et de l'Univers et de
l'Environnement (CESTUE)

Arrêté ministériel : 25 mai 2016

Présentée par

Kévin FOURTEAU

Thèse dirigée par **Patricia MARTINERIE**, Chargée de recherche ,
Communauté Université Grenoble Alpes
et codirigée par **Xavier FAIN**, Chargé de recherche, Communauté
Université Grenoble Alpes

préparée au sein du **Laboratoire Institut des Géosciences de
l'Environnement**
dans l'**École Doctorale Terre, Univers, Environnement**

**Physique de la fermeture des pores dans le
névé polaire, implications pour la
compréhension des rétroactions passées
entre cycle du carbone et climat**

**Physics of pore closure in polar firn, and its
implications for the understanding of past
feedbacks between climate and carbon cycle**

Thèse soutenue publiquement le **6 septembre 2019**,
devant le jury composé de :

Madame PATRICIA MARTINERIE

CHARGE DE RECHERCHE, CNRS DELEGATION ALPES, Directeur de
thèse

Monsieur MASSIMO FREZZOTTI

PROFESSEUR, UNIVERSITE DE ROME III - ITALIE, Rapporteur

Madame RACHAEL RHODES

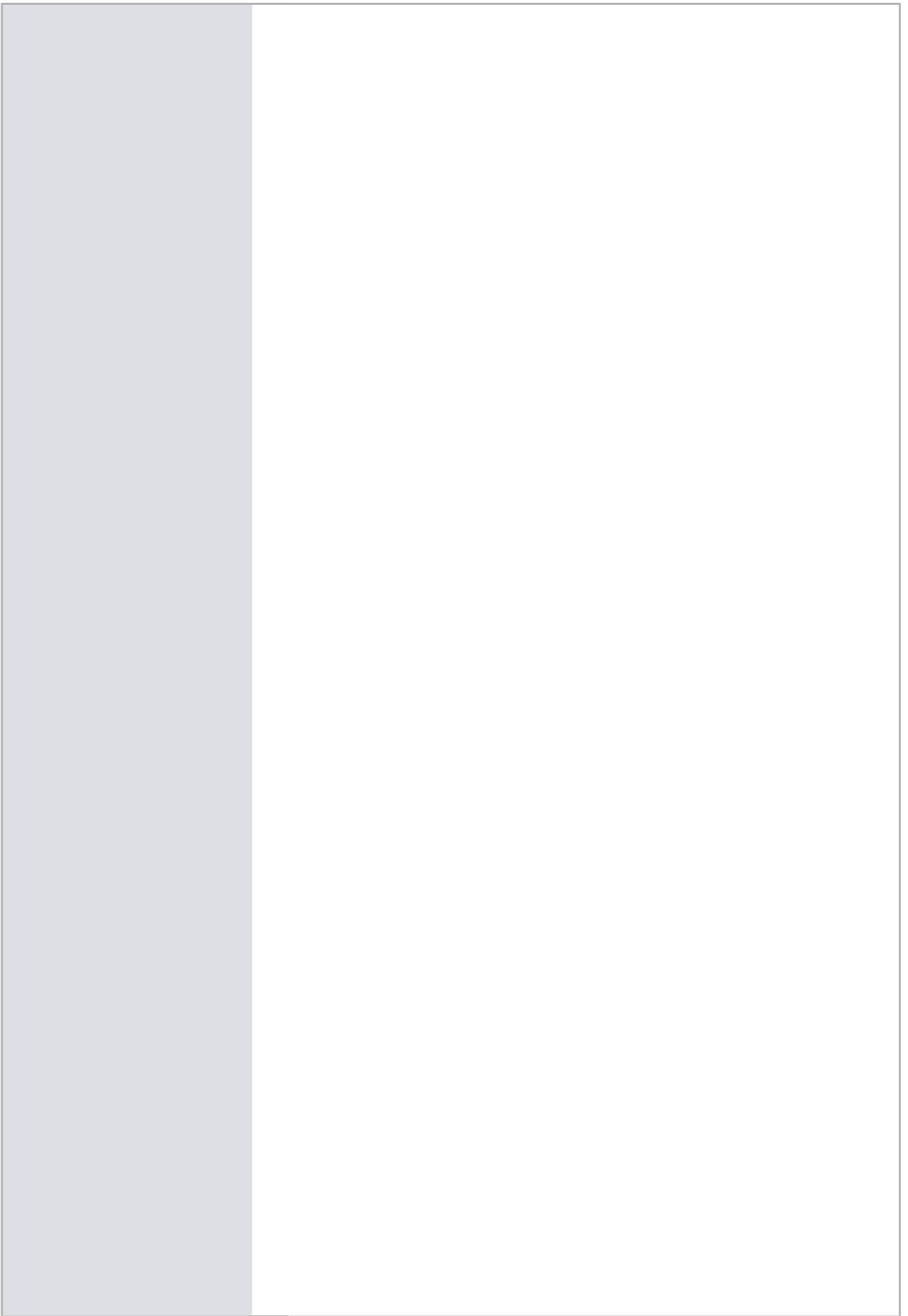
MAITRE DE CONFERENCES, UNIVERSITE DE CAMBRIDGE -
ROYAUME-UNI, Rapporteur

Monsieur LAURENT OXARANGO

PROFESSEUR, UNIVERSITE GRENOBLE ALPES, Président

Monsieur OLIVIER CASTELNAU

DIRECTEUR DE RECHERCHE, CNRS DELEGATION ILE-DE-FRANCE
MEUDON, Examinateur



Abstract

As they contain air from past atmospheres, ice cores are unparalleled climate paleo-archives. The study of the gases enclosed in ice cores from the arid region of East Antarctica allows to infer the past compositions of the atmosphere back to 800,000 years ago. Gases are trapped during the compaction of the snow deposited on top of the ice sheet. In the near-surface snow, also referred to as firn, the interstitial porous network shrinks until it eventually pinches and traps gases in the ice. However, the very process of gas trapping has impacts on the gas signals recorded in ice cores. The interpretation of gas records requires to characterize how ice core and atmospheric signals differ. The aim of this PhD is to study two effects altering ice core gas records, namely gas layered trapping that creates stratigraphic irregularities and firn smoothing that removes fast variability from the record. A specific focus is put on low-accumulation East Antarctic ice cores.

This inquiry starts with the multi-tracer study of a firn core drilled at the Lock-In site, East Antarctica. The results show that the bottom of the firn can be seen as a stack of heterogeneous strata that densify following the same porous network evolution with density. In this vision, the stratification simply reflects the fact that some strata are in advance (or late) in their densification, but that pore closure happens in a similar fashion in all strata. This notably means that all strata contain nearly similar amounts of gases, as supported by direct measurements. High-resolution chemistry data indicate that denser strata are characterized by a high liquid conductivity, suggesting that deep firn stratification is due the impurity-induced preferential densification.

This knowledge is then used to explain abrupt spikes observed in ice core methane records. For this PhD we rely on 6 new high-resolution methane records, measured in several East Antarctic ice cores at IGE. We show that the abrupt variations are layering artifacts due to stratigraphic irregularities caused by dense firn strata closing in advance. A simple model is developed to simulate the irregular occurrence of layering artifacts.

A novel technique is proposed to estimate the age distributions of gases in ice cores, that are responsible for the smoothing of fast atmospheric variations. It can notably be applied to glacial records, and for the first time provides quantitative insights on the smoothing of very low-accumulation records. Our results show that in East Antarctica, the firn smoothing is weakly sensitive to the accumulation rate, meaning that more information than previously thought is preserved.

Finally, we present the development of a new type of micro-mechanical firn model. Its ambition is to simulate the evolution of the porous network of a firn stratum. Such a model could be used to better constrain the enclosure of gases in polar ice under glacial conditions.

Keywords: ice cores, gas trapping, firn smoothing, layering, methane Continuous Flow Analysis, paleoclimate

Résumé

Les carottes de glace sont des archives climatiques sans équivalents : les gaz contenus dans la glace de la région aride de l'Antarctique de l'Est permettent de reconstruire les compositions atmosphériques au cours des derniers 800000 ans. Les gaz sont piégés pendant la compaction de la neige tombée sur l'inlandsis. Dans la neige en surface, aussi appelée névé, le réseau poreux interstitiel diminue jusqu'au pincement des pores qui piègent définitivement les gaz dans la glace. Cependant, le processus même de piégeage des gaz impacte l'enregistrement des signaux mesurés dans les carottes. L'interprétation de ces signaux demande de caractériser en quoi ils diffèrent de l'atmosphère passée. Le but de cette thèse est d'étudier deux effets altérant les enregistrements gaz des carottes, le piégeage par couches qui crée des irrégularités stratigraphiques et le lissage qui retire la variabilité rapide de l'enregistrement. Une attention particulière est portée sur les glaces de l'Antarctique de l'Est.

Ce travail démarre avec l'étude multi-traceurs d'une carotte de névé forée au site de Lock-In en Antarctique de l'Est. Les résultats montrent que le bas du névé est un empilement hétérogène de strates se densifiant suivant une même évolution de leur réseau poreux. La stratification reflète simplement que certaines strates sont en avance (ou retard) dans leur densification, mais la fermeture des pores est similaire dans toutes les strates. Notamment, les strates contiennent toutes des quantités similaires de gaz, comme le montrent des mesures directes. Des mesures de chimie à haute-résolution montrent que les strates denses ont une haute conductivité liquide, suggérant que la stratification profonde du névé est due à une densification préférentielle induite par des impuretés. Ces connaissances sont appliquées pour étudier des variations centimétriques mesurées dans les signaux méthane des carottes de glace. Pour cette thèse, nous utilisons 6 nouveaux signaux méthane à haute résolution, mesurés dans des carottes d'Antarctique de l'Est à l'IGE. Nous montrons que ces variations sont des artefacts dus aux irrégularités stratigraphiques causées par des strates denses se fermant en avance. Un modèle est proposé pour simuler la présence irrégulière de ces artefacts.

Une nouvelle méthode est proposée pour estimer la distribution en âge des gaz dans les carottes, qui est à l'origine du lissage des variations atmosphériques rapides. Elle peut être appliquée aux carottes de la dernière période glaciaire, et donne pour la première fois des indications quantitatives sur le lissage des signaux dans les carottes à très faible accumulation. Nos résultats montrent qu'en Antarctique de l'Est, le lissage est peu sensible au taux d'accumulation, et que plus d'information que prévu est préservée lors du piégeage.

Enfin, nous présentons le développement d'un nouveau type de modèle micro-mécanique du névé. Son but est de simuler l'évolution des pores dans une strate de névé. Un tel modèle pourrait être utilisé pour contraindre le piégeage des gaz dans la glace, dans des conditions de période glaciaire.

Mots Clés : carottes de glace, piégeage des gaz, lissage du névé, stratification, mesure en continu du méthane, paléoclimat

Merci

Je tiens évidemment à remercier en premier lieu Patricia et Xavier pour ces années, non seulement de thèse, mais aussi de Master passées ensemble. On m'a souvent dit que la thèse serait un moment difficile (surtout la deuxième année), mais cela a toujours été un plaisir pour moi de venir travailler sur ce sujet. Vous avez su me laisser travailler en autonomie et poursuivre mes idées, tout en m'épaulant sur mes points faibles (l'ortographe entre autre).

Je remercie chaleureusement Massimo Frezzotti et Rachael Rhodes pour le temps passé à lire et commenter mon manuscrit, et également Olivier Castelnau et Laurent Oxarango pour avoir fait partie de mon jury de thèse.

Durant cette thèse, j'ai également bénéficié de l'aide indispensable d'un certain nombre de membres de l'IGE: Grégory qui m'a dépanné (plus d'une fois) pour des découpes de carottes et du bougeage de caisses, Laurent pour ses connaissances encyclopédiques sur la pycno et les mesures vieilles de 25 ans, Fabien et Olivier pour m'avoir initié au développement d'usine à gaz avec Elmer/Ice, et Maurine pour m'avoir expliqué encore et encore comment fonctionnent les dislocations. Je tiens aussi à remercier le reste des personnes m'ayant fait avancer dans cette thèse (scientifiquement ou non) qu'ils soient de l'IGE ou non: Sophie, Johannes, Amélie, Jérôme, Rob, Anaïs, Amaëlle, Martin, Volodya, Olivier M., Henning, Becky, ...

C'est bien connu, un des gros avantages de la thèse c'est de pouvoir partager ses galères avec les autres thésards du laboratoire: Marion, Lucas, Maria, Fanny, Cédric, Jai, Étienne, Olivier, Jihnwa, Claudio, Julien B. et Julien B., Ugo, Jordi, Romain, Ilann, Albane, Hans, Gabi, Jospeh, Alexis, et David. Si ces années ont été si agréables, c'est aussi grâce à vous. Cette thèse étant officiellement la fin de mon parcours universitaire, j'aimerais aussi y glisser le nom de Pierre B., que je remercie pour les bons moments passés ensemble depuis la prépa.

Et finalement, je remercie mes parents qui m'ont toujours soutenu et m'ont permis de me lancer dans mes études sans que j'ai à me soucier du reste. Nul doute que l'intérêt que j'ai pour la science et la nature du monde qui nous entoure leur est dû.

Et bien sûr, une pensée pour Léa et Molly (qui n'a sans doute pas lu cette thèse) pour les randonnées, le bon temps ensemble, et tout le reste.

Contents

1	Introduction	1
2	Ice Cores and their Gas Records	5
2.1	Climatic cycles of the Quaternary Era	7
2.1.1	Glacial-Interglacial cycles	7
2.1.2	Millennial variability	9
2.1.3	Records of climatic variability in ice cores	10
2.2	From snow to firn and ice	14
2.2.1	Description of the firn column	14
2.2.2	Stratification of the firn	17
2.2.3	Deformation of the ice matrix	21
2.3	The porous network and the gases inside	25
2.3.1	Firn from the standpoint of gases	25
2.3.2	Air content of polar ice	27
2.4	Modeling the firn and gas trapping	29
2.4.1	Firn densification models	29
2.4.2	Gas trapping models	32
2.5	Alterations of the gas record	37
2.5.1	The smoothing effect	38
2.5.2	Layered gas trapping	40
2.6	Objectives of the PhD	41
3	Methods	43
3.1	Continuous Flow Analysis of methane concentrations	45
3.1.1	Description of the CFA apparatus	46
3.1.2	Preparation of the ice	48

3.1.3	Processing of the raw data	49
3.1.4	Correcting for methane dissolution	50
3.1.5	Internal smoothing of the CFA system	56
3.2	Pycnometry	61
3.2.1	Physical basis	61
3.2.2	Experimental protocol	66
3.2.3	Calibration of the chamber volumes	67
3.2.4	Experimental uncertainties	69
3.3	Other measurements performed during the thesis	71
3.3.1	Density measurements by Xray absorption	72
3.3.2	Tomography	75
3.3.3	Air content	76
3.3.4	Chemistry measurements	77
3.3.5	Thin sections and crystalline texture	78
3.4	Conclusion of the chapter	79
4	Study of pore closure in an East Antarctic firn core	81
4.1	Presentation of the chapter	83
4.2	Multi-tracer study of gas trapping in an East Antarctic ice core	84
4.2.1	Introduction	85
4.2.2	Methods	87
4.2.3	Results and discussion	93
4.2.4	Conclusions	113
4.2.5	Supplementary Material	115
4.3	To go further	121
4.3.1	Structural anisotropy of firn	121
4.3.2	Analysis of thin sections	123
4.4	Conclusion of the chapter	126
5	Alterations of methane records in East Antarctic ice cores	129
5.1	Presentation of the chapter	131
5.2	Analytical constraints on layered gas trapping and smoothing of atmospheric variability in ice under low-accumulation conditions	132
5.2.1	Introduction	133
5.2.2	Ice core samples and analytical methods	135
5.2.3	Experimental results	137
5.2.4	Layered bubble trapping	141

5.2.5	Smoothing and age distribution in the Vostok 4G-2 ice core	148
5.2.6	Discussion	151
5.2.7	Conclusions	155
5.2.8	Supplementary Material	156
5.3	Estimation of gas record alteration in very low accumulation ice cores	164
5.3.1	Introduction	165
5.3.2	Methods	167
5.3.3	Results and Discussion	169
5.3.4	Loss of climatic information in a deep and thinned ice core from East Antarctica	182
5.3.5	Conclusions	187
5.3.6	Supplementary Material	188
5.4	Conclusion of the chapter	193
6	Modeling the compression of firn layers	195
6.1	Presentation of the chapter	197
6.2	Description of the model	198
6.2.1	General principles	199
6.2.2	Numerical implementation	200
6.3	Numerical experiments	208
6.3.1	Mass conservation	208
6.3.2	Effect of internal pressure on pore compression	210
6.3.3	Evolution of a firn layer	212
6.4	Discussion	215
6.5	Conclusion of the chapter	217
7	Conclusion and Outlooks	219
7.1	General conclusion	221
7.2	Perspectives	223
7.3	A few personal words	225
A	Historical closed porosity data in polar firn	229
A.1	Introduction	230
A.2	The pycnometry method	231
A.3	Processing of the data	232
A.3.1	Original data processing	233
A.3.2	A new data processing	234
A.4	The Barnola parametrization for closed porosity	236

A.5	Conclusion	237
B	Firn air pumping campaigns at EastGRIP	239
B.1	General principle of firn air pumping	239
B.2	Preparing the firn air pumping system	240
B.2.1	Preparing the bladder	240
B.2.2	Preparing the pumping and tubing system	242
B.3	Field work	243
B.3.1	Protocol of firn air pumping	243
B.4	Tips and tricks	244
	Bibliography	245

Introduction

The Earth's climate and its archives

In the last decades, the Earth's climate and its evolutions became one of the major topics of our time. This broad interest is the consequence of the current climate change, driven by the emission and accumulation of greenhouse gases (GHG) in the atmosphere (IPCC, 2014). If the anthropogenic nature of this change is well established, it remains necessary to accurately characterize the response of the Earth's climate to the increase of GHG concentrations, and this in order to properly predict its evolution by the end of the century and beyond.

Several types of natural archives are used by climatologists to study the previous states of the Earth's climate, to reconstruct its history, and to characterize the mechanisms at play during periods of climate change. Among others, one can cite marine sediment cores that notably enclose information on the past conditions of ocean temperature and salinity (Rothwell and Rack, 2006). Another example are speleothems retrieved in caves, whose isotopic composition is used to deduce temperature variations and biosphere activity (Hendy and Wilson, 1968; McDermott, 2004). Each type of archive is characterized by the time period it covers and by its time resolution. For instance, marine sediment cores cover time periods reaching millions of years, but have a resolution of the order of the century (Shackleton and Opdyke, 1976; Lisiecki and Raymo, 2005). On the contrary, the study of speleothems only covers periods of a few hundred thousand of years, but does so with a resolution of the order

of the year (Lauritzen, 1995). Naturally, the longer is the time coverage of a climatic archive and the shorter is its time resolution, the better is the archive. However, long time coverage usually comes at the expense of a precise time resolution.

Among all the available archives for the study of climate, this thesis deals with a particular type: the polar ice cores.

Polar ice cores

Ice cores have the particularity to enclose bubbles composed of air directly originating from past atmospheres (Stauffer et al., 1985). Thanks to these air bubbles, ice cores are the ideal archive to study the past evolutions of the Earth's atmospheric composition, and notably its concentration of greenhouse gases (Barnola et al., 1987; Loulergue et al., 2008; Lüthi et al., 2008; Mitchell et al., 2013; Marcott et al., 2014). In addition to the bubbles, the ice material of ice cores is used to derive other information about the past conditions of the climate. Notably, the isotopic composition of the ice allows scientists to reconstruct the evolution of past temperatures (Dansgaard et al., 1993; Jouzel et al., 2007). The joint study of the gases trapped in the Vostok ice core (Antarctica) and of its isotopic composition highlighted the close relationship between the concentration in carbon dioxide and the Earth temperature (Barnola et al., 1987; Genthon et al., 1987).

The time coverage of ice cores depends on the local temperature and precipitation conditions under which they were formed. Currently, the oldest ice core has been dated back to 800,000 years in the past, encompassing the last eight glacial cycles (EPICA community members et al., 2004). Yet, the International Partnership in Ice Cores Science (IPICS) set the goal to obtain an ice core old of a million-and-a-half years old (Fischer et al., 2013). The search for this ice core is already carried out on the East Antarctic plateau, and a new deep drilling is planned to start during the 2020/2021 austral summer. The time resolution of the measurements performed in the ice material varies between one month to several hundreds of year, depending on the drilling site conditions and on the history of deformation of the ice. The resolution of the greenhouse gases measurements varies from several decades to several hundreds of years, a point detailed in this thesis. Ice cores can enclose information about abrupt climate evolutions, evolutions under which the climate conditions change in less than a hundred years (Dansgaard et al., 1993; Chappellaz et al., 2013). These abrupt past variations offer crucial insights on the Earth's climate dynamics.

Objectives and organization of the thesis

This thesis deals with the process of gas trapping in polar ice. In other words: how are the bubbles in polar ice formed? Besides the purely theoretical interest, this work aims to help the interpretation of the gas concentrations measured in polar ice cores. Indeed, the concentrations recorded in polar ice are the picture of the past atmospheric concentrations, but also of the processes involved during gas trapping (Spahni et al., 2003; Rhodes et al., 2016). Moreover, the recent development of high-resolution gas measurement techniques (Stowasser et al., 2012; Chappellaz et al., 2013; Rhodes et al., 2013) now gives access to centimeter scale concentration variability in ice cores. In order to provide climatologists with the best possible interpretation of the gas records in ice cores, it is thus necessary to distinguish between what can be attributed to atmospheric variability (climatically relevant) and what originates from the very process of gas trapping. A special emphasis will be put on the gas trapped in the ice of the low-accumulation East Antarctic plateau. This region, which is the most affected by gas trapping effects, encloses the oldest climatically exploitable ice and is where the future oldest-ice core is currently searched (Van Liefferinge et al., 2018; Sutter et al., 2019).

Chapter 2 presents a review of the scientific literature in ice cores science, with a particular focus on gas trapping. This section also introduces the specific questions that this PhD aims to answer. Chapter 3 presents the experimental methods utilized for this work. Chapter 4 is based on the study of a shallow core from East Antarctica, specifically dedicated to a multi-tracer characterization of gas trapping. This chapter aims to improve the description of the processes responsible for the trapping of gases in polar ice. Chapter 5 focuses on the impacts of gas trapping on the recorded gas signals in ice cores. A special emphasis is placed on ice cores from the East Antarctic plateau that were formed during the last glacial period. Chapter 6 describes the development of a numerical model aiming to simulate the compression of a layer of deep firn. Finally, Chapter 7 concludes this manuscript and proposes outlooks to keep improving our understanding of gas trapping in polar ice. Two annexes are also included at the end of the manuscript. The first one covers the processing of historical firn data that were measured in the 1990's at IGE, but haven't been published yet. The second one presents my involvement in the firn air pumping campaigns at EastGRIP,

Greenland.

Ice Cores and their Gas Records

Contents

2.1 Climatic cycles of the Quaternary Era	7
2.1.1 Glacial-Interglacial cycles	7
2.1.2 Millennial variability	9
2.1.3 Records of climatic variability in ice cores	10
2.2 From snow to firn and ice	14
2.2.1 Description of the firn column	14
2.2.2 Stratification of the firn	17
2.2.3 Deformation of the ice matrix	21
2.3 The porous network and the gases inside	25
2.3.1 Firn from the standpoint of gases	25
2.3.2 Air content of polar ice	27
2.4 Modeling the firn and gas trapping	29
2.4.1 Firn densification models	29
2.4.2 Gas trapping models	32
2.5 Alterations of the gas record	37
2.5.1 The smoothing effect	38
2.5.2 Layered gas trapping	40
2.6 Objectives of the PhD	41

2.1 Climatic cycles of the Quaternary Era

During the Quaternary period, starting 2.58 million years ago and still ongoing today, the Earth's climate has been characterized by regular temperature variations. These variations took place across various time scales ranging from a hundred years to tens of thousands of years.

2.1.1 Glacial-Interglacial cycles

One of the characteristic variations of the Earth's climate, is the alternation between cold glacial periods, notably characterized by a large extension of ice sheets in the Northern hemisphere (Svendsen et al., 2004; Abe-Ouchi et al., 2013), and warm interglacial periods. This alternation between glacial and inter-glacial periods forms the so-called glacial-interglacial cycles.

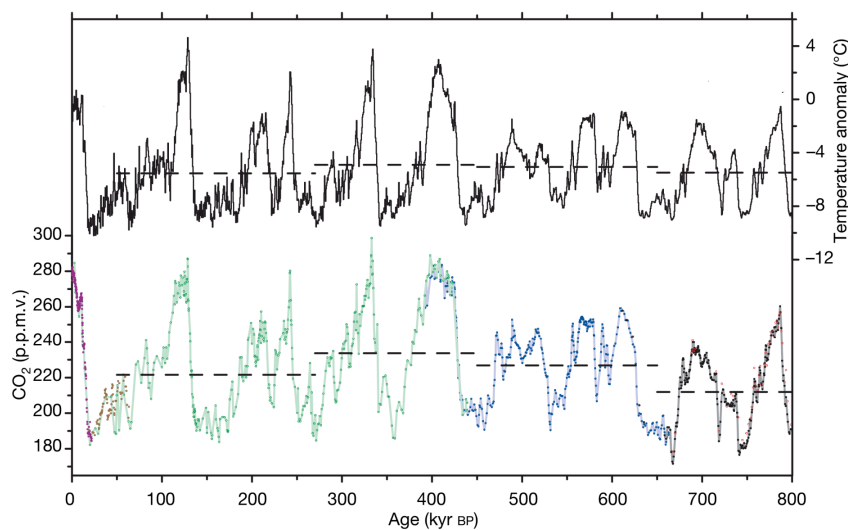


Figure 2.1 – Relationship between Antarctic temperature and CO₂ over the last eight glacial cycles. Figure from Lüthi et al. (2008)

During the last 800,000 years, glacial periods have lasted several ten thousand years. On the other hand, the warmer interglacial periods have been shorter with durations of only ten thousand years. Consequently, over the last million years, the glacial cycle is characterized by asymmetric oscillations of the temperature, with a period of repetition around 100,000 years (Muller and MacDonald, 1997; Lisiecki and Raymo, 2005; Kawamura et al., 2007; Lüthi et al., 2008). Such 100,000 years oscillations are notably visible in ice cores, as seen in Figure 2.1, and in marine sediment cores, as seen in the left side of Figure 2.2. It

is understood that the transitions from glacial to interglacial periods (known as deglaciations or terminations) or the transitions from interglacial to glacial (known as glaciations) are initiated by changes in the distribution of solar irradiance on the Earth surface (Berger, 1988; Daruka and Ditlevsen, 2016). In turn, these variations in solar irradiance are due to changes in the orbital parameters of the Earth's course around the Sun, and are described by the Milankovitch cycles (Milankovitch, 1920; Muller and MacDonald, 1997). However, the change in solar irradiance alone does not suffice to fully explain the observed variations in the Earth's climate. A correct description of glaciations and deglaciations requires to take into account feedbacks in the Earth's climate, notably involving the amount of greenhouse gases (GHG) in the atmosphere (Genthon et al., 1987; Köhler et al., 2010).

Thanks to their particularity of containing both information about past temperatures and GHG concentrations, polar ice cores have been widely used to study glacial-interglacial cycles in the past (Genthon et al., 1987; Barnola et al., 1987; Petit et al., 1999; Delmotte et al., 2004). In particular, climatologists have used ice cores from the arid East Antarctic plateau, as this region contains very old and stratigraphically undisturbed ice (Fischer et al., 2013; Passalacqua et al., 2018). The oldest dated ice retrieved to this day, from the EPICA Dome C ice core (EDC), reaches back 800,000 years in the past and provides a precise description of the temperature and GHG evolution over the last eight glacial cycles (Lüthi et al., 2008; Loulergue et al., 2008). It provides a clear evidence of the link between the temperature and the atmospheric concentrations in GHG (notably CO₂), as illustrated in Figure 2.1

However, marine sediment cores indicate that the typical duration of 100,000 years for the glacial cycles no longer holds true when reaching 1 million years in the past (Shackleton and Opdyke, 1976; Lisiecki and Raymo, 2005). Further back in time, the glacial-interglacial cycles are characterized by a 41,000 years period, much shorter than the 100,000 years of the late Quaternary. This transition from a 41,000 to a 100,000 years climate is known as the Mid-Pleistocene Transition (MPT), and is visible in benthic records as shown in Figure 2.2. However, the precise mechanisms at the origin of the MPT are not yet clear (Clark et al., 2006). The solution to this problem might lie in the feedbacks between GHG and the global temperatures, as a decline in CO₂ concentrations appears in numerical models as a necessary conditions to reproduce the MPT (Willeit et al., 2019). However, marine sediment cores do not provide sufficient information on the past atmospheric compositions. Thanks

to the bubbles they enclose, ice cores could provide a clear picture of the GHG concentrations during the MPT, and help clarify their role this climatic transition. That is notably why the International Partnership in Ice Core Sciences (IPICS) is currently searching for an ice core as old as one-and-a-half million years and covering the MPT (Van Liefferinge et al., 2018; Sutter et al., 2019).

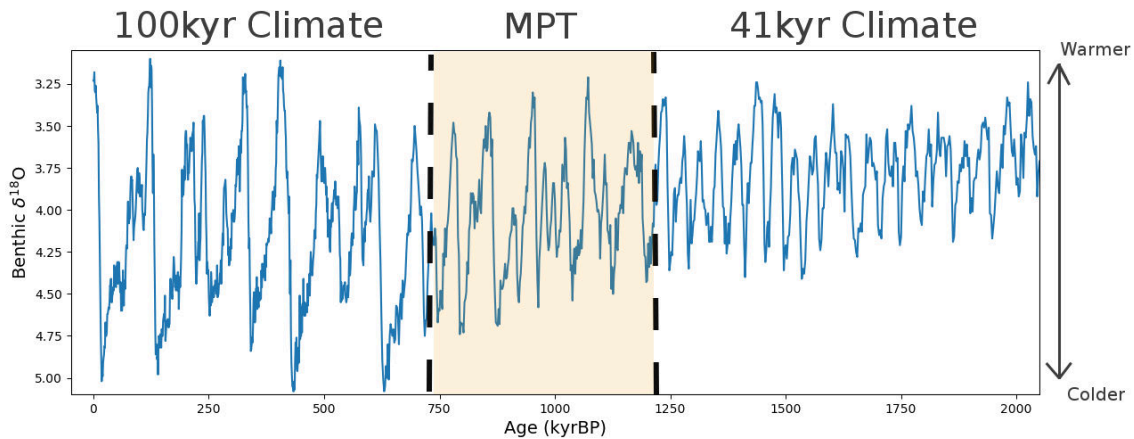


Figure 2.2 – Transition from a 100,000 year climate to a 41,000 year climate. Benthic $\delta^{18}\text{O}$ data from Lisiecki and Raymo (2005).

2.1.2 Millennial variability

The late Quaternary Earth's climate is not only characterized by 100,000 years long cycles. The study of ice cores drilled in the Greenland ice sheet have revealed the presence of fast warming events during the last glacial period (Dansgaard et al., 1993). They are referred to as Dansgaard-Oeschger (DO) events, and are associated with Greenland temperature increases between 8 and 15°C in a few decades, as seen in Figure 2.3 (Huber et al., 2006b). Similar DO events have since then been observed during the other glacial periods of the last eight glacial-interglacial cycles (Louergue et al., 2008). As seen in Figure 2.4, these abrupt warming events are associated with strong increases in methane concentration, that can reach up to 300ppbv with rates up to 3ppbv per year (Chappellaz et al., 2013). The global increases of atmospheric methane during the DO events are due to the activation of methane sources (such as wetlands) in response to the warming and changes in precipitation of the Northern hemisphere (Hopcroft et al., 2011). The proper mechanisms at the origin of the DO events are not yet perfectly understood (Landais et al., 2015), even though they likely involve interactions between the ocean circulation and sea ice (Boers et al., 2018). These abrupt DO events provide valuable insights about the Earth climate dynamics and

the mechanisms at play during fast warming periods.

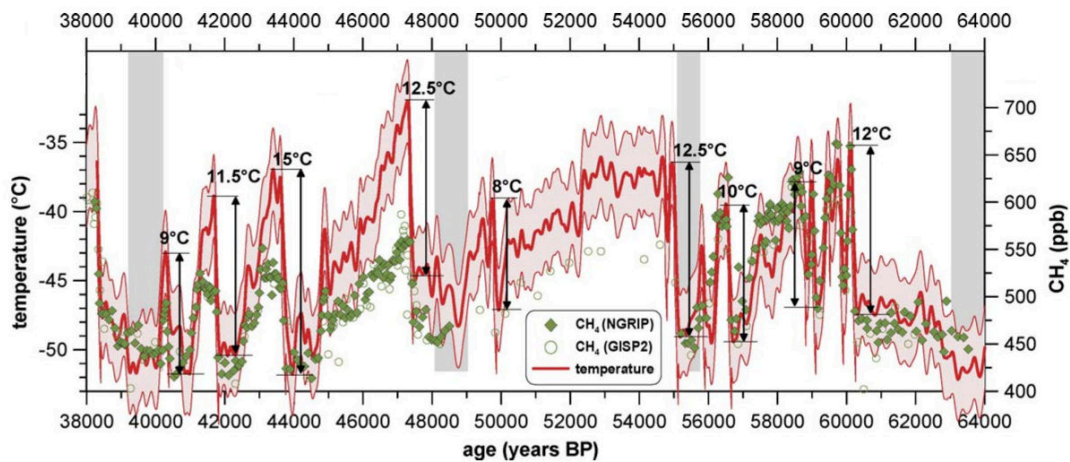


Figure 2.3 – Abrupt temperature rises (DO events) during the last glacial cycles as observed in Greenland ice cores. Figure from Huber et al. (2006b).

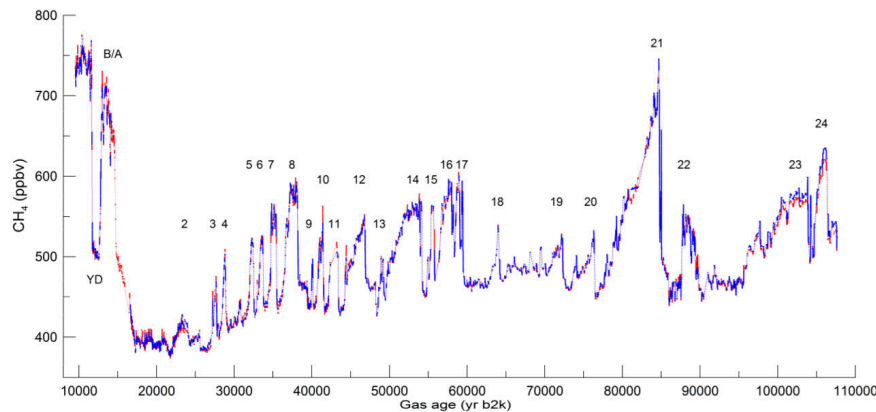


Figure 2.4 – Methane variations during the last glacial period. The abrupt methane variations are associated with DO events. Figure from Chappellaz et al. (2013).

2.1.3 Records of climatic variability in ice cores

Ice cores are used to access information about climate variability and its link with GHG concentrations. Polar ice is a material composed of two distinct phases: the ice and bubbles. By studying the physical and chemical properties of the ice and of the bubbles within, glaciologists can infer past conditions of the Earth' climate and of the atmosphere.

2.1.3.1 Temperature reconstruction

Ice cores can be used to estimate past temperatures over the Greenland and Antarctic ice sheets. In turn, this information can be used to better constrain our understanding of the

evolution of global temperatures in the past. The past temperatures can notably be estimated from ice cores thanks to the isotopic composition of the ice matrix (Dansgaard et al., 1993; Jouzel et al., 2007).

Water on Earth is present under different isotopic forms. The most common one is composed of two ^1H (simply referred to as H after) and one ^{16}O (referred to as O). Yet, other stable water isotopes are naturally encountered on Earth, notably under the form substituting one H atom for one ^2H (denoted D, for deuterium) or substituting the O for one ^{18}O atom. These two stables isotopes, HDO and H_2^{18}O are heavier than the more abundant H_2O , and therefore present slightly different physical properties.

Within the hydrological cycle, water evaporates from the oceans and does it with a certain isotopic composition. It contains less heavy isotopes compared to the ocean, usually referred to as the Standard Mean Ocean Water composition (or SMOW). Indeed, the evaporation of heavier isotopes is harder than the one of lighter isotopes. During their journey to the ice sheets, the air masses condensate and produce precipitations. As HDO and H_2^{18}O are heavier than H_2O , they precipitate more easily. This preferential precipitation of heavy isotopes acts as a distilling mechanism that impoverishes the air masses in heavy isotopes. The result of these combined mechanisms is that the air masses reaching the inland of ice sheets, where ice cores are drilled, are depleted in heavy isotopes compared to the original SMOW. However, the degree of depletion is dependent on the temperatures of the air masses (Dansgaard, 1953). During cold periods, the precipitations over the ice sheets are further depleted than during warmer periods. Climatologists and glaciologists therefore rely on the degree of depletion in heavy isotopes to infer past temperatures.

This degree of depletion of D and ^{18}O is usually expressed in δ units, following the formulas:

$$\delta\text{D} = \left(\frac{R^{\text{D}}}{R_{\text{SMOW}}^{\text{D}}} - 1 \right) \times 1000 \quad (2.1)$$

or

$$\delta^{18}\text{O} = \left(\frac{R^{18}\text{O}}{R_{\text{SMOW}}^{18}\text{O}} - 1 \right) \times 1000 \quad (2.2)$$

where R^X and R_{SMOW}^X are the concentration ratios between the rare isotopes X and the abundant H_2O , respectively in the sample of interest and in the SMOW.

Based on observations and on theories of isotopic fractionation, previous studies have revealed a linear relationship between the δ of D and ^{18}O , and the temperature of the precipitation over the ice sheet (Johnsen et al., 1989). This is the physical basis of the isotopic paleo-thermometer, as depicted in Figure 2.5. By measuring the relative abundance of heavy isotopes in the ice matrix forming ice cores, ice core scientists are able to infer temperature variations over large time scales.

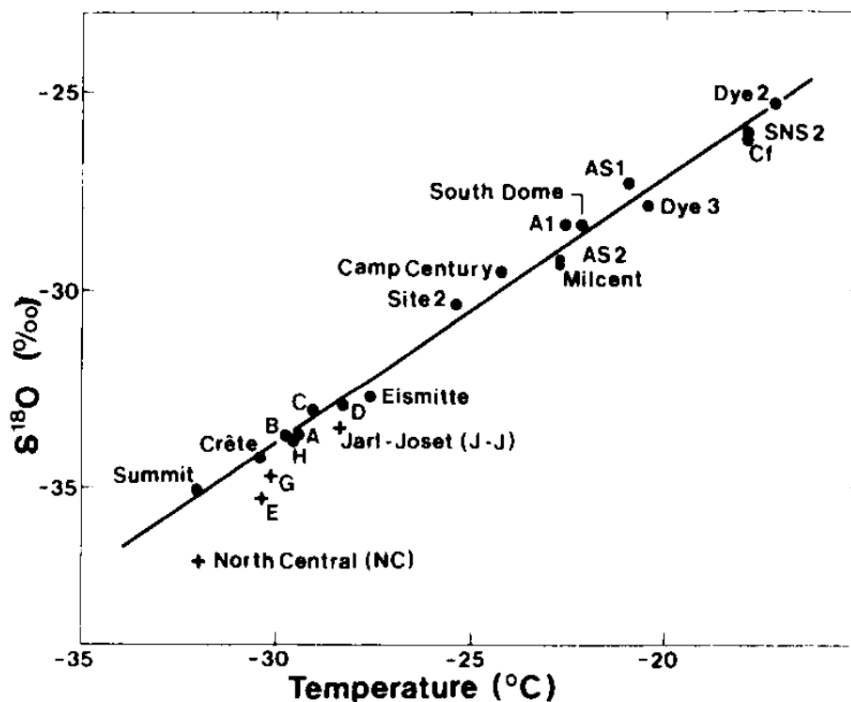


Figure 2.5 – Linear relationship between the mean $\delta^{18}O$ value and the the mean surface temperature at different Greenland sites. Figure from Johnsen et al. (1989)

2.1.3.2 GHG measurements

Bubbles found in ice cores are samples of past atmospheres (Stauffer et al., 1985). The air inside can be liberated and its concentration in greenhouse gases analyzed. Two of the major gases measured in ice cores bubbles are the carbon dioxide (CO_2) and methane (CH_4) (Louergue et al., 2008; Lüthi et al., 2008; Mitchell et al., 2013; Marcott et al., 2014).

Measuring carbon dioxide

To measure CO_2 , the air first needs to be extracted from the ice matrix. While a straightforward solution would be to melt the ice, this method is not suitable for CO_2 . Indeed, melting

the ice induces a chemical reaction between (hydrogen)carbonates and the ice acidity, that results in CO₂ as a product (Raynaud et al., 1982). This artificial production of CO₂ contaminates the air released from the bubbles, and thus carbon dioxide measurements must be performed without melt. This is achieved by crushing or sublimating the ice (Delmas et al., 1980; Wilson and Long, 1997; Schmitt et al., 2011). Once liberated the gas can be collected and sent to a CO₂ concentration analyzer, such as a gas chromatographic column coupled with an ion detector or a laser spectrometer.

Analyzing carbon dioxide is a labor intensive task. Even when fully operational, carbon dioxide analysis systems can rarely measure more than ten samples per day. Thus, CO₂ measurement campaigns span several months to several years, with spatial resolutions ranging from a few meters to a few ten of centimeters (Barnola et al., 1987; Lüthi et al., 2008; Marcott et al., 2014). To overcome these limitations, there is an ongoing effort to develop techniques able to continuously measured CO₂ in ice cores.

Measuring methane

Contrary to CO₂, methane can be extracted by melting the ice. A discrete sampling technique similar to CO₂ analysis has been developed, but where the ice is melted to liberate the gases (Chappellaz et al., 1990; Mitchell et al., 2013). In some systems, the water is slowly refrozen from the bottom after melting, in order to release the dissolved gases from the liquid phase (Chappellaz et al., 1990; Loulergue et al., 2008). The released methane can then be sent to either chromatographic column or a laser spectrometer for analysis. Like CO₂, this type of discrete measurements suffers from being labor intensive, as no more than 20 samples are usually measured per day.

To overcome these limits, a method based on the continuous melt, extraction, and concentration analysis has been developed in the last decade (Chappellaz et al., 2013; Rhodes et al., 2013). This technique is referred to as Continuous Flow Analysis (CFA). It enables to measure a large quantity of ice, with a spatial resolution around the centimeter, in a few days or weeks. This technique of measurement will be addressed in details in Section 3.1.

The parallel analysis of the ice isotopic composition and of the GHG concentrations of the bubbles trapped within, have highlighted the strong link between the Earth temperature

and the CO₂ and CH₄ concentrations (e.g., Lüthi et al., 2008; Shakun et al., 2012). The demonstration of this link is one of the great successes of ice core sciences. However, the precise interpretation of ice core gas records in terms of past atmospheric concentrations requires a good understanding of the mechanisms of gas trapping in ice cores. In order not to over-interpret the gas records of ice cores, it is important to properly characterize how gases get embedded in the ice and how this process affects the variability recorded in the ice.

2.2 From snow to firn and ice

The polar bubbly ice, in which ice cores are drilled, is formed due to the accumulation of snow at the surface of ice sheets. In these regions, snow does not melt during the summer season and accumulates over time. The fallen snow first transforms into firn, a name for compressed and dense snow, and eventually into airtight ice in which air bubbles are encapsulated (Stauffer et al., 1985). Our description of gas trapping thus naturally starts with the transformation of snow into ice, and the description of the firn structure.

2.2.1 Description of the firn column

Surface snow

Snow that falls on top of ice sheets is characterized by its low density, around 350kg.m⁻³ (Herron and Langway, 1980; Hörhold et al., 2011). In this condition, snow is a highly porous material and most of its volume is occupied by the interstitial pores rather than the ice matrix. The upper surface snow (typically above 2m depth) is subject to surface metamorphism due to the effects of temperature gradients and wind (Hutterli et al., 2009; Calonne et al., 2017). This type of metamorphism is controlled by water vapor fluxes due to gradients of concentrations resulting from the variations in curvature of the snow material surface and of the temperature gradients in the snowpack.

The processes involved are complex and not easily taken into account for the study of firn densification and gas trapping. Nonetheless, a link between the surface insolation and the quantity of gas trapped in the ice has been observed in deep ice cores (Raynaud et al., 2007;

Lipenkov et al., 2011). The same observation was made between the surface insolation and the ratio of O₂ to N₂ in bubbles (Bender, 2002; Lipenkov et al., 2011). This indicates that the metamorphism happening at the surface might ultimately influence the process of gas trapping, deeper in the firn.

This surface snow then gets buried under newly precipitated snow, starting its transformation first into firn and eventually into ice. The weight of the newly added precipitations put compressive stresses on the buried snow. In response to the mechanical stress, the ice phase of the snow get deformed and compressed (Maeno and Ebinuma, 1983; Herron and Langway, 1980). This compression is associated with an increase in density and consequently a reduction in the porous phase volume. The densification of snow into ice is usually divided into three zones or stages, depending on the mechanism driving the densification of the medium (Maeno and Ebinuma, 1983; Alley, 1987; Arnaud et al., 2000; Salamatin et al., 2009).

First stage of densification

For densities below 550kg.m⁻³, the deformation experienced by the snow-firn material is reported to be mainly due to geometrical rearrangement driven by the mechanism of aggregates sliding (Anderson and Benson, 1963; Alley, 1987; Arnaud et al., 2000). In this framework, an aggregate is viewed as an ice particle that moves relative to other aggregates, but does so without large deformations. The term of grain sliding is usually used in the literature to refer to aggregates sliding. The sliding of ice aggregates results in a tighter arrangement, and thus an increase in density. However, this denser arrangement also tends to limit the possibility of movement of the ice aggregates (Alley, 1987). Thus, the mechanism of aggregates sliding gradually slows down and eventually stops being the dominant mechanism of densification.

While the mechanism of aggregates sliding is reported to dominate the first stage of densification, there is little observations to support it. This vision mainly originates from the fact that there is a change in densification speed for densities around 550kg.m⁻³, the density of a close packing of spheres (Anderson and Benson, 1963). This suggest that the mechanism of densification at low density is hindered due to geometrical effects.

Second stage of densification

For densities above $550\text{kg}\cdot\text{m}^{-3}$, the main mechanism responsible for the compression of firn is the creep of the ice matrix due to the presence of dislocations in the ice crystals (Wilkinson and Ashby, 1975; Arzt et al., 1983; Maeno and Ebinuma, 1983). Under the creep deformation of the ice phase, the firn keeps increasing in density and consequently keeps losing porous volume. This second stage of firn densification encompasses most of the firn column. With the increase in density, the pores of the firn eventually pinch and become bubbles that encapsulate the air (Stauffer et al., 1985; Shieh and Evans, 1991; Schaller et al., 2017). This marks the transition between the porous firn and the airtight ice. The firn-ice transition, marking the end of the firn column, is located between about 50 to 120m below the ice sheet surface, depending on the local temperature and accumulation conditions (Witrant et al., 2012). Moreover, this transition from firn to ice does not happen instantaneously but rather spans a depth range of about 10m between the formation of the first and last bubbles (Schwander and Stauffer, 1984; Schwander et al., 1993). This firn-ice transition zone will be referred to as the pore closure zone for the rest of the manuscript.

Third stage of densification

Finally, below the pore closure zone, the densification of bubbly ice is still controlled by the ice matrix creep, but it is necessary to take into account the pressure increase in bubbles and its effect on the mechanical deformation (Wilkinson and Ashby, 1975; Maeno and Ebinuma, 1983). The effect of bubble pressure is taken into account by considering the pressure drop between the overburden pressure of the ice column and the building pressure in the bubbles (Wilkinson and Ashby, 1975; Lipenkov et al., 1997; Lipenkov, 2000). During the third stage of densification, the air remains entrapped in the ice and its composition no longer changes (apart from possible radioactive decays and in situ production). Since this third stage of densification does not impact the gas concentrations recorded in polar ice, it will not be discussed in this thesis.

The pore closure zone is of particular interest for the study of gas trapping as this is the zone where most the air gets embedded in the ice. Lipenkov (2000) and Ueltzhöffer et al. (2010) report the presence of microbubbles already sealed in shallower parts of the firn. However, as pointed out by Lipenkov (2000), these microbubbles only account for 0.3% of the air entrapped in deep ice. We can therefore neglect them for our study of gas trapping, as they do not impact the recorded concentrations in the ice.

The transition from firn to airtight ice is not only characterized by the increase in the medium density, but also by the transformation of open pores (connecting to the atmosphere) into sealed bubbles, also referred to as a closed pores. This transformation from open to closed pores can be quantified using the open and closed porosity volumes. Indeed, fully open firn is characterized by a zero closed porosity volume. On the other hand, airtight ice is characterized by a zero open porosity volume. Naturally, partially open firn is characterized by a spectrum of non zero open and closed porosity volumes. The degree of closure of a firn stratum can easily be characterized by comparing the open and closed volumes. Measurements of the open and closed porosity volumes have been performed, and are notably reported by Schwander et al. (1993) and Trudinger et al. (1997) for the sites of Summit in Greenland and DE08 in Antarctica. In both cases, at low density the firn is characterized by a zero closed porosity volume, indicating a fully open porous network. Then, for densities around $800\text{kg}\cdot\text{m}^{-3}$ the closed porosity volume starts to increase with density, indicating the gradual transformation of open pores into bubbles. Then, for densities above $850\text{kg}\cdot\text{m}^{-3}$ the closed porosity volume decreases, due to the compression of the bubbles with the densification of the medium.

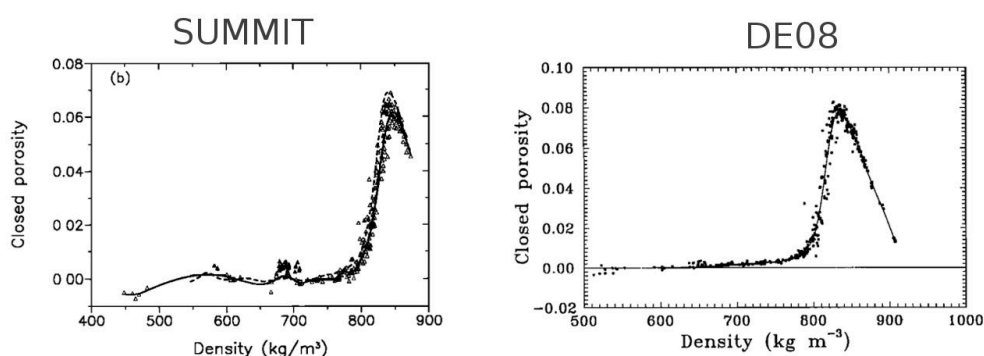


Figure 2.6 – Closed porosity volumes measured in the Summit and DE08 firns. Summit figure from Schwander et al. (1993) and DE08 figure from Trudinger et al. (1997).

2.2.2 Stratification of the firn

Up to now, the laid out vision of the firn has been the one of a medium with a continuous increase of density with depth. While this vision is adequate when considering the firn at a scale of the order of the meter, it no longer accurately describes the state of the firn at the centimeter scale. Indeed, as notably reported by Fujita et al. (2009) or Hörhold et al. (2011), polar firns are characterized by a strong stratification, particularly apparent in terms of density.

The different snow events at the surface of the ice sheet, coupled with the metamorphism induced by the different atmospheric and surface conditions, tend to create a heterogeneous layering near the surface of the firn column (Calonne et al., 2017). Fujita et al. (2009) and Hörhold et al. (2011) report density variations of the order of $35\text{kg}\cdot\text{m}^{-3}$ at the surface of firns from Greenland and Antarctica. This corresponds to a 10% variability when compared to the typically observed density of $350\text{kg}\cdot\text{m}^{-3}$. As seen in Figure 2.7, the upper part of the firn is characterized by a decrease in the density variability with depth, indicating that initially low density firn (ILDF) densify faster than initially high density firn (IHDF). Then, for densities around $650\text{kg}\cdot\text{m}^{-3}$ the density variability starts to increase with depth. This indicates that different firn layers densify at different speeds despite having similar densities.

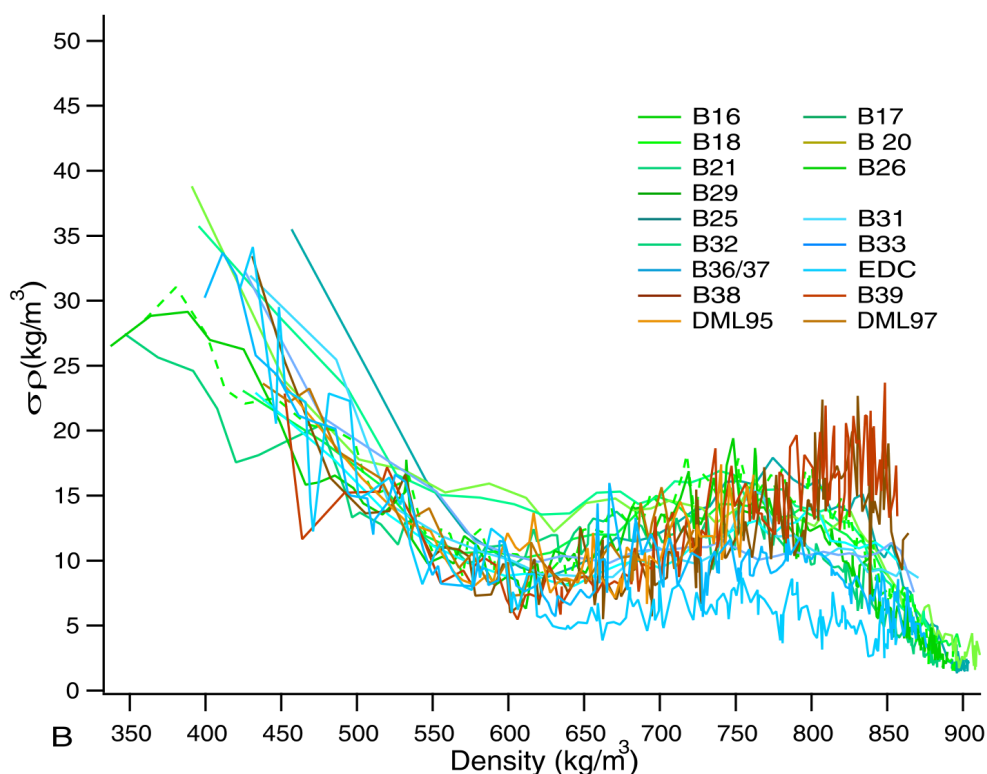


Figure 2.7 – Density variability observed in several firn cores from Greenland and Antarctica. The density variability decreases with increasing density until mean densities of about $650\text{kg}\cdot\text{m}^{-3}$ are reached. Then, the density variability increases towards a second maximum. Figure from Hörhold et al. (2011).

Two mechanisms have been advanced to explain this observation. Fujita et al. (2009) argue that this difference is due to a difference in the ice matrix structure of the firn. They propose that IHDF is due to surface metamorphism, inducing bond like structures between

the ice aggregates of the firn. Because of these bonds, an IHDF stratum densify slower than its ILDF counterpart. IHDF and ILDF reach a similar density around the $650\text{kg}\cdot\text{m}^{-3}$ value, corresponding to the minimum of density variability. After that, the ILDF keeps densifying faster and the density variability thus increases with depth. This mechanism of different densification rate for the IHDF and ILDF is justified by the observations of the anisotropy of the firn structure. As displayed in Figure 2.8, at the surface of the firn dense layers are characterized by a strong structural anisotropy. With the increase in density, the anisotropic layers become less dense than the less anisotropic ones. This suggests that the IHDF strata become the less dense strata.

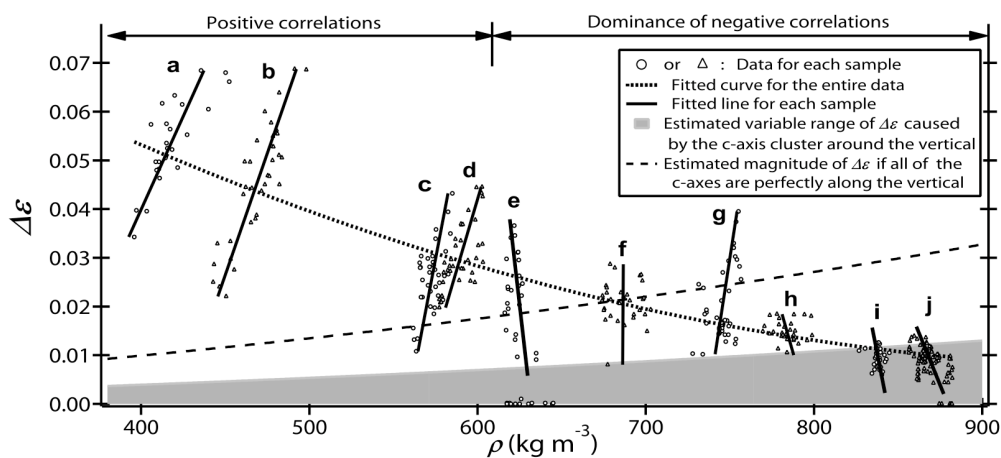


Figure 2.8 – Variations of the firn anisotropy (represented by the variable $\Delta\epsilon$) with the increase in density. The transformation of the anisotropic IHDF strata into the less dense strata is illustrated by the counter clockwise rotation of the $\Delta\epsilon$ - ρ relationship in the curves a-j. Figure from Fujita et al. (2009).

The second proposed mechanism is based on the observation of a building correlation with depth between density and chemical content by Hörhold et al. (2012), as illustrated in Figure 2.9. In this idea, firn strata with a high ionic content densify faster than the rest of the firn. The preferential deformation of ion-rich strata creates the firn stratification observed for density higher than $650\text{kg}\cdot\text{m}^{-3}$. Finally, the link between chemistry and density in strata was confirmed by Fujita et al. (2016) based on three firn cores from Dome Fuji, Antarctica. This link is illustrated in a Dome Fuji firn core in Figure 2.10. They however, argue that the firn stratification is the combined result of both the effect of the ice matrix structure (due to surface metamorphism) and the effect of chemical impurities.

The firn-ice transition inherits the stratified characteristics of the firn column. Hörhold et al. (2011) compiled density variabilities observed at the bottom of firns from Greenland and Antarctica. They report variabilities between 4.5 and $14.5\text{kg}\cdot\text{m}^{-3}$ depending on the sites

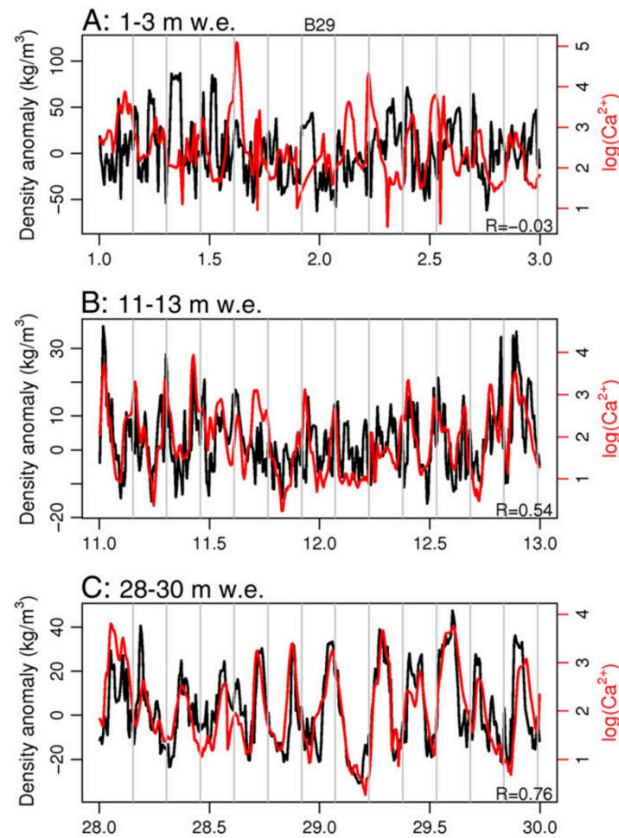


Figure 2.9 – Development with depth of the correlation between density and the calcium concentrations in the B29 ice core, Greenland. Modified from Hörhold et al. (2012).

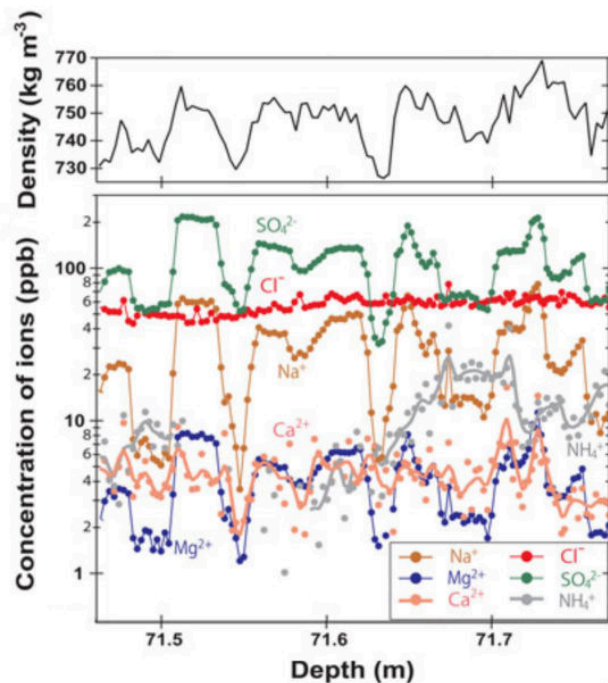


Figure 2.10 – Correlations between the firn density and the major ion concentrations in a Dome Fuji firn core. Modified from Fujita et al. (2016).

where the firn cores were drilled. Cold and low accumulation sites, as encountered on the East Antarctic plateau, tend to have the lowest density variability at the firn-ice transition.

Hörhold et al. (2011) notably report a variability of $4.5\text{kg}\cdot\text{m}^{-3}$ for the East Antarctic site of Dome C.

This layering of the firn column has been reported before the work of Fujita et al. (2009) and Hörhold et al. (2011), for instance by Schwander and Stauffer (1984), Etheridge et al. (1992), or Martinerie et al. (1992). Schwander and Stauffer (1984) notably measured the closed porosity volume in the stratified pore closure zone of a firn column. As depicted in the left panel of Figure 2.11, they observe that similarly to density, closed porosity volumes exhibit a strong and heterogeneous stratification. However, they point out that when plotted versus density, the closed porosity data show a much smaller scatter as seen in the right side of Figure 2.11. This indicates that there is functional dependence of the closed porosity toward density, and this in spite of the strong layering observed in the firn.

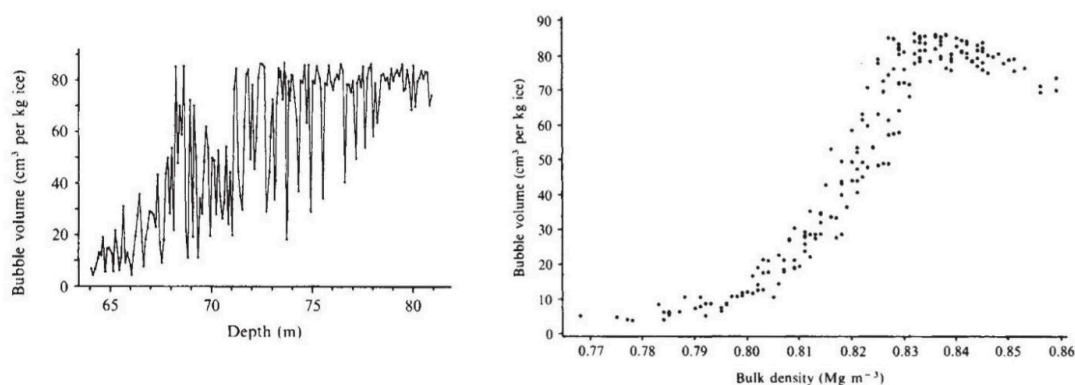


Figure 2.11 – Stratification of the closed porosity in the trapping zone. When observed as a function depth, the heterogeneity is strong. When observed as a function of density, the scattering is strongly reduced. Figures from Schwander and Stauffer (1984).

2.2.3 Deformation of the ice matrix

The second stage of firn densification, including the transition from firn to ice, is due to the creep of the ice matrix under the compressive stress imposed by the overlying column. Therefore, a particular attention will be placed on the physical mechanism of ice creep deformation.

Creep of the ice single crystal

Ice is a crystalline material formed of bonded water molecules. In the ice material, the water molecules are periodically arranged and follow a specific crystalline structure. For the pressures and temperatures naturally observed on Earth, the ice crystal has an hexagonal

structure, referred to as I_h and depicted in Figure 2.12. It is characterized by three crystallographic axes, including the c axis whose normal plane is the basal plane. As optical methods measure the orientation of the c axis, the crystalline orientation of a single crystal is usually summarized by its c axis only. Moreover, as the orientation of the c axis has more repercussion of mechanical properties of the crystal than the orientation of the two others axes, the knowledge of the c axis orientation only is usually sufficient to characterize the properties of the crystal.

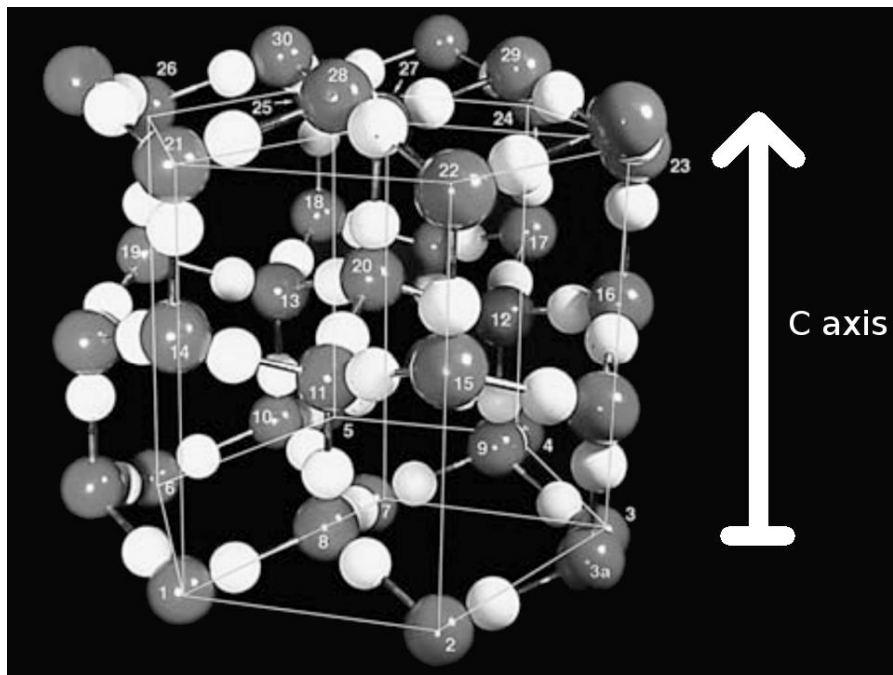


Figure 2.12 – Sticks and balls model of the hexagonal structure of the ice crystal. The numbered gray balls are the oxygen atoms. The white balls are the hydrogen atoms. The orientation of the c axis is displayed on the right side. Modified from [Schulson and Duval \(2009\)](#).

This hexagonal structure confers anisotropic properties to the ice material, and notably anisotropic mechanical properties. It is indeed much easier to break the bonds between two basal planes, rather than the bonds inside a basal plane. For this reason, shear stresses applied parallel to the basal planes (basal glide) will result in more displacement than if applied perpendicularly to the basal planes (non-basal glide). This is clearly seen on the data reported by [Duval et al. \(1983\)](#) and displayed in Figure 2.13. For a given axial stress, basal glide strain rates are up to 3 orders of magnitude higher than non-basal glide ones.

Creep of poly-crystalline ice

Natural ice is rarely composed of a single crystal, but rather of a multitude of small single crystals juxtaposed next to each others. Two different single crystals are thus regions characterized by different crystallographic axes, and the junction between two ice crystals

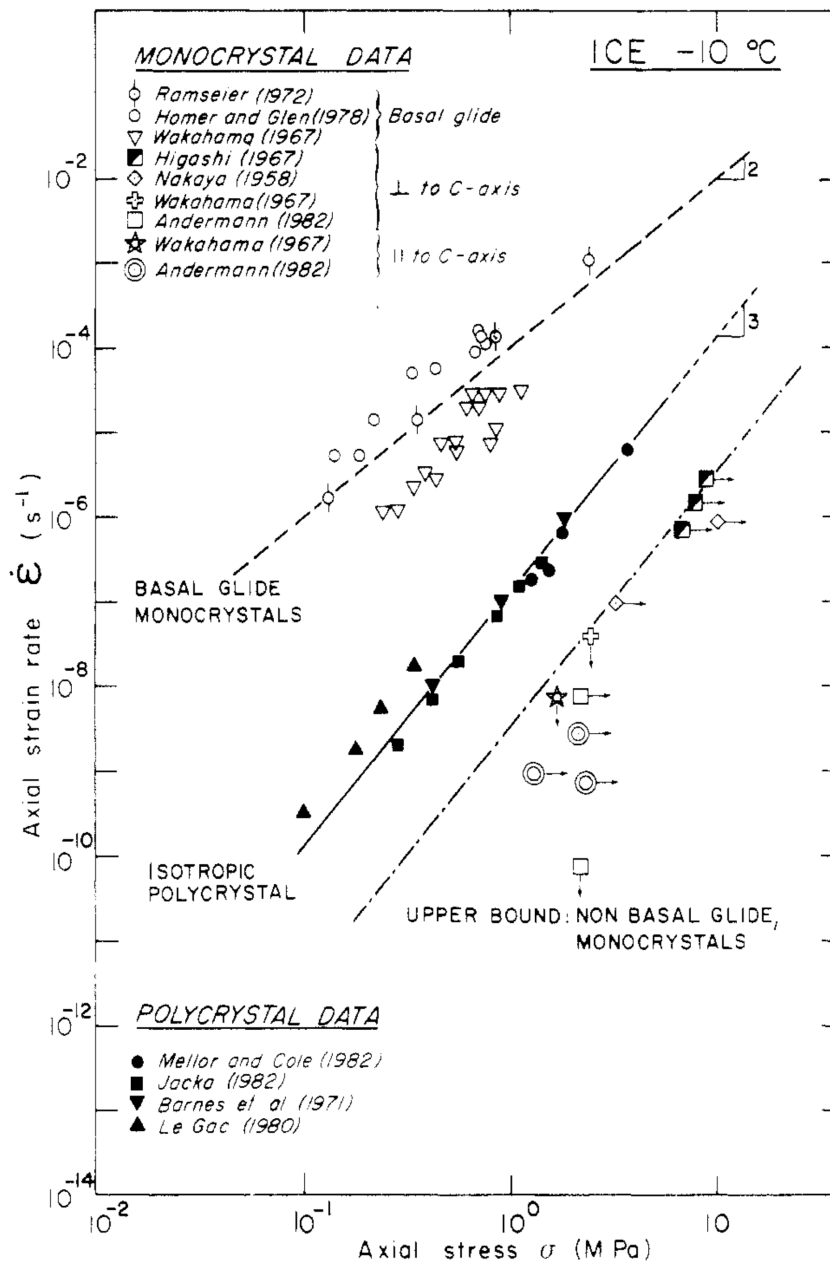


Figure 2.13 – Relationship between strain rate and stress for an axial deformation of ice. The data include basal glide of mono-crystalline ice (upper line), non-basal glide of mono-crystalline ice (lower line), and isotropic poly-crystalline ice (middle line). Figure from Duval et al. (1983).

is referred to as a grain boundary.

The mechanical behavior of poly-crystalline ice is therefore the result of the collective behavior of its multiple constitutive single crystals. In the case where the orientations of the single crystals are uniformly distributed in space, the poly-crystal behaves as an isotropic material. On the other hand, if the single crystal population has a preferential orientation the anisotropy of the single crystal is transferred to the poly-crystalline material, that now exhibits a mechanical anisotropic behavior.

Duval et al. (1983) compiled creep deformation data obtained for isotropic poly-crystalline ice. As seen in Figure 2.13, poly-crystalline ice is less easily deformed than a single crystal under basal gliding, but more easily than a single crystal under non-basal gliding.

Under the stress and temperature conditions encountered in polar firns, it is commonly assumed that the ice material deforms according to a stationary creep (also referred to as secondary creep, Duval et al., 1983; Schulson and Duval, 2009). In this case, the strain rates are linked to the stresses by Glen's law (sometimes referred to as Norton's law):

$$\dot{\epsilon}_{ij} = A\tau^{n-1}\sigma'_{ij} \quad (2.3)$$

where $\dot{\epsilon}_{ij}$ are the strain rate tensor components, $\sigma'_{ij} = \sigma_{ij} - 1/3 \text{Tr}(\sigma)\delta_{ij}$ are the deviatoric stress tensor components (σ being the stress tensor and δ_{ij} the Kronecker delta), and $\tau = \frac{1}{2} \sum_{ij} (\sigma'_{ij})^2$.

The physical parameter n is the stress exponent, which represents the non-linear behavior of the ice material. Values near 3 are reported for this parameter, when estimated in laboratory conditions (Duval et al., 1983; Lipenkov et al., 1997). It can be visualized in Figure 2.13, where the strain rates relationship with stress has a slope of about 3 for isotropic poly-crystalline ice. However, values around 2 are estimated for deviatoric stresses inferior to 0.2MPa (Pimienta and Duval, 1987; Schulson and Duval, 2009).

The parameters A represents the fluidity of the ice material. It is the inverse of its viscosity. This parameter is dependent on the temperature, following an Arrhenius type law with an activation energy around 60 to 80kJ.mol⁻¹ (Duval et al., 1983; Lipenkov et al., 1997; Schulson and Duval, 2009). This temperature dependence implies that the firn of East Antarctica should deform and densify slower during glacial periods than during interglacial ones. However, based on modeling and estimation of past firn heights, Bréant et al. (2017) argue that this reduction of densification in glacial firns is not supported by observations. Yet, the physical basis of this sustained deformation of firn at very-low temperature is still unclear.

Effect of impurities

Mechanical experiments on ice doped with impurities have been performed in late 1960's. Jones (1967) and Jones and Glen (1969) focused on the effect of hydrofluoric (HF) doping. They observed that doping with HF has a softening effect on the ice, meaning that the deformation of the ice material is facilitated and greater strain rates are observed. Similarly, Nakamura and Jones (1970) studied the influence of hydrochloric doping on the ice creep properties. They found a softening effect and facilitated deformation, similar to the one observed for HF. The softening effects observed in these studies are consistent with the hypothesis proposed by Hörhold et al. (2012) or Fujita et al. (2016) for the chemically induced stratification of polar firn.

2.3 The porous network and the gases inside

2.3.1 Firn from the standpoint of gases

From the point of view of the air filling the pores of the firn, the column is generally divided in three main zones: the convective, diffusive and lock-in zones.

The convective zone

The convective zone is the upper part of the firn column. It is the zone in which the air inside the pores exchange rapidly with the atmosphere above the surface. This fast exchange is due to the mechanism of wind pumping (Colbeck, 1989). In the convective zone, the air composition inside a pore is thus similar to the one of the atmosphere. Measurements performed at the Vostok Antarctic site indicates a convective zone spanning 13m (Bender et al., 1994), while measurements performed at at South Pole suggest an almost inexistent convective zone (Battle et al., 1996). Other values of convective zone thicknesses are reported by Severinghaus et al. (2010). It is not clear however, how the thickness of this zone changes with climatic conditions (Dreyfus et al., 2010; Capron et al., 2013).

The diffusive zone

The end of the convective zone marks the start of the diffusive zone, in which the air is no longer rapidly mixed with the atmosphere by the surface wind. In that zone, the primary

mechanism responsible for gas transport is the molecular diffusion in the pore space. It induces a slow mixing of the gases inside the open porosity of the firn. The diffusive zone is notably characterized by the gravitational fractionation of stable isotopes (Craig et al., 1988; Orsi et al., 2014), leading to an enrichment of the air in heavy isotopes with depth. In the diffusive zone, the air still exchange with the atmosphere over timescales of months to years depending on the depth (Buizert et al., 2012; Petrenko et al., 2013; Witrant et al., 2012).

The lock-in zone

Based on inert gas isotope measurements, whose atmospheric concentrations are constant over time, previous studies have highlighted that in some firns, the diffusive fractionation stops before the full closure of the pores (Sowers et al., 1992; Schwander et al., 1993; Landais et al., 2006). This indicates that deep in these firns, the diffusive movement of gases becomes too slow to sustain the barometric equilibrium in the open pores of the firn. In that sense, the air is locked in the pores (it does not exchange easily with the surrounding strata or the atmosphere) without being entrapped in bubbles. This zone is referred to as the Lock-in zone (LIZ), or the non-diffusive zone. The depth marking the onset of the LIZ is referred to as the Lock-In depth (LID). However, it is important to note that low accumulation firns such as Dome C or Vostok do not exhibit LIZ, that is to say a plateau in inert gas isotope composition (Landais et al., 2006; Witrant et al., 2012). In this case, the gases can diffuse until the very end on the firn column.

The three different zones, and their correspondence with the gravitational isotopic fractionation of an inert gas is summarized in Figure 2.14. The pore closure zone, corresponding to the pinching of the pores into bubbles, is also represented in the figure.

Age difference between the gas and the surrounding ice

As air is enclosed at the bottom of the firn column, it is always younger than the surrounding ice (Schwander and Stauffer, 1984; Sowers et al., 1992). The age difference between the gases and the encapsulating ice is referred to as Δ age and ranges from a few decades to a several thousands of years (Trudinger et al., 1997; Bazin et al., 2013; Veres et al., 2013). It is necessary to take it into account to temporally synchronize measurements performed in the ice (such isotopic analysis) and measurements performed in the bubbles (Caillon et al., 2003; Parrenin et al., 2013; Marcott et al., 2014).

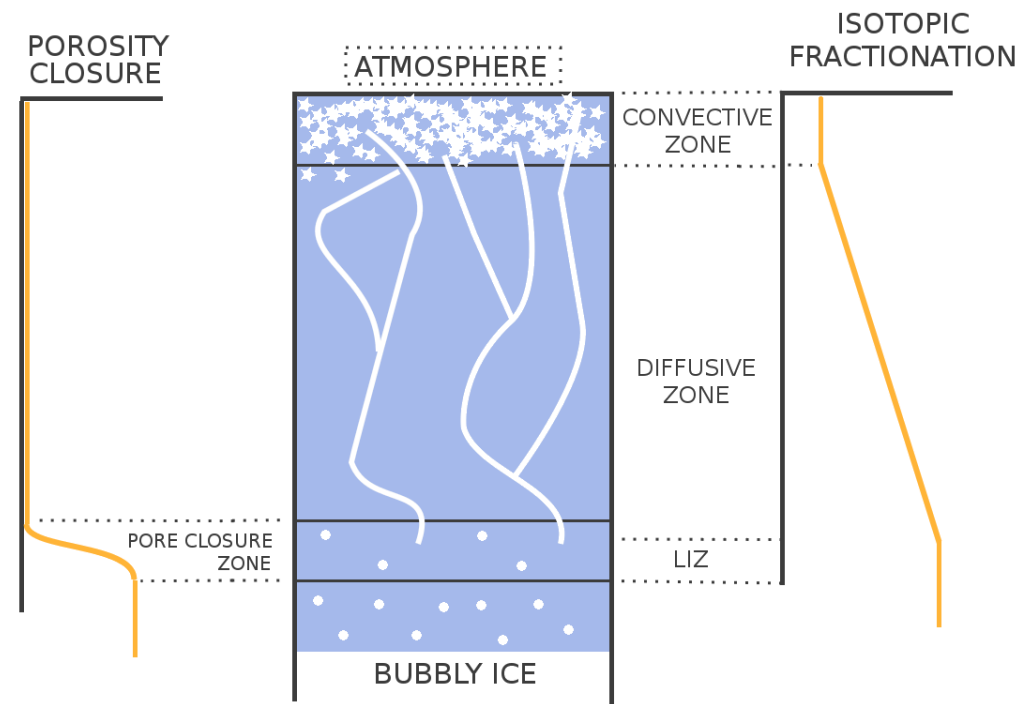


Figure 2.14 – Schematic of a polar firn column. The right side curve illustrates the isotopic fractionation of an inert gas in the diffusive zone, and the plateau reached in the LIZ. The left side curve illustrates the progressive closure of pores in the pore closure zone. Note that in the case of low accumulation firns, the LIZ may not exist.

2.3.2 Air content of polar ice

When bubbles close at the bottom of the firn, they enclose a certain quantity of air. This quantity of air can be quantified, and is referred to as the air content or AC (Raynaud and Lebel, 1979; Martinerie et al., 1992; Lipenkov et al., 1995). It is expressed in cm^3 of air at standard temperature and pressure (STP, defined as $T_0 = 273.15\text{K}$ and $P_0 = 1013\text{hPa}$) per gram of ice material. Due to the conservation of mass, this quantity is constant in a given ice volume, despite the deformation and physical changes that the ice might go through.

Following Raynaud and Lebel (1979), if the temperature and pressure of the air in the pores are known, the air content of an ice core can be used to estimate the total porous volume at isolation V_i :

$$V_i = \text{AC} \frac{P_0 T_i}{T_0 P_i} \quad (2.4)$$

where T_i and P_i are the temperature and pressure in the pores at the moment of isolation from the atmosphere. It is important to note that V_i is not the volume of the porosity when a firn stratum completely stops exchanging with the atmosphere. Rather, it is the sum of the individual pore volumes when they individually stop exchanging with the atmosphere

(Martinerie et al., 1992). Due the compression of pores in the trapping zone, the total porous volume at isolation V_i is always larger than the porous volume at complete closure. Still, V_i can be used to estimate ρ_c , the typical density of the firn during closure (Raynaud and Lebel, 1979; Martinerie et al., 1992).

$$\rho_c = \frac{\rho_{ice}}{1 + V_i \rho_{ice}} \quad (2.5)$$

Variations of ρ_c and V_i can be used to quantify variations in the gas trapping characteristics between different sites. Martinerie et al. (1992) report that the volume V_i decreases with the temperature site, as displayed in Figure 2.15. This indicates that trapping of gases occurs at higher density in cold firns.

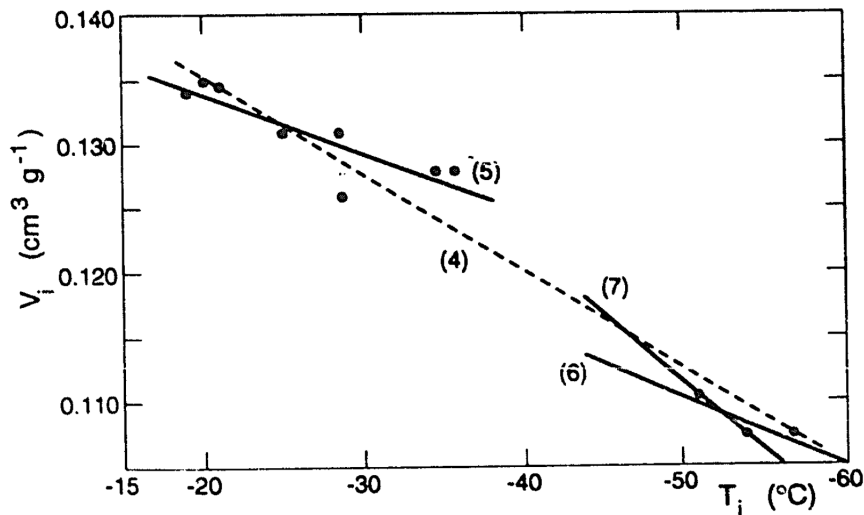


Figure 2.15 – Variations of total volume at isolation V_i as a function of the temperature of the site. The various lines are proposed linear regressions. Figure from Martinerie et al. (1992).

Finally, Raynaud et al. (2007) report a covariation between the air content of the EPICA Dome C ice core and the surface insolation, that is related to the orbital parameters of the Earth. Particularly, it appears that the air content of the ice is related to the obliquity of the Earth's orbit, that is characterized by a 41,000 years cyclicity. This implies that air content could be used as a absolute time marker for the dating of ice cores (Raynaud et al., 2007; Lipenkov et al., 2011). The proposed mechanism for this link relates to the presence of temperature gradient metamorphism at the surface of the firn column (Raynaud et al., 2007; Hutterli et al., 2009).

2.4 Modeling the firn and gas trapping

Gas trapping models have been developed in order to predict the age of the gases trapped in polar ice. The modeling of gas trapping can be divided in two main steps. First, the density profile of the firn has to be known. This can either be achieved by models or by direct field observations and measurements. Once the firn density is characterized, the proper gas transport and trapping can be modeled. Some models are thus specialized in firn densification (Herron and Langway, 1980; Arnaud et al., 2000; Lundin et al., 2017), some others solely address gas transport and trapping (Rommelaere et al., 1997; Buizert et al., 2012; Witrant et al., 2012), while some attempt to describe both firn densification and elements of gas trapping (Goujon et al., 2003).

2.4.1 Firn densification models

The primary characteristics of firn is its density, as it naturally describes the transformation of surface snow into airtight ice, as well as the constriction of the porous network. Moreover, the density of a firn column is a quantity that can directly be measured, and can therefore be used to access the model predicting capabilities. For these reasons, density is the primary quantity addressed by firn models (Lundin et al., 2017).

One of the pioneer firn densification model is the one proposed by Herron and Langway (1980). It is based on the observations of density-depth profiles in Greenland and Antarctic firn cores. In this framework, the firn column is divided in two zones, above and below a density of $550\text{kg}\cdot\text{m}^{-3}$. The rate of change of a firn stratum density ρ in each zone is given by:

$$\frac{d\rho}{dt} = k_0 A^a (\rho_{\text{ice}} - \rho) \quad \text{for } \rho < 550\text{kg}\cdot\text{m}^{-3} \quad (2.6)$$

and

$$\frac{d\rho}{dt} = k_1 A^b (\rho_{\text{ice}} - \rho) \quad \text{for } \rho > 550\text{kg}\cdot\text{m}^{-3} \quad (2.7)$$

where ρ_{ice} is the density of pure ice, A is the accumulation rate, and k_0 , k_1 , a and b are physical parameters that have been experimentally tuned. Herron and Langway (1980) assume that the parameters k_0 and k_1 obey an Arrhenius type dependence to temperature.

While this model is not based on physics first principles, the distinction between the two zones is interpreted as the transition from one dominant mechanism of densification to another. This is consistent with the distinction between the first and second stage of densification presented in Section 2.2.1 (Anderson and Benson, 1963; Maeno and Ebinuma, 1983; Alley, 1987).

The Herron and Langway (1980) model has notably been revised by Freitag et al. (2013) to include the effect of chemical impurities. For this purpose, they introduce a dependence of the densification rate on the concentration of Ca^{2+} ions in the firn. As seen in Figure 2.16, with the addition of a calcium ion parametrization the model of Freitag et al. (2013) is able to represent the stratified nature of the firn, a point not addressed in the original Herron and Langway (1980) formulation.

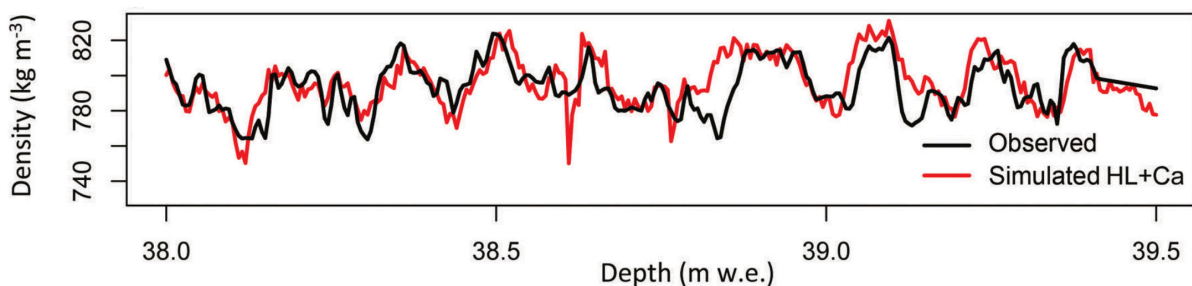


Figure 2.16 – Modeling of the firn density variability including ion softening due to chemical impurities. Figure from Freitag et al. (2013).

While empirical models such as the one proposed by Herron and Langway (1980) yield relatively good results for firns where they can be tuned to, they are not easily applied outside of their calibration range. Notably, their use for paleoclimatic applications suffer from their reliance on empirical data. To overcome this issue, firn densification models relying on a more physically-based representation of the firn have been introduced. Notably, Arnaud et al. (2000) propose a model based on the work of Arzt (1982) on the hot isostatic pressing of powders. This model also divides the firn column in two zones.

For densities below $550\text{kg}\cdot\text{m}^{-3}$ the main densification mechanism is assumed to be the sliding and rearrangement of ice aggregates (Alley, 1987). The equation governing the density

change is:

$$\frac{dD}{dt} = \gamma \left(\frac{P}{D^2} \right) \left(1 - \left(\frac{5}{3} \right) D \right) \quad (2.8)$$

where $D = \rho/\rho_{\text{ice}}$ is the relative density of ice, γ is a physical parameters depending on the ice viscosity and on the ice clusters geometry, and P is the overburden pressure on the firn. Note that the original derivation of [Alley \(1987\)](#) assumes an idealized spherical geometry for the ice aggregates.

For density above $550\text{kg}\cdot\text{m}^{-3}$, the main driving mechanism for densification in the [Arnaud et al. \(2000\)](#) model is assumed to be the sintering and creep of the ice clusters. Following the derivation of [Arzt \(1982\)](#), that assumes spherical ice aggregates at the beginning of this densification stage, the governing equation of this stage is:

$$\frac{dD}{dt} = 5.3A(D^2D_0)^{1/3} \left(\frac{a}{\pi} \right)^{1/2} \left(\frac{P^*}{3} \right)^n \quad (2.9)$$

where

$$P^* = \frac{4\pi P}{aZD} \quad (2.10)$$

with P is the pressure of the above firn column, Z is the coordination number, a is the average contact area expressed in units of R^2 (R being the radius of the ice aggregates before compression), A is a physical parameter with an Arrhenius dependence on temperature, and D_0 is the relative density at the beginning of the second stage.

The [Arnaud et al. \(2000\)](#) model is therefore derived from a physical representation, despite its reliance on strong simplifying assumptions concerning the geometry of the ice aggregates constituting the firn material. The diffusion of heat has been implemented in the [Arnaud et al. \(2000\)](#) model by [Goujon et al. \(2003\)](#), notably to be used in paleoclimatic studies.

Yet, the [Arnaud et al. \(2000\)](#) model do not manage to adequately represent the past variations of firn heights on the East Antarctic plateau, as estimated from ice core data ([Capron et al., 2013](#)). Specifically, the firn model overestimate the height of the firn column for the very cold sites of East Antarctica during glacial conditions. [Bréant et al. \(2017\)](#) propose

two revisions to the model to improve the agreement with data. First, they introduce a parametrization for the enhancement of ice creep due to the presence of impurities, similarly to Freitag et al. (2013). Secondly, they argue that at temperatures below -60°C a physical mechanism becomes dominant for the creep of ice, and balance the reduction of the mechanism responsible for creep at higher temperatures. Consequently, in the case of very cold firn, the creep of ice is not as slow as one would expect in the case of a single mechanism and the firn densify faster. Yet, this mechanical behavior of ice is not supported by laboratory experiments.

2.4.2 Gas trapping models

The sole knowledge of firn density is not enough to characterize the enclosure of gases in polar ice. Indeed, to fully describe the trapping of gases it is necessary to take into account the progressive closure of the porosity, as well as the diffusive mixing of gases in the firn open porosity.

Closure of the porosity

As displayed in Figure 2.6, the open pores progressively transform into closed bubbles for densities around $850\text{kg}\cdot\text{m}^{-3}$. The amount and the age of the trapped gases depend on how this progressive closure takes place, and it therefore has to be included in gas trapping models. For sites where firn core are available, the amount of closed pores can be measured using gas pycnometry (Stauffer et al., 1985) or tomographic imagery (Gregory et al., 2014; Schaller et al., 2017; Burr et al., 2018). Yet, during the excavation of the firn samples some closed pores are open (Martinerie et al., 1990). This leads to an underestimations of the measured closed porosity, that should ideally be corrected for (Schaller et al., 2017).

In cases where the closed porosity volumes cannot be directly measured, for instance for glacial firns that no longer exist, the closed porosity has to be estimated with the aid of pore closure models or of empirical laws.

Using closed porosity data, JM Barnola derived a relationship between the density and the amount of closed pore in a firn stratum. This empirical law was first introduced in the article of Goujon et al. (2003) and writes:

$$P_{\text{closed}} = \gamma P_{\text{total}} \left(\frac{P_{\text{total}}}{P_c} \right)^{-7.6} \quad (2.11)$$

where P_{closed} is the closed porosity (volume fraction occupied by the closed pores), P_{total} is the total porosity (volume fraction occupied by the closed and open pores), γ is a constant equals to 0.37, and where P_c the total porosity at isolation is given by:

$$P_c = 1 - \frac{\rho_c}{\rho_{\text{ice}}} \quad (2.12)$$

with ρ_c the density during closure deduced from air content measurements following Equation 2.5. This Barnola parametrization of the closed porosity has since then been used other in articles and models to estimate the progressive closure of bubbles (Buizert et al., 2012; Witrant et al., 2012). Yet, the proper derivation of this parametrization has not been published in the peer-reviewed literature yet.

The use of the Barnola parametrization requires the knowledge of the density during closure ρ_c . This quantity can be estimated using air content data when they are available. In the absence of available data, Goujon et al. (2003) proposed to use the linear relationship between site temperature and total porous volume at isolation V_i , as reported by Martinerie et al. (1994):

$$V_i = 6.95 \times 10^{-4} T - 0.043 \quad (2.13)$$

where the temperature T is expressed in K and the volume V_i in cm^3 per gram of ice. Using Equations 2.5, 2.11, and 2.13 one can thus estimate the progressive closure of pores for various temperature conditions. The resulting closed porosity for a temperature of -55°C is displayed in Figure 2.17. This approach can notably be used for the studies of past firns, as temperatures can be estimated with isotopic data.

Other parametrizations of the closed porosity have been proposed. One of them was proposed by Mitchell et al. (2015) and assume that not all firn layers close at the same density. Moreover, the formulation of Mitchell et al. (2015) also includes the effect of firn layering

on the amount of closed bubbles. In this framework, the bulk closed porosity relates to the bulk total porosity with:

$$\langle P_{\text{closed}} \rangle = \langle P_{\text{total}} \rangle \left(1 - \phi(u, 0, v) + \exp\left[-u + \frac{v^2}{2} + \ln(\phi(u, v^2, v))\right] \right) \quad (2.14)$$

with

$$\begin{aligned} \phi(x, \mu, \Sigma) &= \frac{1}{2} + \frac{1}{2} \operatorname{erf}\left(\frac{x - \mu}{\sqrt{2\Sigma}}\right) \\ u &= \lambda(\rho_c - \rho) \\ v &= \lambda \sqrt{\sigma_c^2 + \sigma_{\text{layer}}^2} \end{aligned} \quad (2.15)$$

where erf is the error function, $\lambda = 75/\rho_c$, and σ_c and σ_{layer} respectively represent the variability in density of closure and the variability in density due to firn layering. The operator $\langle . \rangle$ stands for the operation of spatial averaging, that is to say looking at variables on a bulk scale rather than at the individual stratum scale. Equation 2.14 can be modified to rather express the relation between closed and total porosity at the local stratum scale. In this case, the variable v of Equation 2.15 simply is $\lambda \sigma_c$. [Mitchell et al. \(2015\)](#) proposed a different formulation than Equation 2.13 to infer the density during closure ρ_c :

$$\rho_c = \frac{1}{1 - 1/75} \left(\frac{1}{\rho_{\text{ice}}} + 7.02 \times 10^{-4} T - 4.5 \times 10^{-2} \right)^{-1} \quad (2.16)$$

where the temperature T is expressed in Kelvin. The resulting closed porosity for a temperature of -55°C , using the value $\sigma_c = 7 \times 10^{-3} \text{g.cm}^{-3}$ ([Mitchell et al., 2015](#)), and neglecting firn layering, is displayed in Figure 2.17.

Finally, based on 3D models of firn samples obtained with tomographic scanning, [Schaller et al. \(2017\)](#) have proposed three new closed porosity parametrizations for three different polar sites. The main particularity of their result, is that they observed a constant porosity at full closure for all the three sites. They propose that the closed and total porosities are

related with:

$$P_{\text{closed}} = P_{\text{crit}}(b e^{-\lambda_1(P_{\text{total}} - P_{\text{crit}})} + (1 - b) e^{-\lambda_2(P_{\text{total}} - P_{\text{crit}})}) \quad (2.17)$$

where $P_{\text{crit}} = 0.10$ is the total porosity at full closure and is independent of the studied site, and where b , λ_1 , and λ_2 are three parameters that depend on the site of study. The closed porosity parametrization proposed for the site of B53 in Antarctica, is displayed in Figure 2.17.

The idea of the density of full closure P_{crit} being independent of the site of study is inconsistent with the parametrization proposed in [Goujon et al. \(2003\)](#) and [Mitchell et al. \(2015\)](#). [Schaller et al. \(2017\)](#) explains this difference by percolation and finite size effects. They argue that the small sample sizes used to measure the closed porosity in previous studies yield non-representative data, due to the opening of closed pores at the surface of the samples ([Martinerie et al., 1990](#)). Therefore, the parametrizations based on these data suffer from this problem. On the other hand the large samples used in the study of [Schaller et al. \(2017\)](#) should be less sensitive to this opening of bubbles at the firn surface. The closed porosity parametrization proposed by [Schaller et al. \(2017\)](#) suggest that gas trapping occurs at a lower density than in the case of the [Goujon et al. \(2003\)](#) and [Mitchell et al. \(2015\)](#) parametrizations.

Gas transport and mixing

In order to properly model the age of the gas trapped in the ice, it is necessary to estimate the age of the gases in the open porosity of the firn column. As discussed in Section 2.3.1, the age of the air in the open pores is mainly controlled by the molecular diffusion of gases in the pores. The molecular diffusion in the open porosity is characterized by an effective diffusivity coefficient, that encapsulates the limitation of diffusion in firn, due to the increasing tortuosity and constriction of the porous network with depth.

Due to the finite size of the samples excavated, it is not possible to measure this effective diffusion coefficient directly using firn cores ([Fabre et al., 2000](#)). Instead, the standard method is to determine the diffusivity profile of the firn based on firn air pumping data. Briefly, air

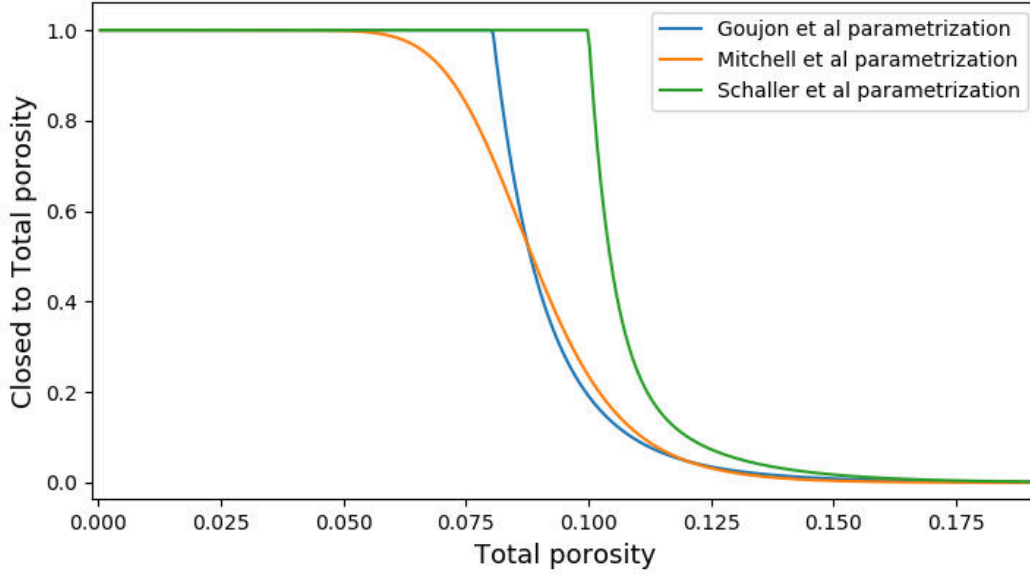


Figure 2.17 – Closed porosity parametrization proposed in the literature. The Goujon et al. (2003) and Mitchell et al. (2015) parametrizations are estimated using a temperature of -55°C . The Schaller et al. (2017) parametrization corresponds to the site of B53 that has a local temperature of -55°C .

is first sampled from the open porosity at various depths during the drilling of a firn core. Then, air samples are analyzed for chemical components whose atmospheric concentrations are known over the past century. Finally, the effective diffusivity of the model is adjusted so it can best reproduce the concentrations measured in the open porosity (Severinghaus and Battle, 2006; Buizert et al., 2012; Witrant et al., 2012; Petrenko et al., 2013). This methodology is summarized in Figure 2.18.

Once the effective diffusivity profile is known, the ages of the air inside the porosity can be deduced. In particular, the ages are known in the open porosity of the pore closure zone. In order to be able to predict the ages and concentrations in the closed porosity, one has to know at which rates the open and closed porosity get compressed in the trapping zone. All models make the assumption that the closed and open porosities compress at the same rate (Rommelaere et al., 1997; Severinghaus and Battle, 2006; Buizert et al., 2012). This is justified by the relative low pressure difference in closed and open pores compared to the pressure in the surrounding ice (Martinerie et al., 1992). In this case, Rommelaere et al. (1997) state that the concentration q_X^b of the chemical component X obeys:

$$\frac{\partial q_X^b}{\partial t} + \frac{\partial(vq_X^b)}{\partial z} + vq_X \frac{\epsilon}{f} \frac{\partial}{\partial z} \left(\frac{f}{\epsilon} \right) + \lambda_X q_X^b = 0 \quad (2.18)$$

where q_X^b is the concentration of X in the bubbles (expressed in moles per m^3 of bubble

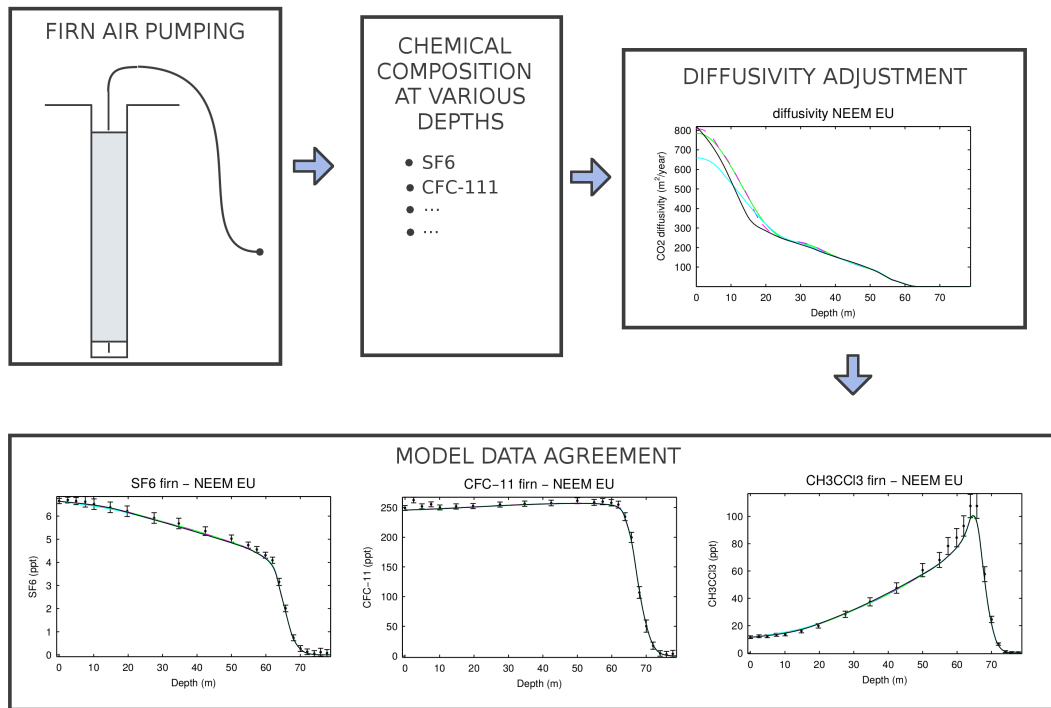


Figure 2.18 – Estimation of the firn effective diffusivity profile based on firn air pumping measurements. The diffusivity profiles and the predicted concentrations graphs are from [Witrant et al. \(2012\)](#).

space), q_X is the concentrations of X in the open pores (expressed in moles per m^3 of open pore space), v is the sinking speed of the firn, ϵ is the total porosity, f is the open porosity, λ_X is the radioactive decay period of X , and z and t are the depth and time. Equation 2.18 is essentially an equation of mass conservation, and equivalents are used in other models ([Buizert et al., 2012](#)).

2.5 Alterations of the gas record

There are several differences between the atmospheric concentrations over time and their imprint in the ice. To take full advantage of the GHG measurements for paleoclimatic interpretations, it is thus important to understand what are those differences, in order to avoid over-interpretation of the gas records.

2.5.1 The smoothing effect

Spahni et al. (2003) compared the methane records in a Dome C ice core (Antarctica) and the GRIP ice core (Greenland). Looking at the two records in Figure 2.19, one can see that the Dome C record displays less variability than the GRIP one. As methane is a well mixed GHG, Antarctic and Greenland atmospheric concentrations should be similar (apart from an inter-hemispheric gradient, Dällenbach et al., 2000). The difference between the two records cannot therefore be explained by a smaller methane variability over Antarctica. Rather, this highlights that the imprints of the same atmospheric variation are different in the Dome C and GRIP ice cores. One can then wonder, which of the two records presented in Figure 2.19 is the closest to the actual atmospheric variability. This also raises the question of how to best reconstruct the true past state of the atmosphere based on ice core gas records.

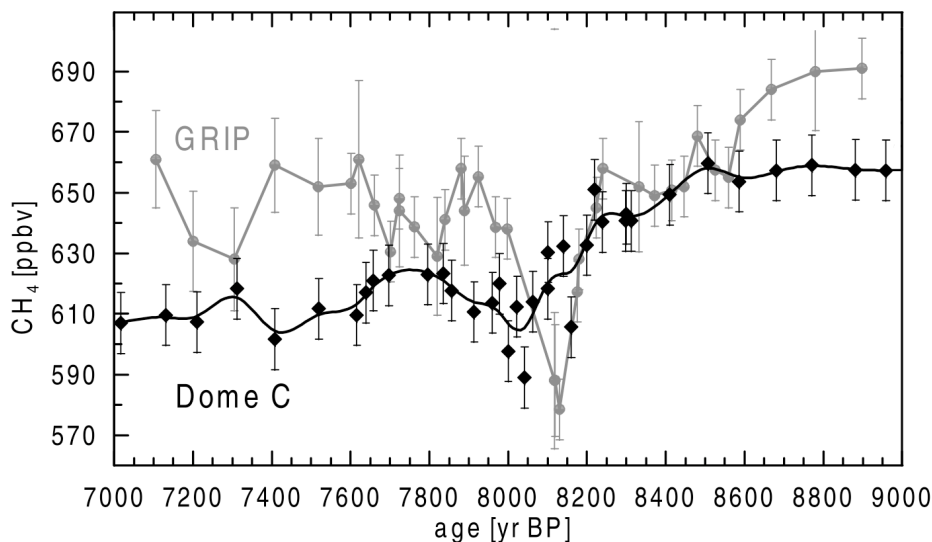


Figure 2.19 – Comparison of the imprints of the same atmospheric event in the Dome C and GRIP ice cores. Modified from Spahni et al. (2003).

The difference between the Dome C and GRIP records presented in Figure 2.19, is due to the smoothing effect (Spahni et al., 2003; Joos and Spahni, 2008; Köhler et al., 2011; Ahn et al., 2014). The origin of this smoothing effect is twofold. First, due to the molecular diffusion in the firn column, gases are mixed in the open porosity of the firn (Schwander et al., 1993; Trudinger et al., 1997; Petrenko et al., 2013). Thus, the air in the open porosity of a given firn stratum is not composed of atmospheric molecules originating from a single date. Rather, the air is composed of molecules that were taken from the atmosphere at different periods (Buizert et al., 2012; Witrant et al., 2012). Therefore, the age of the gases in the firn is described by an age distribution. As seen in Figure 2.20, the age distribution

of gases in the firn broadens with depth. This means that at the firn-ice transition, air is composed of molecules originating from atmospheres with a broad range of ages. Beside the mixing of gases in the open porosity, the bubbles in a given firn stratum do not all close simultaneously, but rather over a time span (Schwander and Stauffer, 1984; Schwander et al., 1993). Between the closure of the different bubbles, the air in the open porosity has enough time to be partially replaced by new air (Buizert et al., 2012; Witrant et al., 2012). Therefore, two bubbles of the same stratum that close at different times enclose air with different ages. Both of these phenomena, diffusive mixing and progressive bubble closure, imply that the gases enclosed in the bubbles of a given ice stratum are characterized by a range of ages, adequately represented by a gas age distribution (Köhler et al., 2011; Ahn et al., 2014). Therefore, when measuring concentration in ice cores, one actually measures the average concentration over the age distribution. The age distribution acts as moving average, removing the fast variability from the record (Spahni et al., 2003; Joos and Spahni, 2008; Köhler et al., 2011; Ahn et al., 2014).

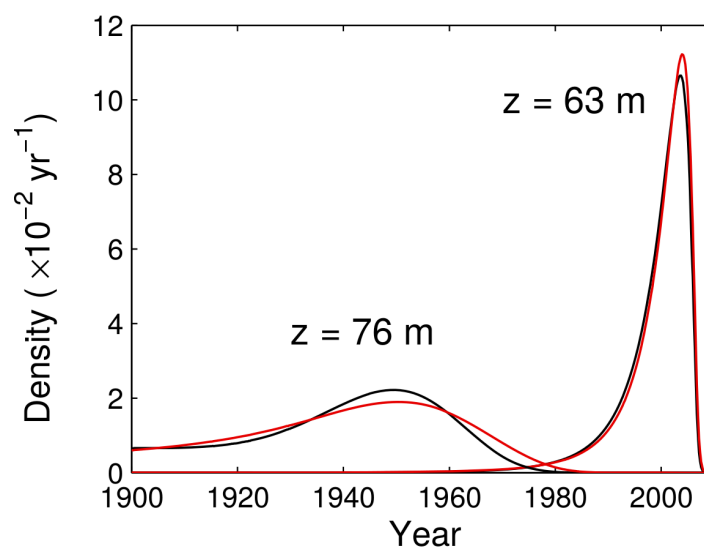


Figure 2.20 – CO₂ age distributions at depths 63 and 76m in the firn of NEEM, Greenland. The two colors represent, the results obtained from two different firn pumpings. Modified from Buizert et al. (2012).

The smoothing effect is more pronounced in ice cores formed under cold and arid conditions (Spahni et al., 2003; Ahn et al., 2014). Indeed, under low temperatures the ice matrix of firn deforms less easily (see Section 2.2.3 and Schulson and Duval, 2009). It implies that the closure of bubbles spans a longer period and therefore the age distribution of trapped gases is broader. Furthermore, low accumulation means a slow mechanical load increase of the firn column. This further slows the progressive closure of bubbles, resulting in broad gas age distributions. Combined, these two effects broaden the age distributions encoun-

tered in cold and arid sites, which result in a stronger smoothing effect. This is exemplified in Figure 2.19: the lower accumulation site of Dome C exhibits a stronger smoothing effect than the site of GRIP.

A proper interpretation of the fast variations recorded in ice cores requires to quantify the degree of smoothing of the gas record, and consequently to know the gas age distribution of the gases. This can be achieved thanks to the use of firn and gas trapping models, discussed in Section 2.4.2. However, several problems arise with this methodology. First these models require a profile of bubble closure as input. This type of data has only been obtained for a few sites (Schwander et al., 1993; Trudinger et al., 1997; Schaller et al., 2017), and are associated with large uncertainties due to finite size of the excavated firn samples (Martinierie et al., 1990; Schaller et al., 2017). For sites without such measurements, modelers have to rely on parametrizations (see Section 2.4.2 and Goujon et al., 2003; Severinghaus and Battle, 2006; Mitchell et al., 2015), that further add uncertainties to the final result. Secondly, gas transport models requires firn air data to constrain the diffusion of gases in the open porosity (Buizert et al., 2012; Witrant et al., 2012). The firn air pumping and diffusivity profiles obtained in modern firns cannot be extrapolated to the case of glacial East Antarctic firns, as they do not have modern equivalent. Yet, ice cores formed under glacial conditions on the East Antarctic plateau are of particular importance to the field of climatology.

2.5.2 Layered gas trapping

A second discrepancy between the actual atmospheric history and its imprint in the ice is due to heterogeneous stratification of the firn. Etheridge et al. (1992) reports that Δage in the summer layers of an ice core from Law Dome, Antarctica, is two years larger than for other layers. The authors suggest that the low density summer layers enclose the air with a delay compared to the rest of the firn. This stratified gas enclosure creates anomalies and inversions in the gas chronology (Mitchell et al., 2015). It is thus possible that older air is enclosed above younger air. Rhodes et al. (2016) build upon this notion of stratigraphic heterogeneity to explain abrupt variations observed in the methane records of Greenland and Antarctic ice cores. Such an example of abrupt methane variations observed by Rhodes et al. (2016) is displayed in Figure 2.21.

One of the proposed mechanism for these abrupt variations is that especially dense (respectively less dense) layers close in advance (respectively late), enclosing older (respectively younger) air than their surrounding, as already described by [Etheridge et al. \(1992\)](#). On the other hand, a study by [Gregory et al. \(2014\)](#) highlights the importance of the microstructure of the firn strata for the process of gas trapping, and argue that the less dense firn layers close-off shallower. [Rhodes et al. \(2016\)](#) highlighted that the difference in concentrations between adjacent layers closing at different times, is controlled by the rate of change of atmospheric concentrations. If concentrations are stable, then the different layers all have the same methane concentration and therefore no variations appears in the record. The amplitudes of the methane abrupt variations observed by [Rhodes et al. \(2016\)](#), display a consistent relationship with the rate of change of methane concentrations, indicating that the mechanism responsible for these artifacts is the layered trapping of gases.

Moreover, [Rhodes et al. \(2016\)](#) pointed out that the amplitudes of the layered trapping artifacts are also dependent on the accumulation rate under which the ice core is formed, with low accumulation ice cores displaying stronger layering artifacts. This raises the question: to what extent the low accumulation ice cores from East Antarctica are affected by gas layered trapping artifacts?

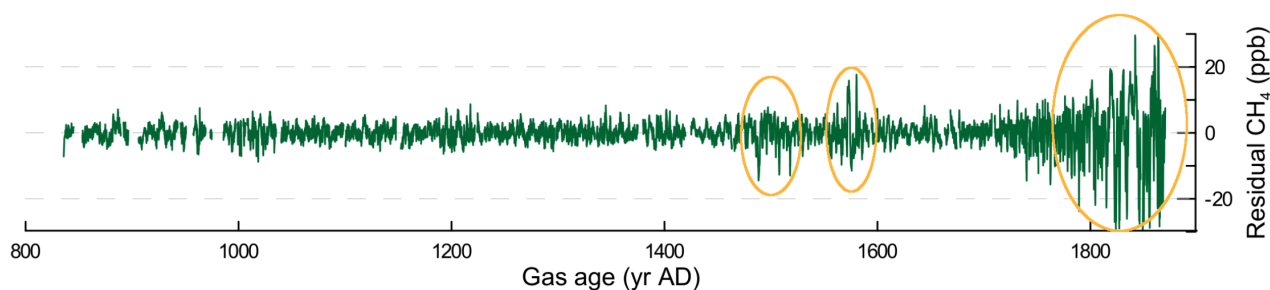


Figure 2.21 – Residuals between the methane concentrations in the Tunu13 ice core (Greenland) and a spline adjusted to the record. The circled abrupt variations are the ones explained by the firn heterogeneous stratification of the firn. Modified from [Rhodes et al. \(2016\)](#).

2.6 Objectives of the PhD

This PhD aims to provide a better understanding on the alterations of gas signals observed in low-accumulation ice cores from East Antarctica, notably for ice cores formed under glacial conditions. The specific questions it aims to answer are the following:

- What are the physical characteristics of early and late gas trapping layers? What is the

origin of their presence in the firn?

- What is the influence of accumulation on the progressive closure of pores in firn of the East Antarctic plateau? What can be known about the closing of pore at very-low accumulation?
- What is the degree of smoothing encountered in glacial and interglacial period ice core samples from East Antarctica? What is the relationship of smoothing with accumulation?
- What is the loss of atmospheric information that one can expect, in the case of low-accumulation and highly thinned deep ice cores drilled on the East Antarctic plateau?

Methods

Contents

3.1	Continuous Flow Analysis of methane concentrations	45
3.1.1	Description of the CFA apparatus	46
3.1.2	Preparation of the ice	48
3.1.3	Processing of the raw data	49
3.1.4	Correcting for methane dissolution	50
3.1.5	Internal smoothing of the CFA system	56
3.2	Pycnometry	61
3.2.1	Physical basis	61
3.2.2	Experimental protocol	66
3.2.3	Calibration of the chamber volumes	67
3.2.4	Experimental uncertainties	69
3.3	Other measurements performed during the thesis	71
3.3.1	Density measurements by Xray absorption	72
3.3.2	Tomography	75
3.3.3	Air content	76
3.3.4	Chemistry measurements	77
3.3.5	Thin sections and crystalline texture	78
3.4	Conclusion of the chapter	79

This chapter describes the different experimental methods used during this PhD. Even though these methods are recapitulated in the method sections of the articles composing Chapters 4 and 5, more details will be given here. In particular, an in depth discussion of the Continuous Flow Analysis of methane and the gas pycnometry measurements of firn porosity is provided.

3.1 Continuous Flow Analysis of methane concentrations

A large part of this PhD work relies on the study of methane concentrations measured in polar ice cores. Methane sources (such as mid-latitude wetlands) have a short enough response time to produce abrupt increases of methane atmospheric concentrations when activated (Brook et al., 2000). Moreover, methane has a residence time in the atmosphere long enough to be well mixed at the global scale, but short enough to display abrupt decrease when sources are shut down (Mayer et al., 1982). Atmospheric methane thus exhibits a fast atmospheric variability with some variations occurring in a few decades only, and is therefore an ideal tracer to study the impact of layered gas trapping and firn smoothing on the gaseous signals recorded in the ice. Furthermore, methane is a major greenhouse gas and measuring its concentration in polar ice cores is of particular importance for the study of climate (Gedney et al., 2004; Shindell et al., 2004).

Methane was also chosen for this thesis as it is relatively easy to measure with a high resolution. The availability of high resolution datasets is necessary to fully resolve the variability recorded in the ice, in order to study how it is affected by gas trapping. Contrary to CO₂, melting the ice containing the bubbles does not contaminate the freed air. Accordingly, a measurement system of methane based on the continuous melting and analysis of the ice has been developed at IGE, notably by J. Chappellaz and X. Faïn, with the help of R. Dallmayr and O. Pascual. This system is referred to as a Continuous Flow Analysis (CFA) system. It is able to resolve methane concentration variations in ice cores at the centimeter scale. Moreover, it is possible to analyze up to 15m of ice per day, which in turns enables to analyze a 100m ice core in about two weeks. The methane CFA data of this thesis have been obtained with X. Faïn and with the occasional help of G. Teste.

The CFA method is partially described in the article reported in Chapter 5. However, a more detailed description will be given here.

3.1.1 Description of the CFA apparatus

The CFA apparatus of IGE used during this thesis is based on the same principles that the system presented by [Stowasser et al. \(2012\)](#), [Chappellaz et al. \(2013\)](#), and [Rhodes et al. \(2013\)](#). To be measured, the ice core is first cut into 34mm×34mm sticks. Such a stick is shown in Figure 3.1. The ice is then melted on a square melt head ([Bigler et al., 2011](#)) at an average rate of $3.6\text{cm}\cdot\text{min}^{-1}$. The melting of a CFA stick and the met head are shown in Figure 3.2. This melting rate is continuously monitored and recorded.

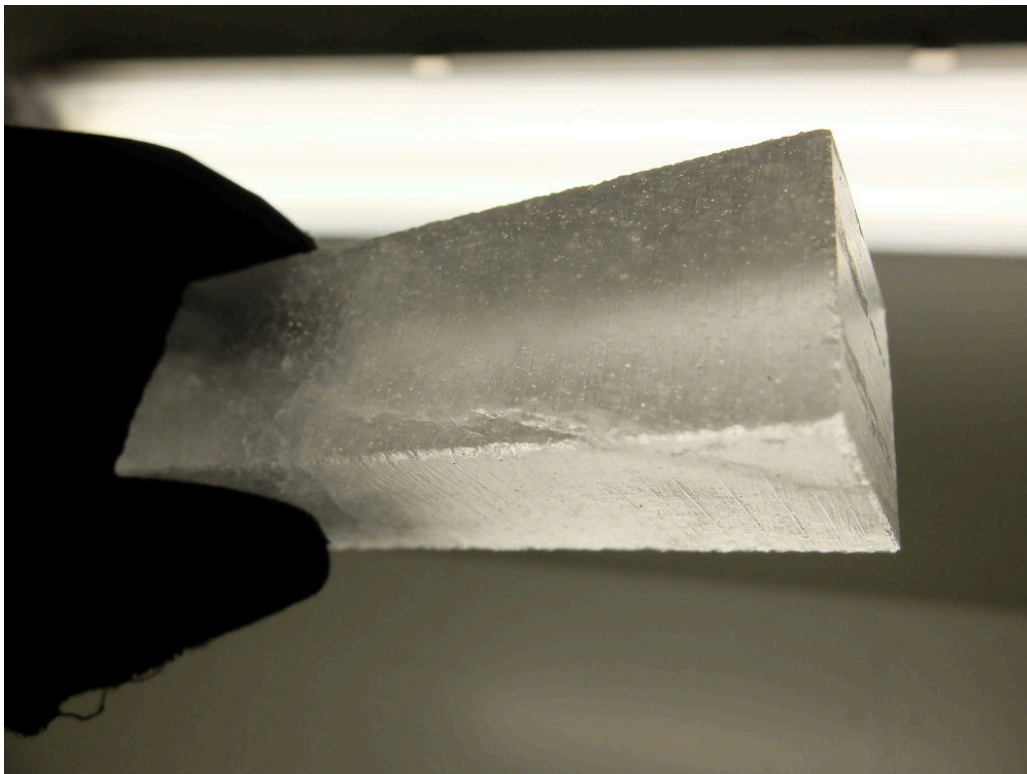


Figure 3.1 – Example of a CFA stick ready to be melted and analyzed. Picture by X. Fain.

The meltwater and the gases it contains are retrieved and pumped outside of the cold room for analysis. In order to avoid contaminations, only the meltwater originating from the center of the sticks is retrieved, while the rest of the water is discarded ([Bigler et al., 2011](#)). This water/bubbles mixture is sent to a glass, home made, T-shaped debubbler through pumps and ETFE tubing. This debubbler routes a part of the melt water, now free of bubbles, toward sensors monitoring dust particle concentration (Abakus[®]) and liquid conductivity (Dionex[™]). As it is important for these sensors to receive a perfectly bubble free water, a second open split is added on this line to ensure that absolutely no bubble remains in the water. The T-shaped debubbler was designed to minimize the dead volume added in the system. It is important to limit the presence of dead volumes to avoid internal mixing of the

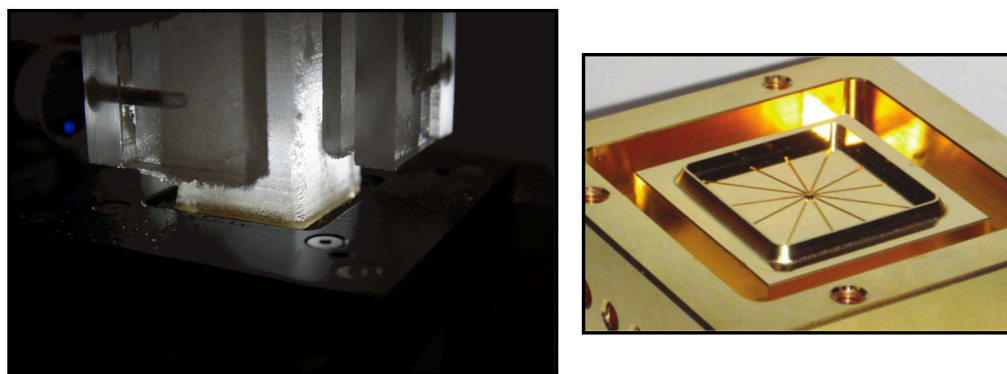


Figure 3.2 – Left: Picture of a CFA sticks being melt, by X. Fain. Right: Picture of the melt head, from Bigler et al. (2011).

sample stream and ensure a good spatial resolution during measurements.

The water/bubbles mixture is then transported to a thermally regulated box, maintained at 30°C. This box encloses an IDEX[®] Transfer Line degasser¹. It separates the bubbles from the meltwater by applying a ~ 450 mbar depression through a porous membrane. The extracted gas is then dried by an ultra-pure nitrogen counter flux (ALPHAGAZ[™] 2, 99.9999% purity) inside Nafion tubing. The gas, now free of water vapor, can be sent to an optical spectrometer for methane concentration analysis. The spectrometer used at IGE is a SARA spectrometer developed at the Laboratoire Interdisciplinaire de Physique (LiPhy) in Grenoble. This spectrometer is based on optical feedback cavity enhanced absorption spectroscopy (OF-CEAS; Morville et al., 2005; Chappellaz et al., 2013; Rhodes et al., 2013), and has a precision of 1ppbv (one standard deviation) when measuring methane in a standard gas. The OF-CEAS technique makes possible the use of a low volume laser cavity of only 12cm³. Furthermore, the pressure inside the cavity is maintained at 20mbar, meaning that the spectrometer only requires 0.22cm³ of gas at standard pressure and temperature (STP, 1013mbar and 0°C). The renewal time of gases in the cavity is about 10s for a typical CFA gas flow of 1.5mL.min⁻¹. Minimizing dead volumes in the tubing results in a spatial resolution of about a centimeter for the CFA system.

Finally, the IGE CFA system also includes a set up able to produce a synthetic water/bubbles mixture, notably for calibration purposes. This section is referred to as the Full Loop and will be further discussed in Section 3.1.4.3. The Full Loop can also be used to estimate the analytical noise of the CFA system. Using it to measure a synthetic mixture of water and

¹<https://www.idex-hs.com/store/fluidics/degassers/debubblers/transfer-line-degasser.html>

standard gas, the analytical noise of the CFA system was determined to be around 10ppbv peak-to-peak (X Faïn, personal communication). The different elements of the CFA system are summarized in Figure 3.3.

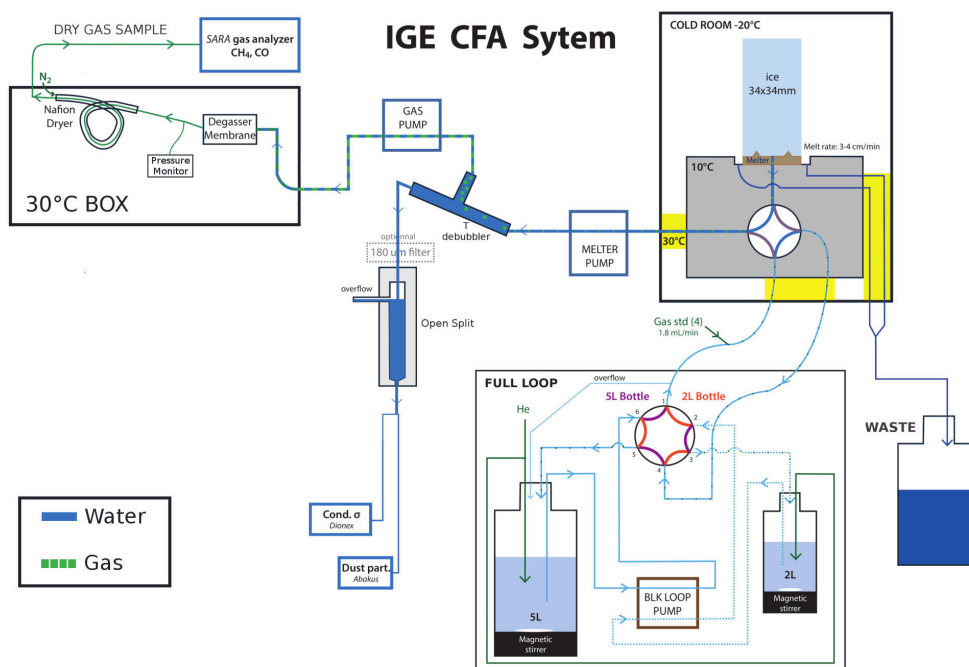


Figure 3.3 – Schematic of the IGE CFA system, courtesy of S Darfeuil.

3.1.2 Preparation of the ice

To be analyzed for methane concentration by the CFA system, the ice cores measured for this PhD have to be prepared into 34×34 cm section sticks. These sticks are cut directly in the center of the ice cores, in the IGE cold rooms. A picture of an ice core where a CFA stick is to be cut is given in Figure 3.4. The preparation of the CFA sticks for this PhD have been done with the help of X. Faïn, P. Martinerie, G. Teste and G. Aufresne. The presence of cracks in the CFA sticks might let ambient air enter the analysis system during measurements. This ambient air will contaminate the ice core gases and lead to abnormally high measured methane concentrations. In order to prevent such contaminations, the sticks are preferentially cut in crack free zones of the core.

Ice sticks are melted continuously and sequentially on top of each other. Similarly to cracks, ambient lab air may enter the sample line when the transition between two consecutive sticks reaches the melter. We refer to these spaces between consecutive sticks as breaks. Moreover, as seen Figure 3.1, we systematically checked for the end of the sticks to be as flat as possible, to ensure an optimal contact between the consecutive sticks in order to limit air

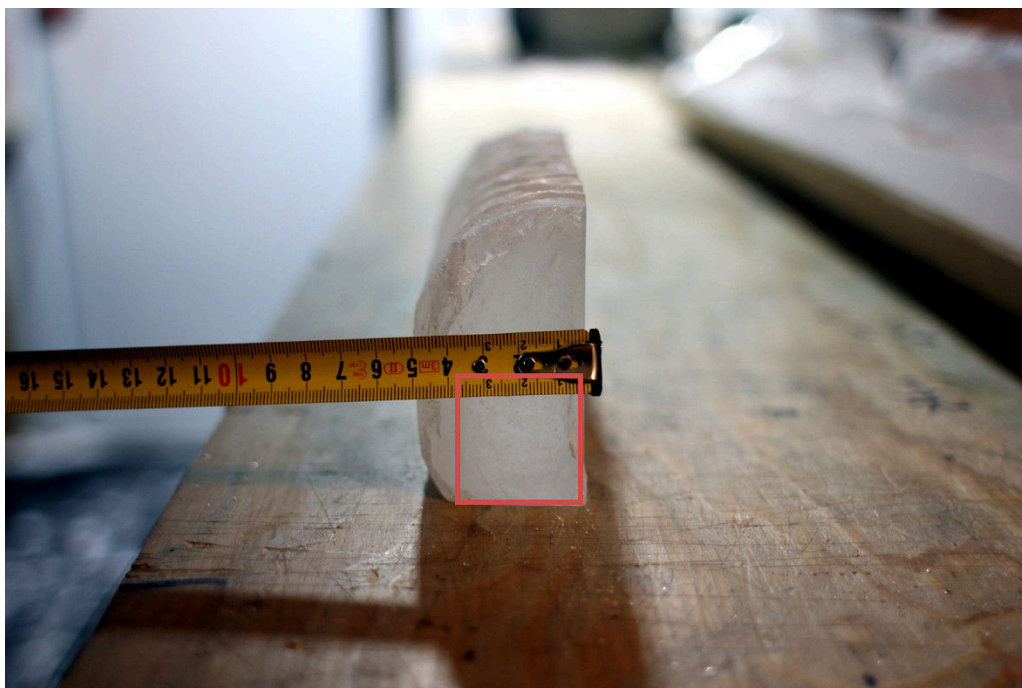


Figure 3.4 – Example of an ice core piece from where a CFA stick is to be cut. The stick will be cut following the 34×34 mm red square. Picture by A. Ekaykin.

from entering the system.

During our measurement campaigns, we observed that the melt rate sometimes sharply dropped after a non-freshly-cut break reached the melthead. Cleaning the melt head with ethanol is enough to recover a proper melting rate. We believe that it suggests that the uncleaned ends of CFA sticks can deposit dirt on the melt head and prevent a proper melting. Therefore, we decided that before melting, each end of the CFA sticks should be trimmed to remove potential dirt. The length of the cuts made on the CFA sticks are recorded in a cutting log and later taken into account to produce the depth scale.

3.1.3 Processing of the raw data

The CFA sticks are melted sequentially and the methane concentration continuously analyzed by the SARA spectrometer. During the measurements, the times at which a break, or a crack in the ice, reaches the melt head are recorded as they may coincide with ambient air contaminations. Such contaminations need to be removed from the dataset as they do not represent actual methane concentrations recorded in the ice core. They appear as spikes of high concentrations lasting roughly 1min. They are manually removed from the dataset by an operator using a dedicated computer program that I developed during this PhD using python3. The recorded times of potential contaminations are displayed during the cleaning

to ensure that they are all removed.

The records provided by the spectrometer are originally expressed as a function of the measurement time. To be interpreted in terms of ice core concentrations, they need to be expressed on the core depth scale. The conversion from a time to a depth scale relies on the fact that the top and bottom ends of each CFA stick have a depth that is known from the drilling and cutting logs. The depth scale between two breaks is reconstructed taking into account the melt rate, as illustrated in Figure 3.5. To produce the depth scale of a CFA campaign, I developed a dedicated program (python3).

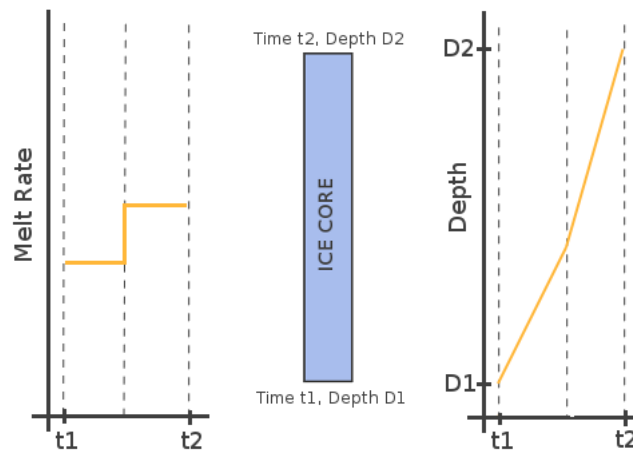


Figure 3.5 – Conversion of the time based data from the SARA spectrometer are converted to depth based data. The bottom and top depths of the sticks are known.

3.1.4 Correcting for methane dissolution

The CFA data need to be corrected for the preferential dissolution of methane in the meltwater (Rhodes et al., 2013; Chappellaz et al., 2013). Indeed, methane has a higher solubility than oxygen and nitrogen in water. As a consequence, the methane mixing ratio in the bubbles carried by the meltwater is biased towards lower values, and need to be raised to its absolute level by the application a correcting factor f .

3.1.4.1 Dissolution correction using other measurements

One way to estimate this correcting factor is to compare the CFA concentrations with data already on an absolute scale. During this thesis, I notably used methane data obtained using discrete measurement methods (Loulergue et al., 2008; Mitchell et al., 2013). For discrete measurements, the effect of methane dissolution can either be mitigated using a melt-refreeze technique (Raynaud et al., 1988; Chappellaz et al., 1990) or empirically estimated (Mitchell et al., 2011; Mitchell et al., 2013). The overall agreement between the melt-refreeze and empirically corrected discrete measurements suggests that the two methods are properly corrected for the preferential dissolution of methane. I also used CFA data provided by other laboratories, and already corrected for methane dissolution (Rhodes et al., 2015). Using such comparisons, I found that the correcting factor f for the IGE system is close to 1.13 for East Antarctic ice cores.

Yet, this method requires the availability of methane records not affected or corrected for dissolution. This type of data is however not always available. That is why there is an ongoing effort to estimate this factor independently of other data, to which I contributed during my PhD.

3.1.4.2 Theoretical dissolution correction

One possible way is to theoretically estimate the dissolution of methane in the meltwater. For this purpose, I derived a simple analytical model of dissolution that assumes: i) the water/bubbles mixture is characterized by a unique temperature T , ii) gaseous molecules are in equilibrium between the water and gas phases, iii) the two phases are homogeneous and iv) surface tension effects at the boundaries of bubbles are negligible.

Let us consider a volume V^0 of ice core containing N_X^0 molecules of the gas species X . Melting the ice core will result in two distinct phases of water and air, with volumes V^w and V^g . These two phases respectively contain N_X^w and N_X^g molecule of X . Following Henry's law and considering the gas in the bubbles to be an ideal gas, the condition of chemical

equilibrium between the two phases reads:

$$[X]^w = [X]^g RT H_X \quad (3.1)$$

where $[X]^w$ and $[X]^g$ are the volumic concentrations of the species X in the water and gas phase respectively, R is the ideal gas constant ($8.314 \text{ J.K}^{-1} \cdot \text{mol}^{-1}$), T is the temperature, and H_X is the Henry's constant of species X (in $\text{mol.m}^{-3} \cdot \text{Pa}^{-1}$). Expressing the concentrations in terms of volumes and numbers of molecules we obtain:

$$N_X^w = N_X^g \frac{V^w}{V^g} RT H_X = N_X^g rw RT H_X \quad (3.2)$$

where N_X^w and N_X^g are the numbers of molecules of X in the water and gas phases, V^w and V^g are water and gas volumes, and rw is the ratio of water volume to air volume in the meltwater/bubbles mixture. Moreover, the conservation of molecules yields $N_X^0 = N_X^w + N_X^g$. Injecting this in Equation 3.2 yields:

$$N_X^0 = N_X^g (1 + rw RT H_X) \quad (3.3)$$

Moreover, the initial mixing ratio of species X in the ice core (the quantity of interest) is given by:

$$M_X^0 = \frac{N_X^0}{\sum_I N_I^0} \quad (3.4)$$

where the sum over I encompass all the species in the bubbles. Using Equation 3.3:

$$M_X^0 = \frac{N_X^g (1 + rw RT H_X)}{\sum_I N_I^0} \quad (3.5)$$

Then, dividing both the numerator and denominator of the right hand side by the the total number of molecules in the gas phase, one has:

$$M_X^0 = M_X^g \frac{1 + rw RT H_X}{\frac{\sum_I N_I^0}{\sum_I N_I^g}} = M_X^g f_X \quad (3.6)$$

where M_X^g is the mixing ratio in the gas phase (the one measured by the spectrometer) and f_X is the correcting factor to be applied. One can further simplify the computation by using the fact trace gas concentrations are negligible in front of O_2 and N_2 . Then, the sums over all species are reduced to the sums over O_2 and N_2 only. The denominator of Equation 3.6 then becomes:

$$\frac{\sum_I N_I^0}{\sum_I N_I^g} = \frac{N_{O_2}^0 + N_{N_2}^0}{N_{O_2}^g + N_{N_2}^g} = \frac{N_{O_2}^0}{N_{O_2}^g + N_{N_2}^g} + \frac{N_{N_2}^0}{N_{O_2}^g + N_{N_2}^g} \quad (3.7)$$

Using Equation 3.3 for O_2 and N_2 , one can rearrange Equation 3.7 to:

$$\frac{\sum_I N_I^0}{\sum_I N_I^g} = \frac{1 + rwRTH_{O_2}}{1 + \frac{N_{N_2}^0}{N_{O_2}^0} \frac{1 + rwRTH_{N_2}}{1 + rwRTH_{O_2}}} + \frac{1 + rwRTH_{N_2}}{1 + \frac{N_{O_2}^0}{N_{N_2}^0} \frac{1 + rwRTH_{O_2}}{1 + rwRTH_{N_2}}} \quad (3.8)$$

Therefore, one finally has:

$$f_X = \frac{1 + rwRTH_X}{\frac{1 + rwRTH_{O_2}}{1 + \frac{N_{N_2}^0}{N_{O_2}^0} \frac{1 + rwRTH_{N_2}}{1 + rwRTH_{O_2}}} + \frac{1 + rwRTH_{N_2}}{1 + \frac{N_{O_2}^0}{N_{N_2}^0} \frac{1 + rwRTH_{O_2}}{1 + rwRTH_{N_2}}}} \quad (3.9)$$

The ratio of N_2 to O_2 in the ice core bubbles is considered to be 80:20. Note that in the special case where all species have the same solubility, that is to say that all Henry's constants are equal, the correcting factor f_X is valued at one. This is consistent with the consideration that in this special case, the mixing ratios of species is not affected by the dissolution.

To be applicable to the case of methane dissolution in meltwater, Equation 3.9 requires the knowledge of Henry's constants of O_2 , N_2 and CH_4 . These physical parameters are published in the NIST Chemistry WebBook², as well as their dependence on temperature. The water to air ratio rw is not directly measured in the CFA system. A closed equation can however be inferred using the air content of the ice:

$$rw = \frac{1}{AC\rho_w} \frac{T_0}{T} \frac{1}{\frac{0.2}{1 + rwRTH_{O_2}} + \frac{0.8}{1 + rwRTH_{N_2}}} \quad (3.10)$$

²<https://webbook.nist.gov/chemistry/>

where AC is the air content measured in ice, expressed in $\text{cm}^3 \cdot \text{g}^{-1}$ (see Section 3.3.3), ρ_w is the density of water, expressed in $\text{g} \cdot \text{cm}^{-3}$, T is the temperature of water/bubbles mixture, and $T_0 = 273.15\text{K}$. The temperature ratio comes from the fact that air content measurements are reported at standard pressure and temperature. This closed equation takes into account the dissolution of the part of the ice core gases in the liquid water. [Martinerie et al. \(1992\)](#) report air content values ranging between 0.0745 and $0.136\text{cm}^3 \cdot \text{g}^{-1}$, which correspond to rw between 15.9 and 7.7 . For an East Antarctic ice core with an air content value of $0.09\text{cm}^3 \cdot \text{g}^{-1}$, the rw ratio is expected to be 11.0 . Theoretical correcting factors for methane are displayed in Figure 3.6, as a function of temperature and rw . To compute the correction factor for ice cores measured at IGE, I further assume that the water/bubble mixture has a temperature of 20°C . It is lower than the temperature in the thermally regulated box, as meltwater does not stay long enough to reach thermal equilibrium. The theoretical value is consistent with the correcting factors of 1.13 observed for East Antarctic ice cores in the previous paragraph.

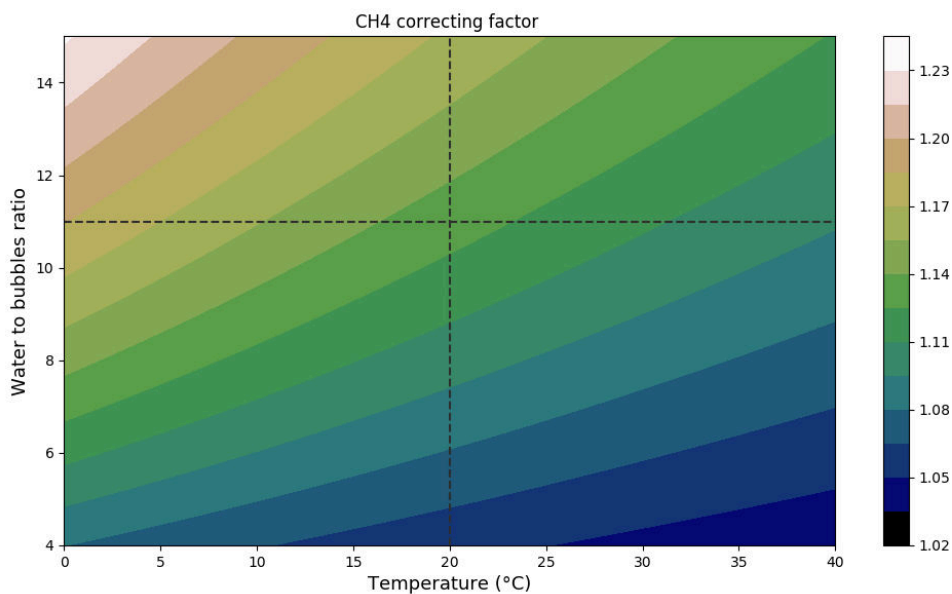


Figure 3.6 – Correcting factor for methane dissolution in CFA meltwater, as a function of temperature and water to air ratio. The dashed lines mark the temperature and rw expected during the analysis of an East Antarctic ice core at IGE.

The same computation can be made for carbon monoxide (CO), a gas also measured at IGE with the CFA apparatus. The theoretical dissolution coefficients for CO are displayed in Figure 3.7. The lower theoretical correcting factors for carbon monoxide are a result of the lower dissolution of CO compared to CH_4 . It is also interesting to note that the preferential dissolution of CO increases with temperature, whereas it decreases for CH_4 . This results from the observation that CO solubility decreases slower with temperature, compared to

other gases.

As there currently is no apparatus for the discrete measurement of CO, we cannot compare this result with independent data corrected for CO dissolution.

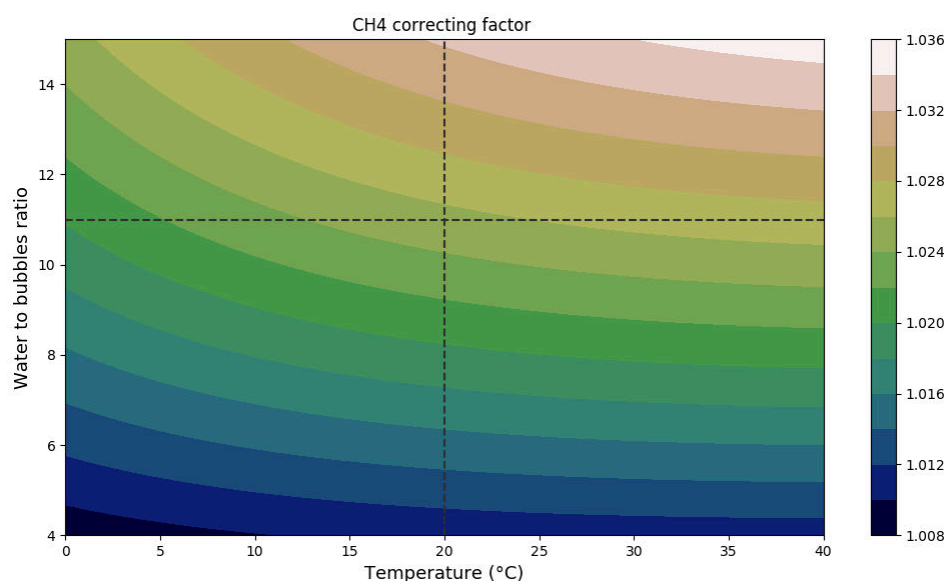


Figure 3.7 – Correcting factor for carbon monoxide dissolution in CFA meltwater, as a function of temperature and water to air ratio. The dashed lines mark the temperature and rw expected during the analysis of an East Antarctic ice core at IGE.

3.1.4.3 Dissolution correction using the Full Loop

Another strategy to estimate this correction factor is to emulate the dissolution of methane using standard gases of known concentrations. This is done on the CFA system of IGE using the so called Full Loop (FL), which is displayed in Figure 3.3. The idea behind it is to inject standard gases in de-ionized (DI) and degassed water with a specific water to air ratio. This synthetic mixture of water and bubbles is then transported to the spectrometer like ice core meltwater would be. Then, by measuring the methane concentration in the spectrometer one is able to estimate the degree of dissolution and the correcting factor required.

Experiments using the FL have shown that the methane concentration is not at equilibrium in the IGE CFA line. An increase in the length of the tubing results in a higher dissolution (personal communication from X. Faïn). It is thus not clear how to set up the FL to faithfully reproduce the dissolution of methane in ice core meltwater. Moreover in the case of CO, FL experiments performed at IGE contradict the theoretical model with correcting factor closer to 1.10. One possible way to use the FL for CO would be to tune it to recreate the estimated dissolution for CH₄ (using discrete measurements), and to directly measure the correcting factor needed for CO. Yet, this methodology assumes a direct relation between the dissolu-

tion of methane and carbon monoxide. It is however possible that in a dynamical system such as the CFA, different tunings of the FL (playing on the length of the tubes or the water to air ratio for instance) can reproduce similar CH_4 dissolution but several degrees of CO dissolution.

In conclusion, there is currently no clear strategy to be implemented to correct for the dissolution of methane using only CFA-based data. Theoretical derivation is limited by simplifying assumptions (such as thermodynamical equilibrium) that are not necessarily met in the case of ice core measurements. This strongly limits the confidence in these theoretical results. On the other hand, it seems reasonable that the FL can be tuned to faithfully reproduce the dissolution of methane and of other gases such as carbon monoxide. Yet, there are several adjustable parameters to determine in order to reproduce the gas dissolution, and is still an ongoing development at IGE.

Finally, a potential way of escaping the dissolution problem would be the development of an extraction system able to fully extract dissolved gases. Such a system would also make possible the measurement of highly soluble gases such as N_2O .

3.1.5 Internal smoothing of the CFA system

Due to the mixing of gases in the tubing, the data provided by the CFA system are a smoothed version of the record in the ice core. This limits the spatial resolution of the data, as variability faster than the smoothing limit of the CFA are removed from the data. Even though the CFA system has been designed to minimize this smoothing, it is however important to properly characterize it to interpret the final data. In particular, I needed the precise degree of smoothing of the CFA system in order to study the fast, centimeter-scale, methane variabilities observed in ice cores (Rhodes et al., 2016). The smoothing of the CFA is fully characterized through a single function G , such as:

$$S_s = S * G \quad (3.11)$$

where, S_s and S are respectively the smoothed and un-smoothed ice core records, and $*$ is the operator standing for the convolution product of two real-valued functions. The aim of my work in this section is thus to determine the function G and to study its characteristics.

For normalization reasons the integral of G over the whole time domain is equals to one.

Following [Stowasser et al. \(2012\)](#), G can be determined thanks to a step experiment. This experiment consists of abruptly changing the concentration of the methane sent in the CFA line from one value C_1 to another value C_2 . Due to the smoothing, the measured concentrations appears as a smeared step. The analytical expression of the concentrations is:

$$\begin{aligned} S_s(t) &= [C_1 + (C_2 - C_1)H(t)] * G(t) \\ &= \int_{-\infty}^{+\infty} [C_1 + (C_2 - C_1)H(\tau)] \times G(t - \tau) d\tau \end{aligned} \quad (3.12)$$

where $H(t)$ is the Heaviside function (also called step function). Time derivation of the measured concentrations is given by:

$$\begin{aligned} \frac{dS_s(t)}{dt} &= \frac{d}{dt} [C_1 + (C_2 - C_1)H(t)] * G(t) \\ &= (C_1 - C_2) \frac{dH}{dt} * G(t) \\ &= (C_1 - C_2) \delta * G(t) \\ &= (C_1 - C_2) G(t) \end{aligned} \quad (3.13)$$

where δ is the Dirac distribution. Integrating Equation 3.13, one has:

$$\begin{aligned} S_s(t) - S_s(0) &= S_s(t) - C_1 \\ &= (C_1 - C_2) \int_0^t G(t) \end{aligned} \quad (3.14)$$

Therefore, the smeared step measured by the CFA system is simply the integral of the smoothing function G . To determine this function, the protocol is thus to perform a step experiment to find the integral form of G , and finally derive the function G itself.

Similarly to Stowasser et al. (2012), I search the function G under the form of a log-normal law. This allows me to express G as a smooth analytical function, that nonetheless matches the data. Therefore, once the step experiment is performed, the results are fitted, using a dedicated python program, with the cumulative function of a log-normal law as displayed in Figure 3.8. This yields the set of parameters best representing the smoothing function. The smoothing function of the IGE CFA system is displayed in Figure 3.9.

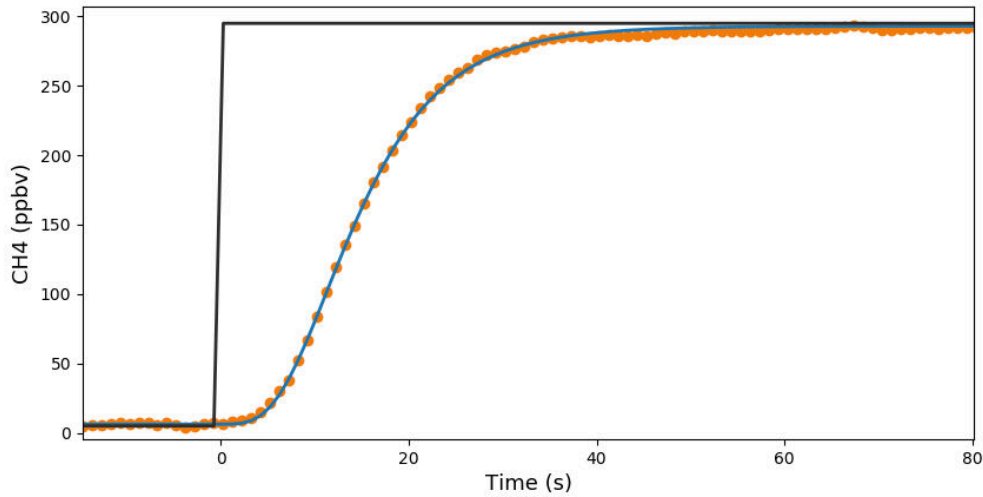


Figure 3.8 – Methane concentrations during a step experiment. Measured data are the blue dots, and the orange curve is the cumulative log-normal fit to these data. As a reference, the step in concentrations imposed at the start of the CFA system is shown in black.

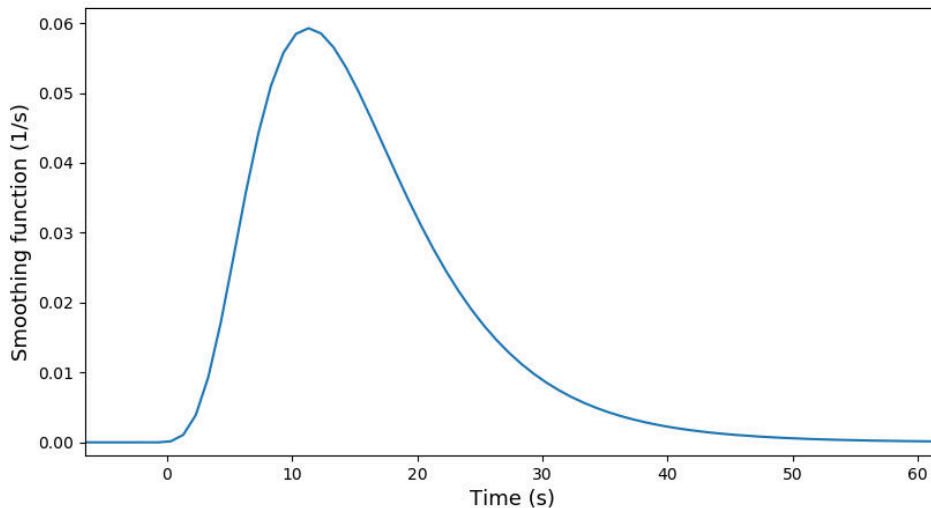


Figure 3.9 – Lognormal smoothing function of the IGE CFA system deduced from the step experiment.

The smoothing function deduced from the step experiment has a width of around 50s. Combined with the typical $3.6\text{cm}\cdot\text{min}^{-1}$ meltrate, the gases are mixed in the CFA system on a depth range of about 3.5cm. In order to better quantify the mixing and smoothing of ice core signals, one can use a frequency response diagram. This type of diagrams links the

attenuation of a sine signal to its frequency (or period). These diagrams are generally expressed in terms of temporal frequency (in Hertz), but here we expressed them using the wavelength λ (in m) of the sine signals in ice cores. This diagram can be obtained with the Fourier transform of the smoothing function G :

$$\text{FR}(1/\lambda) = |\text{FT}[G(d)]| \quad (3.15)$$

where FR is the frequency response, G is expressed as a function of depth in the ice core by taking into account the melt rate, and FT is the Fourier transform. The frequency response is displayed on Figure 3.10. It allows us to determine that a sine signal with a wavelength of 2.4cm has its amplitude dampened by a factor 2 when measured by the CFA system. That being said, one should be careful when using frequency responses graphs. Indeed, the attenuation factor for a particular wavelength is only valid for a sine signal. In the presence of square, sawtooth or concentration pulses, the attenuation should be computed directly using the G function and not simply read from the frequency response diagram. For instance, Figure 3.11 shows the attenuation experienced by different signals depending on their shape. It can be seen that the sine signal is more smoothed than a square or a pulse signal, but less than a sawtooth. In particular, pulses with widths of the order of the centimeter are resolved by the CFA system. It notably means that the centimeter scale layering artifacts discussed in Chapters 4 and 5 are resolved by the CFA system.

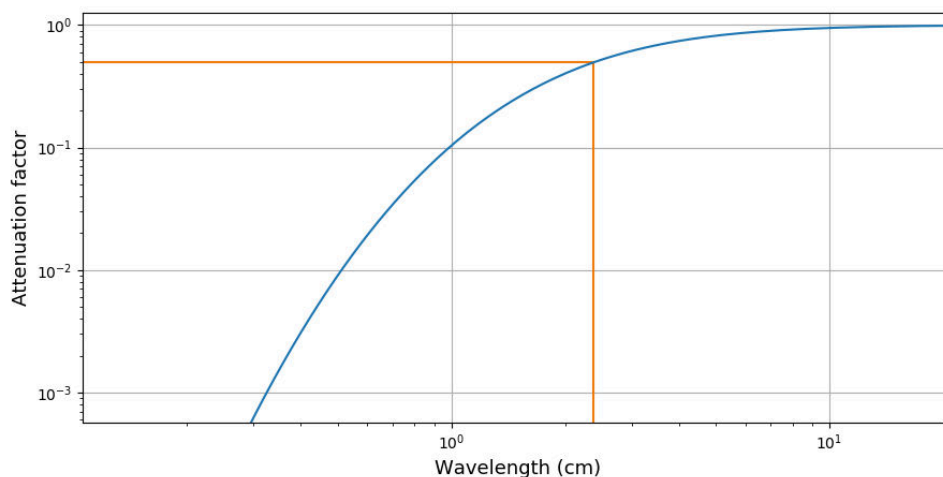


Figure 3.10 – Frequency response of the CFA system in blue. The y-axis represents the attenuation underwent by a sine signal in an ice core, and the x-axis represents the wavelength of the sine signal. The orange lines mark the wavelength where a 50% attenuation is obtained.

Finally, as explained at the beginning of Section 3.1.3, the breaks between two consecutive ice core sticks let outside air enter the CFA system. These abrupt spikes of high methane

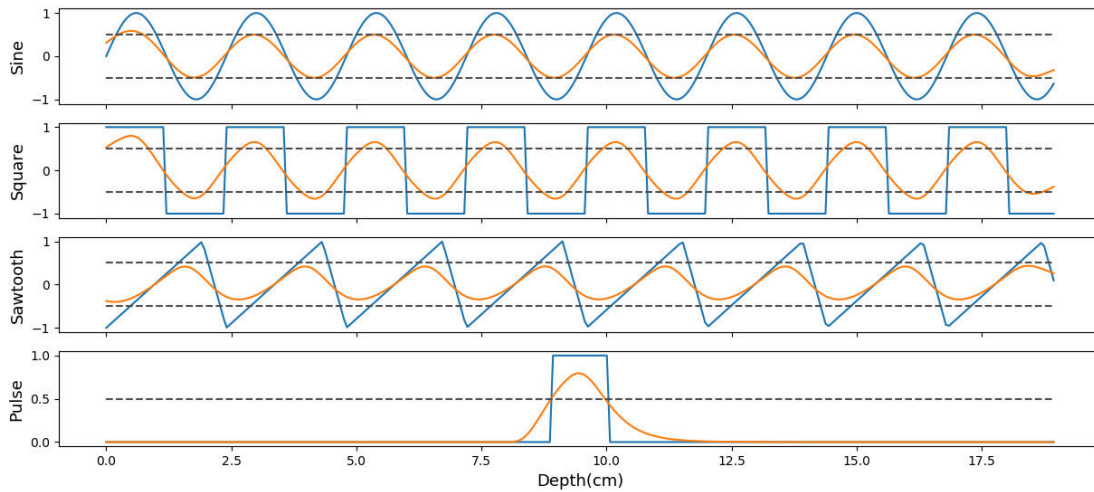


Figure 3.11 – Attenuation experienced by signals depending on their shape. The unaltered signals are in blue, and their corresponding smoothed version in orange. The sine, square, and sawtooth signals have a wavelength of 2.4cm, and the pulse signal has a width of 1.2cm. The dashed lines mark the 50% amplitude attenuation level.

concentration can be seen as impulse inputs to the system. Theoretically, the response of the CFA system to such an impulse is directly the smoothing function G , simply scaled according to amount of air entering the system. Figure 3.12 shows next to each other, the response of the CFA to a contamination due to a break, and the smoothing function calculated with the step experiment. As seen, they are in good agreement, indicating the validity of the step-experiment method.

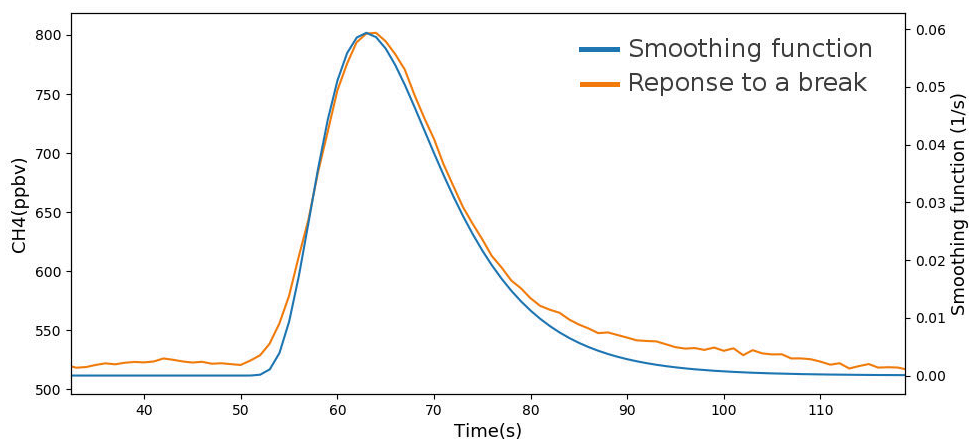


Figure 3.12 – In blue: smoothing function G derived from the step experiment. In orange: CFA system response to air contamination due to a break.

3.2 Pycnometry

Gas pycnometry is a method which allows us to measure the closed and open porosity volumes in firn samples, based on a gas dilation experiment (Stauffer et al., 1985). In this context, a pore is considered open if it reaches an edge of the firn sample. The IGE pycnometry system was first developed by J.M. Barnola during the 1990's. It was then restored by O. Magand and L. Arnaud a couple of years prior to this PhD. The pycnometry measurements made for this thesis were obtained with the help of X. Faïn and S. Pion.

3.2.1 Physical basis

The determination of the closed and open porosity volumes is based on the measurement of V_s , the volume inaccessible to outside gases in a firn sample. This volume V_s is composed of the ice phase and of the closed porosity. Therefore the closed and open porosity volumes V_c and V_o are given by:

$$\begin{cases} V_c = V_s - V_{ice} \\ V_o = V_{cyl} - V_s \\ V_{ice} = M/\rho_{ice} \end{cases} \quad (3.16)$$

where V_{ice} is the volume of the ice phase calculated from the sample weight and V_{cyl} is the volume of the firn sample measured geometrically. M and ρ_{ice} are respectively the mass of the firn sample and the density of pure ice.

The measurement of V_s is based on the dilation of an ideal gas between two chambers of known volumes V_1 and V_2 , depicted in Figure 3.13. The volume of the tubing between the two chambers is included in the value of V_1 . The firn sample to be analyzed is placed in chamber V_1 , while the chamber V_2 is isolated by a valve and then vacuum-pumped. A pressure gauge is attached to chamber V_1 in order to monitor its internal pressure. Then, the valve isolating the two chambers is opened, resulting in the dilation of the gas originally contained in V_1 , in a larger volume $V_1 + V_2$. The dilation creates a pressure drop that is recorded with the pressure gauge. Application of the ideal gas law before and after the

dilation yields:

$$P(V_1 - V_s) = NRT \quad (3.17)$$

$$P'(V_1 + V_2 - V_s) = (N + \Delta N_w)RT$$

where P and P' are the pressures monitored respectively before and after the dilation, R is the ideal gas constant, T is the temperature, N is the number of gas moles present before the dilation, V_s is the volume rendered inaccessible to gases by the firn sample, and ΔN_w is the additional water vapor molecules that have sublimated from the firn surface to establish the thermodynamical equilibrium between vapor pressure and ice in the expanded $V_1 + V_2$ volume.

To calculate V_s , one has to determine the number of moles of water molecules ΔN_w that have been sublimated from the firn sample. This number depends on whether the establishment of the equilibrium in the expanded volume is fast or slow, compared to the duration of the experiment.

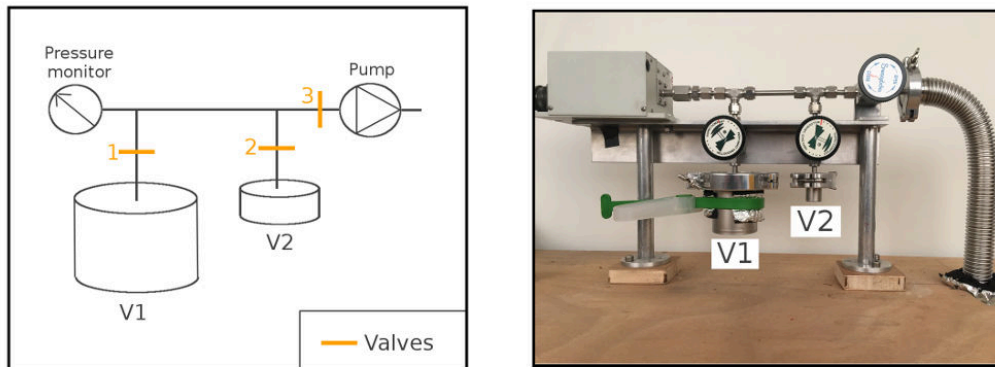


Figure 3.13 – Left: Schematics of the pycno apparatus including the two chambers of known volume V_1 and V_2 , and three valves in orange. Right: Picture of the pycnometry system.

Fast equilibrium case:

Assuming that the establishment of the equilibrium vapor pressure is fast compared to the time of the experiment (which is of the order of the minute), one can assume that the vapor pressure equals its equilibrium value P_w . The amount of added water vapor molecules ΔN_w is then simply linked to P_w by:

$$\Delta N_w RT = P_w V_2 \quad (3.18)$$

This fast equilibrium hypothesis is notably assumed by [Stauffer et al. \(1985\)](#) while perform-

ing pycnometry experiments. Re-arranging Equations 3.17 and 3.18, the inaccessible volume V_s can be determined by the pressures recorded during the experiment.

$$V_s = V_1 - \frac{\mathcal{R}}{1 - \mathcal{R}} V_2 + \frac{P_w V_2}{P - P'} \quad (3.19)$$

where \mathcal{R} equals P/P' . The last term of the right-hand side of Equation 3.19 is a correction term taking into account the effect of equilibrium vapor pressure over ice. For a typical temperature of -8°C during the measurements performed in this thesis, the equilibrium vapor pressure of ice is equals to 310Pa (Lide, 2005). Using pressures recorded during experiments, the correcting factor has been estimated to be about 0.2cm^3 . This is about 10% of the closed or open porosity volumes.

Slow equilibrium case:

In the case where the time to establish the vapor pressure equilibrium is much larger than the time of the experiments, one can neglect the release of water molecules from the firn sample. Then, ΔN_w is close to zero and the correction term of 3.19 vanishes. The equation then writes:

$$V_s = V_1 - \frac{\mathcal{R}}{1 - \mathcal{R}} V_2 \quad (3.20)$$

The problem is now to estimate if the pycnometry experiments performed during this PhD correspond to a fast or slow equilibrium case, that is to say if Equation 3.19 or 3.20 should be used. To answer this question, I used pycnometry experiments performed on cylinders of pure ice. As the pycnometry method yields the inaccessible volume to gases, it should directly yield the volume of the cylinder in the case of pure ice. Moreover, the volume of an ice cylinder can be determined with a good accuracy by measuring its mass and knowing the density of pure ice (Bader, 1964; Goujon et al., 2003).

One way to determine if Equation 3.19 or 3.20 should be used, is thus to examine which one yields the best results with pure ice samples. Figure 3.14 shows the difference between the volumes determined by pycnometry and the weighting methods. It indicates that the fast equilibrium hypothesis results in a systematic overestimation of the sample volume. On the other hand, the slow equilibrium hypothesis yield more consistent results. For this reason, I consider the slow equilibrium hypothesis to hold true and use Equation 3.20 for the rest of

the manuscript.

Note that for these experiments I had to know the volume of the chambers V_1 and V_2 . This was done following the calibration method described in Section 3.2.3, except that only stainless steel balls were used during this calibration.

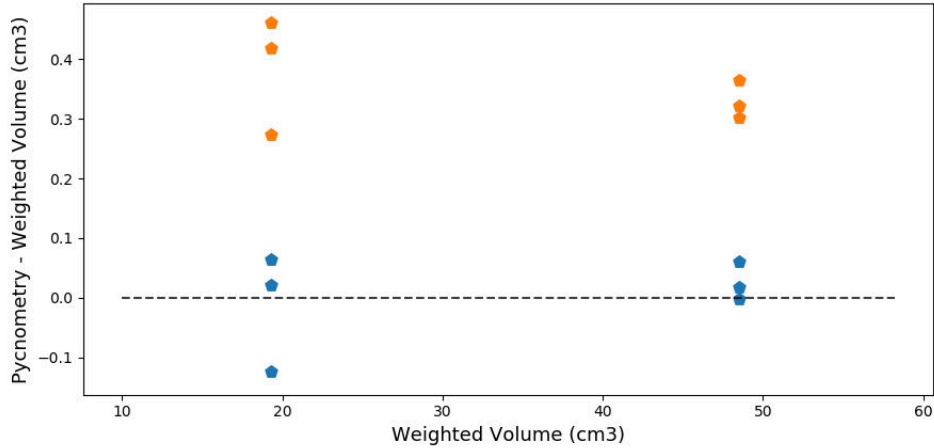


Figure 3.14 – Difference in volume between the pycnometry and weighting methods against weighted volume. The blue markers correspond to the slow equilibrium hypothesis, and the orange ones to the fast equilibrium. The dotted line illustrates the equality between the pycnometry and weighting methods.

As seen in Figure 3.14, the fast equilibrium hypothesis overestimates the inaccessible volume V_s . In turns, this overestimation bias the measured closed and open volumes. Following Equations 3.16, an overestimation of V_s results in an overestimation of the closed porosity volume V_c and an underestimation of the open porosity volume V_o . Indeed, application of Equation 3.19 to the samples of this PhD predicts the presence of a closed porosity occupying about 0.75% of the total sample volume for densities around $750\text{kg}\cdot\text{m}^{-3}$. On the other hand, such a large closed porosity is not visible on $25\mu\text{m}$ resolution tomographic images (described in Section 3.3.2). Therefore, the use of the fast equilibrium hypothesis by [Stauffer et al. \(1985\)](#) might explain why they report a large closed porosity at low density. Still, we do not know under what conditions the [Stauffer et al. \(1985\)](#) experiments were conducted, and it is possible that vapor equilibrium was established in their case.

One may wonder what is the physical explanation for the slow establishment of the vapor pressure equilibrium. One possible factor limiting the rapid establishment of this equilibrium are the kinetics of sublimation from the firm sample surface. Following the Hertz-

Knudsen equation, one has:

$$\frac{dN}{dt} = A \frac{\alpha_e (P_w - P)}{\sqrt{2\pi m k T}} \quad (3.21)$$

where $\frac{dN}{dt}$ is the number of water molecules leaving the ice through sublimation, A is the area of sublimation, m is the mass of a water molecule, k is the Boltzmann constant, and α_e is the evaporation coefficient. [Hobbs \(1974\)](#) report values of α_e close to 0.67. Considering the vapor to be rapidly mixed in the total accessible volume V of the experiment, the rearrangement of Equation 3.21 yields:

$$\frac{dP}{dt} + \frac{P}{\tau} = \frac{P_w}{\tau} \quad (3.22)$$

with

$$\tau = \frac{V \sqrt{2\pi m}}{A \alpha_e \sqrt{k T}} \quad (3.23)$$

The solution to Equation 3.22 is a rising exponential with an e-folding time equals to τ . Numerical application in the case of the pycnometry case ($V = 150\text{cm}^3$ and $A = 70\text{cm}^2$) yields an e-folding time of 0.2ms. This indicates that the establishment of vapor equilibrium is not limited by the kinetics of sublimation at the surface of the sample.

A second factor limiting the establishment of vapor equilibrium is the time required for the homogenization of the gases in the pycnometry apparatus. [Lide \(2005\)](#) reports a diffusion coefficient D_w of $0.219\text{cm}^2.\text{s}^{-1}$ at 0°C . To diffuse over a typical length scale of l of 10cm (the size of the pycnometry apparatus), water vapor requires a time $t = l^2/D$ equals to about 450s, that is to say 7min30s. Note that the diffusion coefficient at 0°C is an overestimation of the diffusion coefficient at -8°C , and therefore leads to an underestimation³ of the diffusion time. Therefore, vapor equilibrium cannot be achieved over the course of one experiment by the process of diffusion alone. My understanding is thus that the apparition of equilibrium is limited, not by the kinetics of surface evaporation, but rather by the homogenization time of the gases within the pycnometry apparatus.

3.2.2 Experimental protocol

Firn samples first need to be carved into cylinders directly from the firn core, following the cutting procedure of Figure 3.15. For that, we use the half of the core that was not dedicated to gas and chemistry measurements. Sections of about 30cm long are carved into cylinders using a lathe at IGE. This step is crucial as it influences the quality of the sample's shape and the precision with which its volume can later be determined. Extra care must be taken to ensure that the indentations made at the top and bottom of the core, which are used to maintain the core in the lathe, are well aligned. If not, the core will have a wobbly motion on the lathe that will result in a poor geometry. Moreover, the core must be carved slowly to avoid any shock that could deteriorate the indentations or the surface of the sample. The 30cm section is lathed until all initial faces are removed, which usually yields a cylinder with a 4cm diameter. Once carved, the 30cm long cylinder is cut into approximately 5cm long pieces using a vertical wheel saw. These 5cm pieces are the ones measured in the pycnometry apparatus. The samples are cleaned with a brush to remove potential inclusions of snow dust in the open porosity, and they are let one day in the cold room to reach thermal equilibrium. To avoid sublimation, the samples are sealed in plastic wrap and stored in packing plastic.

The protocol for the pycnometry measurements is as follows:

- The sample is weighted using a high precision scale.
- The radius and height are measured with a digital caliper.
- Chamber V_1 is open. Valve 1 is closed, while valves 2 and 3 are open.
- Chamber V_2 is vacuum-pumped (pressure inferior to 10^{-3} mbar).
- Valve 2 and 3 are closed, and valve 1 is opened. Chamber V_2 is thus isolated and outside air enters the tubing connecting the chambers.
- The firn sample is placed in chamber V_1 and the chamber is closed.
- The system is let 1min to reach pressure equilibrium, and the internal pressure P is recorded using a LabView virtual instrument.
- Valve 2 is slowly opened, and the gas expands in the volume $V_1 + V_2$.
- The system is let 1min to reach pressure equilibrium, the internal pressure P' is recorded.

The firn sample can then be removed from chamber V_1 , and the experiment started over

for a new sample. It is important during the experiment to ensure that the first chamber is properly sealed and airtight. The internal pressure of the chamber should increase while tightening the sealing bolt and not rapidly drop after sealing. If a leak is detected, chamber V_1 should be opened to re-position the seal. To ensure that volume V_1 is consistent between experiments, the sealing bolt needs to be tightened in the same fashion in all experiments. It is important that all manipulations on the sample and on the pycnometry apparatus are made with thick and insulating gloves, to ensure that the whole system is at equilibrium temperature. Moreover, the movable parts of the system should not touch any heated element, including the wood box containing the pumps and other heated elements, still in order to maintain the system at a unique temperature. Drifts in the cold room temperature over time scales of ten minutes have been observed. By monitoring the variations in internal pressure and in the cold room temperature, we observed that the internal pressure varies greatly with the external temperature. Therefore, after dilation the pycnometry system should not be allowed more than a couple of minutes to reach the pressure equilibrium. Finally, valves need to be opened slowly not to overwhelm the pressure monitor and the pump with abrupt pressure variations.

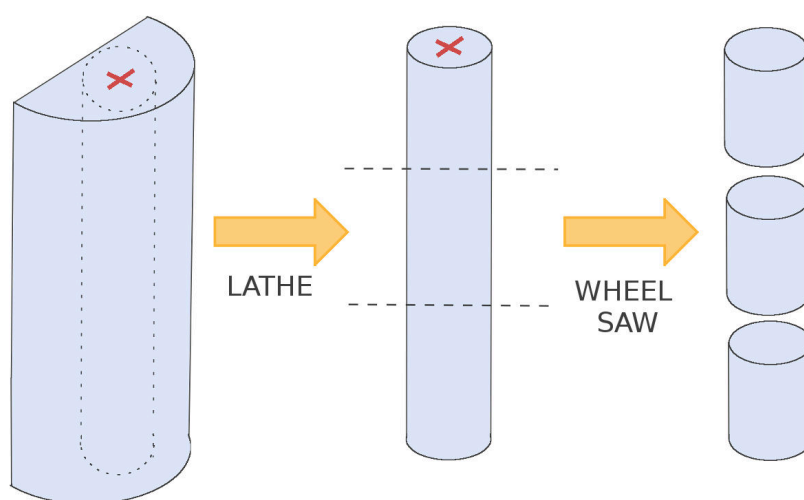


Figure 3.15 – Cutting procedure for the pycnometry samples. The red cross marks the position of the top indentations maintaining the sample to the lathe.

3.2.3 Calibration of the chamber volumes

To be applicable, Equation 3.20 requires to know the volumes V_1 and V_2 of the chambers. For this PhD, I developed a calibration procedure based on the fact that these volumes can be determined using the pycnometry apparatus itself. For this purpose, we execute gas dilation as one would do with firm samples, but instead with non porous object of known

volumes. Since these objects do not have pores, the volume V_s they render inaccessible to gases is simply their full volume. Performing N experiments we thus have the system of equations:

$$\left\{ \begin{array}{l} V_s^1 = V_1 - \frac{R^1}{1-R^1} V_2 \\ V_s^2 = V_1 - \frac{R^2}{1-R^2} V_2 \\ \dots \\ V_s^N = V_1 - \frac{R^N}{1-R^N} V_2 \end{array} \right. \quad (3.24)$$

where V_s^i and R^i are the volume of the object and the recorded pressure ratio during the i th experiment. This linear system can be expressed in matrix form:

$$X\beta = y \quad (3.25)$$

where X is a $N \times 2$ matrix with $X_{i1} = 1$ and $X_{i2} = R^i/(1 - R^i)$, $y = [V_s^1 \dots V_s^N]^T$ is the vector of the known volumes, and $\beta = [V_1, V_2]^T$ is the vector of the unknown parameters. This problem is overdetermined, and can be solved by minimizing the sum of the squared residuals between the known volumes and their estimations. The optimal $\hat{\beta}$ vector is given by:

$$\hat{\beta} = (X^T X)^{-1} X^T y \quad (3.26)$$

Moreover, the variance of the vector of unknowns $\hat{\beta}$ is given by:

$$\sigma_{\beta} = \sigma(X^T X)^{-1} \quad (3.27)$$

where σ is the variance of the residuals between y (vector of known volumes) and $\hat{y} = X\hat{\beta}$ (estimation of the known volumes).

To calibrate the pycnometry apparatus for this PhD, we used two types of non porous objects. We first used commercial stainless balls of known volumes and bought from the Marteau & Lemarié company. These balls respect the ANSI 440C norm and have volumes of 22.3, 33.5 and 46.0 cm³. Similar stainless steel balls were used by J.M. Barnola, L. Arnaud and O. Magand when using and restoring the pycnometry apparatus. However, the firm samples measured during this thesis have volumes of about 60cm³, outside of the volume range of the stainless steel balls. One might then wonder about the validity of the calibra-

tion for firm samples that lay outside the calibration range. This problem can be corrected by using larger non-porous objects. However, it is not possible to use larger stainless steel balls, as they do not fit in chamber V_1 for volumes over than 46.0cm^3 . As a solution, I proposed to use cylinders of pure ice grown at IGE. Their volumes were determined by a weighting method, knowing that $V_s = M/\rho_{\text{ice}}$. As explained in the next section, this method is much more precise than measuring volumes with calipers. With this method, we created four new calibration samples with volumes of 19.3, 48.5, 81.7, and 104.4cm^3 . Each stainless steel ball and ice cylinder was measured three times. We also performed three experiments without any object in the chamber, corresponding to the case $V_s = 0$, for a total of 24 calibration experiments.

The volumes V_1 and V_2 have been determined to be 138.97 ± 0.05 and $6.875 \pm 0.003 \text{ cm}^3$. The good agreement between the estimated and known volumes V_s , with residuals around 0.07cm^3 , is highlighted in Figure 3.16.

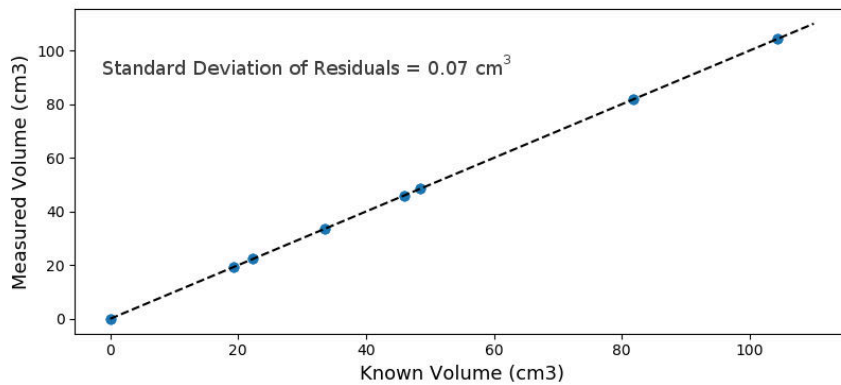


Figure 3.16 – Estimation of V_s against known values of V_s after calibration. The dashed line represents the Measured Volume = Known Volume curve.

3.2.4 Experimental uncertainties

For a firm sample, the volume of the ice phase V_{ice} is derived using the weight of the sample and the density of pure ice. For this purpose a high precision weighting scale is used, that yields results with a precision of 0.01g. The density of pure ice is determined using the temperature parametrization proposed by Goujon et al. (2003) and based on data from Bader (1964):

$$\rho_{\text{ice}} = 0.9165(1 - 1.53 \times 10^{-4}T) \quad (3.28)$$

where the temperature T is expressed in $^{\circ}\text{C}$, and ρ_{ice} is expressed in $\text{g}\cdot\text{cm}^{-3}$. The temperature during the measurements was regulated to be at -8°C . The discontinuities of cooling cycles lead to variations of $\pm 2^{\circ}\text{C}$ in the cold room. The density of pure ice is thus $0.9176 \pm 0.0003 \text{ g}\cdot\text{cm}^{-3}$, that is to say an uncertainty lower than 0.05%. The firn samples measured during this PhD have a mean mass of 50g, with extremal values of 39 and 71g. This corresponds to a mean ice volume of $51.46 \pm 0.019\text{cm}^3$, with extremal values of $40.14 \pm 0.016\text{cm}^3$ and $73.08 \pm 0.025\text{cm}^3$. The ice phase volume is thus determined with a precision better than 0.04%. Note that the same method was used to determine the volumes of the calibration cylinders made of pure ice and used in Section 3.2.3, with the same degree of precision.

The volumes of the samples V_{cyl} are determined by geometrical measurements using a digital caliper. As the samples are carved into cylinders, their volumes are determined by measuring the diameter and the height of each sample. The digital caliper used has a precision of 0.02mm. However, due to irregularities and defaults in the shapes of the samples it does not follow that the diameters and heights are determined with a 0.02mm accuracy. By performing multiple diameter and height measurements on the same samples, we concluded that these quantities are rather known with a precision closer to 0.05mm. For a typical diameter of 4cm and height of 5cm, firn samples have a volume of $63 \pm 3\text{cm}^3$. The sample volumes are thus determined with a precision of about 5%, and are consequently the main source of uncertainty of the method.

I combined the impacts of the different sources of uncertainties using the propagation formula:

$$\left(\Delta X\right)^2 = \sum_i \left(\frac{\partial X}{\partial x_i} \Delta x_i\right)^2 \quad (3.29)$$

where X is the quantity the uncertainty is computed for, x_i are the independent sources of uncertainties, and ΔA is the standard deviation of a variable A . The uncertainty for the closed porosity ratio (ratio of closed pores to open pores) and the density have been computed for the samples of the measurement campaign of this PhD. They are displayed in Figure 3.17 as a function of the firn sample density.

The uncertainty on the density of the samples is relatively constant with a value of $0.0082 \text{ g}\cdot\text{cm}^{-3}$, that is to say an uncertainty of 0.009 in density relative to pure ice. On the other

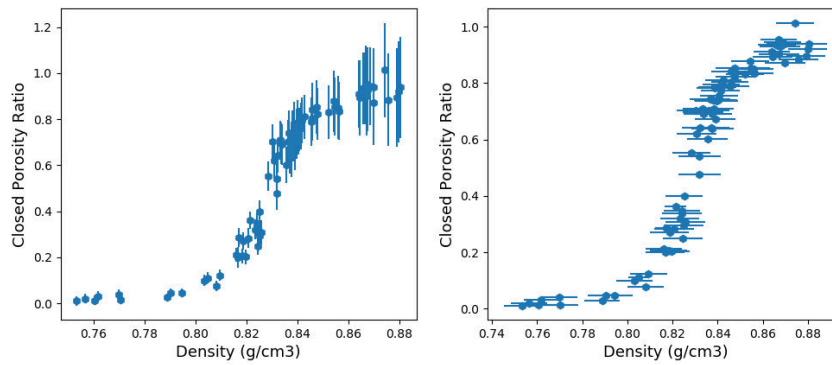


Figure 3.17 – Closed porosity against relative density in firn samples. The left panel highlights the uncertainties on the closed porosity ratio, and the right panel highlight the uncertainties on the relative density of the samples.

hand, the uncertainty on the closed porosity ratio increases with higher density. For low density the uncertainty is close to 0.02, and reaches up to 0.2 for high density firn. Equation 3.29 enables to differentiate the contribution of each uncertainty source to the total uncertainty. The individual contributions for two firn samples are displayed in Figure 3.18. It appears that the uncertainties on the open and closed volumes do not significantly change between low and high density firn. The determination of the open volumes is strongly affected by the uncertainty associated with the radius estimation, with a contribution close to 1.5cm^3 . On the other hand, determination of the closed pores volume is independent of the volume of the firn sample, and is therefore not affected by the radius uncertainty. In that case the largest contributions are due to determination of the pressure values in chamber V_1 . Concerning the closed porosity ratio, the contributions of the error sources depend on density. At low density, the contributions are similar to the ones affecting the closed volume with no influence of the sample volume determination. At high density, the closed porosity ratio is greatly affected by the determination of the sample radius similarly to the open volume. We can therefore conclude that the increase of the closed porosity ratio uncertainty with density is due to increasing effect of the radius determination. Future work to improve the pycnometry precision should focus on improving the radius and volume determination of the sample.

3.3 Other measurements performed during the thesis

For the work of this PhD, other measurements have been performed to characterize the physical and chemical properties of firn and ice cores. These methods are well established

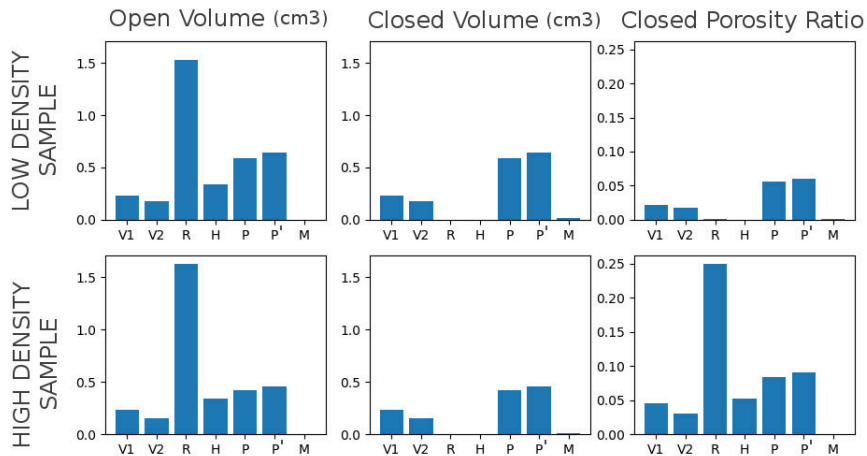


Figure 3.18 – Contribution of each uncertainty source to the final uncertainty of open porosity volume (first column), closed porosity volume (middle column) and closed porosity ratio (last column). The sources of uncertainties are in order volumes of chambers V_1 and V_2 , radius, height, pressures before and after dilation, and mass. The top panels represent the case of a low density firn sample, and the bottom panels the case of a high density firn sample.

in the ice core community. Therefore, I will present them, what can be learned from their interpretation, and what are their limitations, but with less details than the CFA or pycnometry methods.

3.3.1 Density measurements by Xray absorption

Density is one of the key parameters to characterize the trapping of gases in polar ice. Indeed, the constriction and closure of the pore network is characterized by an increase in density. Measuring density by weighing and size measurement only allows one to obtain density averages over large firn or ice pieces. To overcome this issue, high resolution density measurements based on the absorption of Xrays have been developed, notably at the Alfred Wegener Institut (AWI) in Bremerhaven, Germany. I performed the high resolution density measurements later used in Chapter 4 at AWI, with the help of C. Schaller and J. Freitag.

This method relies on Beer's law, describing the absorption of electromagnetic waves in the ice material (Hörhold et al., 2011). The attenuation of a ray traversing a section dx of ice material reads:

$$I(x + dx) = I(x) - I(x)Adx \quad (3.30)$$

where I is the intensity of the ray (in W.m^{-2}) and A is an absorption coefficient (in m^{-1}). Equation 3.30 can be rearranged to:

$$\frac{dI}{dx} + AI = 0 \quad (3.31)$$

whose general solution is:

$$I(x) = I_0 e^{-Ax} \quad (3.32)$$

where x is the distance traversed in the ice material. Let us suppose that the absorption of Xray in the air is negligible compared to the absorption in the ice. If we now consider the absorption by firn or bubbles containing ice, we have:

$$I(x) = I_0 e^{-AL_{\text{ice}}} \quad (3.33)$$

where L_{ice} is the distance traveled by the ray in the ice phase only. Therefore, the ratio between the ray after and before traversing a piece of firn is:

$$\frac{I}{I_0} = e^{-AL_{\text{ice}}} \quad (3.34)$$

If the firn sample has a length L , then L_{ice} can be expressed as:

$$L_{\text{ice}} = L \frac{\rho}{\rho_{\text{ice}}} \quad (3.35)$$

Rearranging Equations 3.34 and 3.35, the density ρ is related to the attenuation of the Xray by:

$$\rho = -\ln\left(\frac{I}{I_0}\right) \frac{\rho_{\text{ice}}}{AL} = -\ln\left(\frac{I}{I_0}\right) \frac{1}{\mu_{\text{ice}}L} \quad (3.36)$$

where $\mu_{\text{ice}} = A/\rho_{\text{ice}}$ is the mass absorption coefficient of ice (expressed in $\text{m}^2.\text{kg}^{-1}$). As seen in Figure 3.19, dense layers are characterized by high Xray attenuations and thus lower intensities recorded by the sensor.

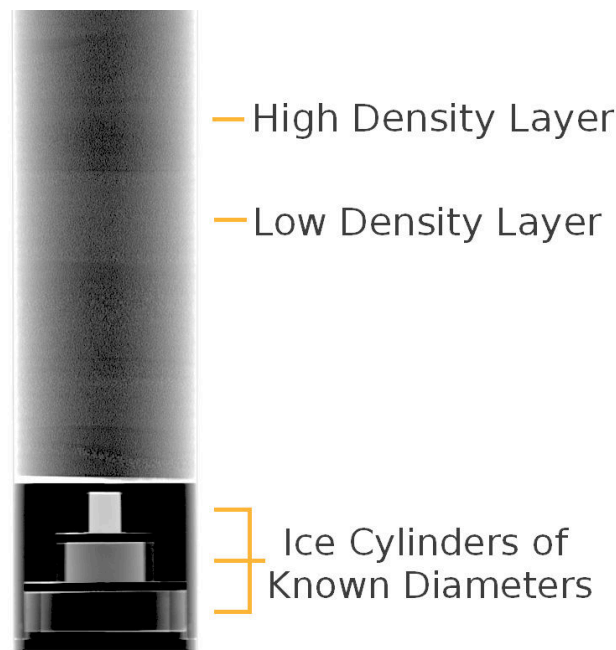


Figure 3.19 – Example of the Xray scan of a firn core. High attenuation layers correspond to high density layers. The ice cylinders used for calibration are visible at the bottom.

The density measurements are performed on the whole core. The core is measured by section of 1m, with the Xray source and sensor oriented towards the middle of core. To retrieved the density from the measured attenuation, it is necessary to know the diameter of the core, that corresponds to L in Equation 3.36, and the mass absorption coefficient μ_{ice} . The diameter of the core was measured for each 1m long section using a caliper. The parameter μ_{ice} is determined for each new scan, by using cylinders of pure ice of known diameters at the bottom of core, as seen in Figure 3.19. However, the diameter measured with the caliper might not be representative of the entire 1m long section, and might result in non accurate density values. Moreover, ice cores are regularly damaged during the drilling by the core catchers, resulting in missing pieces of ice. One should therefore be careful not to confuse density variations representative of the stratified nature of the firn, and apparent density variations due to damaged firn core.

When measuring deep firn, this method allows one to clearly distinguish between adjacent low and high density layers. However, the determination of the absolute density values are sensitive to estimation of the core diameter and of the ice absorption coefficient. As a results one should be aware of potential biases when discussing absolute density values.

3.3.2 Tomography

Tomography is a technique used to reconstruct 3D models of objects. In this thesis, I use it to produce voxelized models of firn samples, with voxels either being part of the ice or pore phase. Similarly to the density measurements, Xray scans of the firn samples are performed. However for tomography, the same firn sample is scanned from different angles. These scans are used as a set of different projections of the same firn sample. Then, a tomography algorithm is used to reconstruct the structure of the firn sample from its projections and to create a voxelized model of the sample (Ritman, 2004). The 3D models are segmented to produce the final binary models (Hagenmuller et al., 2013). Tomographic scanning is a well established technique with a wide range of application fields, from medical to earth sciences (Mees et al., 2003; Bouxsein et al., 2010). Therefore, commercial apparatuses are available, and can be used for the study of firn samples.

I selected and lathed 10 firn samples to be analyzed with tomography for my PhD. The tomographic scans of the selected samples were performed by M. Schneebeli, H. Löwe and A. Marshal at the Institut für Schnee und Lawinenforschung (SLF) in Davos, Switzerland. The samples scanned have the same geometry as the pycnometry samples, that is to say cylinders of radius and height of 4 and 5cm. Examples of the obtained 3D representation of the firn are displayed in Figure 3.20.

The tomography models of the thesis are composed of $25\mu\text{m}$ cubes. Burr et al. (2018) report that the size of voxels influence the determination of closed and open porosity in firn samples. However, Burr et al. (2018) also report that changing from 12 to $30\mu\text{m}$ voxels, only modify the total amount of closed pores by a few percent, and that this effect decreases with firn density.

During my PhD, I analyzed these tomographic images to characterize the changes of the porous network with the increase in density, with a specific focus put on the study of centimeter scale stratification. This analysis was made with python, ImageJ, and MATLAB[®] scripts that I coded during this PhD. I am grateful to A. Burr for introducing me to the scripting language of ImageJ. Moreover, a comparison of the closed porosity volumes obtained with the pycnometry and tomography methods is reported in Chapter 4.

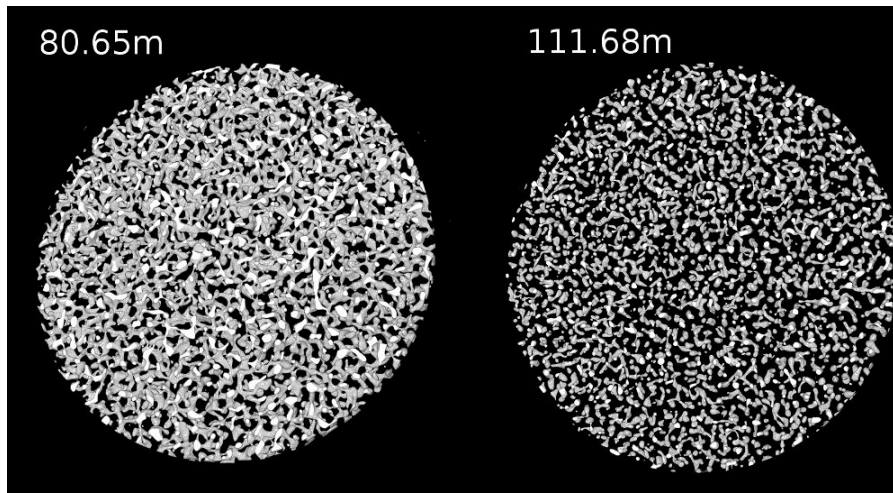


Figure 3.20 – Porous networks as obtained from two tomography images.

3.3.3 Air content

Air content is a direct measurement of the amount of air trapped in polar ice. It is expressed in cm^3 of trapped air at STP per gram of ice. The measurements used in thesis were performed by V. Lipenkov at IGE, following the method detailed in [Lipenkov et al. \(1995\)](#). Briefly, an ice sample of mass M is placed in a cell of known volume V_{cell} . The cell is then vacuum-pumped to remove all air, except the one enclosed in the ice sample. The ice sample is melted to liberate the gas inside. The meltwater is then slowly refrozen from the bottom to extract all gases from the ice phase. The cell is thermalized at a temperature T , and the pressure P_{meas} in the cell is measured. The air content is:

$$\text{AC} = \frac{V_{\text{air}} P T_0}{M T P_0} \quad (3.37)$$

where AC is the air content expressed in cm^3 at STP per gram of ice, $V_{\text{air}} = V_{\text{cell}} - M/\rho_{\text{ice}}$ is the volume occupied by the air in the cell, $P = P_{\text{meas}} - P_w$ is the pressure of gas corrected for the pressure of water vapor P_w , and T_0 and P_0 are the standard pressure and temperature. [Lipenkov et al. \(1995\)](#) report an uncertainty of about 1% on the determination of AC.

Typical samples have a volume of less than 30cm^3 . Therefore, a significant portions of bubbles that are closed at the scale of the firn column might be re-opened when cutting the sample. Such cut bubbles release the gas they contain before the measurements, resulting in underestimated values of air content. It is therefore necessary to correct for the presence of these cut bubbles at the surface of the sample ([Martinerie et al., 1990](#)). This correction

was taken into account by V. Lipenkov using the surface to volume ratio of the ice samples and bubble size measurements.

3.3.4 Chemistry measurements

Chemical ions and impurities are present within the ice phase of polar firn. Previous studies, such as Hörhold et al. (2012) or Fujita et al. (2016), have highlighted the role of chemical impurities on the densification of firn. To study the potential effect of chemical species on polar firn, I participated to high resolution chemistry measurements during this PhD. They were realized at the British Antarctic Survey (BAS) in Cambridge, UK, with the help of R. Tuckwell, R. Mulvaney, E. Ludlow, S. Jackson, and S. Miller. The measurements were done using a Continuous Flow Analysis system, similarly to the methane measurements.

Sticks of 34mm×34mm section are cut in the firn core, similarly to the methane CFA sticks. Prior to melting, the chemistry CFA sticks are flattened at the end to avoid outside air entrance in the system, and cleaned to avoid contamination. They are continuously melted and the meltwater retrieved through a pumping system. The meltwater is then debubbled and sent to an array of analyzers. They notably include the continuous analysis of Ca^{2+} , Na^+ , and NH_4^+ using colorimetry, the continuous measurement of liquid conductivity, the continuous measurement of dust concentration and a Fast Ion Chromatography (FIC). The FIC consists of two ion chromatographs working in parallel. While one chromatograph is collecting meltwater, the other one is performing the chromatographic separation of anions and their concentration analysis. The chromatographs are designed so they can analyze anion concentrations (notably F^- , Cl^- , and SO_4^{2-}) in less than a minute, meaning that a data point is obtained roughly every 4cm. Finally, a part of the meltwater is collected in clean vials for later ion chromatography (IC) measurements. Besides anions, the IC is used to obtain the concentrations of cations that cannot be determined with the FIC, including Mg^{2+} , Na^+ , and Ca^{2+} . Moreover, the IC data have a resolution of about 2.5cm, better than the FIC. However, the IC is more labor intensive to operate and therefore only 4m of firn core have been analyzed with it during this PhD. The IC measurements were performed by S. Jackson in the weeks following my visit to BAS.

Only the liquid conductivity measurements and concentrations from IC will be discussed

in this thesis (in Chapter 4). Indeed, the continuous colorimetry was not able to resolve the low ion concentrations present in firn cores from the East Antarctic plateau. Moreover, the spatial resolution of the FIC data is too coarse to properly identify centimeter scale variations of anions. Nonetheless, I ensured that the concentrations measured by the IC are consistent with the FIC, indicating that the collecting vials were not contaminated.

3.3.5 Thin sections and crystalline texture

As discussed in Section 2.2.3, the hexagonal crystalline structure of an ice single crystal is characterized by its c axis, specifying the orientation of the hexagonal structure (see Figures 2.12 and 3.21). The orientation of this vector is defined by an azimuth angle θ and a colatitude angle ϕ , as defined in Figure 3.21.

The ice in firn and polar ice sheets is poly-crystalline, composed of multiple single ice crystals, each with its own c -axis. The size and orientation distribution of the crystals (also called its texture) influence the behavior of ice at the macroscopic scale. This ice texture can be determined with the aid of thin sections.

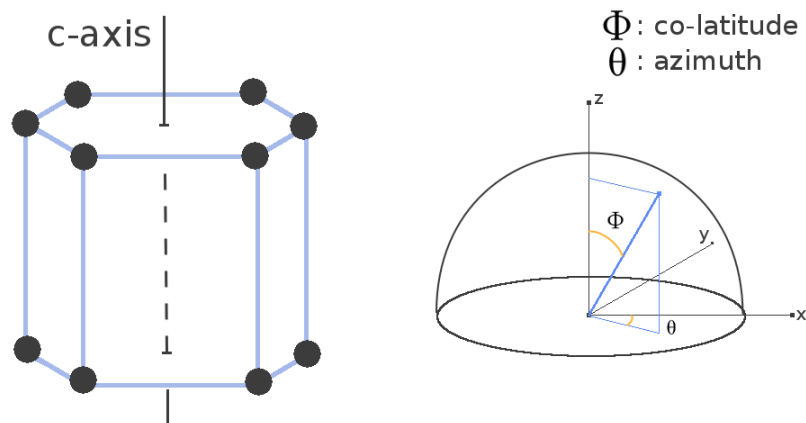


Figure 3.21 – Left: Hexagonal structure of an ice single crystal with the c -axis represented as a vertical line. Right: Definition of the azimuth angle θ and the colatitude angle ϕ , specifying the orientation of the blue vector.

The thin sections of ice and firn are prepared by trimming rectangular samples to a thickness of about 0.3mm with a dedicated microtome. To determine the orientation of the c -axis, the thin sections are then observed between two light polarizers. Indeed, ice is a birefringent medium meaning that its refraction index depends on the light direction of polarization. When a linearly polarized wave propagates within a birefringent medium, the polarization rotates around the propagation direction. The degree of rotation of the polarization can

be estimated by studying the light intensity transmitted through the second polarizer as a function of its orientation. In the case of ice, the rotation of the light polarization in the medium depends on the orientation of the *c*-axis. Automated analyzers exploit the birefringent properties of ice to construct a map of the crystalline orientations of a thin section (Peternell et al., 2010).

Thin sections and texture maps were made for this PhD. They were performed by M. Montagnat and C. Argenville at IGE using the Automatic Ice Texture Analyzer (AITA). An example of an analyzed thin section is displayed in Figure 3.22.

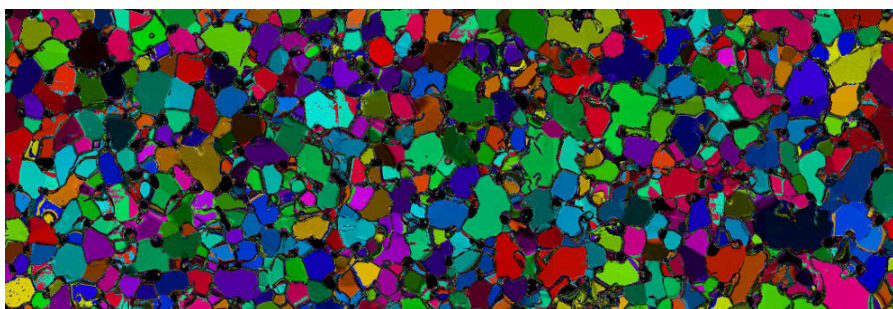


Figure 3.22 – Example of the crystalline texture of a thin section. Each color represents a *c*-axis orientation.

3.4 Conclusion of the chapter

This chapter presents the experimental methods used during this thesis and my implication in the measurement campaigns. A specific focus is put on the Continuous Flow Analysis of methane and on the gas pycnometry method, as I contributed to their ongoing development at IGE.

In the case of the CFA, I performed the measurements and developed the programs currently used to process the raw CFA data and to express them on a proper depth scale. To help with the estimation of methane solubility correction, I proposed a theoretical model with an analytical solution. I also characterized the smoothing function of the IGE CFA system, that is notably used in Chapter 5 and Fourteau et al. (2017) to estimate the impact of CFA smoothing on centimeter scale variations and on very-thinned ice cores. In total, 250m of ice were analyzed with X. Faïn during this PhD, representing a total of about 115 hours of melting.

For the pycnometry method, I set up the processing chain used to analyze the dilation experiments. I notably revised the calibration procedure using pure ice cylinders, in order to provide a calibration range consistent with the size of the measured samples. I also performed an uncertainty analysis in order to identify the sources of error in the method. For this PhD, 80 firn samples have been characterized to study the closure of pores at the bottom of the Lock-In site firn column.

I also participated in other measurement campaigns at AWI (high resolution density) and BAS (high resolution chemistry). In the case of the tomography imagery at SLF, I prepared the samples but only assisted for the measurements of the first two firn samples. The rest of the measurements were performed after my visit. I performed the post-processing and analysis of all the experimental data, with the help of my co-authors and PhD supervisors.

Thanks to the acquisition of a broad type of high resolution data on the same firn core, I was able to perform a multi-tracer study of the pore closure in a firn of East Antarctica, as described in Chapter 4. Moreover, the high-resolution datasets of methane mixing ratio measured in deep ice allowed me to characterize the impact of gas trapping processes on the gas records in ice cores of the East Antarctic plateau, as discussed in Chapter 5. The tomographic images acquired at SLF were also used to study the compression of a firn layer in the model presented in Chapter 6.

Study of pore closure in an East Antarctic firn core

Contents

4.1	Presentation of the chapter	83
4.2	Multi-tracer study of gas trapping in an East Antarctic ice core	84
4.2.1	Introduction	85
4.2.2	Methods	87
4.2.3	Results and discussion	93
4.2.4	Conclusions	113
4.2.5	Supplementary Material	115
4.3	To go further	121
4.3.1	Structural anisotropy of firn	121
4.3.2	Analysis of thin sections	123
4.4	Conclusion of the chapter	126

4.1 Presentation of the chapter

This chapter is based on an article submitted to the journal *The Cryosphere*. It deals with the study of a new firn core drilled in East Antarctica, at the Lock-In site 136km away from Dome C. It was chosen as it exhibits a surface temperature similar to Dome C (around -53°C) but a higher accumulation rate. One of the original goals motivating this new drilling was to estimate the effect of accumulation, independently of temperature, on the trapping of gases in polar ice.

The study of this new firn core, and the ability to use the whole core without saving an archive, motivated to restart the IGE pycnometry system and to optimize its operating procedures. Moreover, thanks to the high resolution of the data collected from this firn core, a specific focus could be placed on stratification, on the presence of early closure firn strata and their physical origins. Using the new collected data, the ability of a standard gas trapping model to predict the quantity of trapped air is also assessed.

As the pycnometry method is detailed in Section 3.2, the original Supplementary Information of the article has been revised to remove repetitions. The references in the text of the article have been modified accordingly.

Additional investigations of the firn structural anisotropy and crystalline texture (not presented in the submitted article or in its supplement) are presented at the end of the chapter, in Section 4.3.

4.2 Multi-tracer study of gas trapping in an East Antarctic ice core

Kévin Fourteau¹, Patricia Martinerie¹, Xavier Fain¹, Christoph F. Schaller², Rebecca J. Tuckwell³, Henning Löwe⁴, Laurent Arnaud¹, Olivier Magand¹, Elizabeth R. Thomas³, Johannes Freitag², Robert Mulvaney³, Martin Schneebeli⁴, and Vladimir Ya. Lipenkov⁵

[1] Univ. Grenoble Alpes, CNRS, IRD, Grenoble INP, IGE, 38000 Grenoble, France

[2] Alfred Wegener Institute, Helmholtz Centre for Polar and Marine Research, 27568 Bremerhaven, Germany

[3] British Antarctic Survey, Natural Environment Research Council, Cambridge, UK

[4] WSL Institute for Snow and Avalanche Research (SLF), CH-7260 Davos Dorf, Switzerland

[5] Climate and Environmental Research Laboratory, Arctic and Antarctic Research Institute, St. Petersburg, 199397, Russia

Abstract

We study a firn and ice core drilled at the new Lock-In site in East Antarctica, located 136km away from Concordia station towards Durmont d'Urville. High resolution chemical and physical measurements were performed on the core, with a particular focus on the trapping zone of the firn where air bubbles are formed. We measured the air content in the ice, closed and open porous volumes in the firn, firn density, firn liquid conductivity and major ion concentrations, as well as methane concentrations in the ice. The closed and open porosity volumes of firn samples were obtained by the two independent methods of pycnometry and tomography, that yield similar results. The measured increase of the closed porosity with density is used to estimate the air content trapped in the ice with the aid of a simple gas trapping model. Results show a discrepancy, with the model trapping too much air. Experimental errors have been considered but do not explain the discrepancy between the model and the observations. The model and data can be reconciled with the introduction of a reduced compression of the closed porosity compared to the open porosity. Yet, it is not clear if this limited compression of pores is the actual mechanism responsible for the low amount of air in the ice. High resolution density measurements reveal the presence of a strong layering, manifesting itself as centimeter scale variations. Despite this heterogeneous stratification, all layers, including the ones that are especially dense or less dense compared to their surroundings, displays similar pore morphology and closed porosity as function of density. This implies that all layers close in a similar way, even though some close in advance or later than the surrounding normal layers. Investigation of the chemistry data suggests that in the trapping zone, the observed stratification is mainly due to the effect of

chemical impurities.

4.2.1 Introduction

Deep ice cores drilled in polar ice sheets are climatic archives of first importance in the field of paleoclimatology (e.g. [Masson-Delmotte et al., 2013](#)). Indeed, ice cores have the unparalleled characteristic of containing various past climatic information in the ice matrix and the bubbles within (e.g. [Petit et al., 1999](#); [Jouzel et al., 2007](#); [Brook and Buizert, 2018](#)). In particular, the bubbles enclosed in polar ice contain air from past atmospheres, and their analysis can be used to reconstruct the atmospheric composition history of the last 800kyr ([Stauffer et al., 1985](#); [Loulergue et al., 2008](#); [Lüthi et al., 2008](#)). The bubbles get progressively enclosed in the ice at depths approximately ranging from 50 to 120m below the surface of the ice sheet, depending on the local temperature and accumulation conditions. These depths correspond to the transformation of the firn, a name for dense and compacted snow, into airtight ice encapsulating bubbles.

The firn column is characterized by the increase of its density with depth, as the material gets compressed by the load pressure of the newly accumulated snow (e.g. [Arnaud et al., 2000](#); [Salamatin et al., 2009](#)). As the firn density increases, the interstitial pore network is reduced. Eventually, some sections become small enough to prevent gas movement and pinch, enclosing part of the interstitial air ([Schwander et al., 1993](#)). This marks the beginning of the trapping zone where bubbles are closing and encapsulate atmospheric air. The trapping zone usually spans over about 10m ([Witrant et al., 2012](#)).

The process of gas trapping has impacts for the interpretation of ice core gas records. First, since bubbles are trapped deep in the firn, the enclosed air is always younger than the surrounding ice (e.g. [Schwander and Stauffer, 1984](#)). This age difference between the ice and the air is known as Δ age in the ice core community, and needs to be taken into account to synchronize the measurements performed in the bubbles, such as greenhouse gas concentrations, and the ones performed in the ice, such as temperature reconstruction ([Shakun et al., 2012](#); [Parrenin et al., 2013](#)). Secondly, due to the progressive closure of bubbles, an ice layer does not contain air corresponding to a single date, but rather from a wide distribution of ages (e.g. [Buizert et al., 2012](#); [Witrant et al., 2012](#)). These distributions act as a moving

average on the recorded gas signal, and attenuate the variability in the record compared to the true variability in the atmosphere (Spahni et al., 2003; Joos and Spahni, 2008; Köhler et al., 2011; Fourteau et al., 2017). Finally, due to the heterogeneous stratification of the firn at the centimeter scale, some layers might close in advance or late compared to their surroundings (Etheridge et al., 1992; Mitchell et al., 2015). The gases enclosed in these layers are thus older or younger than the gases in adjacent layers and appear as anomalous values in the record (Rhodes et al., 2016; Fourteau et al., 2017). Several studies have investigated the closing of porosity and increase of density in firns from both Greenland and Antarctica (Martinerie et al., 1992; Schwander et al., 1993; Trudinger et al., 1997; Fujita et al., 2014; Gregory et al., 2014), and linked it with the trapping of gas in polar ice (Rommelaere et al., 1997; Goujon et al., 2003; Schaller et al., 2017). One of the major results is the observation of a strong and heterogeneous stratification in polar firn and its correlation with ionic and impurity content (Hörhold et al., 2012; Freitag et al., 2013; Fujita et al., 2016). Moreover some studies have highlighted the direct relationship between the density of a firn layer and the amount of closed pores (Schwander and Stauffer, 1984; Martinerie et al., 1992; Mitchell et al., 2015).

Among the polar regions, East Antarctica is of particular interest for ice core drilling as this is where the oldest ice is retrieved. While several studies focus on the cold and arid sites of this region, none of them to our knowledge attempts to encompass a detailed description of stratification, closed porosity and gas trapping within the same firn. As particular examples, the study of Fujita et al. (2016) describes the link between density variability and ionic content in three firns core near Dome Fuji without addressing pore closure, while the studies of Schaller et al. (2017) and Burr et al. (2018) propose detailed descriptions of the of the pore network closure but without discussing stratification.

Our study thus aims to provide a detailed description of chemical and physical properties along the trapping zone of an Antarctic firn core. This core was drilled at the site of Lock-In in East Antarctica. It was chosen as its temperature is similar to the cold sites of Dome C and Vostok where deep ice cores have been drilled. Nonetheless, Lock-In displays a higher annual precipitation rate than Dome C and Vostok. When possible, the measurements were performed with a resolution allowing us to observe stratification and variabilities at the centimeter scale in the firn. Using high-resolution data sets, we intend to investigate the impact of firn stratification on gas trapping.

4.2.2 Methods

4.2.2.1 Lock-In study site

The ice core studied in this article was drilled in January 2016 at a site called Lock-In, located on the East Antarctic plateau, 136km away from Dome C along the traverse road joining Concordia and Dumont d'Urville stations (coordinates 74°08.310' S, 126°09.510' E). As an East Antarctic plateau site, Lock-In exhibits a fairly low temperature of -53.15°C (measured at 20m depth in the borehole), slightly higher than at the deep drilling sites of Dome C and Vostok. The site has an elevation of 3209m above sea level, and the surface atmospheric pressure was estimated to be 645mbar using the value at Dome C of 643mbar (data from the Automatic Weather Station Project) and a pressure elevation gradient of $0.084\text{mbar}\cdot\text{m}^{-1}$ (evaluated using pressure differences between D80 and Dome C). Lock-In is also characterized by a relatively low accumulation rate of $3.6\text{cm}\cdot\text{we}\cdot\text{yr}^{-1}$. The accumulation rate was evaluated by locating volcanic events with solid conductivity measurements. Hence, Lock-In has a similar temperature but a higher accumulation rate than Vostok and Dome C.

The drilling operation retrieved ice down to 200m below the surface. The amount of material was sufficient in the 10cm diameter core to perform several parallel measurements, which are described below. During the drilling procedure, air was sampled from the firn open porosity along the firn column. The last pumping was performed at 108m depth, indicating the depth where the firn reaches full closure and transforms into airtight ice.

4.2.2.2 High resolution density profile

Density is a parameter of particular interest when studying the enclosure of gas in polar ice. Indeed, the densification speed measures the amount of compaction of the firn and the reduction in pore volume. Hence, the density was continuously measured in the Lock-In firn and ice core. The measurements were performed on the whole 10cm diameter core from 6m down to 131m below the surface, at the Alfred Wegener Institute, Bremerhaven, Germany. The measurement technique is based on the absorption of gamma rays by the ice phase while traversing the core. The density is then derived from the ray attenuation using Beer's law. The method of measurement is described in details in [Hörhold et al. \(2011\)](#).

To be applicable, Beer's law requires the estimation of the core diameter d and the ice specific absorption coefficient μ_{ice} . The diameter of the core was measured using a caliper for one meter long sections. However, due to irregularities this value might not be representative of the entire section. Therefore, ice core parts where ice was missing (for instance parts broken during drilling) were removed from the final dataset. Finally, the value of the specific absorption coefficient μ_{ice} was calibrated for each new scan using cylinders of pure ice with known diameters. One should note that the results are quite sensitive to the determination of d and μ_{ice} . Thus, the high-resolution density data will not be discussed in terms of absolute values but rather in terms of centimeter scale variations, which are better constrained. This measurement method allows one to retrieve density variations at the sub-centimeter scale.

4.2.2.3 Pycnometry measurements

Pycnometry is an experimental method for the measurement of closed and open porosity volumes in a firn sample (Stauffer et al., 1985; Schwander et al., 1993). In this context, a pore is determined as open if it reaches the edge of the sample.

The pycnometry experimental set-up is composed of two sealed chambers of known volumes V_1 and V_2 , with a pressure gauge connected to the first chamber and a valve allowing the operator to isolate V_2 from V_1 . The sample is placed in chamber V_1 , while chamber V_2 is isolated and vacuum pumped. Then, the two chambers are connected, resulting in a homogeneous pressure in both chambers lower than the initial pressure in V_1 . This pressure drop is linked to V_s , the volume rendered inaccessible to gases by the sample in the first chamber, by the relation:

$$V_s = V_1 - \frac{R}{1-R} V_2 \quad (4.1)$$

where $R = P'/P$ with P' and P being the pressure value in chamber V_1 respectively after and before the dilation. The application of the equation requires the knowledge of the volumes V_1 and V_2 . The two volumes V_1 and V_2 were calibrated using stainless steel balls and bubble free ice pieces of known volumes. The derivation of Equation 4.1 and the description of the calibration procedure are provided in the Section 3.2.

Then the closed and open porosity volumes are computed given that:

$$\begin{aligned} V_c &= V_s - V_{ice} \\ V_o &= V_{cyl} - V_s \\ V_{ice} &= M/\rho_{ice} \end{aligned} \quad (4.2)$$

where V_c is the closed pore volume, V_o is the open pore volume, V_{ice} is the volume occupied by the ice phase, V_{cyl} is the volume of the sample, M is the mass of the sample, and ρ_{ice} is the density of pure ice. The density of pure ice was taken as 0.918g.cm^{-3} , for a recorded temperature of -8°C during the measurements (Bader, 1964; Goujon et al., 2003).

A total of 80 samples were taken within the Lock-In core, with depths ranging from 76m to 130m. The measured samples were cylinders with typical diameters and heights of 4cm, obtained with a vertical lathe at the Institut des Géosciences de l'Environnement (IGE), Grenoble, France. The radius and height were measured for each sample using a digital caliper in order to estimate the volume of the firn sample V_{cyl} . To estimate the ice volumes V_{ice} , the samples were weighted. Finally, the densities ρ of the samples were computed as $\rho = M/V_{cyl}$.

The treatment of uncertainties is reported in the Section 3.2.4. One of the main results of this uncertainty analysis is the large uncertainties associated with the sample volumes V_{cyl} due to their sensitivity to the radii measurements. The large uncertainty on V_{cyl} affects the determination of the density ρ with a typical uncertainty of 0.01g.cm^{-3} .

Following the definition of an open pore from a pycnometry point of view, some pores that are closed in the firn (they no longer connect to the atmosphere) might appear open in small samples. For instance, the blue pore in Figure 4.1 is closed when taken in the whole firn column, but open when observed in a small cylindrical sample. This opening of closed pores when sampling firn is known as the cut-bubble effect, and will be discussed in section 4.2.3.1.

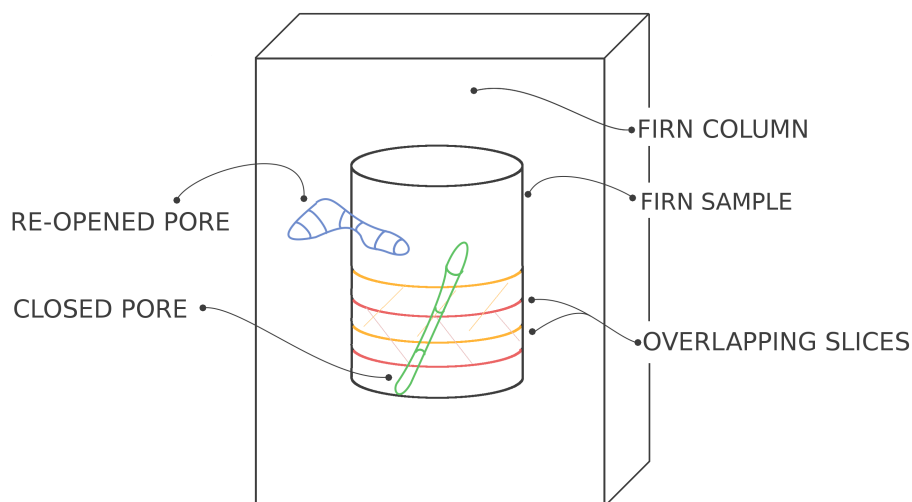


Figure 4.1 – Depiction of a cylindrical firn sample, numerical slices in tomographic images, and pores. The yellow and orange slices, represent two overlapping slices. The blue pore illustrates the cut-bubble effect: a pore initially closed in the firn column appears open in the cylindrical sample. The green pore is fully enclosed in the cylindrical sample, and is thus considered closed in the slices even if it intersects with their boundaries.

4.2.2.4 Tomography measurements

Computed X-ray tomography is a technique gaining traction for the study of firn densification and pore closure (Barnola et al., 2004; Freitag et al., 2004; Gregory et al., 2014; Schaller et al., 2017; Burr et al., 2018). Briefly, several 2D X-ray scans of the samples are performed under different angles. Then, based on the contrast of X-ray absorption between the ice and pore phases, tomography techniques are able to reconstruct a voxelized 3D model of the scanned samples. Ten samples from the Lock-In firn core were measured at the Institut für Schnee und Lawinenforschung (SLF), Davos, Switzerland, using a commercial tomography apparatus. The tomography samples have the same geometry as the pycnometry ones, and were also prepared at IGE using a lathe. Four of the samples measured using tomography were also measured by pycnometry. The obtained 3D models are gray scale images, composed of square voxels of $25\mu\text{m}$ in length. The gray scale images were automatically segmented by fitting the gray value histogram to three Gaussian curves (based on Hagenmuller et al., 2013), producing binary images of pore and ice voxels.

Using the 3D images, one can then compute the relative density to pure ice $\rho^R = \rho/\rho_{\text{ice}}$ of the samples as the ratio of ice voxels to the total number of voxels. The relative density represents the volume fraction occupied by the ice phase in the firn sample. Throughout the article, we use relative densities instead of densities (mass to volume ratio). This was chosen as relative densities are not sensitive to temperature, and thus allow an easier comparison between sites.

Tomographic images give access to the pore network, and can thus be used to determine the volume of closed and open porosity. As with the pycnometry measurements, a pore is considered open if it reaches the boundary of the sample. Using the software ImageJ and the plug-in Analysis_3D (Boulos et al., 2012), we differentiated the open and closed pores in the 3D images. The volume of the open and closed porosity is then simply computed by summing the volume of the voxels belonging to an open or closed pore.

4.2.2.5 Air content

Air content, denoted AC in this article, is a measure of the quantity of air enclosed in polar ice. It is expressed in cm^3 of trapped air at standard temperature and pressure (STP) per gram of ice. Air content is directly related to the volume of pores during closure, and can thus be used to estimate the density at which a particular firn layer closed.

Air content was measured in the Lock-In firn core using the method described in Lipenkov et al. (1995). In order to correct the AC values for the cut-bubble effect, an estimation of the re-opened volume has been performed (based on bubble size measurements, Martinerie et al., 1990). In total 10 samples were measured, including 4 replicates. Six of these samples were taken around 122m depth, with a specific focus on stratification, and the four others were taken deeper at 145m.

4.2.2.6 Chemistry along the trapping zone

Several studies highlight the link between density heterogeneities and ionic content in firn layers (Hörhold et al., 2012; Freitag et al., 2013; Fujita et al., 2016). To study the presence of this link in the trapping zone of the Lock-In firn, chemical analyses were performed on this part of the core. The measurements were performed at the British Antarctic Survey, Cambridge, United-Kingdom, using a continuous flow analysis (CFA) system. Sticks were cut from the center of the core ($34 \times 34\text{mm}$), covering depths from 90 to 115m. The sticks were then continuously melted, and the meltwater analyzed for conductivity. Additional meltwater was collected in vials, using a fraction collector, for later analysis with ion chromatography (IC). Four one meter sections were analyzed at 2.5cm resolution using a dionex reagent-free ion chromatography system in a class-100 cleanroom. The measured species,

Table 4.1 – Summary of chemistry and impurity measurements, with associated species and typical resolution.

Method	Resolution (cm)	Depth coverage	Measured species and quantities
Continuous Analysis	< 0.1	90 to 115m	Liquid conductivity
IC	~ 2.5	92-93, 95-96, 100-101, and 113-114m	SO ₄ ²⁻ , NO ₃ ⁻ , Cl ⁻ , Na ⁺ , Mg ²⁺ , Ca ²⁺

associated resolutions, and depth coverages are summarized in Table 4.1.

4.2.2.7 Continuous methane measurements

During the drilling operation, about 100m of airtight ice was retrieved. This ice was analyzed for methane concentration in enclosed bubbles, using the continuous flow analysis system of IGE coupled with a laser spectrometer SARA based on optical-feedback cavity enhanced absorption spectroscopy (OF-CEAS; Morville et al., 2005). Ice cores were cut in 34 by 34mm sticks, and melted at a mean rate of 3.8cm.min⁻¹. The description of this system and data processing is available in Fourteau et al. (2017) and references therein. The continuous measurements were performed from the very bottom of the core (~ 200m deep), and melting upward to 100m below the surface. In the upper part of the core, porous layers are present and let laboratory air enter the measurements system, creating spurious values. The measurements were stopped around 100m depth, where most of the layers were still porous at the sample scale.

4.2.2.8 Dataset synchronization

This study produced three high resolution and continuous datasets: density, chemistry and methane. Although the chemistry data are composed of various species, they are all based on a unique depth scale and were thus treated as a single dataset for synchronization. In order to produce precise depth scales, notes and measurements were taken when beveled breaks had to be removed from the analyzed ice. Still, uncertainties on the depth scales of the order of a centimeter remain. Since this paper will discuss centimeter scale variability, it is necessary to synchronize the datasets to properly observe the presence or absence of covariation. The synchronization was performed manually by matching similar patterns. In order not to over interpret the data, we defined only depth shifts of the order of one centimeter and with a constant value between two core breaks.

4.2.3 Results and discussion

4.2.3.1 Closed porosity ratios

Deep firn densification is characterized by the transformation of the open pore network into bubbles encapsulating the air. Notably, pore closure is quantified through the evolution of the closed porosity ratio CP , defined as the ratio between the closed pores volume and the total pore volume (Mitchell et al., 2015; Burr et al., 2018). This closed porosity ratio falls to zero when the porosity is fully open and reaches 1 when the firn sample porosity is fully closed, making it a simple indicator of pore closure.

For the pycnometry measurements, CP was simply computed for each cylindrical sample from the measured open and closed volumes. On the other hand, thanks to the explicit representation of the pore network, tomography data can be used to access variations at scales finer than the sample size. Hence, the tomography images were numerically divided into 1cm thick slices, as depicted in Figure 4.1. The spacing between two slices was set as 0.5cm, meaning that slices are overlapping. The closed porosity ratio, as well as density, were then determined for each slice. To minimize the impact of the cut-bubble effect, the distinction between closed and open pores was performed on the full cylindrical images as displayed in Figure 4.1. Moreover, the top and bottom slices of each sample were discarded since, as in described Section 4.2.5.1 of the Supplement, they are the most affected by cut bubbles. The values of closed porosity obtained using both pycnometry and tomography are displayed Figure 4.2-a against relative density.

Burr et al. (2018) proposed to use the connectivity index as an indicator of pore closure. This index is defined as the ratio between the volume of the largest pore and the volume of all pores in a given sample, and is less sensitive to the cut-bubble effect (Burr et al., 2018). However, this index cannot be used in models of gas transport and trapping as it does not explicitly represent the amount of closed pores. Therefore, we will use the closed porosity ratio, rather than the connectivity index as an indicator of closure.

Consistency between pycnometry and tomography

The first closed porosity datasets have been obtained using pycnometry or similar methods

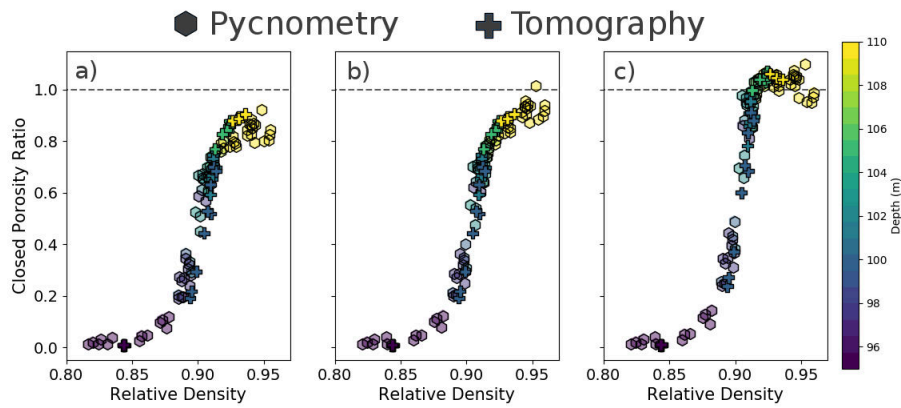


Figure 4.2 – Closed porosity ratio against relative density. a) Raw closed porosity ratios obtained from pycnometry and tomography. b) Pycnometry results corrected for volume overestimation, and unaltered tomography data. c) Pycnometry and tomography data corrected for cut-bubble effect. Colors stand for the depth of the sample. Note that the color scale has been limited to the range 95 to 110m to emphasize the middle of the trapping zone.

(Schwander et al., 1993; Trudinger et al., 1997; Goujon et al., 2003; Mitchell et al., 2015). However, the last decade has seen the development of tomography for the study of firn, and estimations of porosity closure based on tomographic images (Barnola et al., 2004; Gregory et al., 2014; Schaller et al., 2017; Burr et al., 2018). It is thus important to evaluate the consistency between the two types of methods.

A comparison of the results obtained for Lock-In in Figure 4.2-a indicates an inconsistency between the two datasets, with the tomography data closing at higher densities. To investigate this difference, we focused our attention on four specific cylindrical samples that have been measured both with the pycnometry and tomography methods. Comparison of the densities of these samples confirm a disagreement between the two methods, with systematically higher density values obtained with tomography. While the differences fall within the uncertainty range of the pycnometry measurements, a stochastic error cannot explain the observed systematic discrepancy. To estimate a possible bias of the tomography based density, four gray scale images were manually re-segmented. Relative deviations in density values were of the order of $9 \cdot 10^{-4}$, that is to say 0.1%. These deviations are similar to the uncertainties reported by Burr et al. (2018). Moreover, Burr et al. (2018) estimated the influence of voxel size on the determination of density values. They found that reducing voxel size from 30 to $12 \mu\text{m}$ does not change the density by more than 0.1% for relative densities in the range considered here. Therefore, it appears that the densities obtained with tomographic scanning are fairly robust. On the other hand, the densities obtained by size measurements and weighting are sensitive to the volume estimation, particularly through

the radius measurement. A close look at the cylindrical samples, notably using the tomography 3D models, revealed rough surfaces and some broken edges. An overestimation of the measured radius by 0.05mm is enough to explain the density discrepancy between the four samples measured with both pycnometry and tomography. Our understanding is that while measuring with a caliper, the operator tends to overestimate the actual radius of the sample because of the irregular geometry, leading to a density underestimation. We thus corrected the whole pycnometry dataset by considering a systematic overestimation of the radius by 0.05mm. This is consistent with the observation of sample surfaces using tomography models, reduces the overall discrepancy between the two methods and is within the uncertainty range for radius measurements. This radius correction has an influence on the density values but also on the open pore volumes (Equation 4.2). The corrected pycnometry results are displayed Figure 4.2-b, along with the unaltered tomography results. This correction is sufficient to explain the discrepancy in density between the two methods, while also improving the agreement on measured closed porosity ratios. Thus, after correction, pycnometric and tomographic methods produce consistent results of closed porosity.

Cut-bubble effect

As mentioned in Sections 4.2.2.3 and 4.2.2.4, during pycnometry or tomography measurements, a pore is considered open if it reaches the edge of the sample. However, some pores that are closed in the firn (that is to say not reaching the atmosphere), are considered as open if the edges of the sample intersect with them. This leads to the cut-bubble effect, where a fraction of the closed bubbles are considered as open pores (Martinerie et al., 1990; Lipenkov et al., 1997; Schaller et al., 2017). The impact of the cut-bubble effect is clearly visible Figure 4.2-a and b: while closed porosity ratio should reach 100% for high densities (corresponding to a fully closed material), an upper limit of $CP = 90\%$ appears in the data. This is due to the presence of cut bubbles at the surface of the cylindrical samples, even in fully closed ice. This cut-bubble effect can be partially mitigated by the use of large samples.

To correct for this effect, one has to estimate the fraction f of bubble volume opened during sampling. Then, the true close porosity ratio CP_{true} is given by:

$$CP_{\text{true}} = \frac{CP}{1 - f} \quad (4.3)$$

Martinerie et al. (1990) reports a fraction of cut bubbles up to 10% for deep ice samples nearly the same size as the sample used in this paper. However, this value should not be used to correct for cut-bubble effect in the trapping zone. Indeed, this 10% value was obtained in deep ice where bubbles tend to have cylindrical or spherical shapes. As pointed-out by Schaller et al. (2017), closed pores tend to have elongated and tortuous geometries in the trapping zone. The opening of a single pore reaching far into the sample can re-open a significant portion of the closed porosity. They estimated the impact of cut-bubble effect for cylindrical samples of 5cm in diameter and height, taken from the East Antarctic firn of the site B53 (-55°C temperature and $3.0\text{cm}\cdot\text{we}\cdot\text{yr}^{-1}$ accumulation rate). Using tomography, they scanned large firn samples of 10cm in diameter and 5cm in height. They then extracted 5cm diameter cylinders from the large samples. By comparing the state of pores before and after the extraction, they were able to determine which bubbles have been opened. Their findings indicate that up to 60% of the closed porosity gets re-opened near the density of full closure. Moreover, they find that still 30% of bubbles are re-opened when measuring deep ice samples with relative density close to 0.94 (Figure 4 in Schaller et al., 2017).

However, when applied to the Lock-In closed porosity ratio, the correction proposed by Schaller et al. (2017) leads to unphysical results. For high relative densities, direct application of their correction yields a closed porosity ratio well over 100%. This indicates an overestimation of the fraction of re-open bubbles for the Lock-In firn.

Two methods were used to estimate the fraction of cut bubbles specifically for the Lock-In samples. First, for depths well below the firn-ice transition, one knows that the samples are fully closed. Using pycnometry, we thus measured closed and open pore volumes in deep samples, and attributed all the open volumes to the cut-bubble effect. However, this only allows us to access the correction for fully closed firn. The second method was used to estimate the correction in partially closed samples. Similarly to Schaller et al. (2017), a tomography image was numerically re-shaped into a smaller sub-sample. The distinction between closed and open pores in the sub-sample was then performed following the method of section 4.2.2.4. Then, by comparing with the full sample image, one is able to measure the fraction of closed pores that have been opened. To produce the sub-samples we trimmed the original cylinder to remove 1cm in height and 0.5cm in diameter. The goal is to remove most of the immediate boundary effect described Section 4.2.5.1 of the Supplement, while

conserving a size and a geometry close to the full-sample. The method would yield more robust results if, similarly to Schaller et al. (2017), larger volumes would be reduced to 4cm diameter cylinders. However, large volume tomography was not available for the Lock-In firn core. The deduced fraction of re-opened bubbles is displayed in Figure 4.3 as a function of relative density. Our findings suggests that up to 25% of the bubble volume is re-opened in our samples for relative densities closed to 0.90. This value drops to around 7.5% for high densities.

In order to correct the CP values obtained by both pycnometry and tomography, we derived a linear piecewise relationship relating the relative density of a sample and the cut bubbles fraction f , displayed in black in Figure 4.3. This linear law was derived to match the estimated re-open fraction, while still resulting in physically sound closed porosity ratios, i.e. a monotonous increase without ratios well above 100%. We then applied the correction from Equation 4.3 to the pycnometry and tomography datasets. The cut-bubble corrected values are displayed Figure 4.2-c.

Unfortunately, there is a lack of available data for relative densities ranging from 0.86 to 0.89, as no tomography sample falls in this range. To test the possible sensitivity to a bad estimation of the re-open fraction at these densities, we derived a second correction law with a re-open fraction set at about 25% for all the relative densities below 0.91. This correction and the corrected data are displayed in the Supplement Section 4.2.5.1. Application of this correction does not significantly change the final closed porosity data, as low closed porosity values are obtained for relative densities below 0.91.

4.2.3.2 Reconciling air content and closed porosity

The air content measurements in the Lock-In core indicate a value of $0.0915 \pm 0.0017\text{cm}^3$ of air at standard temperature and pressure per gram of ice based on four samples at 145m depth, and of $0.0874 \pm 0.0013\text{cm}^3.\text{g}^{-1}$ based on six samples at 122m. These values of air content have been corrected for the effect of cut bubbles, with correction factors of 9.2% and 5.8% for the samples from 122 and 145m respectively. The difference in air content between the two depth ranges cannot be solely attributed to the effect of cut bubbles. Similar low values of air content have been reported in the upper part of a Vostok ice core (Lipenkov

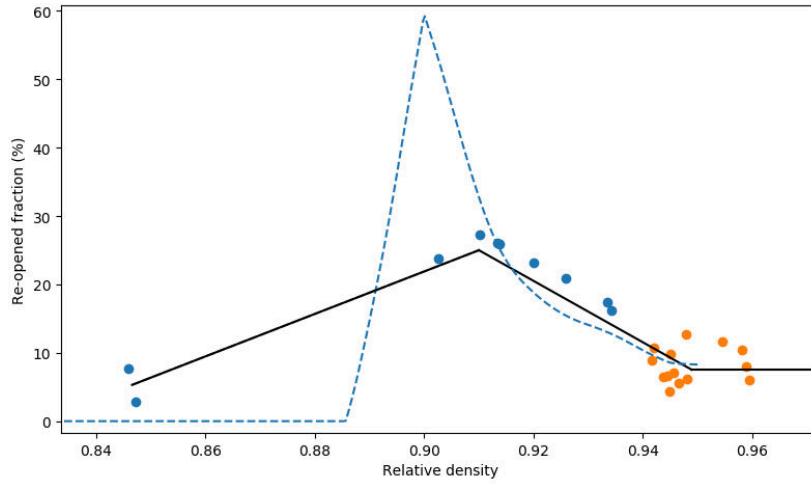


Figure 4.3 – Fraction of re-opened bubbles as a function of relative density. Values obtained from tomography samples are represented as blue dots, and values obtained from pycnometry measurements as orange dots. The piecewise linear model used to correct for cut-bubble effect is displayed as a solid black line. The correction necessary to reproduce the closed porosities observed by Schaller et al. (2017) is displayed as a dashed blue line.

et al., 1997), but not observed in Dome C ice cores (Raynaud et al., 2007). This suggests a potential change of local conditions of the Lock-In and Vostok sites during the late Holocene, that did not occur at Dome C.

Lipenkov et al. (1997) report an air content value of $0.0862\text{cm}^3.\text{g}^{-1}$ for the Holocene part of Vostok, while Martinerie et al. (1992) report air content values of 0.0865 and $0.0925\text{cm}^3.\text{g}^{-1}$ for the sites of Dome C (1970's drilling site) and South Pole. These three sites have respective elevations of 3471, 3240 and 2835m above sea level. With an elevation of 3209m and air content values of 0.0874 and $0.0915\text{cm}^3.\text{g}^{-1}$, Lock-In is consistent with these reported values.

The air content value can be used to estimate the density of the firn during closure. For this purpose, following Raynaud and Lebel (1979) and Martinerie et al. (1990) we use:

$$V_i = AC \frac{T_i}{P_i} \frac{P_0}{T_0} \quad (4.4)$$

$$\frac{1}{\rho_c} = V_i + \frac{1}{\rho_{\text{ice}}}$$

where V_i is the total porous volume at air isolation (expressed in cm^3 per gram of ice), T_i and P_i the temperature and pressure of pores at isolation, $T_0 = 273.15\text{K}$ and $P_0 = 1013\text{mbar}$ are the standard temperature and pressure, and ρ_c the estimation of the density during clo-

sure. Note that V_i is not the porous volume when the firn reaches full closure. Indeed, the volumes of the closed pores evolve in the trapping zone due to compression. Therefore, V_i is the sum of the individual pores volume when they close, and is larger than the porous volume at complete closure. This means that ρ_c is smaller than the density at which full closure is reached, and should rather be seen as the typical density at which bubbles are formed when the air pressure starts to deviate from the atmospheric value. Finally, ρ_c can be expressed as a relative density ρ_c^R by assuming a density of pure ice at -53.15°C equal to $0.924\text{g}\cdot\text{cm}^{-3}$ (Bader, 1964; Goujon et al., 2003).

The air content values determined at depths 122 and 145m, combined with the local temperature and the pressure at the bottom of the firn column, yield ρ_c^R values of 0.909 and 0.905, respectively. As shown by the dashed lines in Figure 4.4, these densities roughly correspond to the middle of the trapping zone. To further analyze the consistency between the air content values and the closed porosity data, we use a gas trapping model to estimate the air content value.

For this purpose we use the gas trapping model of Rommelaere et al. (1997) (Equations 19a and 21a of their article). This model takes as inputs the surface pressure and temperature of the site, as well as density versus depth and closed porosity data. Using the hypothesis of similar compression between closed and open pores, the model is able to compute q_{air}^b , the quantity of air in bubbles expressed in moles of air per cm^3 of ice. This quantity can directly be converted to air content knowing that $AC = q_{\text{air}}^b \frac{RT_0}{P_0\rho}$, where R is the ideal gas constant. To apply the model to the Lock-In core, the measured closed porosity ratios have been fitted by a spline to obtain a smooth porosity curve (in blue in Figure 4.4). Moreover, the high resolution density data were fitted by a polynomial function of degree 5 to produce a smooth density curve. Using these smooth closed porosity and density curves in the model, leads to an estimated air content value of $0.102\text{cm}^3\cdot\text{g}^{-1}$. This is about 10% higher than the measured values, and well outside the uncertainty range of the measurements.

To explain the discrepancy between data and model, we first investigate the impact of the input uncertainties on the modeled air content value. A first source of discrepancy between the modeled and observed air content values could be an underestimation of the densities in the closed porosity-density relationship. Indeed, if densities are underestimated, then the model would trap air at too low densities, resulting in a too large bubble volume and

too much air. To test this hypothesis, we shifted the smooth closed porosity ratio curve towards higher densities in order to obtain the measured air content values. To achieve this result, the relative densities have to be shifted by an amount of $9 \cdot 10^{-3}$. The resulting closed porosity curve is displayed in orange in Figure 4.4. However, such a large shift cannot be reconciled with the pycnometry and tomography measurements. Indeed, the absolute errors on relative densities from the tomography apparatus, estimated as $9 \cdot 10^{-4}$ in Section 4.2.3.1, are much smaller than $9 \cdot 10^{-3}$.

A second explanation could be a bad estimation of the cut-bubble correction. Indeed, if we overestimated the cut-bubble effect in the middle of the trapping zone, the model would also trap too much air at low densities and thus overestimate the air content. To test this hypothesis, we used the extremal case of a cut-bubble correction corresponding to only 7.5% of opened bubbles throughout the trapping zone. The modeled air content then decreases to $0.096 \text{cm}^3 \cdot \text{g}^{-1}$, still much higher than the measured values of 0.0874 and $0.0915 \text{cm}^3 \cdot \text{g}^{-1}$. A bad estimation of the cut-bubble correction thus cannot explain the model overestimation.

Finally, the discrepancy could be due to a poor estimation of the surface atmospheric pressure and of the temperature at the Lock-In site. Using a surface pressure of 643mbar, similar to Dome C, and a temperature of -50°C , the modeled air content only decreases to $0.0994 \text{cm}^3 \cdot \text{g}^{-1}$. Therefore it appears that the discrepancy between the modeled and measured air content is not due to errors in the input data of the model.

The discrepancy should thus originate from an incomplete representation of the physical process of gas trapping in the model itself. [Schaller et al. \(2017\)](#) hypothesized a possible impact of stratification on the amount of air trapped. As previous studies ([Stauffer et al., 1985](#); [Martinerie et al., 1992](#)) they argue that the presence of impermeable layers above an open firn layer could retain air in the open porosity. However, this mechanism yields an increase in the amount of air trapped, and can therefore not explain the low value measured in Lock-In ice.

Another explanation could be the wrong representation of closed pores compression in the trapping zone. Originally, the model is based on the iso-compression of bubbles with the

rest of the firn, that is to say that bubbles compress at the same rate as the open porosity. However during compression, the pressure inside bubbles increases with the diminution in bubble volume. This potentially makes bubbles less easily compressed than the open porosity. To test the sensitivity of the total air content towards bubble compression, we modified the Equation 8 of Rommelaere et al. (1997) to reflect a limited compression of bubbles. For this purpose, we introduce a new parameter α such that when the total porosity decreases of $X\%$ during compression, the closed porosity only diminishes by $\alpha X\%$. With this new parameter, the equation governing $q_{\text{air}}^{\text{b}}$, the quantity of air in bubbles, now writes:

$$\partial_z(vq_{\text{air}}^{\text{b}}) = -c_{\text{air}}v(\partial_z f + \partial_z \epsilon(\alpha - 1 - \alpha \frac{f}{\epsilon})) \quad (4.5)$$

where, similarly to Rommelaere et al. (1997), z is the depth, v is the sinking speed of the firn, c_{air} is the air concentration in the open porosity expressed in mol.m^{-3} of pore space, ϵ is the total porosity, f the open porosity, and α the parameter representing the degree of compressibility of the bubbles. The detailed derivation of Equation 4.5 is described in Section 4.2.5.3 of the Supplement. The original Rommelaere et al. (1997) model corresponds to the case $\alpha = 1$. The value $\alpha = 0$ represents the case of incompressible closed pores: when a pore reaches closure, it keeps its volume until the end of the trapping process. The intermediate values $0 < \alpha < 1$ corresponds to partially compressible closed pores: they are compressed, but less than the open porosity. Note that this model does not intend to properly represent bubble compression in the trapping zone. Its primary goal is to evaluate the sensitivity of air content to the degree of compressibility of bubbles, and if this mechanism could explain the model-data discrepancy.

Using the model with incompressible bubbles yields an air content value of $0.0804\text{cm}^3.\text{g}^{-1}$, well below the measured value. Even if the hypothesis of fully incompressible bubbles is not physically supported, this result highlights the sensitivity of the air content to the compression of closed pores in the trapping zone. To yield a value close to the observed air content values in the case of incompressible bubbles, the closed porosity curve needs to have its relative density values shifted by an amount of 0.10 towards lower density. The resulting closed porosity law is displayed in green in Figure 4.4. Finally, in order to obtain the measured air contents of 0.0874 and $0.0915\text{cm}^3.\text{g}^{-1}$ using the measured porosity data, the α parameter has to be set to 35 and 50% respectively. This indicates that a smaller

rate of compression for the closed pores can reconcile the air content and closed porosity measurements. The optimal α value is sensitive to the cut-bubble correction applied to the closed porosity data. If we use a closed porosity data corrected for a maximal re-opened volume fraction of 20%, the α parameter has to be set to close to 70% to reproduce the measured air content values. Yet, even if a smaller compressibility of bubbles can reproduce the measured air content, it is not entirely satisfactory as it currently lacks supporting observations. The driver of pore compression in the firn is the difference in stresses between the ice and pore phase (Lipenkov et al., 1997). As reported by Martinerie et al. (1992), the difference in driving stresses between open and closed pores compression is lower than 8%, and it is not clear how this difference translates in terms of bubble compressibility. It is therefore possible that another mechanism is responsible for the discrepancy between the modeled and observed air content. The explanation could be related to the release of gases through capillaries not observable with pycnometry or tomography techniques (Huber et al., 2006a; Severinghaus and Battle, 2006). Finally, we also wonder if some bubbles might get re-opened in the firn due to the building pressure inside them. Such a re-opening of bubbles in the firn would release the gas enclosed at low density and lower the air content value.

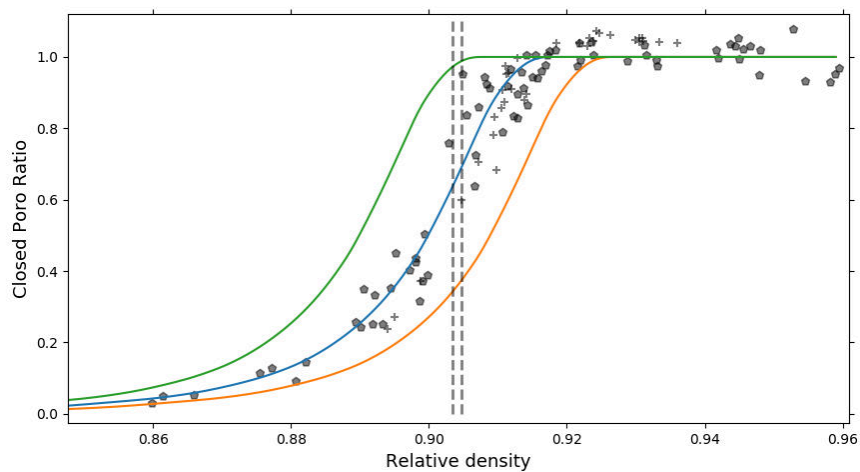


Figure 4.4 – Closed porosity law used in the gas trapping model. Pentagons and crosses are respectively the pycnometry and tomography data (similar to Figure 4.2-c). The blue curve is a fit to these data. The orange and green curves are the closed porosities needed to reproduce the measured air content respectively in the case iso-compression and incompressible bubbles. The dotted vertical lines represent the relative densities during closure estimated from the two air content values.

The same calculations can be performed for the Vostok firn, where air content (Lipenkov et al., 1997), density (Bréant et al., 2017, and references therein), and pycnometry data (L Arnaud and JM Barnola, personal communication) are available. The pycnometry measure-

ments also need to be corrected for the cut-bubble effect. However, contrary to Lock-In we do not have tomographic images of the Vostok trapping zone that could be used to quantify the re-opened volumes. Thus, we apply the correction previously derived for Lock-In in Section 4.2.3.1 to the raw Vostok pycnometry data. The application of this correction yields physically sound closed porosity values, with continuously increasing closed porosity ratios up to 1. The uncorrected Vostok data are displayed in the Supplement Figure 4.14. Finally, the Vostok corrected closed porosity data have been fitted to obtain a smoothed closed porosity curve to be used in the gas trapping model.

Similarly to Lock-In, a direct application of the original [Rommelaere et al. \(1997\)](#) gas trapping model with iso-compression of bubbles yields a predicted air content of $0.0960\text{cm}^3.\text{g}^{-1}$ much higher than the measured value of $0.0862\text{cm}^3.\text{g}^{-1}$. This provides further insights that the gas trapping process might not be well represented in the [Rommelaere et al. \(1997\)](#) model. Again, the introduction of a limited compressibility of the bubbles with a coefficient $\alpha = 50\%$ is able to reconcile the modeled and observed air content values.

4.2.3.3 Comparison with other sites and porosity laws

The comparison in Figure 4.5 of the measured closed porosity data for Lock-In with the proposed parametrization for the B53 site by [Schaller et al. \(2017\)](#) reveals a discrepancy between the two East Antarctic sites. While the B53 closed porosity curve reaches full closure for relative densities of 0.90, the data we obtained for Lock-In reach closure for relative densities closer to 0.92. Therefore, we were not able to reproduce one of their main findings, namely that firn should close at a common critical relative density of 0.90, independently of the studied sites. This discrepancy could be due to an underestimation of the cut-bubble effect for the Lock-In data set. To test this hypothesis, we derived a new cut-bubble correction that reproduces the closed porosity parametrization proposed by [Schaller et al. \(2017\)](#). As seen in Figure 4.3, this new correction assumes a very large re-open fraction around relative densities of 0.90. This is consistent with the results of [Schaller et al. \(2017\)](#), but inconsistent with the re-opened fraction of 24% deduced from the tomography image at a relative density of 0.9025. It is therefore possible that the true Lock-In closed porosities are similar to the ones observed by [Schaller et al. \(2017\)](#) at B53, but a better estimation of the cut-bubble effect is required to answer this question. However, a closed porosity curve similar to the one

observed in B53 would trap a higher quantity of air, and further increases the discrepancy between the modeled and measured air content described in Section 4.2.3.2. Even in the extreme case of incompressible bubbles ($\alpha = 0$), the gas trapping used Section 4.2.3.2 predicts an air content value of $0.0974\text{cm}^3.\text{g}^{-1}$, larger than the values of 0.0874 and $0.0915\text{cm}^3.\text{g}^{-1}$ measured in Lock-In.

Based on previous pycnometry measurements, JM Barnola proposed an analytical formulation to represent the closed porosity of firn. This parametrization is fully characterized by the total porous volume V_i (or equivalently the density during closure ρ_c) as a single parameter. The derivation of this parametrization is not published in the scientific literature, but Goujon et al. (2003) included this Barnola parametrization in their model (Equation 9 of Goujon et al., 2003) and used the linear relationship between site temperature and V_i by Martinerie et al. (1994) to model closed porosity data using temperature as the only parameter. Application of the Goujon et al. (2003) parametrization using the Lock-In site temperature yields a predicted total porous volume V_i of $0.110\text{cm}^3.\text{g}^{-1}$ and the closed porosity curve displayed in orange in Figure 4.5. The resulting closed porosity curve for Lock-In clearly underestimates the closed porosity ratios. In the case of Lock-In, the two air contents values can be used to estimate the total porous volume V_i at 0.109 and $0.114\text{cm}^3.\text{g}^{-1}$, indicating a possible underestimation of V_i by the temperature relationship. Using the V_i value of $0.114\text{cm}^3.\text{g}^{-1}$ in the Barnola parametrization results in the closed porosities displayed in black in Figure 4.5. This curve is more consistent with the pycnometry and tomography data, but still displays a clear underestimation of the closed porosity ratio. Two problems thus arise when using the Goujon et al. (2003) parametrization to predict the Lock-In closed porosities. First, the estimation of the total porous volume V_i using the temperature relationship might be underestimated, which in turns tends to predict pore closure at too high densities. Then, even with a better constrained V_i , the Barnola curve appears to underestimate the closed porosity ratios in the Lock-In firn.

Finally, the closed porosity data measured in a Vostok firn core (JM Barnola and L Arnaud, personal communication) are displayed in blue in Figure 4.5 alongside the Lock-In data in black. As explained Section 4.2.3.2, these data were corrected for cut bubbles using the Lock-In correction derived Section 4.2.3.1. In the case of Vostok, the Goujon et al. (2003) parametrization predicts closed porosity ratios (in red in Figure 4.5) that are more in line

with the data than in the case of Lock-In. Yet, an underestimation of the closed porosity subsists. However, it is possible that this discrepancy between the Goujon et al. (2003) parametrization and the Vostok data is due to a bad estimation of the cut-bubble effect. Comparison of the Lock-In and Vostok data suggests that the Vostok firn reaches closure at a higher density. This is corroborated by air content measurements: the Vostok ice core has a lower total porous volume at isolation V_i , also indicating that the firn reaches closure at a higher density. The difference between the two datasets is more pronounced than the difference between the Lock-In and Vostok Goujon et al. (2003) parametrizations in Figure 4.5. Therefore the temperature difference between the two sites does not fully explain the contrast between the two datasets, and it suggests that other climatic parameters such as the accumulation rate or the insolation also influences the porous network and the density range of bubble closure. This is consistent with the work of Burr et al. (2018) that observed different pore network structures in the Lock-In and Dome C firns, two sites with similar temperatures.

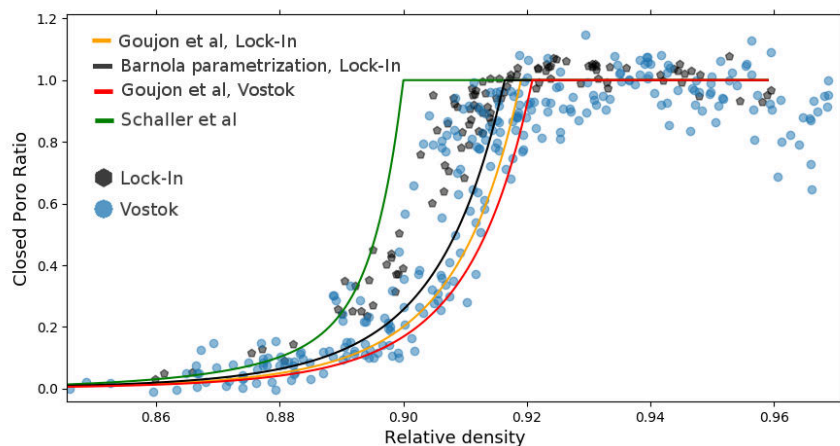


Figure 4.5 – Comparison of closed porosity ratio data and parametrizations. The Lock-In closed porosity ratio obtained by pycnometry and tomography are displayed as black hexagons (this study). The closed porosity ratios measured by pycnometry in the Vostok firn are displayed as blue circles (JM Barnola and L Arnaud, personal communication). The black curve is the Barnola parametrization for Lock-In, using $V_i = 0.114\text{cm}^3.\text{g}^{-1}$ (derived from air content data). The orange and red curves are the Lock-In and Vostok parametrizations proposed by Goujon et al. (2003) using site temperatures as parameters. The green curve is the parametrization proposed for the B53 site by Schaller et al. (2017).

4.2.3.4 Density as a predictor of a firn layer closure

In previous studies, the closed porosity ratio of a firn layer at a given polar site has primarily been linked to its density (Martinerie et al., 1992; Schwander et al., 1993; Mitchell et al., 2015; Burr et al., 2018), despite the firn heterogeneities. This observation is con-

firmed by our work in the Lock-In firn, where both pycnometry and tomography indicate that the closed porosity ratio of a sample is primarily determined by its density. As depicted Figure S4.15 of the supplement, a larger dispersion is obtained when plotting the closed porosity ratios as a function of depth. In other words, two firn layers with same density, no matter how far apart they are in the firn column, have nearly the same closed porosity ratio. For example, a particular pycnometry sample taken at depth 97.40m has a relative density of 0.90 and a closed porosity ratio close to 60%. Such values are usually expected for samples around 102m depth.

However, the fact that different firn layers exhibit a functional relationship between their density and closed porosity ratio, does not imply that they are equivalent in terms of pore structure. One can then wonder if especially high or low density layers display similar pore structure as the rest of the firn, or if they have a significantly different porous networks. To answer this question we used the tomography 3D images, which explicitly represent the porous network. Three different pore structure indicators were computed on each of the 1cm thick slices.

The first indicator is the Structure Model Index or SMI. This index was developed by [Hildebrand and Rüegsegger \(1997\)](#) to analyze the structure of bones. It is traditionally used to quantify the degree of rodness, flatness, and sphericity in 3D images. In this study the SMI will be used as a simple indicator of pore shape, considering that different pore morphologies should result in different SMI. As pointed out by [Salmon et al. \(2015\)](#) this index only provides sensible results when used on convex structures. For the Lock-In firn, the SMI was computed in each slice using the BoneJ plug-in within ImageJ ([Doube et al., 2010](#)). Results from the plug-in indicated that the porous structure is more than 90% convex, justifying the use of SMI for firn studies ([Gregory et al., 2014](#); [Burr et al., 2018](#)). Nonetheless, the obtained SMI values were sensitive to the resolution of the mesh used to compute the index.

The second indicator is the ratio of pore surface to pore volume, denoted S/V here. This surface to volume ratio was determined using the method presented in [Krol and Löwe \(2016\)](#), and is based on the determination of the two-point correlation function. The S/V ratio is notably dependent on the size of the pore, as smaller objects tend to have higher surface to

volume ratio.

Finally, we estimated the effective diffusivity of the firn samples (Schwander et al., 1988; Fabre et al., 2000; Freitag et al., 2002). The estimation was performed using the open-source matlab application TauFactor (Cooper et al., 2016). Effective diffusivity coefficients were obtained for vertical percolations between the bottom and top sides of each 1cm thick slice. However, the resulting values should not be used to model gas diffusion in the firn, as the small size of the samples might not properly capture the large-scale behavior of the firn column (Fabre et al., 2000). Still, the comparison of effective diffusivity between individual samples can be used to highlight similarities or differences in their ability to transport gases. In that sense, our effective diffusivity coefficient is similar to the Qualitative Measure of Permeability (QMP) used by Fujita et al. (2009).

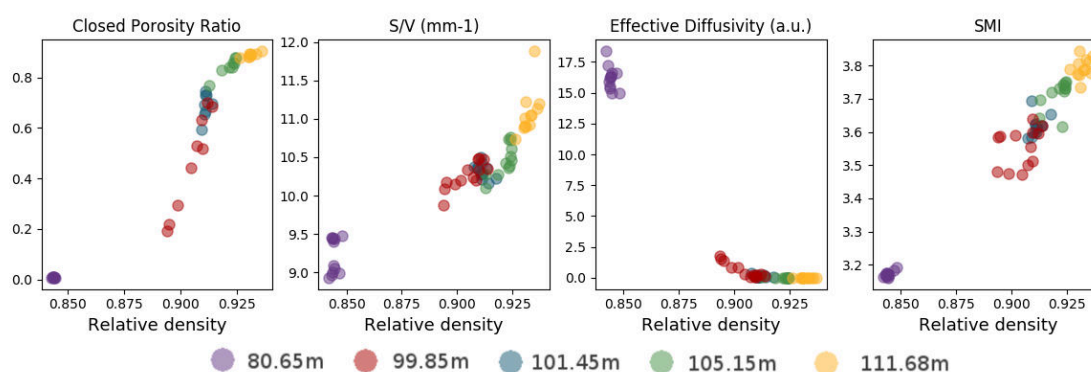


Figure 4.6 – Closed porosity ratio and morphology indicators against relative density: closed porosity ratio, S/V ratio, effective diffusivity, and structural model index. Each color corresponds to the depth where the firn samples were taken, and covers a 10cm in the firn core.

In terms of general trend, the changes of the S/V ratio in Figure 4.6 are characterized by an increase with higher densities. This is to be expected as increasing S/V ratio is linked to a decrease in pore size with the compression of the firn. Moreover, our results are consistent with the ones reported by Burr et al. (2018) for the same Lock-In firn. They are also consistent with the S/V values reported by Gregory et al. (2014) for the WAIS Divide and Megadunes sites. Similarly, the decrease in effective diffusivity with density is consistent with the constriction of the pore network, where there is less and less straight paths traversing the whole sample. Even though our results are not directly comparable to the ones of Freitag et al. (2002) due to the difference in methodology, we also find that the effective diffusivity is related to the open porosity by a power law. However, the exponent found in our case is of 2.9, rather than the 2.1 reported by Freitag et al. (2002). Finally, the evolution of

SMI is characterized by an increase in values with density, indicating a transformation of the pore shapes with increasing density. The values displayed Figure 4.6 are consistent with the ones reported by Burr et al. (2018) for the Lock-In firn. Similarly to Burr et al. (2018), our SMI values are higher than the ones reported by Gregory et al. (2014) for the WAIS Divide and Megadunes firns. This can be explained by the fact that the SkyScan software used by Gregory et al. (2014) yield lower SMI values (Salmon et al., 2015; Burr et al., 2018).

The tomography data of closed porosity ratio for the firn slices are also reported in Figure 4.6. Note that the closed porosity values displayed in Figure 4.6 have not been corrected for cut-bubbles. It is particularly apparent for the slices taken at the depth 99.85m (in red Figure 4.6) that the firn stratification can lead to a wide range of closed porosity ratios within a 10cm section. Nonetheless, these layers with especially closed or open porosity do not appear as outliers in terms of pore morphology. Their morphological indicators are overall consistent with the other firn samples. Hence, this indicates that all layers tend to follow a similar evolution with density not only in terms of closed porosity ratio, but also in terms of pore morphology and gas transport properties.

4.2.3.5 Origin of the density variability

We have seen in the previous sections that the degree of closure of a firn layer is primarily a function of its density. However, an important variability of the density is observed at the centimeter scale. One may then wonder about the origin of this density variability in the trapping zone. Previous studies have advanced two mechanisms for the appearance of firn stratification in upper parts of the firn.

The first one is the softening of firn layers due to chemical impurities in the ice phase. Layers with a high concentration of specific ions densify faster, thus creating the density layering. Hörhold et al. (2012) observed a positive correlation between Ca^{2+} and density anomalies in Greenland and Antarctic firn cores. They however do not argue that calcium is the ion specifically responsible for ice softening. Similarly, based on observation in three Dome Fuji firn cores (East Antarctic plateau) Fujita et al. (2016) advanced that the presence of F^- and Cl^- ions facilitates the densification of a firn layer. They also proposed a hardening effect of NH_4^+ , preventing the deformation and compaction of firn. The second stratification mecha-

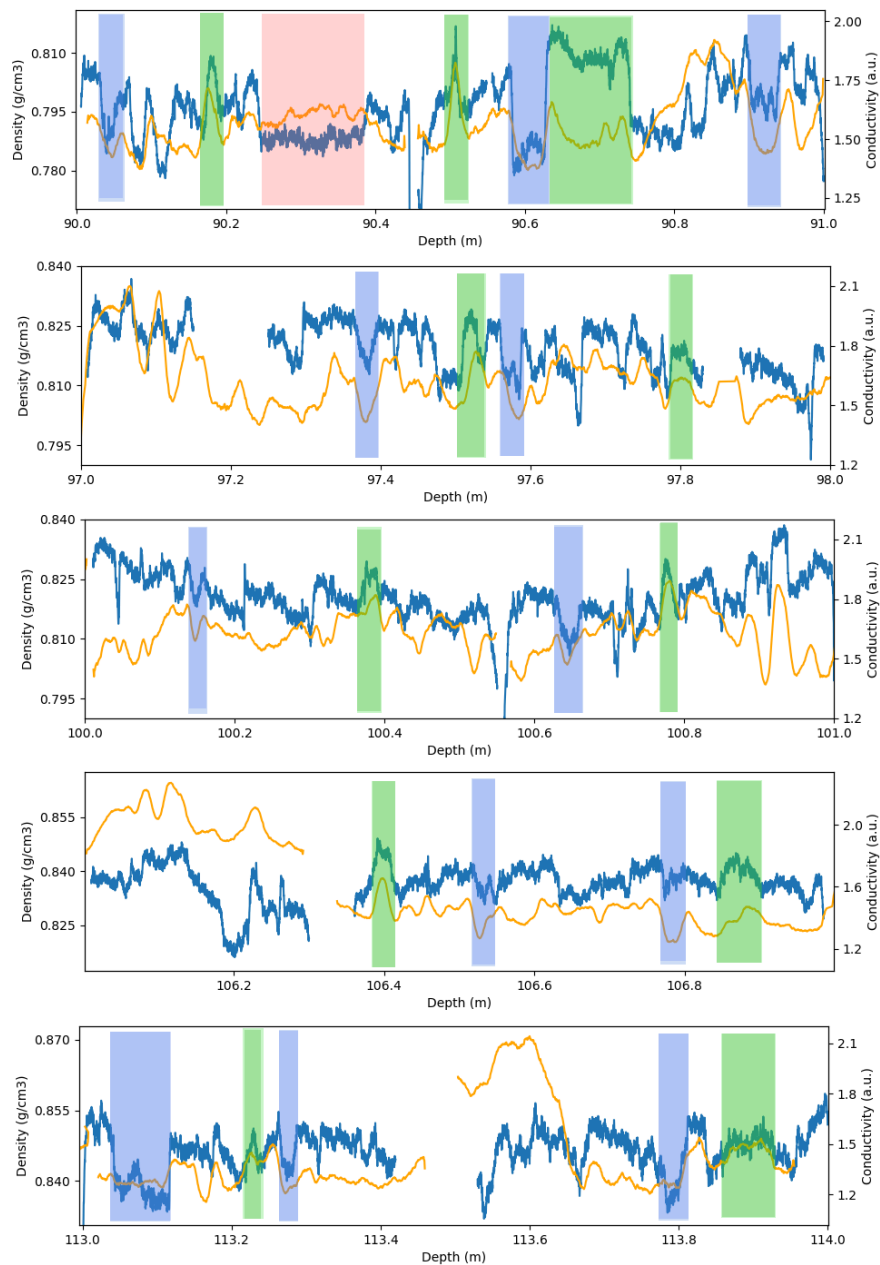


Figure 4.7 – Density (blue curve) and liquid conductivity (orange curve) variations in five one-meter long core sections. The green and blue portions respectively highlight some sections where density and liquid conductivity show simultaneous increase or decrease. The pink portion highlights a section where the decrease in density is not matched by a decrease in liquid conductivity.

nism is detailed in Fujita et al. (2009), and takes into account the ice phase structure of firn layers. Briefly, due to surface metamorphism, some layers develop bonds between the ice clusters giving them more resistance to deformation. These layers, that are initially denser at the surface, thus densify slower and are associated with negative density anomalies in deep firn.

Concerning the Lock-In firn core, the comparison of the high resolution density and liquid conductivity datasets indicates a covariation between the two signals, with denser layers

having higher conductivities. Density and liquid conductivity variations for five one-meter long sections are displayed in Figure 4.7, with green and blue portions highlighting some of the observed covariations. The covariation is present throughout the whole trapping zone, and is consistent with the preferential deformation of firn with high ionic contents. Even though liquid conductivity cannot distinguish between ions with and without ice-softening effects, an increase in liquid conductivity indicates a greater ionic content, and therefore potentially more ice-softening ions in the ice matrix. Thus, we conclude that the centimeter scale stratification observed in the trapping zone of Lock-In is largely related to the presence of chemical impurities. Yet, liquid conductivity does not account for all the observed density variability. An illustration can be seen at the depth 90.30m (pink section Figure 4.7), where a lower density layer does not show low values of liquid conductivity. This means one of two things. Either this less dense layer is due the absence of ice softening impurities but still contains enough conductive species for the liquid conductivity no to drop. In this case the density variability is still due to chemical impurities, but is simply not reflected in the liquid conductivity. Or this less dense layer is not due to a chemistry based effect but rather to another mechanism, potentially related to the ice structure as described by [Fujita et al. \(2009\)](#). Moreover, due to its inability to distinguish between specific ions, the measurement of liquid conductivity can only provide a quantitative relationship between chemistry and density.

To better understand the effect of specific ions on the firn density, four one meter long sections been measured using ion chromatography with a resolution of 2.5cm. The concentration of H^+ was obtained by closing the ionic balance following Equation 3 of [Legrand and Mayewski \(1997\)](#). Since H^+ ions have a high mobility, H^+ concentration estimates could therefore help to explain the centimeter scale variations of liquid conductivity. The ion concentrations measured on the 113 to 114m section are displayed in lower panels of Figure 4.8, with density and liquid conductivity variations above. On this section, the data highlight that in one occasion, the sulfate and conductivity undergo strong increases, uncorrelated with other species (green section in Figure 4.8). We interpret this spike as a volcanic event, depositing sulfuric acid. This volcanic event is not associated with any particular effect on the firn density, and we therefore conclude that sulfate has no impact on the layering in the trapping zone. Unfortunately for other species, we were not able to decipher the effect of particular ions on densification due to the frequent correlations between the different

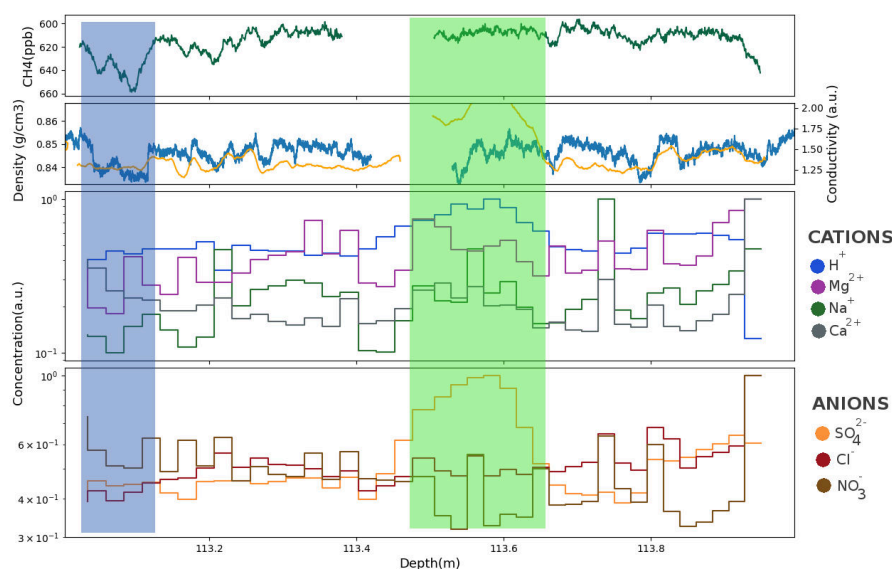


Figure 4.8 – Upper panel: Methane concentration measured by CFA between 113 and 114m depth, with a reversed axis. Upper middle panel: Density (blue) and liquid conductivity (orange) variations. Lower middle panel: Cation concentrations obtained with ion chromatography. Lower panel: Anion concentrations obtained with ion chromatography. The ion concentrations are expressed in arbitrary units to highlight their variability. The green portion highlights the presence of a volcanic event. The blue portion highlights a partially open layer.

species and the limited spatial resolution. Moreover, the diffusion of ions in the firn tends to smooth out the ion variations (Barnes et al., 2003; Fujita et al., 2016). The same inconclusive observations were made on the three other sections (displayed in Figures 4.16 to 4.18 of the Supplement), where density variations could not be attributed to a particular species measured by ion chromatography. Measurements with a better spatial resolution could potentially help to decipher the impact of specific ion species, similarly to the work of Fujita et al. (2016).

4.2.3.6 Examples of stratified gas trapping

Thanks to the continuous methane record, we were able to identify layers which were not entirely closed below the bulk firn-ice transition. In the upper part of the methane record, these layers appear as spikes of high concentrations. This is due to the presence of modern air that entered the center CFA stick through the open porosity. An example of a partially open layer is displayed in the blue portion of Figure 4.8. This still open layer is associated with low density and low liquid conductivity values. Please note that the methane axis is reversed in this figure, and in the following ones. The same observation was made on the ice core section displayed in Figure 4.9. Two late closure layers, depicted by the blue sections, are associated with lower density values and lower liquid conductivities than in

the surrounding layers. All these examples are consistent with the previous observation that layers with low ionic content are less dense and thus reach closure deeper in the firn.

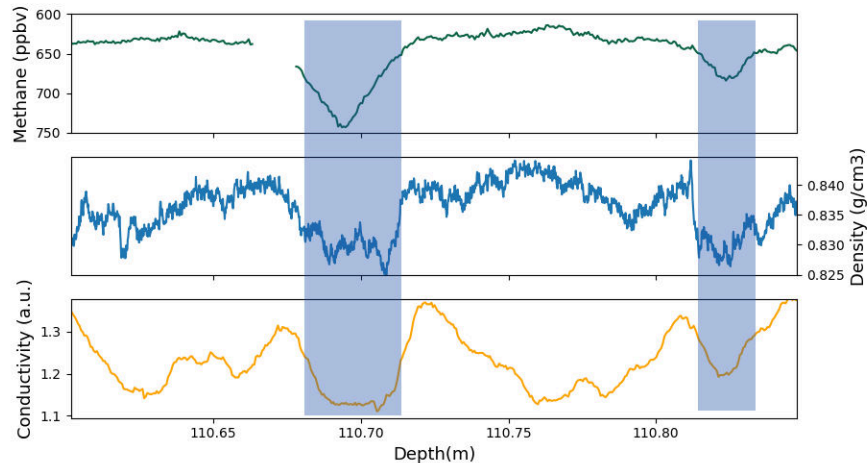


Figure 4.9 – Examples of late closure layers highlighted by the blue shadings. The positive spikes in methane around 110.69 and 110.82m reveal the presence of open pores reaching the middle of the sample (reversed axis). These open layers are associated with low density and liquid conductivity values.

Similarly, an early closure layer was found in the bubbly-ice portion of the core (Figure 4.10). Following Rhodes et al. (2016) and Fourteau et al. (2017), this layer was detected as a negative methane anomaly during a period of methane rise. This section corresponds to a part of the core with a poor geometry due to a broken edge, and we were not able properly determine the absolute density values. Still, using the X-ray scan of the non broken part of the core we could identify the density variability. However, as we do not know the actual thickness of the core that was crossed by the ray, the resulting density variability is expressed in arbitrary units and rather than in $\text{g}\cdot\text{cm}^{-3}$. The comparison between density and the methane records in Figure 4.10, indicates that the early closure layer corresponds to a denser layer. Air content measurements were performed on this section of the core. Results indicates that the early closure layer does not undergo outlier values of air content. This implies that the early closure layer trapped gases at similar densities as the rest of the firn. It is in line with the description of stratified gas trapping supported in this article, where dense layers close in advance but with the same critical density as others. Unfortunately, no chemical analysis could be performed on this section.

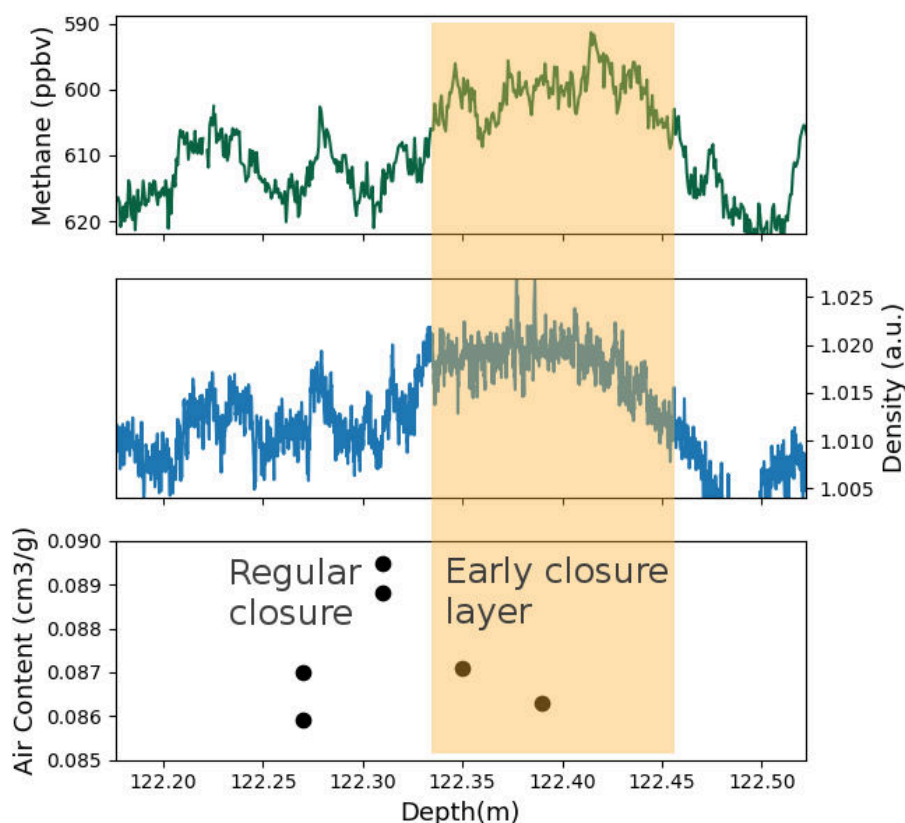


Figure 4.10 – Example of an early closure layer highlighted by the orange shade. The reduced methane concentration around 112.40m is indicative of early gas trapping in the ice (reversed axis). This early closure layer is associated with high density values, but air content values similar with the adjacent layer.

4.2.4 Conclusions

We studied the enclosure of gases at the East Antarctic site of Lock-In, characterized by a temperature of -53.15°C and an accumulation rate of $3.6\text{cm}\cdot\text{we}\cdot\text{yr}^{-1}$. The closed porosity ratio profile in the trapping zone was measured using two independent methods: pycnometry and tomography. Our findings suggest that the two methods yield consistent results when measuring similar samples, and can thus be interpreted in similar ways. However, pycnometry measurements are very sensitive to the determination of sample volumes. On the other hand, tomography appears to provide more robust results and can be used to access more complex characterization of the firn, including pore size and shapes. One important remaining problem in the study of pore closure is the estimation of the cut-bubble effect in the trapping zone as it can drastically change the shape of the closed porosity curve and the estimation of the full closure density. Thus, we encourage the usage of large volume tomography for future studies of gas trapping and firn densification. Notably, large volume tomographies of firn where pycnometry data are available could help understand the dis-

crepancy between our results and the results of Schaller et al. (2017).

Using a gas trapping model, we found that under the assumption of iso-compression of open and closed pores, the measured air content and closed porosity ratios are inconsistent, with the model predicting too much enclosed air. The same overestimation of air content by the gas trapping model have been found in the Vostok ice core. We have shown that this discrepancy cannot be explained by a poor estimation of the closed porosity data or of the cut-bubble effect. On the other hand, the introduction of a reduced compressibility for closed pores in the gas trapping model is able to resolve this discrepancy. Yet, this mechanism is not fully satisfactory as it requires a very limited compression of bubbles that has no direct supporting observations. The mechanism responsible for these low quantities of air trapped in ice cores is thus not clear.

Consistently with previous studies conducted at other sites, we observed a strong layering in the Lock-In firn, manifesting itself as centimeter scale density and firn structure variations (Hörhold et al., 2011; Fujita et al., 2016). Despite this heterogeneity, it appears that all firn layers roughly follow the same behavior relating their closed porosity ratio and pore structure to their density. Layers associated with positive density anomalies close in advance, but at the same critical density as others. This vision simplifies the modeling of stratified gas trapping, as it reduces the firn to a stack of equivalent layers.

Finally, using liquid conductivity as a proxy for ionic content, our results suggest that when focusing on the trapping zone, chemical impurities play a major role in establishing the firn stratification. This does not mean that effects due to the ice phase structure, as described by Fujita et al. (2009), does not strongly influence firn stratification in upper parts. But, as a first approximation, the effect chemical impurities appears as the main mechanism for stratified gas trapping. However, we were not able to determine which chemical species are responsible for the preferential densification of firn. Continuous impurity measurements along the trapping zone with a resolution higher than a centimeter could help decipher the species responsible for the presence of firn heterogeneities.

4.2.5 Supplementary Material

4.2.5.1 Pycnometry and Tomography

Boundary effects on the tomography samples

Figure 4.11 shows the variation of relative density and closed porosity ratio along a tomography sample taken at 111.68m depth. The vertical dashed lines correspond to the separation between numerical slices. It appears that the first and last 5mm of the sample are strongly affected by the cut bubbles due the presence of large boundaries at the top and bottom of the samples. These boundary effects manifest as a sharp drop of the closed porosity ratio while approaching the end of the sample. The same behavior is observed for the other tomography samples. Therefore, the first and last slices of each tomography image have been discarded to limit the influence of this large boundary effect.

Similarly, in order to estimate the cut-bubble effect, the firn samples were trimmed by an amount of 5mm at the top and the bottom and by an amount of 2.5mm on the side. This allows us to remove the large boundary effect visible on the first few millimeters (visible in Figure 4.11), while maintaining a final geometry close to the original one.

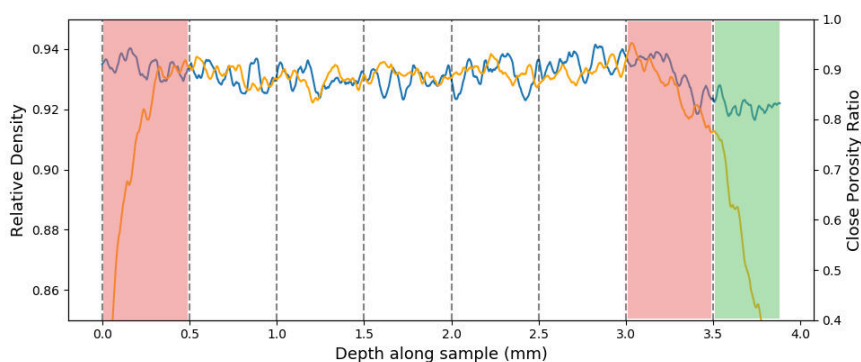


Figure 4.11 – Relative density (blue) and closed porosity ratio (orange) along a tomographic sample taken at 111.68m depth. The vertical dashed lines correspond to spacing between the numerical slices. The two red shaded sections are particularly affected by boundary effects. The green section at the end of the sample is less than 5mm thick, and is thus not used as a tomographic slice.

Impact of cut-bubbles at low densities

The fraction of re-open porosity due to the cut-bubble effect was estimated in Section 4.2.3.1 of the main article. For firn samples that are not totally closed, this estimation is based on

the tomography images. However, no tomography data is available for relative densities ranging from 0.86 to 0.89. This implies that the cut-bubble effect is poorly constrained for these densities. In order to estimate a possible impact of this lack of data on the final closed porosity law, we used a second correction relationship, displayed in black in Figure 4.12. It is expected to overestimate the amount of re-opened bubbles for low values of density. Application of this correction yields the closed porosity ratios depicted in the right panel of Figure 4.13. For comparison the data obtained using the correction of the main article are displayed on the left panel. The two datasets differ for relative densities below 0.89, but in a minor fashion. As the closed porosity ratios are low in this part of the curve, the modification of the re-open volume fraction does not result in a large closed porosity ratio change. Therefore, in the case of an underestimation of the re-open volume at low densities, the closed porosity law proposed in the main article is only slightly affected.

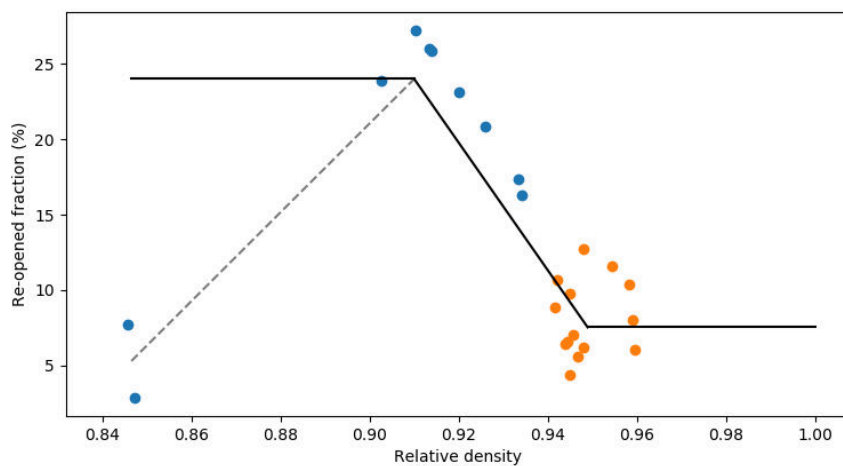


Figure 4.12 – Fraction of re-opened bubbles as a function of relative density. Similarly to the main article, values obtained from tomography samples are represented as blue dots, and values obtained from pycnometry measurements as orange dots. The piecewise linear model used to test the data sensitivity to an overestimation of re-open fraction at low density is shown in black. The dashed line represents the correction used in the main article.

Uncorrected Vostok pycnometry data

In the main article Vostok closed porosity data were corrected for the cut-bubble effect using the correction derived for Lock-In. However, it is not clear that this correction is suited for the Vostok firm, as it might have a different porous network than Lock-In. For instance [Burr et al. \(2018\)](#) observed a structural difference between the Lock-In and Dome C porous networks. The uncorrected Vostok pycnometry data are displayed in blue Figure 4.14, alongside with the uncorrected Lock-In data.

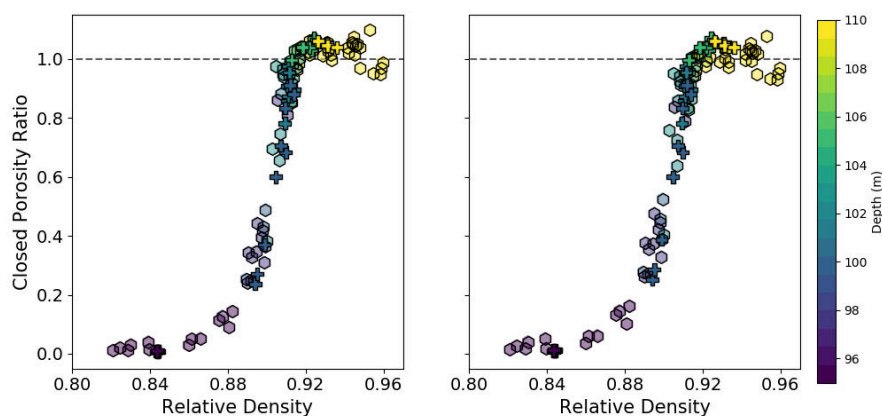


Figure 4.13 – Closed porosity ratios with two different cut-bubble corrections. Left: Using the correction proposed in the main article. Right: Sensitivity test to a large re-open volume fraction at low densities.

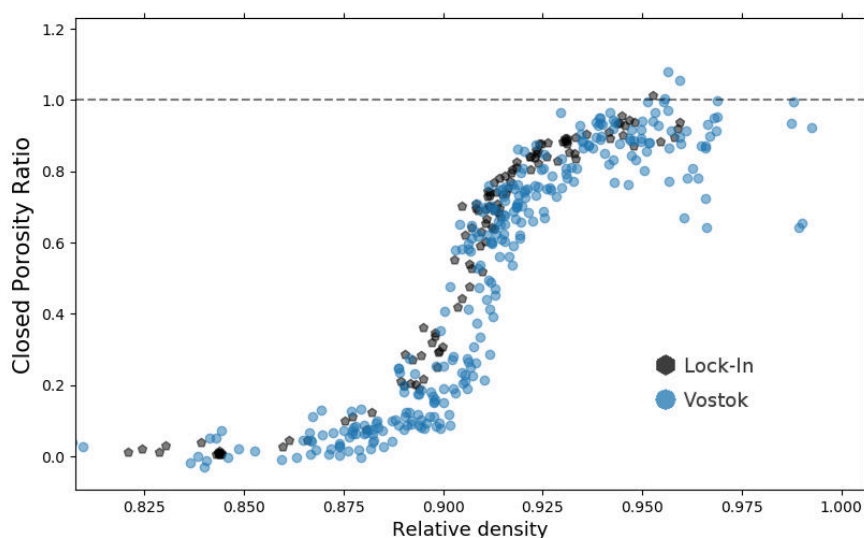


Figure 4.14 – Closed porosity data for Lock-In and Vostok without correction for the cut-bubble effect.

Closed porosity versus depth

The figures provided in the article are plotted using relative density as the abscissa. Here, we display in Figure 4.15 the closed porosity data as a function of the sample depth. This highlights the firn layering, as samples taken at similar depths display a large variability of closed porosity and density values.

4.2.5.2 Ion Chromatography

In total four one-meter long sections were analyzed using ion chromatography. One of the sections is displayed in Figure 8 of the main article. The three remaining sections are displayed in Figure 4.16 to 4.18 with density, liquid conductivity and major ion concentrations

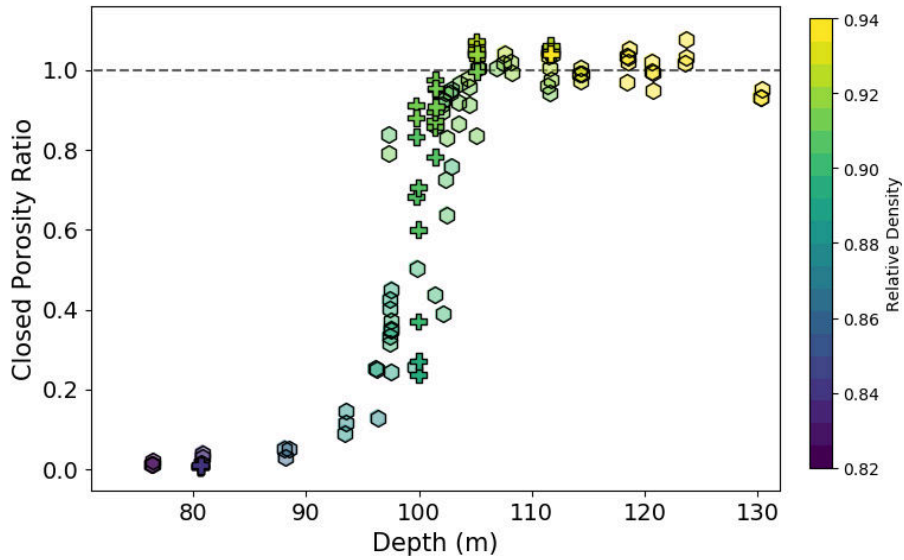


Figure 4.15 – Closed porosity ratios versus sample depth. Colors stand for the measured relative density.

data.

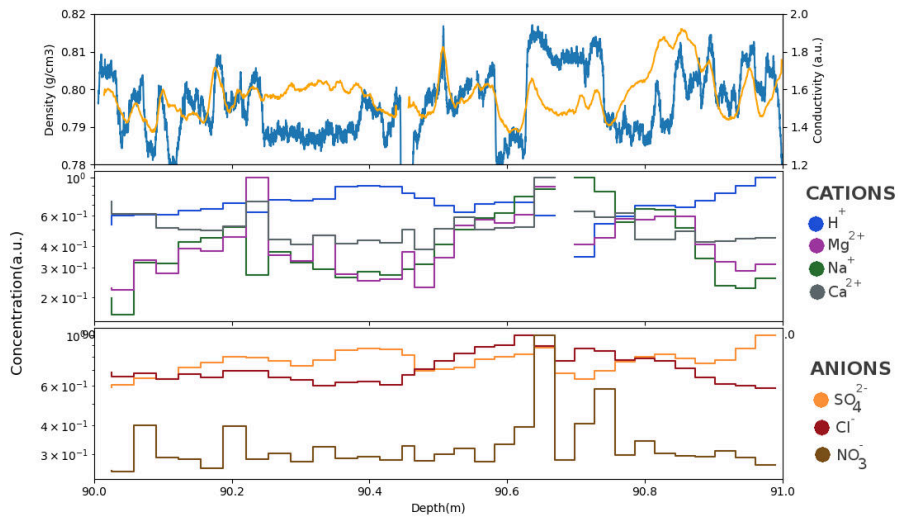


Figure 4.16 – High resolution density (in blue), liquid conductivity (in orange) and major ion concentrations for the section between 90 and 91m depth. The ion concentrations are split between anion and cations, and normalized to emphasis variability.

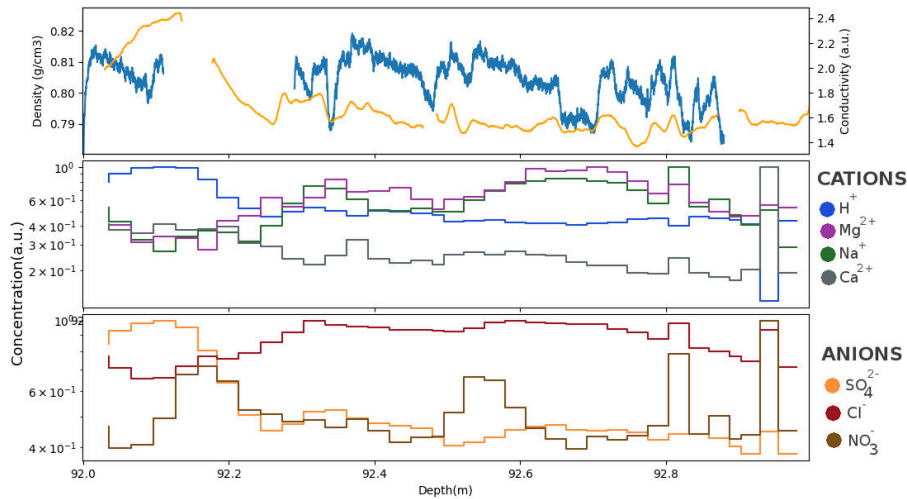


Figure 4.17 – Same as Figure 4.16 for the section between 92 and 93m depth.

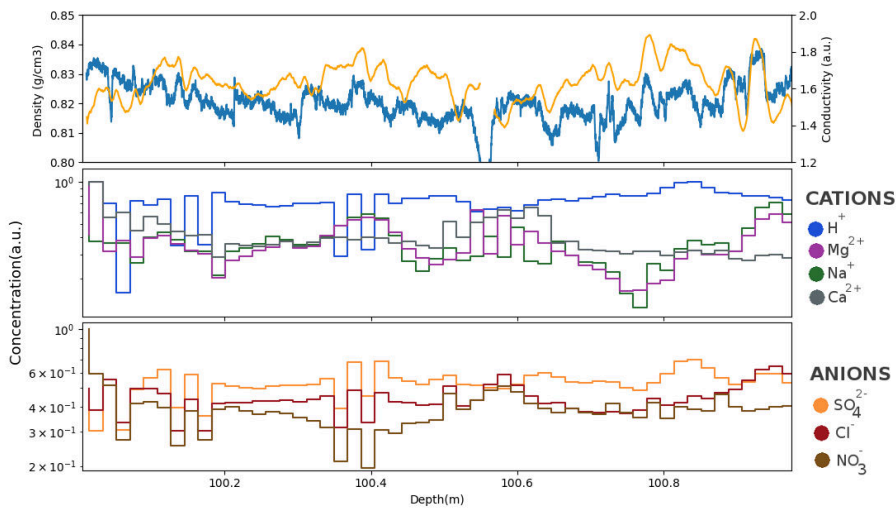


Figure 4.18 – Same as Figure 4.16 for the section between 100 and 101m depth.

4.2.5.3 Gas trapping model

To model the air content in ice, we used a modified version of the Rommelaere et al. (1997) gas trapping model, introducing a limited compressibility for the closed pores. Here, we describe how the new equation representing air trapping is obtained. The derivation is similar to the one of Rommelaere et al. (1997), and we only detail the differences with the original calculation. The symbols used and the quantities they represent are the same as in Rommelaere et al. (1997).

Our new model is based on the replacement of Equation 8 of Rommelaere et al. (1997)

by:

$$\frac{(\epsilon_1 - f_1) - (\epsilon - f)}{\epsilon - f} = \alpha \frac{\epsilon_1 - \epsilon}{\epsilon} \quad (4.6)$$

where ϵ and ϵ_1 are the total porosity before and after compression, f and f_1 are the open porosity before and after compression, and α is rate of compression of closed bubbles. This equations simply means that during compression, if the total porosity diminishes by $X\%$, the closed porosity diminishes by $\alpha X\%$. The original study by [Rommelaere et al. \(1997\)](#) corresponds to the case $\alpha = 1$.

The air conservation in bubbles is expressed by the Equation 13 of [Rommelaere et al. \(1997\)](#). Re-arranging the equations to eliminate the intermediate subscripts 1, and taking the time step dt as infinitely small leads to the equation:

$$d[(\epsilon - f)c_{\text{air}}^{\text{b}}] = -\partial_z v dt (\epsilon - f)c_{\text{air}}^{\text{b}} + (d\epsilon(1 - \alpha + \alpha \frac{f}{\epsilon}) - df)c_{\text{air}} \quad (4.7)$$

This equation replaces Equation 15 of [Rommelaere et al. \(1997\)](#).

Finally under the assumption of stationarity, this Lagrangian description is converted into an Eulerian one:

$$\partial_z (v q_{\text{air}}^{\text{b}}) = -c_{\text{air}} v (\partial_z f + \partial_z \epsilon (\alpha - 1 - \alpha \frac{f}{\epsilon})) \quad (4.8)$$

The quantity of air trapped in ice $q_{\text{air}}^{\text{b}}$ can then be calculated from this equation. The required inputs for the model are density and closed porosity profiles, to compute the v , f and ϵ variables. For this study Equation 4.8 was solved using a finite difference scheme.

4.3 To go further

4.3.1 Structural anisotropy of firn

Fujita et al. (2009) and Fujita et al. (2016) argue that one of the reasons for differential densification of certain firn strata, and thus the establishment of deep firn stratification, is linked to the structural anisotropy of firn strata in response to surface metamorphism. One can then wonder if such a structural isotropy is visible in the pore closure zone of the firn. To study this point, I used the tomographic images, as they explicitly represent the firn structure. To access the degree of anisotropy, I compared correlation lengths in the vertical and horizontal directions. The correlation lengths are deduced from the two-point correlation function C (Krol and Löwe, 2016).

$$C(\mathbf{r}) = \overline{\mathcal{I}(\mathbf{x} + \mathbf{r})\mathcal{I}(\mathbf{x})} - \phi^2 \quad (4.9)$$

where \mathbf{x} and \mathbf{r} are vectors, \mathcal{I} is the characteristic function of the ice phase (it is valued to 1 if \mathbf{x} lies in the ice phase, and 0 otherwise), $\overline{\bullet}$ stands for the averaging over space, and ϕ is the ice volume fraction.

The two-point correlation function in the direction x can be fit by a decaying exponential, with a parameter ξ_x .

$$f(x) = C(0) \exp(-x/\xi_x) \quad (4.10)$$

where f is the fit to the function $C(x)$, the correlation function restricted to the x axis. The parameter ξ_x is defined as the correlation length in the direction x . The exponential is adjusted on the first 5 voxels, as displayed in orange in Figure 4.19. The correlation lengths ξ_y and ξ_z in the directions y and z can be obtained similarly by fitting decaying exponentials. We further define $\xi_{xy} = 0.5 \times (\xi_x + \xi_y)$ as the correlation length in the x - y plane.

The degree of anisotropy of a firn sample can be quantified by the quantity $A = 1 - \xi_z/\xi_{xy}$. If $A < 0$, then the firn displays a preferential elongation in the z direction. If $A > 0$, then the firn displays a preferential elongation in the x - y plane. Finally, if $A = 0$ the firn is considered as isotropic.

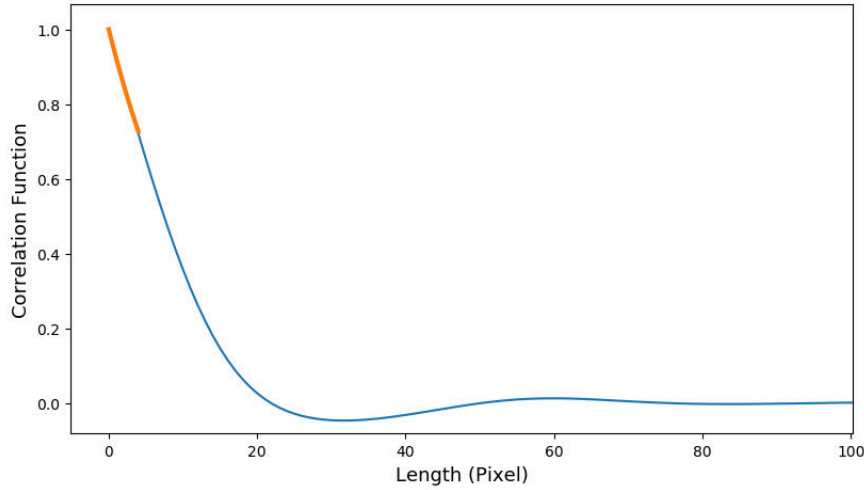


Figure 4.19 – In blue: Correlation function as determined using Fourier transform. In orange: Exponential fit to determine the correlation length.

To compute the two-point correlation function, we rely on Fourier transform, following Newman and Barkema (1999).

$$\tilde{C}(\mathbf{k}) = \frac{1}{N} \|\tilde{\mathcal{I}}'(\mathbf{k})\|^2 \quad (4.11)$$

where $\mathcal{I}' = \mathcal{I} - \bar{\mathcal{I}}$, and $\tilde{\bullet}$ stand for the Fourier transform. The correlation function C is then obtained with a inverse Fourier transform.

I computed the degree of anisotropy A for each tomographic slice, using Equations 4.9, 4.10, and 4.11. The Fourier transforms are estimated with the use of Fast Fourier Transforms. The resulting anisotropies A are displayed in Figure 4.20 as a function of local density. They indicate that the deep part of the firm does not display a strong anisotropic structure. There appears to be a small vertical elongation for the shallowest samples (in purple in Figure 4.20). However, this preferential elongation do not exceed a couple of percents. In deeper firm, this potential preferential elongation disappears, in favor of a general isotropy of the firm structure. A closer look at the centimeter scale indicates that firm strata that are especially dense compared to their surroundings do not exhibit a particular degree of anisotropy. Therefore, we cannot confirm the hypothesis of Fujita et al. (2009) that less dense layers are associated with a higher anisotropy in the deeper parts of firm. That being said, Fujita et al. (2009) report the gradual disappearance of anisotropy with depth. Therefore, our observations do not invalidate their hypothesis.

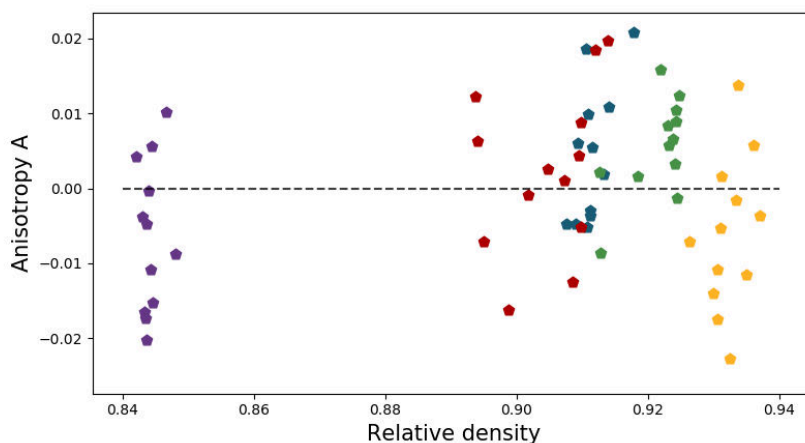


Figure 4.20 – Anisotropy of firn slices as a function of relative density. Same color code as Figure 4.6, where each color represent the depth were the firn sample is taken.

4.3.2 Analysis of thin sections

Thin sections of the Lock-In firn core have been performed and analyzed for crystalline texture using an the Automatic Ice Texture Analyzer (AITA; [Peternell et al., 2010](#)). The principal products of the AITA are maps of the azimuth and colatitude angles of the crystals inside the thin sections. These maps can be used to differentiate single crystals from each others, and thus to infer the typical size of the crystals.

The thin sections in the Lock-In firn core were prepared to investigate whether or not density variability can be associated with variability in the crystalline texture. However as seen in Figure 4.21, because of noise in the obtained images it is not possible for a simple algorithm to directly count the number of crystals and to estimate their size.

A first solution to this problem is to manually redraw each crystal boundary, for the computer to have a clean image to work with. However, this method is rather cumbersome and not suited to treat a large number of single crystals.

A second method is to draw a network of lines crossing the thin section, as displayed in Figure 4.22, and to manually count the number of intersections between a line and crystal boundaries. This number of intersections is related to the size of the crystals, as zones characterized by small crystals exhibit higher numbers of intersections. The results obtained for two 10cm long thin sections of the Lock-In core are displayed in Figure 4.23, alongside with density. No clear link between density and crystal size is apparent using this methodology.

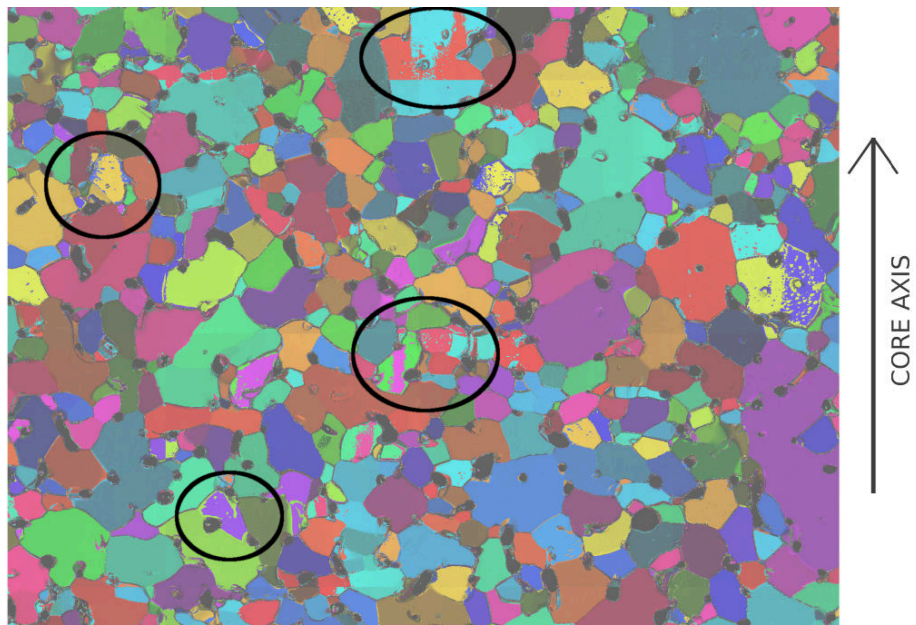


Figure 4.21 – Example of a thin section from the Lock-In core. Each color on the image corresponds to a crystalline orientation. The black circles highlight zones with defaults preventing the automatic counting of crystal size.

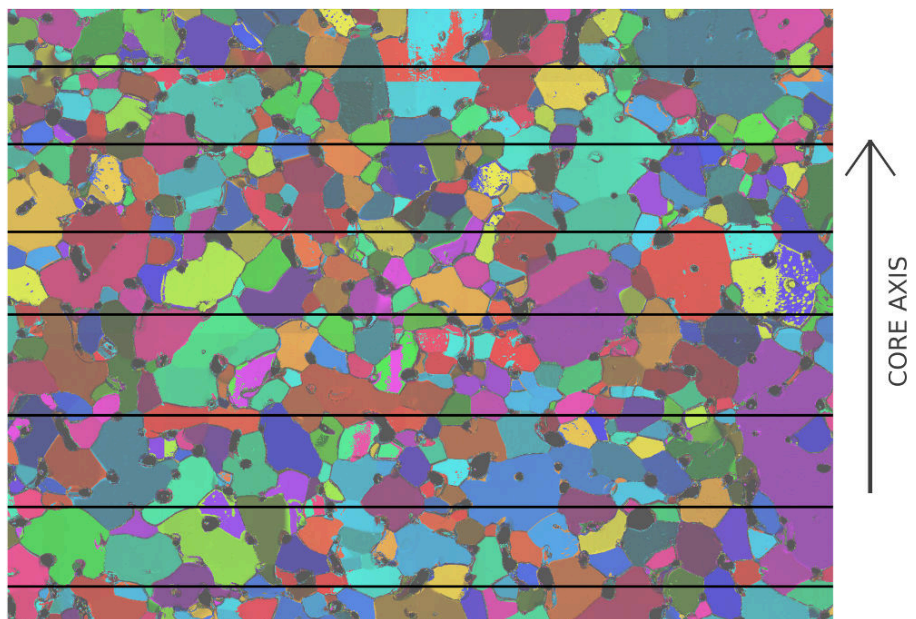


Figure 4.22 – Network of parallel horizontal lines on a thin section in order to characterize the size of the crystals.

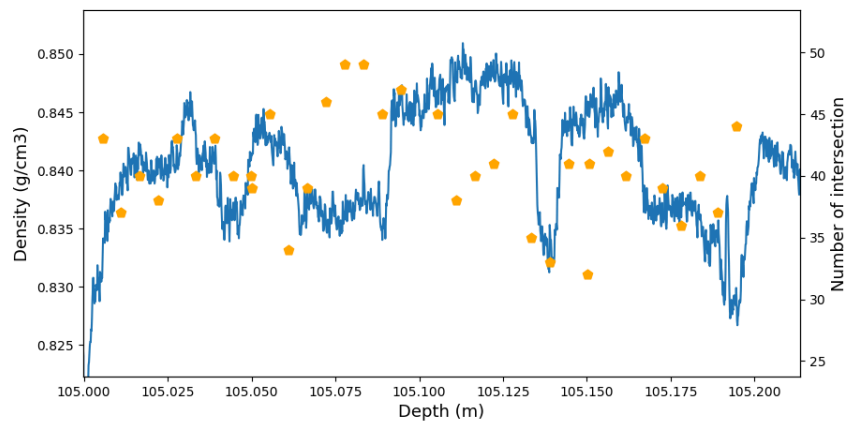


Figure 4.23 – Density (in blue) and number of line intersections (in orange) over a 20cm section. The number of line intersections is related to the size of the crystals.

4.4 Conclusion of the chapter

This chapter reports a multi-tracer analysis of gas trapping in an East Antarctic firn. For this purpose, I exploit datasets obtained with the different methods described in Chapter 3.

A first issue discussed in the chapter is the acquisition of reliable closed porosity data. The data obtained by pycnometry and tomography, two independent methods, are compared. The initial discrepancy between the two types of data can be resolved if one considers the geometrical radius measurement of firn samples to be systematically overestimated by 0.05mm. To support this hypothesis, I use the tomographic images to estimate the roughness of the sample surfaces. I finally propose a method, similar to [Schaller et al. \(2017\)](#), to correct for the effect of cut-bubbles in firn samples.

Using the air content data measured by V. Lipenkov and the closed porosity data, I assess the ability of the [Rommelaere et al. \(1997\)](#) gas trapping model to predict the right amount of trapped air. It appears that there is a large disagreement between the modeled and measured air content. I first ensure that this discrepancy was not due experimental errors on the air content or the closed porosity data. As the mismatch does not seem to originate from experimental issues, I conclude that it must be related to the mechanism of gas trapping implemented in the model. As it can easily be added to the model, I test the influence a limited compressibility of bubbles on the discrepancy. To reconcile the data and model, the compressibility of bubbles must be heavily reduced. It is thus probable than an other mechanism, not yet identified, is responsible for the low amount of air measured in the ice. Potential mechanisms could be the transport of gases outside the bubbles through capillaries not detectable with the tomography and pycnometry methods, or the re-opening of closed bubbles in the firn due to the building pressure inside them. Finally, the same observations of model-data mismatch are made in the case of the Vostok ice core where pycnometry and air content data are available, indicating that the model-data discrepancy is not limited to the sole case of Lock-In.

The rest of the article is centered around the study of firn stratification and its impact on gas trapping. Using the pycnometry and tomography data, I reproduce the observation of [Schwander and Stauffer \(1984\)](#) and [Martinerie et al. \(1992\)](#) that there is a direct relationship

between the density of a firn stratum and its amount of closed pores. I then check if the same observation could be made for other parameters characterizing the porous network. It appears that indexes characterizing the morphology and size of the porous network are closely linked to density. In particular, strata that are especially dense compared to their surroundings still obey the same relationship between pore morphology and density. It implies that all layers close at nearly the same density, and present similar transport properties. In particular, layers that are especially dense close at shallower depths but at the same density as the rest of the firn. This idea will be used in Chapter 5 to model layered gas trapping.

The origin of especially dense layers is then studied thanks to the high resolution density and chemistry measurements. Using liquid conductivity, I observe a clear link between the density of firn strata and their ionic contents. This observation supports the idea that chemical softening of ice might enhance the densification of some strata, and thus create a stratification deep in the firn (Hörhold et al., 2012; Fujita et al., 2016). However, I am not able to distinguish the particular ion(s) responsible for this preferential densification. In the additional content of the chapter, I investigate the potential link of densification with the structural anisotropy of the firn or with the size of ice crystals. Fujita et al. (2009) and Fujita et al. (2016) report that dense layers at the bottom of firns are associated with weaker structural anisotropy. However, using the tomography images I do not find any clear link supporting the Fujita et al. (2009) and Fujita et al. (2016) hypothesis. It is possible that differences in anisotropy between dense and less dense layers have attenuated with densification, and that they are no longer easily observed in our deep samples.

Finally, a few examples of layered gas trapping of methane are provided. They are consistent with the vision laid out in this chapter, namely that firn strata with a high (respectively low) ionic content are denser (respectively less dense) at the bottom of the firn and thus close in advance (respectively late). Air content data support the idea of firn strata all closing at the same density.

Alterations of methane records in East Antarctic ice cores

Contents

5.1	Presentation of the chapter	131
5.2	Analytical constraints on layered gas trapping and smoothing of atmospheric variability in ice under low-accumulation conditions	132
5.2.1	Introduction	133
5.2.2	Ice core samples and analytical methods	135
5.2.3	Experimental results	137
5.2.4	Layered bubble trapping	141
5.2.5	Smoothing and age distribution in the Vostok 4G-2 ice core	148
5.2.6	Discussion	151
5.2.7	Conclusions	155
5.2.8	Supplementary Material	156
5.3	Estimation of gas record alteration in very low accumulation ice cores . . .	164
5.3.1	Introduction	165
5.3.2	Methods	167
5.3.3	Results and Discussion	169
5.3.4	Loss of climatic information in a deep and thinned ice core from East Antarctica	182
5.3.5	Conclusions	187

5.3.6	Supplementary Material	188
5.4	Conclusion of the chapter	193

5.1 Presentation of the chapter

This chapter presents two articles, one published in the journal *Climate of the Past* (<https://www.clim-past.net/13/1815/2017/>) and the other one to be submitted to the same journal. It deals with the discrepancies that exist between the atmospheric history and its measurement in ice core records, due to the effect of gas layered trapping and firn smoothing.

The first article is based on a high-resolution methane record measured in a glacial section of the Vostok ice core from East Antarctica. These data were obtained at IGE with X. Fain during my Master's degree internship, a few months prior to my PhD in the spring of 2016. Using these data I aim to quantify the alterations due to effects of layered gas trapping and smoothing. Moreover, I propose a model to simulate the effect of layered gas trapping and present a novel methodology able to estimate the gas age distribution of a low-accumulation record, applicable to climatic conditions without present-day equivalent. These two methods can easily be extended to other ice cores from East Antarctica.

The second article builds on the ideas introduced in the first one. Five new high-resolution methane records have been measured at IGE and exploited to estimate the impact of gas layered trapping and smoothing. I notably investigate the impact of impurities in the ice phase on layered gas trapping artifacts. The high-resolution methane records are used to estimate new gas age distributions for a range of accumulation conditions typical of the East Antarctic plateau for both glacial and interglacial periods. I finally apply the knowledge gained on layered gas trapping and smoothing to the case of a low-accumulation and very-thinned ice core from East Antarctica. The goal is to estimate the degree of alteration of methane and carbon dioxide signals that can be expected in the future ice core of the Oldest-Ice project.

5.2 Analytical constraints on layered gas trapping and smoothing of atmospheric variability in ice under low-accumulation conditions

Kévin Fourteau¹, Xavier Faïn¹, Patricia Martinerie¹, Amaëlle Landais², Alexey A. Ekaykin³, Vladimir Ya. Lipenkov³, and Jérôme Chappellaz¹

[1] Univ. Grenoble Alpes, CNRS, IRD, Grenoble INP, IGE, 38000 Grenoble, France

[2] Laboratoire des Sciences du Climat et de l'Environnement, UMR8212, CEA-CNRS-UVSQ-UPS/IPSL, Gif-sur-Yvette, France

[3] Climate and Environmental Research Laboratory, Arctic and Antarctic Research Institute, St. Petersburg, 199397, Russia

Abstract

We investigate for the first time the loss and alteration of past atmospheric information from air trapping mechanisms under low-accumulation conditions, through continuous CH₄ (and CO) measurements. Methane concentration changes were measured over the Dansgaard-Oeschger event 17 (DO-17, ~ 60,000yrBP) in the Antarctic Vostok 4G-2 ice core. Measurements were performed using continuous-flow analysis combined with laser spectroscopy. The results highlight many anomalous layers at the centimeter scale that are unevenly distributed along the ice core. The anomalous methane mixing ratios differ from those in the immediate surrounding layers by up to 50ppbv. This phenomenon can be theoretically reproduced by a simple layered trapping model, creating very localized gas age scale inversions. We propose a method for cleaning the record of anomalous values that aims at minimizing the bias in the overall signal. Once the layered-trapping-induced anomalies are removed from the record, DO-17 appears to be smoother than its equivalent record from the high-accumulation WAIS Divide ice core. This is expected due to the slower sinking and densification speeds of firn layers at lower accumulation. However, the degree of smoothing appears surprisingly similar between modern and DO-17 conditions at Vostok. This suggests that glacial records of trace gases from low-accumulation sites in the East Antarctic plateau can provide a better time resolution of past atmospheric composition changes than previously expected. We also developed a numerical method to extract the gas age distributions in ice layers after the removal of the anomalous layers based on the comparison with a weakly smoothed record. It is particularly adapted for the conditions of the East Antarctic plateau, as it helps to characterize smoothing for a large range of very low-temperature and

low-accumulation conditions.

5.2.1 Introduction

In a context of climate change, the study of paleoclimate is an important tool for understanding the interactions between climate and atmospheric conditions (Masson-Delmotte et al., 2013). Ice cores have been used to retrieve climatic and atmospheric conditions back to 800,000 years before present (BP) (Jouzel et al., 2007; Loulergue et al., 2008; Lüthi et al., 2008). Notably, ancient atmospheric gases get enclosed within bubbles in the ice and allow us to reconstruct the past history of atmospheric composition (Stauffer et al., 1985). The trapping of air in ice is due to the transformation of firn (porous compacted snow) into airtight ice at depths ranging from ~ 50 to ~ 120 m depending on temperature and accumulation conditions. It is characterized by an increase in bulk density and a decrease in porosity with depth along the firn column. It is only at the bottom of the firn column that the porosity of the medium gets closed and traps the interstitial air. From a gas point of view the firn is traditionally divided in three main parts from the surface to the bottom: the convective zone, the diffusive zone and the trapping zone (e.g., Schwander, 1989; Buizert et al., 2012). The convective zone is characterized by the mixing of air in the snow with atmospheric air through wind action (Colbeck, 1989). In the diffusive zone the dominant gas transport processes are molecular diffusion and gravitational settling. Finally, the trapping zone corresponds to the enclosure of air into bubbles through the closure of the porosity. The process of densification and pore closure can last for thousands of years at the most arid sites in Antarctica.

Air trapping affects the recording of atmospheric variability in ice cores. One known effect of the gas enclosure mechanism is the damping of fast variations in the atmosphere, also called smoothing (Spahni et al., 2003; Joos and Spahni, 2008; Köhler et al., 2011; Ahn et al., 2014). This smoothing arises for two reasons: (i) the gas diffusion in the firn mixes air from different dates, and thus a bubble does not enclose gases with a single age but rather an age range (Schwander et al., 1993; Rommelaere et al., 1997; Trudinger et al., 1997; Witrant et al., 2012); (ii) in a given horizontal layer, bubble enclosure takes place over a range of time rather than instantaneously. These two phenomena combined mean that at a given depth, the air enclosed is represented by a gas age distribution and not by a single age

(Schwander et al., 1993; Rommelaere et al., 1997). Gas enclosure mechanisms thus act as a low-pass filter, attenuating signals whose periods are too short compared to the span of the distribution. Spahni et al. (2003) reported the only existing observations of the smoothing effect under low-accumulation conditions. They concluded that the abrupt methane variation during the cold event of 8.2kyrBP recorded in the EPICA Dome C ice core, compared with its counterpart from the Greenland GRIP ice core had experienced an attenuation of 34% to 59%. Sites with low accumulation tend to have broader age distributions leading to a stronger damping effect (Spahni et al., 2003; Joos and Spahni, 2008; Köhler et al., 2011; Ahn et al., 2014). A heuristic explanation is that the span of the age distribution is directly related to the densification speed of a firn layer, which is slow at the low-temperature and arid sites of the Antarctic plateau. For the most arid sites the impact of diffusive mixing is negligible compared to progressive trapping, and the smoothing is hence mainly driven by the speed of porosity closure.

Even if the bulk behavior in firn is the increase in density and decrease in open porosity with depth, local physical heterogeneities affect firn densification and gas trapping (Stauffer et al., 1985; Martinerie et al., 1992; Hörhold et al., 2011; Fujita et al., 2016). Working on ice cores and firn from high-accumulation sites, Etheridge et al. (1992), Mitchell et al. (2015), and Rhodes et al. (2016) have discussed the influence of centimeter-scale physical variability in firn on recorded gas concentrations. They argue that physical heterogeneities can lead to variations in closure depth for juxtaposed ice layers. For instance, a given layer could reach bubble enclosure at a shallower depth and earlier (respectively deeper and later) than the surrounding layers in the firn, thus trapping relatively older gases (respectively younger gases). In periods of atmospheric variations in trace gas composition occurring on a similar timescale as the trapping process, this mechanism can lead to gas concentration anomalies along depth in an ice core and has been called layered bubble trapping. Based on observations in high-accumulation Greenland ice cores, and modeling for the WAIS Divide ice core, Rhodes et al. (2016) report that such artifacts can reach 40ppbv in the methane (CH₄) record during the industrial time. In addition, the amplitude of the artifacts increases with lower accumulation rates.

Here we investigate for the first time the existence and impacts of heterogeneous trapping and smoothing in very low-accumulation conditions using continuous measurements

of trace gases. High-resolution methane concentration (combined with carbon monoxide) measurements were performed along a section of the Vostok 4G-2 ice core drilled in the Antarctic plateau. The section studied corresponds to the Dansgaard-Oeschger event number 17 (DO-17, $\sim 60,000$ yrBP, a climatic event associated with particularly fast and large atmospheric methane variations (Brook et al., 1996; Chappellaz et al., 2013; Rhodes et al., 2015). This makes this event especially adapted for the quantification of both gas record smoothing and layered trapping. To interpret our data we compare them with the much less smoothed methane record measured in the WAIS Divide ice core (WDC, Rhodes et al., 2015), where the accumulation rate is an order of magnitude larger than at Vostok.

5.2.2 Ice core samples and analytical methods

5.2.2.1 Vostok ice samples

The ice core analyzed in this study is the 4G-2 core drilled at Vostok, East Antarctica in the 1980s (Vasiliev et al., 2007). Measured depths range from 895 to 931m, with a cumulative length of 27.5m due to several missing portions in the archived ice at Vostok station. The ice core sections analyzed have been stored at Vostok Station since the drilling, and were transported to the Institut des Geosciences de l'Environnement (IGE, Grenoble, France; formerly LGGE) 3 months before analyses. Although stored at Vostok at temperatures of $\sim -50^{\circ}\text{C}$, the samples showed clathrate relaxation cavities. The gas age over this depth interval spans over a 3,000-year interval centered on $59,400 \pm 1,700$ yrBP (Bazin et al., 2013; Veres et al., 2013). The estimated snow accumulation rate at the Vostok core site for this period is $1.3 \pm 0.1 \text{ cm.ice.yr}^{-1}$ (Bazin et al., 2013; Veres et al., 2013). Even though DO events are associated with large warmings in the Northern Hemisphere, isotopic records indicate that DO-17 temperatures on the Antarctic plateau remain at least 5°C below modern temperatures (Fig. 2 in Jouzel et al., 2007).

5.2.2.2 Continuous methane measurements

The Vostok 4G-2 ice core sections were analyzed at high resolution for methane concentration (and carbon monoxide as a by-product) at IGE over a 5-day period and using a continuous ice core melting system with online gas measurements (CFA, continuous flow analysis). Detailed descriptions of this method have been reported before (Stowasser et al., 2012;

Chappellaz et al., 2013; Rhodes et al., 2013). Ice core sticks of 34 by 34mm were melted at IGE at a mean rate of $3.8\text{cm}\cdot\text{min}^{-1}$ using a melt head as described by Bigler et al. (2011), and the water and gas bubble mixture was pumped toward a low-volume T-shaped glass debubbler. All the gas bubbles and approximately 15% of the water flow were transferred from the debubbler to a gas extraction unit maintained at 30°C . The gas was extracted by applying a pressure gradient across a gas-permeable membrane (optimized IDEX in-line degasser, internal volume 1mL). The gas pressure recorded downstream of the IDEX degasser was typically 500 – 600mbar and was sufficiently low to extract all visible air bubbles from the sample mixture. A homemade Nafion dryer with a $30\text{mL}\cdot\text{min}^{-1}$ purge flow of ultrapure nitrogen (Air Liquide 99.9995% purity) dried the humid gas sample before entry into the laser spectrometer. Online gas measurements of methane were conducted with a SARA laser spectrometer developed at Laboratoire Interdisciplinaire de Physique (Grenoble, France) based on Optical Feedback-Cavity Enhanced Absorption Spectroscopy (OF-CEAS, Morville et al., 2005; Romanini et al., 2006). Such a laser spectrometer has been used before for continuous flow gas analyses (e.g., Chappellaz et al., 2013; Rhodes et al., 2013, 2015, 2016; Fain et al., 2014); however, the IGE CFA system was specifically optimized to reduce experimental smoothing by limiting all possible dead and mixing volumes along the sample line. For this study the rate of OF-CEAS spectrum acquisition was 6Hz. The 12cm^3 optical cavity of the spectrometer was maintained at 30mbar of internal pressure, which corresponds to an equivalent cavity volume of only 0.36cm^3 at STP and allows for a fast transit time of the gaseous sample in the cavity. Consequently, the SARA instrument introduces a significantly lower smoothing than the CFA setup. The SARA spectrometer was carefully calibrated onto the NOAA2004 scale (Dlugokencky et al., 2005) before the CFA analyses using three synthetic air standards with known methane concentrations (Scott Marrin Inc.; Table 5.3, Supplementary Information (SI)). CH_4 concentrations measured during the calibration agreed with NOAA measurements within 0.1 % over a 360-1790ppbv range. A linear calibration law was derived and applied to all CH_4 data (Fig. S1, SI).

Allan variance tests (Allan, 1966; Rhodes et al., 2013) were conducted using mixtures of degassed deionized water and synthetic air standard to evaluate both the stability and the precision of the measurements. The best Allan variance was obtained with an integration time larger than 1000s, illustrating the very good stability of the CFA system. However, in order to optimize the depth resolution of our measurements, we used an integration time of 1s for which a precision of 2.4ppbv (1σ) was observed. This corresponds to a peak-to-peak CH_4 variability of $\sim 10\text{ppbv}$. Hereafter, this variability will be referred to as analytical

noise.

The mixing of gases and meltwater during the sample transfer from the melt head to the laser spectrometer induces a CFA experimental smoothing of the signal. The extent of the CFA-based damping was determined by performing a step test (Figure 3.8), i.e., a switch between two synthetic mixtures of degassed DI water and synthetic air standards of different methane concentrations, following the method of [Stowasser et al. \(2012\)](#). It shows that the CFA system can resolve signals down to the centimeter scale. We were also able to extract the impulse response of the system, that will be used in Section 5.2.4.3 to emulate CFA smoothing. A more detailed discussion of the frequency response of the system can be found in Section 3.1.5. Breaks along the core regularly let ambient air enter the system, resulting in strong positive spikes in methane concentration. In order to remove these contamination artifacts, exact times corresponding to a break running through the melt head were recorded during the measurements and later used to identify and clean the data from contamination.

5.2.2.3 Nitrogen isotopes

The ratio of stable nitrogen isotopes, $^{15}\text{N}/^{14}\text{N}$, was measured at the Laboratoire des Sciences du Climat et de l'Environnement (LSCE), France. Briefly, a melting technique followed by gas condensation in successive cold traps was used to extract the air from the ice, and the air samples were then transferred to a dual-inlet mass spectrometer (Delta V Plus, Thermo Scientific). The analytical method and corrections applied to the results are described in [Landais et al. \(2004\)](#), and the references therein.

The results are expressed as deviations from the nitrogen isotopic ratio in dry atmospheric air ($\delta^{15}\text{N}$). Discrete samples every 50 cm and duplicates were analyzed when possible. A total of 96 data points, including 39 duplicates were obtained. The pooled standard deviation over duplicate samples is 0.011‰.

5.2.3 Experimental results

5.2.3.1 Methane record

The methane record spanning the DO-17 event extracted from the Vostok 4G-2 ice core is presented in blue in Fig. 5.1. Two corrections were applied to these data: (i) data screening

and removal of kerosene contamination, and (ii) full dataset calibration to account for the preferential dissolution of methane during the melting process.

Kerosene, used as drilling fluid for the Vostok 4G-2 ice core extraction, was detected in some of the meltwater from our continuous flow analysis. This contamination induces surface iridescent colors and a strong characteristic smell; it and was detected not only in the meltwater from the outer part of our ice sticks but also in some of the meltwater from the center of the ice samples. However, the continuous flow of the meltwater does not allow us to clearly identify the contaminated ice core sections. Carbon monoxide (CO) was measured simultaneously with methane by using our laser spectrometer (Fain et al., 2014). We attributed simultaneous anomalies in CH₄ (increase of about 20ppbv or more) and CO (increase of about 100ppbv or more) mixing ratios to kerosene contamination, and suppressed the corresponding data by visual inspection of the dataset. An example of such a kerosene contamination is visible in Fig. 5.10 (SI). Chappellaz et al. (1990) indicate that methane contamination lower than 40ppbv was observed by discrete measurements in the brittle zone of the Vostok 3G core, which is consistent with our observation in 4G-2. The impact of kerosene contamination on CO in ice cores has not been quantified so far. Adding the length of all kerosene-affected ice core sections, a total of 2.1 of data was removed. The calibration of the methane mixing ratio for preferential solubility (Rhodes et al., 2013) was achieved by matching our continuous methane measurements with the already calibrated WDC methane dataset (Rhodes et al., 2015), as described in Section 5.2.8.1 of Supplementary Information. The resulting methane record has a high resolution, but presents numerous discontinuities due to missing ice, ambient air infiltration, and kerosene contamination. The signal displays two distinct scales of variability.

Atmospheric-history-relevant variability. The general shape of the signal can be divided in two parts, a stable zone extending from 931 to 915m of depth and two consecutive methane variations of approximately 100ppbv each, extending respectively from 915 to 907m and from 907 to 895m. They respectively correspond to the plateau preceding the DO-17 event and the DO-17 event itself.

Centimeter-scale variability. The signal also displays centimeter-scale methane variations. A portion of these variations is explained by the 10ppbv analytical noise of the CFA system. However, in the upper part of the core (above 915m) the signal also exhibits abrupt

variations with amplitudes reaching up to 50ppbv and widths of about 2cm. Most of those spikes is negatively orientated and therefore laboratory air or kerosene contamination can be ruled out. It should be noted that the width of the spikes are in the attenuation range of the CFA system, meaning that the true signal in the core has a somewhat larger amplitude than the measured signal. Moreover, the spikes exhibit a specific distribution with depth. For instance no spike is observed in the lower part of the ice core where the methane concentration is essentially flat, and only negative spikes appear between 900 and 905m of depth as seen in the zoomed part of Fig. 5.1.

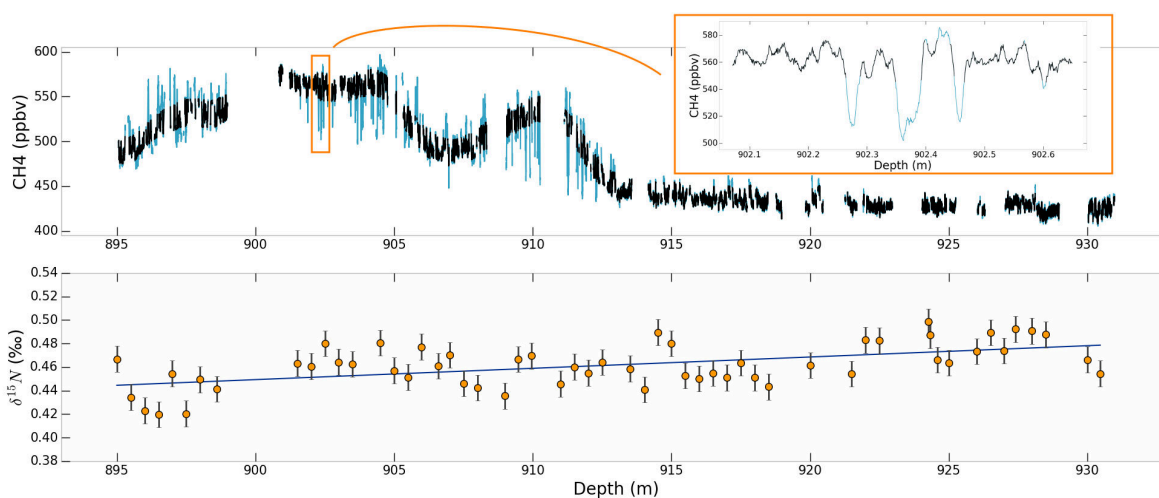


Figure 5.1 – Top: Methane concentration along the Vostok 4G-2 ice core. In blue: data cleaned from ambient air and kerosene contamination, and calibrated. In black: data cleaned from layered trapping. Top right corner: zoom of the section from 902.0 to 902.7m. Bottom: $\delta^{15}\text{N}$ of N_2 as a function of depth in the Vostok 4G-2 ice core. Orange dots: isotopic measurements. The vertical error bars correspond to the pooled standard deviation. In blue: linear regression.

5.2.3.2 Revised age scale using Nitrogen isotopes

The current reference chronology for the Vostok ice core is the Antarctic Ice Core Chronology 2012 (AICC2012; Bazin et al., 2013; Veres et al., 2013). However, only two gas stratigraphic links between Vostok and other cores are available for the DO-17 period in AICC2012, leading to relatively large uncertainties in the Vostok gas age scale over this period. The $\delta^{15}\text{N}$ of N_2 profile over the DO-17 event in the Vostok core is shown Fig. 5.1. We fitted the experimental values with a linear regression (slope of $9.63 \times 10^{-4}\text{‰m}^{-1}$ and intercept of -0.417‰). Considering the diffusive zone of the firn to be stratified according to a barometric equilibrium (Craig et al., 1988; Orsi et al., 2014), its height can be expressed as $H = (RT/g\Delta M)\ln(1 + \delta^{15}\text{N})$, where R is the ideal gas constant, T the temperature, g the

gravitational acceleration, and ΔM the difference in molar mass between ^{14}N and ^{15}N . With a firn temperature of 217K (Petit et al., 1999), the mean $\delta^{15}\text{N}$ value of 0.46‰ translates into a diffusive column height of 85m, and an LIDIE (lock-in depth in ice equivalent) of 59m (using a mean firn relative density of $D = 0.7$). This value lies in the lower range of the AICC2012 LIDIE estimations for this depth range in the Vostok ice core: 58 to 70m (Bazin et al., 2013; Veres et al., 2013).

The age difference between the ice and the enclosed gases (ΔAge) can be estimated using the height of the firn with $\Delta\text{Age} = (H + H_{conv})D/accu$, where H and H_{conv} are the heights of the diffusive and convective zones, respectively, D is the average density of the firn column and $accu$ the accumulation rate. Present-day observations report a convective zone spanning down to 13m at Vostok (Bender et al., 1994). We used this value as an estimate for the convective zone depth during DO-17. In Fig. 5.2, the ΔAge values inferred from our $\delta^{15}\text{N}$ record using $D = 0.7$ and an accumulation rate of 1.3cm.ice.yr^{-1} are compared with the values from AICC2012 (Bazin et al., 2013; Veres et al., 2013). The AICC2012 ΔAge values display a variability of several centuries as shown by the dashed black line in Fig. 5.2. These variations are sufficient to induce significant distortions in the duration of methane events. These distortions affect the comparison between our measurements and the WDC record from Rhodes et al. (2015), as seen in Fig. 5.18 of the supplement. Furthermore, the amplitude of the ΔAge variations is similar to the uncertainty in gas age (1479 to 1841 years). The studied period is fairly stable in terms of temperature and accumulation at Vostok (Petit et al., 1999; Bazin et al., 2013; Veres et al., 2013); thus the ΔAge changes in the AICC2012 chronology are likely to result from artifacts of the optimization method rather than to correspond with actual variations. We hence revised the AICC2012 gas age scale by deriving a new smooth gas age using the AICC2012 ice age scale and our ΔAge values inferred from the linear interpolation of $\delta^{15}\text{N}$ data (Fig. 5.2). This new smooth chronology enables us to visually identify the different subparts of the DO-17 event between the Vostok and WDC methane records. It is important to note that this gas age chronology will again be improved by matching the Vostok and WDC methane records (see Section 5.2.5.2). The corresponding ΔAge of this final chronology is displayed as the green line in Fig. 5.2.

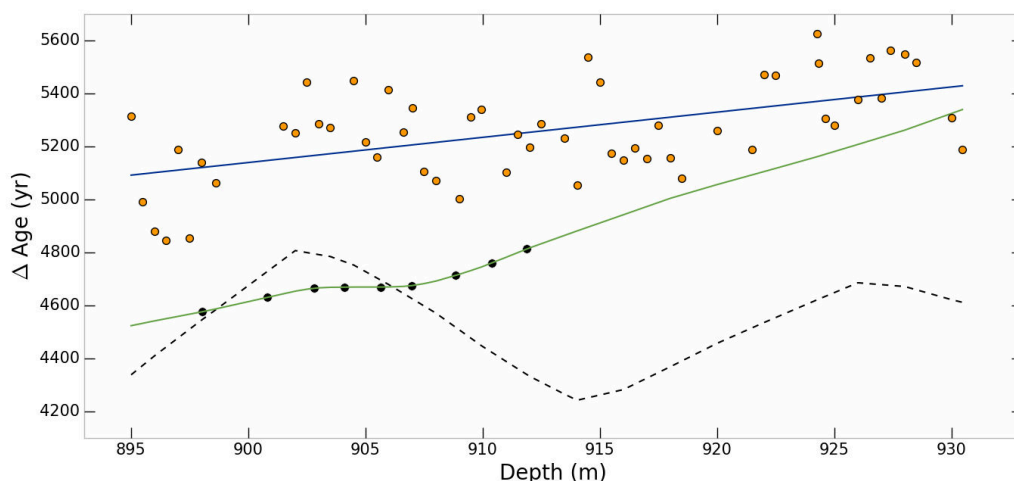


Figure 5.2 – Δ Age along the Vostok record. Orange dots: Δ Age directly estimated from $\delta^{15}\text{N}$ measurements. In blue: Δ Age derived from the linear regression on isotopic measurements. Black dashed line: Δ Age as given by AICC2012. In green: Δ Age after matching with the WDC CH_4 record. Black dots: tie points (minima, maxima, and mid-slope points) used to match the WDC record (see 5.2.5.2).

5.2.4 Layered bubble trapping

5.2.4.1 Conceptual considerations of the layered trapping mechanism

Due to heterogeneities in firn density and porosity, an ice layer may undergo early gas trapping (Etheridge et al., 1992; Rhodes et al., 2013; Mitchell et al., 2015; Rhodes et al., 2016). Thus during gas trapping, the corresponding layer is at a more advanced state of closure than the surrounding bulk layers. Similarly, some layers may undergo a late closure. If gases can circulate through the open porosity surrounding the anomalous layers, the early closed layers will contain abnormally ancient gas with respect to the surrounding layers. On the other hand, layers closed late will contain abnormally recent gas. This leads to very local inversions of the gas age scale along depth. As explained in Rhodes et al. (2016), such a mechanism affects trace gas records only during periods of variations in the concentration of atmospheric gases. Then, abnormal layers contain air significantly different in composition from surrounding layers and appear as spikes in the record. On the other hand, during periods without atmospheric variations, the abnormal layers do not contain air significantly different in composition from their surroundings, and the gas record is not affected.

The orientation of layered trapping spikes depends on the type of atmospheric variations, as illustrated in Fig. 5.3. For instance, in a period of local maximum in methane concentrations, both early and late closures tend to enclose air with lower mixing ratios, as displayed in case

A in Fig. 5.3. Similarly, in periods of methane minima, abnormal layers tend to enclose air with larger mixing ratios, as displayed in case C in Fig. 5.3. In the case of monotonous increase or decrease, early and late closures lead to artifacts with opposite signs, as represented by case B in Fig. 5.3. It should be noted that early and late closures are not expected to affect the record with the same importance. Indeed, a late pore closure means that the surrounding firn is sealed and prevents long-distance gas transport. The latest closure layers will not be able to trap young air if gas transport is impossible in the surrounding firn layers, resulting in less important artifacts.

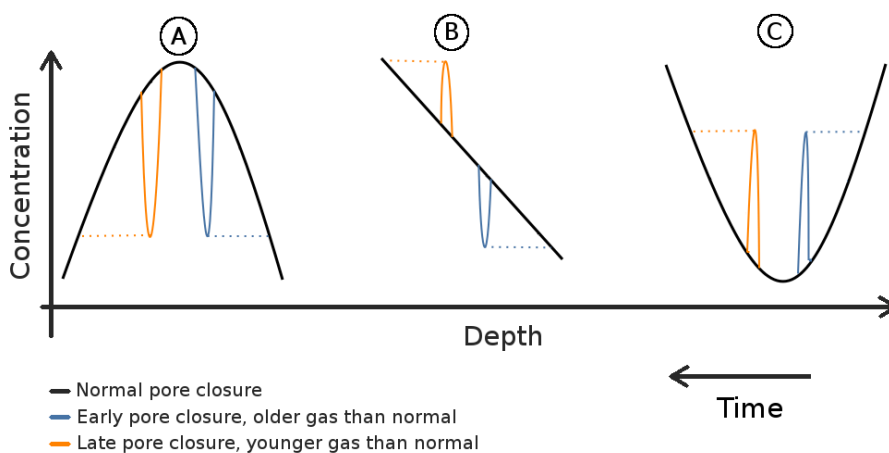


Figure 5.3 – Expected orientation of layered trapping artifacts depending on the characteristics of atmospheric variations. Black curves correspond to a normal chronological trapping, blue to early pore closure, and orange to late pore closure. Cases A, B, and C respectively represent local maximum, monotonous trend, and local minimum situations.

5.2.4.2 Observed layered trapping in the Vostok 4G-2 ice core

The positive and negative spikes observed in the Vostok 4G-2 methane record introduced in Section 5.2.3.1, are consistent with the expected impacts of layered trapping. First, the absence of spikes in the lower part of the record below 915m is consistent with the absence of an overall methane trend over the corresponding period. Moreover, in periods of methane local maxima at around 903 and 910m of depth, most of the spikes are negatively oriented as expected with the conceptual mechanism of layered bubble trapping (cf. case A in Fig. 5.3).

Thin sections of ice covering the depth range between 902.0 and 902.42m (zoomed range in Fig. 5.1) have been analyzed, to investigate whether structural anomalies were associated with anomalous trapping. The method is described in detail in Section 5.2.8.4 of the Sup-

plement. We were not able to observe any link between the grain sizes and abnormal layers in the methane record. Nonetheless, structural anomalies may have existed at the time of pore closure before disappearing with $\sim 60,000$ years of grain evolution. Explanations for the methane anomalies other than layered trapping were considered as well. Looking for a correlation between ice quality and methane anomalies was also a motivation for the above thin section analysis. Although the samples showed small clathrate relaxation cavities, the CFA sticks did not reveal visual signs of stratification possibly associated with abnormal layers. Examples of a CFA stick picture and thin section results are provided in the Supplement. The ice samples were not large enough to allow for CFA duplicate analysis, but the sticks were not melted in a regular depth order so that instabilities in the measurement system could be more easily detected. As contamination cannot explain negative methane concentration anomalies, we could not find a convincing alternate explanation for layered bubble trapping in our results.

5.2.4.3 Simple model of layered trapping

A major difficulty for understanding the gas trapping in ice is to relate the structural properties measured in small samples to the three-dimensional behavior of the whole firn. For example, pore closure anomalies have been associated with tortuosity anomalies, with more tortuous layers closing earlier (Gregory et al., 2014), or to density anomalies, with denser layers closing earlier (Etheridge et al., 1992; Mitchell et al., 2015; Rhodes et al., 2016). In this section we used the latter hypothesis supported by observed relationships between local density and closed porosity (e.g., Stauffer et al., 1985; Mitchell et al., 2015), to test whether density-driven anomalies could result in artifacts as observed in the Vostok methane record.

In our simple model, the ice core is discretized in layers of 2cm width. Abnormal layers are stochastically distributed along the ice core. Based on the characteristics of our Vostok methane signal, we use a density of 10 abnormal layers per meter. They are given a random density anomaly ($\Delta\rho$, normally distributed) representing the density variability at the bottom of the firn. Based on various sites, Hörhold et al. (2011) propose linear regressions in which the close-off density variability declines for declining accumulation and temperature. Their lowest-accumulation site is Dome C, with an accumulation of 2.5cm.ice.yr^{-1} and a density variability ($\Delta\rho$) of 4.6kg.m^{-3} . Applied to Vostok DO-17

conditions, the accumulation-based extrapolation leads to a variability of $7\text{kg}\cdot\text{m}^{-3}$ and the temperature-based extrapolation leads to a variability of $2.7\text{kg}\cdot\text{m}^{-3}$. This defines our extreme values (7 and $3\text{kg}\cdot\text{m}^{-3}$), and we chose the middle number of $5\text{kg}\cdot\text{m}^{-3}$ as the best-guess value. Hence, in the model, the abnormal layers are given a firn density anomaly distributed according to a zero-centered Gaussian distribution of standard deviation of $5\text{kg}\cdot\text{m}^{-3}$. In order to convert density anomalies into a closure depth anomaly (the difference in pore closure depth between an abnormal layer and an adjacent layer following the bulk behavior), we assume that all layers have similar densification rates ($d\rho/dz$). Using the data-based density profiles at Dome C, Vostok, and Dome A in [Bréant et al. \(2017\)](#), $d\rho/dz$ in deep firn is estimated to be in the range 1.7 to $2.5\text{kg}\cdot\text{m}^{-4}$. Thus, the gradient is set to be $2\text{kg}\cdot\text{m}^{-4}$. Specifically, a layer closing in advance (or late) closes higher (or lower) in the firn. Dividing the above typical density anomaly ($\Delta\rho$) by the depth gradient ($d\rho/dz$), the characteristic depth anomaly in deep firn of anomalous layers is about 2.5 meters. Using the estimated accumulation rate of $1.3\text{cm}\cdot\text{ice}\cdot\text{yr}^{-1}$ for this period, it translates into an age anomaly (the gas age difference between an abnormal layer and an adjacent layer following the bulk behavior) of about 207 years. As explained in Section 5.2.4.1, late pore closure tends to produce weaker age anomalies than early closure due to the sealing of the surrounding firn. To take into account the lack of explicit gas transport in the model, we reduce the standard deviation of late closure age anomalies to 52yr , i.e., 25% of the value used for early closure artifacts. The value of 25% has been chosen to limit late trapping artifacts in a visually consistent manner with the observations. The methane mixing ratio at a given depth is computed using an atmospheric trend history and a gas age distribution (GAD) of trapped gases ([Rommelaere et al., 1997](#)). The atmospheric methane scenario used is the high-resolution methane record from the WAIS Divide ice core ([Rhodes et al., 2015](#)). The WDC gas age chronology (WD2014) was scaled to the GICC05 chronology (with present defined as 1950) dividing by a factor of 1.0063 as in [Buizert et al. \(2015\)](#). For the rest of the paper we use this scaled WD2014 chronology to express WDC gas ages. All layers are assumed to have the same GAD, simply centered on different ages. The GAD used here is the one derived in Section 5.2.5.2 specifically for the Vostok ice core during the DO-17 event. A sensitivity test using a very different GAD is described in the next paragraph. Finally, in order to reproduce the gas mixing in the CFA system discussed in Section 5.2.2.2, the modeled concentrations have been smoothed by convolving the signal with an estimated impulse response of the CFA system (Fig. S2, SI). The smoothing characteristics of our measurement system were determined experimentally as in [Stowasser et al. \(2012\)](#). The CFA smoothing induces a

damping of about 18% of the modeled artifacts.

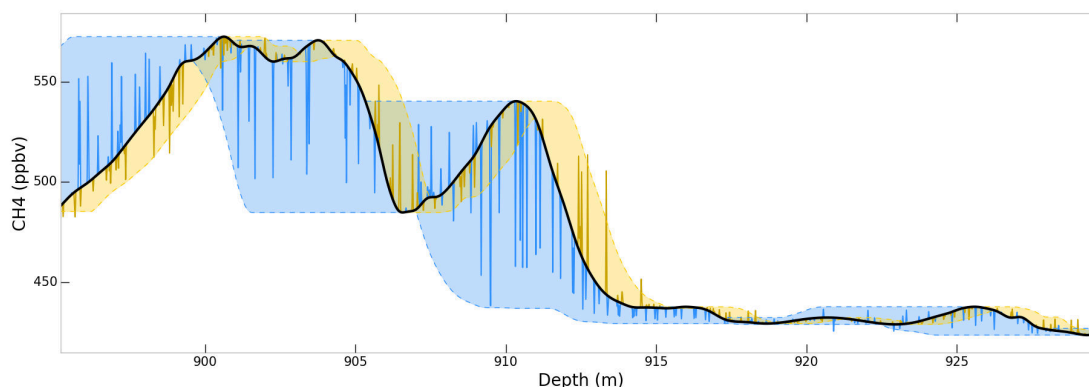


Figure 5.4 – Modeled layered trapping artifacts. The black curve represents the results of smooth trapping. Spikes correspond to a single stochastic realization of the layered trapping with CFA smoothing. Blue stands for early closure and yellow for late closure. Blue shaded areas correspond to the range of concentration anomalies for early closure anomalies up to 2 standard deviations (depth anomaly of 5m corresponding to an age anomaly of 415 years). Yellow shaded areas correspond to late closure anomalies with 25% of the early closure extent (depth anomaly of 1.25m corresponding to an age anomaly of 104yr).

The modeled artifacts (Fig. 5.4) globally reproduce the depth distribution and amplitude of the methane anomalies observed in the Vostok ice core (Fig. 5.1 and Section 5.2.4.2). To test the robustness and sensitivity of our model to uncertainties and underlying assumptions, we modified several model parameters. First, the limitation of late closure trapping was removed, hence simulating symmetrical behavior between early and late trapping. The results displayed in supplementary Fig. 5.14, show a clear increase in the amplitude of late closure artifacts. In particular, the enhanced late trapping produces artifacts of about 50ppbv before the onset of the DO-17 (in the 914 to 917m depth range). Their absence in the CFA measurements confirms our assumption of the predominance of early closure artifacts. On the other hand, as shown in case B of Fig. 5.3, some limited late trapping is required to reproduce what appear as positive anomalies at the onset of the DO-17 event (912 to 913m depth range). We also estimated the sensitivity of the model to the density variability ($\Delta\rho$) and densification rate ($d\rho/dz$). The extremal values for these two parameters provided at the beginning of this section, result in typical depth anomalies of 1.2 and 4.1m, corresponding to age anomalies of 99 and 341 years. The model results are displayed in Fig. 5.15 and 5.16 (SI). Using a reduced depth anomaly of the anomalous layers leads to largely reduced amplitudes of the anomalies. Using an increased depth anomaly of the anomalous layers leads to overestimated amplitudes of the anomalies, especially between 903 and 910m of depth. As using a Gaussian distribution of density anomalies is equivalent

to using a random depth anomaly, the smallest anomalies produced by the model do not exceed the analytical noise. We imposed a density of 10 anomalies per meter, which results in about 5 significant anomalies per meter (exceeding 10ppbv) in the 895 to 915m depth range. About 70% of these significant artifacts correspond to early closure layers. The width of the anomalous layers also influences the amplitude of the modeled anomalies because it is in the attenuation range of the CFA system. While 2cm layers experience a damping of 18%, an attenuation of about 30% is observed with 1cm layers. The anomalies observed in the Vostok signal have widths ranging between 1 and a few centimeters. Their smoothing by the CFA system is thus limited. We also tested an alternative to the homogeneous GAD hypothesis, assuming that anomalous layers have a strongly reduced GAD similar to the gas age distribution in the WDC core. The results are displayed in Fig. 5.17 (SI). As the WDC record of the DO-17 event is less smooth than the Vostok record, the reduced GAD assumption leads to large positive artifacts, especially around 912m of depth, which are not observed in the Vostok signal.

Finally, under the hypothesis of density-based layering, age anomalies strongly depend on accumulation as explained by Rhodes et al. (2016). A lower accumulation leads to a weaker density variability in the firn (Hörhold et al., 2011), but at the same time leads to a larger age difference between successive firn layers due to a steeper age-depth slope. The second effect tends to dominate and the net effect of a lower accumulation is an increase in age anomalies due to layered trapping. Moreover, it is important to note that the good agreement between our density-driven model and observations does not imply that tortuosity is not an important factor in anomalous trapping. High-resolution air content measurements could potentially help us better understand the physical properties of anomalous layers at closure time.

Table 5.1 – Layering model parameters and resulting depth anomaly, age anomaly, and associated figure. The first row corresponds to the reference simulation and the sensitivity tests are below. The depth and age anomaly values refer to the standard deviation (1σ) of early trapping artifacts. These 1σ values are half the 2σ values mentioned in the corresponding Figure captions.

$d\rho/dz$ ($\text{kg}\cdot\text{m}^{-4}$)	$\Delta\rho$ ($\text{kg}\cdot\text{m}^{-3}$)	Limit late anomalies	Narrow GADs	Depth anomaly (m)	Age anomaly (yr)	Figure
2	5	Yes	No	2.5	207	5.4
2	5	No	No	2.5	207	S7
2.5	3	Yes	No	1.2	99	S8
1.7	7	Yes	No	4.1	341	S9
2	5	Yes	Yes	2.5	207	S10

5.2.4.4 Removing layering artifacts in the methane record

To extract an undisturbed (chronologically monotonous and representative of atmospheric variability only) methane signal from the Vostok 4G-2 core, layered trapping artifacts need to be removed from the high-resolution CFA record. Some sections of the core exhibit mainly positive or negative artifacts. Hence removing them using a running average would bias the signal. To account for this specificity, a cleaning algorithm has been developed. The underlying assumptions are that the chronological signal is a slowly varying signal with superimposed noise composed of the analytical noise and the layered trapping artifacts. Using a looping procedure, the artifacts are progressively trimmed until the resulting noise is free of spikes. The detailed algorithm is described in the following.

- Using the CFA signal (with or without already partially removed layering artifacts during the cleaning process) a running median is computed with a window of 15cm. Then a binned mean is computed with bins of 50cm. The goal of this step is to remove noise, without introducing a bias due to layering artifacts.
- A spline of degree 3 is used to interpolate between the binned points on the original CFA depth scale. This interpolating spline does not further smooth the signal, and is used as an approximation of the chronologically monotonous signal, free of layering artifacts.
- By removing the spline from the CFA signal we obtain the detrended noise of the signal composed of the analytical noise and the remaining artifacts.
- We then compute the Normalized Median Absolute Deviation (NMAD) of the detrended noise. The expression of the NMAD is $1.4826 \times \text{med}(|x_i - \text{med}(x_i)|)$, where x_i represents the noise values and med the median. This is a robust estimator of variability, weakly sensitive to outliers (Höhle and Höhle, 2009; Rousseeuw and Hubert, 2011). It enables the estimation the variability of the noise without the artifacts, i.e. the analytical noise.
- The detrended noise is cut off with a threshold of 2.5 times the NMAD.
- We then check whether the noise is free of spikes. For this we compare the NMAD (estimation of the variability without spikes) and the Standard Deviation (estimation of variability with spikes) of the detrended noise. If these two quantities are similar, the noise is free of anomalous layers. Once the Standard Deviation is lower than 1.5 times the NMAD, the procedure is finished. Otherwise, the algorithm is looped.

This algorithm does not require an estimation of the analytical noise beforehand, since this value is dynamically computed. However, it is sensitive to the value of 1.5 used to compare the NMAD and standard deviation to test the presence of artifacts. The remaining signal

after cutting off the layered trapping anomalies has a noise amplitude of ± 16 ppbv, and is represented in black in Fig. 5.1. With our method 15% of the methane data points have been removed. As expected, the signal is almost unmodified below 915m, with a portion of removed points of only 1.3%. On the other hand, the variability above 915m is greatly reduced and about 26% of the methane data points have been removed.

5.2.5 Smoothing and age distribution in the Vostok 4G-2 ice core

5.2.5.1 The smoothing of the methane record

Once the methane signal is cleaned from layered trapping artifacts, we consider the data to be a chronologically ordered and unbiased signal recorded in the core. It is smoothed (high frequencies are damped) with respect to the true atmospheric signal and can be used to infer the degree of smoothing in the Vostok ice core. The damping can be visualized in Fig. 5.5 by comparing the Vostok record with the WDC record. High-frequency atmospheric variability is much better preserved in the WAIS Divide ice core because the accumulation rate is more than an order of magnitude higher (in the range from 18 to 22cm.ice.yr⁻¹ for the studied period, [Buizert et al., 2015](#)) and thus the firn densification and gas trapping are faster. For instance, the methane variation spanning between 59,000 and 58,800yrBP is damped by $\sim 50\%$ in the Vostok record compared to WDC. Moreover, a 20ppbv sub-centennial variation is present in the WDC record between 58,700 and 58,600yrBP. In the Vostok record, however, this short-scale variability event has been smoothed out. On the other hand the multi-centennial variability visible between 58,700 and 58,400yrBP is well preserved with only a slight damping. From the comparison between WDC and Vostok, we can infer that the smoothing in Vostok 4G-2 prevents us from retrieving information below the centennial scale during the DO-17 period.

5.2.5.2 Estimate of the gas age distribution

The smoothing of gas concentrations in ice core records is the direct consequence of the broad gas age distributions in the ice ([Spahni et al., 2003](#); [Joos and Spahni, 2008](#); [Köhler et al., 2011](#); [Ahn et al., 2014](#)). We call absolute GAD the age distribution expressed on an absolute timescale, in years before present. The relative GAD is the distribution expressed relatively to its mean age. For a given layer, absolute and relative GAD thus only differ by a

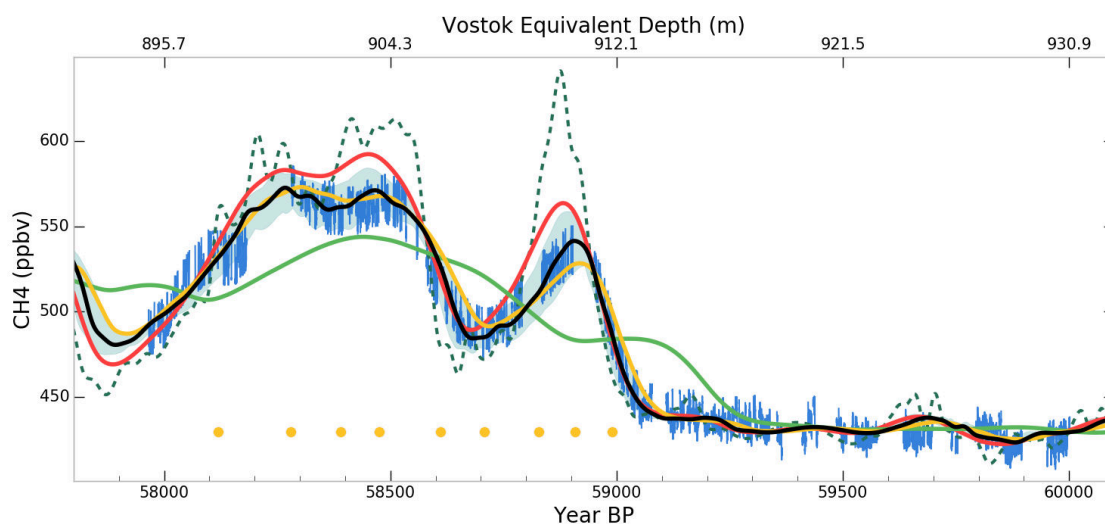


Figure 5.5 – WDC CH₄ signal convolved with different GADs: the Dome C GAD estimated for the Bølling-Allerød by Köhler et al. (2015) in red, the Dome C GAD estimated for the Last Glacial Maximum by Köhler et al. (2011) in green, a lognormal fit to the modern Vostok GAD from Witrant et al. (2012) in yellow, and the Vostok DO-17 GAD estimated in Section 5.2.5.2 in black (uncertainty envelope shown in light blue). The WDC record (Rhodes et al., 2015) is displayed in dashed green, and the CFA Vostok measurements in blue. Yellow dots show the tie points used to match the WDC and Vostok records.

translation in age. Here we assume that all layers densified under the same physical conditions, hence share the same relative GAD. Since computing concentrations along an ice core using GADs is equivalent to a convolution product (Rommelaere et al., 1997), the resulting concentrations will be called convolved signals.

The climatic conditions of the glacial period on the Antarctic plateau have no modern analogue, and thus relevant GADs cannot be inferred from modern firn observations. High-resolution CFA based gas records offer a new opportunity to estimate GADs without modern analogue. We thus developed such a method, which requires a reference atmospheric scenario with much higher frequencies resolved. The method can be extended to gases other than methane or to low-accumulation records other than the Vostok 4G-2 core. The principle of the method is to determine a GAD able to convolve the high-accumulation record (in our case, WAIS Divide) into a smoothed signal that minimizes the differences with the observed low-accumulation record (in our case, Vostok). It can be seen as an inverse problem. Two assumptions are made to reduce the number of adjusted parameters and thus ensure that the problem is well defined in a mathematical sense. First, all ice layers have the same relative GAD over the considered period. Second, following Köhler et al. (2011), this relative GAD is assumed to be a lognormal distribution that is fully characterized by two free parameters (for instance, its mean and standard deviation). Due to the asymmetry of the

GAD, the resulting convolved signal displays age shifts when compared with the original atmospheric scenario. Hence for a valid comparison between the record and convolved signals, it is necessary to modify the age scale and to optimize the GAD in an iterative process. Using an initial age scale, the steps are as follows.

-1: First, a new gas age scale is derived. Tie points are manually selected between the low-accumulation record and the convolved high-accumulation record. The tie points we selected correspond to minima, maxima, and mid-slopes points of the methane record. For the initialization, since no GAD has been optimized yet, we use the atmospheric scenario instead of the convolved signal. The new gas chronology is then generated by interpolation and extrapolation between tie points.

-2: A new lognormal GAD is optimized by modifying its two parameters in order to minimize differences between the simulated and observed smoothed signals. We performed this optimization with a differential evolution algorithm (Storn and Price, 1997).

-3: If the definition of a new chronology and a new GAD does not improve the RMSD (root mean square deviation) between the convolved signal and the measurements five times in a row, then the algorithm is stopped.

The above methodology can be applied to different ice drilling sites. Here we describe the specific aspects to match the Vostok record with WDC. Rhodes et al. (2015) state the following: "Only at gas ages > 60ka BP is there a possibility that the continuous measurement system caused dampening of the CH₄ signal greater than that already imparted by firn-based smoothing processes". Moreover, Fig. S1 of the supplement to Rhodes et al. (2015) predicts a GAD width of about 40yr for the DO-17 event, which is much smaller than the width of the Vostok GAD. This ensures that the WDC signal resolves enough high frequencies to be used as the weakly smoothed atmospheric scenario compared to the Vostok record, and that the convolving function given by the algorithm is close to the actual Vostok GAD. As explained in Section 5.2.4.2, the WD2014 gas chronology is converted to the GICC05 scale (Buizert et al., 2015) and not further modified. The algorithm only adjusts the Vostok gas ages, which remain well within AICC2012 uncertainties. The initial gas ages used are the ones derived from nitrogen isotope measurements in Section 5.2.3.2, and the optimization has been performed on data ranging from 900 to 915m of depth. This depth interval has been chosen since it corresponds to a significantly dampened event in the Vostok record, which is sensitive to the choice of the GAD. The optimized gas age distribution is displayed

in Fig. 5.6 in black, with uncertainty intervals shown as light blue shaded area. The uncertainty envelope encloses all the distributions resulting in simulated Vostok signals with a RMSD from the measurements lower than 150% of the optimal an RMSD. The optimal lognormal parameters are given in Table 5.2. The chosen tie points are displayed in Fig. 5.5, and the optimized ΔAge values along the Vostok core are depicted in green in Fig. 5.2. The optimal convolution of the WDC methane record from Rhodes et al. (2015) into a Vostok signal can be seen in black in Fig. 5.5, with the impact of the uncertainty on the GAD displayed as the light blue envelope. The convolution fits the methane measurements within the analytical noise. The overall consistency between the measured and simulated Vostok signals confirms that the Vostok record is a smoothed version of the WDC record, and that the choice of a single GAD for the whole DO-17 record is a credible hypothesis. This last point is consistent with the fairly stable climatic conditions on the Antarctic plateau over this time period (Petit et al., 1999; Bazin et al., 2013; Veres et al., 2013).

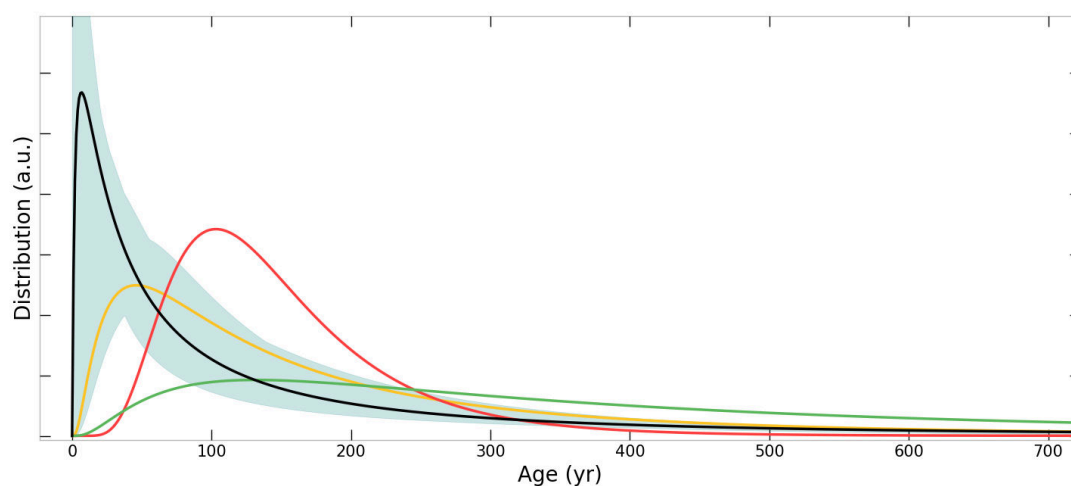


Figure 5.6 – Gas age distributions. In black: the Vostok GAD during the DO-17 estimated with our optimization scheme, the uncertainty envelope is shown in light blue. In yellow: a lognormal fit to the modern-condition Vostok GAD from Witrant et al. (2012). In red: the estimated Dome C GAD during B/A from Köhler et al. (2015). In green: the estimated Dome C GAD during LGM from Köhler et al. (2011).

5.2.6 Discussion

5.2.6.1 Understanding the smoothing of ice core signals under low-accumulation conditions

In Fig. 5.6, our GAD adjusted to produce the expected smoothing rate for the DO-17 event in the Vostok ice core (in black) is compared to other available gas age distributions for

low-accumulation-rate conditions. The different parameters of the lognormal GADs used in this section are displayed in Table 5.2. For modern ice cores, GADs can be estimated with gas transport models constrained by firn air composition data (Buizert et al., 2012; Witrant et al., 2012). However, the results directly depend on the closed versus total porosity parameterization used, which is insufficiently constrained (e.g., Mitchell et al., 2015). We performed a comparison of our optimized GAD for Vostok during DO-17 with the lognormal fit to a GAD constrained with modern-condition firn air measurements at Vostok (Witrant et al., 2012, in yellow in Fig. 5.6). Note that using the modern GAD from Witrant et al. (2012) or a lognormal fit to this GAD leads to the same smoothing, but the lognormal GAD enables us to provide simple GAD parameters in Table 2. The comparison with our optimized DO-17 GAD suggests a slightly narrower distribution for the glacial period, despite lower temperatures. On the other hand, the GAD estimate from Köhler et al. (2015) for Dome C during the Bølling-Allerød (B/A; accumulation of about 1.5cm.ice.yr^{-1}) is narrower (in red Fig. 5.6) and results in a slightly too-weakly smoothed methane record in Fig. 5.5. Finally, the GAD proposed by Köhler et al. (2011) for Dome C during the Last Glacial Maximum (LGM) is broader than the other presented GADs (in green Fig. 5.6) and thus leads to a stronger smoothing in the record in Fig. 5.5. The GADs calculated for modern conditions from Köhler et al. (2011) at Dome C and Witrant et al. (2012) at Vostok are very similar, which is consistent with the comparable accumulation rates of the two sites: 2.7cm.ice.yr^{-1} at Dome C (Gautier et al., 2016) and 2.4cm.ice.yr^{-1} at Vostok (Arnaud et al., 2000). We therefore do not observe a systematic broadening of GADs for lower accumulation rates, even at a given site. This questions either the relationship between GAD widths and accumulation rate or the consistency between GADs derived from gas transport models in firn and the GAD obtained with our method of record comparison.

Table 5.2 – Parameters defining the lognormal distributions used as GADs for Vostok DO-17 (this study), lognormal fit to modern Vostok (Witrant et al., 2012), Dome C during the Bølling-Allerød (Dome C B/A; Köhler et al., 2015), and Dome C during the Last Glacial Maximum (Dome C LGM; Köhler et al., 2011). Location and scale respectively refer to the parameters μ and σ used in Equation 1 in Köhler et al. (2011). Std Dev stands for standard deviation.

Site and period	Location	Scale	Mean (yr)	Std Dev (yr)
Vostok DO-17	4.337	1.561	259	835
Vostok modern	4.886	1.029	226	308
Dome C B/A	4.886	0.5	150	79
Dome C LGM	5.880	1	590	773

The most likely reason for an inconsistency between GADs inferred from firn models and from CFA data is the large uncertainty in the representation of gas trapping in firn models. As mentioned above, the closed versus total porosity ratio is very uncertain, as it was measured only at a few sites and in small size samples. Better constraints on the physics of gas trapping would thus be helpful. However, there is no modern analogue of the central Antarctic plateau sites (such as Vostok or Dome C) under glacial conditions. Thus, using CFA high-resolution gas measurements at different sites to constrain Holocene GADs at low-accumulation sites would be the only way to check the consistency of the two methods. Previous comparisons between sites indicate that the smoothing is larger for low-accumulation conditions (Spahni et al., 2003; Joos and Spahni, 2008; Köhler et al., 2011; Ahn et al., 2014). Indeed, a simple argument is that the lower the accumulation and the temperature, the slower a firn layer will densify, and thus the broader the GAD. The comparison of the DO-17 records between WDC and Vostok 4G-2 corroborates this relationship: the higher-accumulation WDC signal is less smooth than the Vostok signal (Fig. 5.5). The weaker-than-expected smoothing during DO-17 at Vostok could be due to the presence of a strong layering preventing air renewal and mixing, as suggested in Mitchell et al. (2015).

From a paleoclimatic point of view, an important conclusion of this work is that the smoothing of atmospheric trace gases recorded in ice cores from the central Antarctic plateau could be less than expected under glacial conditions, resulting in more retrievable information about past atmospheric conditions. Ice cores with the oldest enclosed gases, such as in the Oldest Ice project (Fischer et al., 2013), will be retrieved from very low-accumulation sites. They could thus potentially provide meaningful information down to the multi-centennial scale.

5.2.6.2 Layered trapping and atmospheric trend reconstructions

The anomalous layers in the Vostok methane record discussed in Section 5.2.4.2 are 1 to a few centimeters thick, and discrete samples used for methane measurements in ice cores are typically also a few centimeters thick. In our study, the use of high-resolution continuous analysis made it possible to identify abnormal methane values that appeared as spikes in the record. However, in the case of discrete measurements, the absence of continuous information makes it hard to discriminate between normal and abnormal layers.

For instance, the comparison of the WDC continuous record and the EPICA Dome C (EDC) discrete methane record (Loulergue et al., 2008) indicates a potential artifact during the onset of the Dansgaard-Oeschger event 8 ($\sim 38,000$ yrBP), as displayed in Fig. 5.7. One of the EDC samples shows a reduced methane concentration, which should be visible in the less smooth WDC record as well if this corresponded to a true atmospheric feature. Moreover, the measured mixing ratio in this EDC sample is consistent with an artifact resulting from early gas trapping. As mentioned in Rhodes et al. (2016) and as confirmed by our study, it is important for paleoclimatic studies to avoid interpreting such abnormal values as fast atmospheric events.

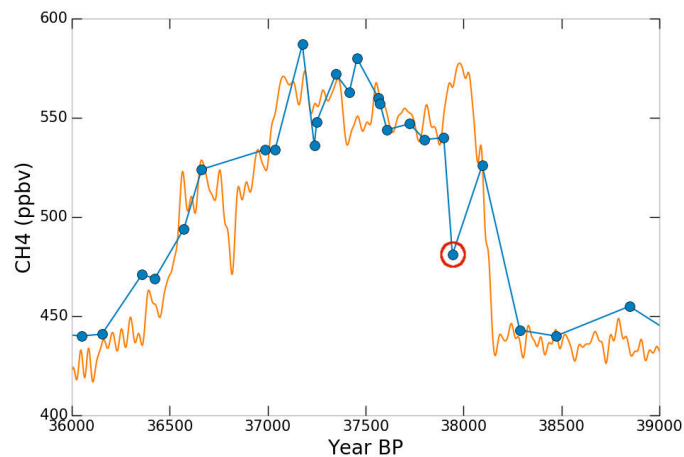


Figure 5.7 – Discrete EDC methane record (blue) and continuous WDC methane record (orange). The WDC record was put on the GICC05 timescale, and then shifted by 250yr to improve matching. We suggest that the circled point corresponds to a layered trapping artifact.

However, continuous flow analysis may not always allow us to distinguish between layering artifacts and the chronologically ordered signal. The deep parts of ice cores with low accumulation and high thinning are of particular interest in paleoclimatology since they enclose very old gases (Loulergue et al., 2008; Lüthi et al., 2008). However, with a strong thinning, the width of abnormal layers may shrink below the spatial resolution limit of analytical systems. In such a case, an average mixing ratio over several layers is measured. Since layered trapping artifacts are unevenly distributed in terms of sign, they bias the measured average signal. In the very simple case of a record with artifacts that are all negatively orientated, cover 15% of the ice core, and all reach 50ppbv, this bias is about -7 ppbv. In the case of records with lower accumulation or stronger methane variations the bias will be even more important. The development of very high-resolution gas measurement techniques thus offers important perspectives for analyzing the deepest part of ice cores. In intermediate situ-

ations in which anomalous layers could be distinguished but a high-accumulation record is not available (before the last glacial-interglacial cycle), the effect of smoothing is more difficult to constrain, but the presence of layered trapping artifacts is in itself an indication that some smoothing may occur because layered trapping occurs only under fast atmospheric change conditions.

5.2.7 Conclusions

We presented the first very high-resolution record of methane in an ice core sequence formed under very low-accumulation-rate conditions. It covers the gas record of Dansgaard-Oeschger event 17, chosen for its abrupt atmospheric methane changes on a similar timescale as gas trapping.

The continuous flow analysis system, optimized to reduce gas mixing, allowed us to reveal numerous centimeter-scale methane concentration anomalies. Positive anomalies affecting both the methane and carbon monoxide records were attributed to kerosene contamination and discarded. The remaining anomalies are unevenly distributed, a few centimeters wide and mostly negatively oriented with dips as low as -50 ppbv. The anomalies occur only during time periods of fast atmospheric methane variability. The main characteristics of the size and distribution of the anomalies could be reproduced with a simple model based on relating realistic firn density anomalies to early or (to a lesser extent) late trapping. Such layered trapping anomalies may be confused with the climatic signal in discrete climate records or bias the signal if too narrow to be detected by a CFA system (e.g., under the high-thinning conditions of the deep part of ice cores). It is important for future paleoclimatic studies not to interpret those abrupt variations as fast chronologically ordered atmospheric variations. Further use of high-resolution continuous analysis will allow us to discriminate layered trapping artifacts and to better identify their statistical characteristics. Moreover, the sign of the trapping artifacts is not random: some sections of the record display only positive or negative artifacts. Thus, simple averaging would result in a systematic bias of the signal. Hence, we developed a cleaning algorithm aiming at minimizing this bias.

After removing the centimeter-scale anomalies, the remaining Vostok methane signal is distinctly smoother than the WDC record (Rhodes et al., 2015). The snow accumulation rate

being more than 1 order of magnitude higher at WDC than at Vostok, the WDC signal contains higher-frequency features. The comparison of the two signals opens the possibility to estimate gas age distributions for conditions of the East Antarctic plateau during the last glacial period, which have no modern analogue. For the DO-17 event at Vostok, the resulting gas age distribution is narrower than expected from a comparison with modern firns (Köhler et al., 2011; Witrant et al., 2012). It may be due to an incorrect prediction of gas trapping by firn models and/or an incorrect extrapolation of the firn behavior to very low-temperature and low-accumulation conditions. The apparently similar smoothing at Vostok under DO-17 and present conditions contradicts the expected primary effect of temperature and accumulation rate: lower temperature and accumulation rates induce a longer gas trapping duration and thus a stronger smoothing. On the other hand, Mitchell et al. (2015) point out the lack of firn layering representation in most firn models and conclude that firn layering narrows gas age distribution in ice. From a paleoclimatic point of view, ice cores with the lowest accumulations contain very old gases. The smoothing under glacial conditions being less important than expected implies that atmospheric information on a shorter timescale than previously expected might be retrieved. However, similar measurements need to be performed on other low-accumulation records, to confirm our results for different sites and/or periods. For the DO-17 event at Vostok, multi-centennial atmospheric variations are still accessible in the record. Further comparisons of high- and low-accumulation records of the last glacial cycle will allow us to better constrain the relationship between ice cores and atmospheric gas signals, even with no modern analogue conditions.

5.2.8 Supplementary Material

5.2.8.1 Calibration of methane measurements

Calibration of SARA on NOAA2004 scale

The laser spectrometer used for the continuous methane measurements (SARA) was calibrated against the NOAA2004 scale (Dlugokencky et al., 2005) before starting the ice core analyzes. Three calibrated standard gases of known methane mixing ratios, listed Table 5.3, were measured with the SARA instrument. We derived a linear relationship between measured and calibrated mixing ratios over the range of 361 to 1790ppbv, with a coefficient of determination $R = 0.9999993$. The data and regression line are displayed Fig. 5.8. This correction was applied to the SARA Vostok 4G-2 measurements.

Table 5.3 – Calibrated and measured methane mixing ratios of Scott Marrin Inc. standard gases.

Gas Reference	Calibrated value (pbbv)	Measured value (pbbv)
CB09722	703.90	695.5
CB09752	1789.42	1775.9
CB09754	360.09	355.3

Correction for methane solubility

In the measurement line, once the ice core is melted, the liberated gases dissolve in the melt water. However, methane has a higher solubility than oxygen or nitrogen, and it follows that CH₄ dissolves preferentially, leading to reduced methane mixing ratios in the extracted air reaching the SARA spectrometer. The solubility correction was evaluated by comparing the Vostok signal with WAIS Divide ice core (WDC) data: a CFA record already corrected for solubility effects (Rhodes et al., 2015). The solubility factor was estimated by comparing the mean concentration over the plateau preceding the DO-17 event, unaffected by smoothing. This corresponds to a depth interval from 920 to 931m in the Vostok ice core. The resulting solubility correction coefficient of 1.125, consistent with the previous estimate for our CFA system, was applied to the whole Vostok dataset.

5.2.8.2 Quantification of the smoothing by the CFA system

Due to mixing and dead volumes, the CFA system introduces a smoothing of the gas signals. Using the method described in Stowasser et al. (2012), we measured the switch between two mixes of deionized water and standard gas (Fig. S2, left panel). It allowed us to determine the step response of the CFA system, which is not instantaneous but spreads over time. The observed step response was fitted using the cumulative density function of a log-normal distribution. This log-normal distribution (Fig. S2, middle panel) can be further used as a Green's function, or impulse response of the CFA system, to estimate the smoothing of other signals such as the simulated density-related concentration anomalies in Section 5.2.4.3 of the article. Finally, the Green's function can be used to derive the frequency response of the system using Fourier transform, that is to say the attenuation factor (also referred to as a gain) experienced by a sine signal depending on its frequency/period/wavelength.

A cut-off wavelength can be defined as the wavelength of a sine signal experiencing a 50% attenuation in amplitude. For our CFA system with a melting rate of 3.8cm.min⁻¹, the cut-

off wavelength is about 2.4cm. It is important to note that this cut-off is defined for sine signals, and therefore cannot be directly applied to other types of signals. For instance, a square spike with a width of 2.4cm will not be attenuated by 50%. Indeed, it has a low-frequency rich harmonic content and thus undergoes a weaker attenuation. This explains why layered trapping artifacts with widths slightly below the cut-off wavelength used in Section 5.2.4.3 of the article are weakly damped in the CFA signal.

5.2.8.3 Kerosene contamination

As explained in Section 5.2.3.1 of the article, traces of kerosene producing iridescent colors and a strong smell were occasionally detected in the meltwater. Concomitant increases in CH₄ and CO were assumed to result from kerosene contaminations. An example of such typical simultaneous increases is displayed on Fig. 5.10. Even though the origin of these kerosene contaminations is not clear, they might come from cracks observed in the CFA sticks as seen in Fig. 5.11.

5.2.8.4 Thin sections of the Vostok 4G-2 core

Four thin sections were prepared over a region of the Vostok 4G-2 ice core which shows layered trapping artifacts. The crystallographic orientations of grains were measured using an Automatic Texture Analyzer (Wilson et al., 2003; Peternell et al., 2010). The images were then segmented to visualize grain boundaries, using a high-pass filter and a threshold technique. Grain boundaries were enhanced with cycles of dilate/erode. The segmented thin sections are displayed on Fig. 5.12. The numbers of intersections between grain boundaries and constant depth lines were computed as a metric for local grain size. However, the thin sections displayed various degrees of noise, impacting the number of intersection counted. To reduce the influence of noise, we normalized the numbers of intersections of each section by dividing them by the mean number of intersections of the whole thin section. This did not affect the interpretation of our results, as we were searching for local variations of grain size rather than absolute size values. Figure 5.13 shows the methane record together with the normalized number of intersections around 902m depth. The methane record presents two clear layered trapping artifacts, marked by red dots on Fig. 5.13. However, the grain size metric does not show a correlation with the two anomalous layers.

5.2.8.5 Sensitivity of the layered trapping model

In Fig. 5.14 to 5.17, black solid lines correspond to normal trapping. Blue and yellow areas correspond to the expected extent of layering artifacts, respectively for early and late closure. Spikes correspond to the artifacts for a stochastic realization of layered trapping with CFA smoothing. Blue spikes show early closure artifacts and yellow spikes late closure artifacts.

5.2.8.6 AICC2012 gas chronology over the DO-017 event

Figure 5.18 presents the comparison between the WDC and Vostok methane records of the DO-17 event, using respectively the WD2014 and AICC2012 chronologies (Bazin et al., 2013; Veres et al., 2013; Buizert et al., 2015). Two dating method features explain the differences with Fig. 5 of the article. First the WD2014 chronology is scaled by a factor 1.0063 with respect to the GICC05 chronology (with present defined as 1950), used in the AICC2012 synchronization (Buizert et al., 2015). Second the variability of AICC2012 Δ Age values shown in Fig. 2 of the article affect the duration of the events in the Vostok ice core.

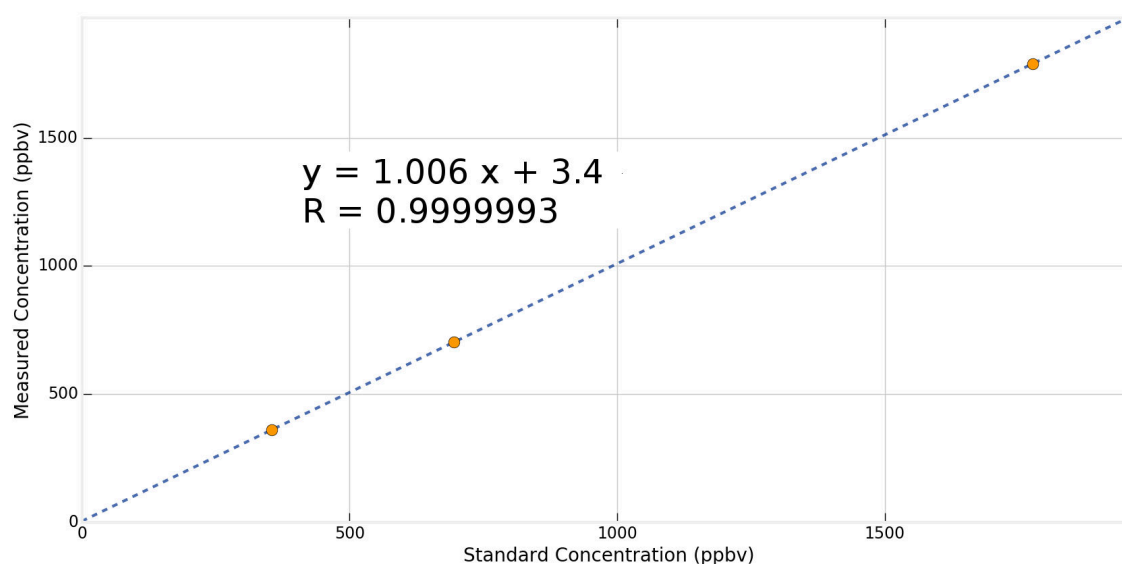


Figure 5.8 – Linear regression between NOAA certified methane mixing ratios and SARA measurements. The blue dotted line is the regression, and the orange dots are measurements.

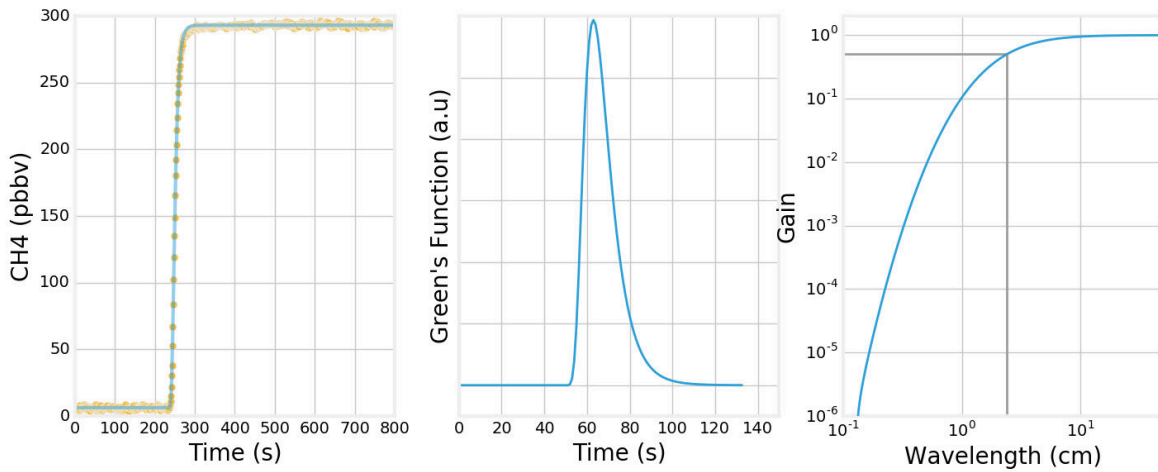


Figure 5.9 – Left panel: step response of the CFA system. Orange dots: measurement points. In blue: fit by the cumulative density function of a log-normal law. Middle panel: Green's Function of the CFA system approximated by a log normal law. Right panel: Gain of the CFA system against the wavelength of sine signals. Gray lines correspond to the cut-off wavelength and a 50% attenuation.

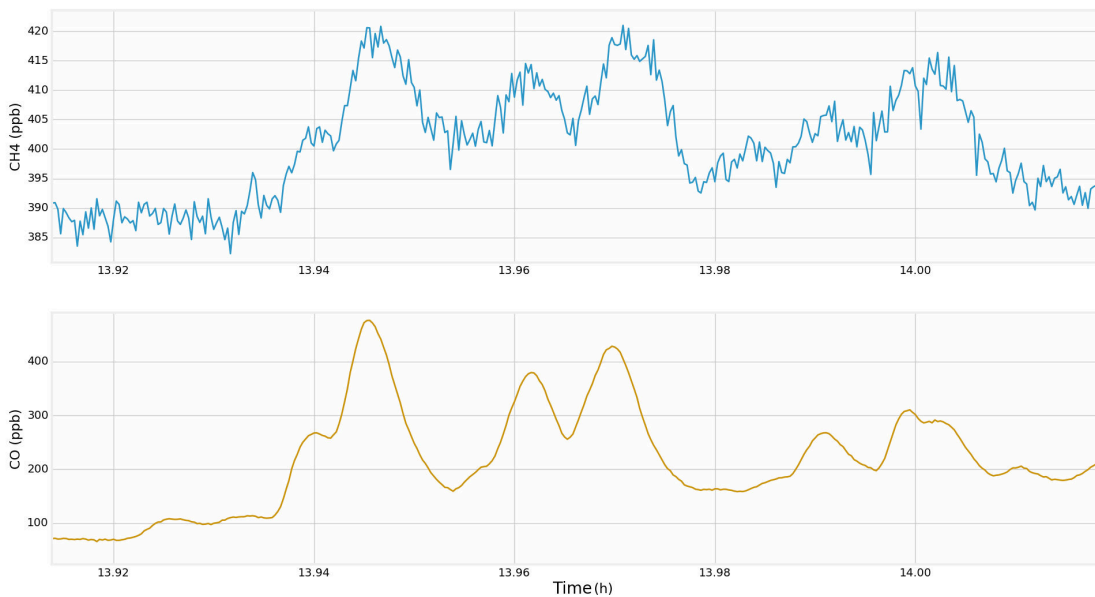


Figure 5.10 – Example of concomitant increases in CH₄ and CO attributed to kerosene contamination. Methane (in blue) and carbon monoxide (in yellow) records display simultaneous fast variability. The x-scale represents the measurement time. The length of ice melted in the data shown is about 25cm.

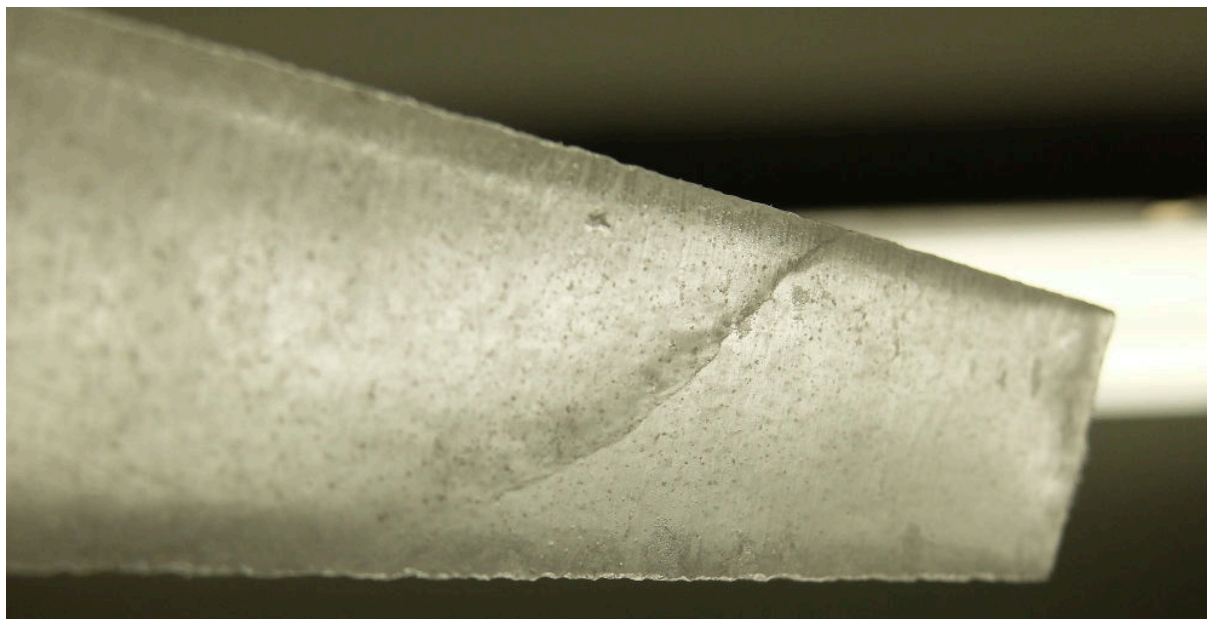


Figure 5.11 – Pictures of a CFA stick. A large crack is visible in the middle, as well as relaxation cavities. Visual observations did not allow us to detect a variability in the ice aspect (e.g. cloudy bands, small fractures, or variability in the size and distribution of cavities) that could be associated with methane concentration anomalies.

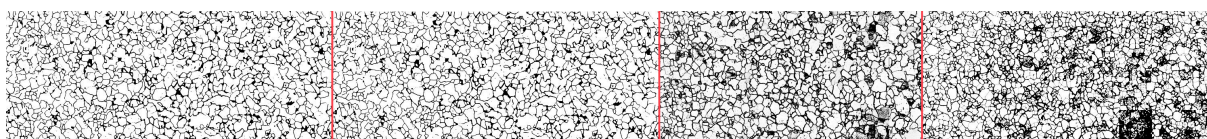


Figure 5.12 – Segmented thin sections with grain boundaries shown in black. Individual thin sections are separated by red lines. The shallowest thin section is on the left. The total length of the four thin sections is about 40cm

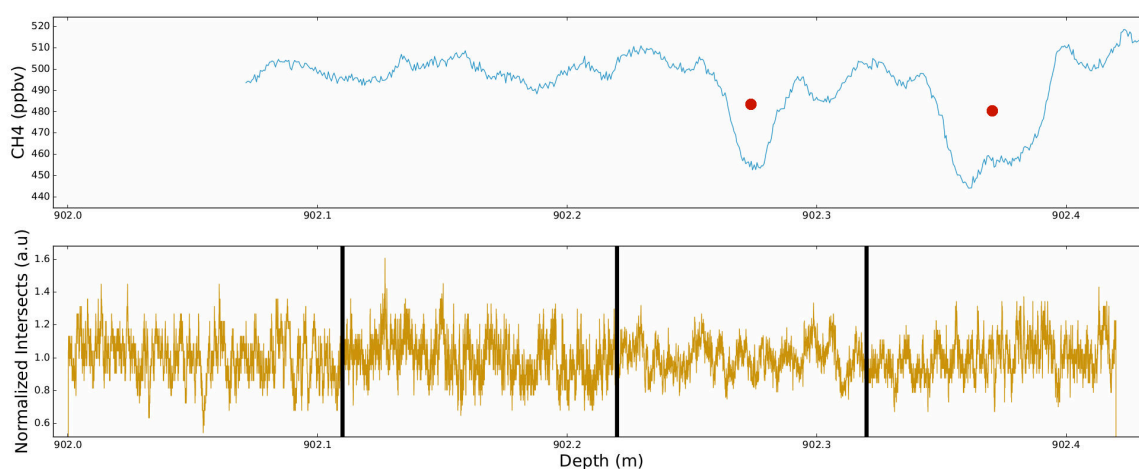


Figure 5.13 – Top panel: continuous methane measurements with two anomalous layers marked by red dots. Bottom panel: normalized number of intersections along the thin sections. The different thin sections are separated by vertical black lines.

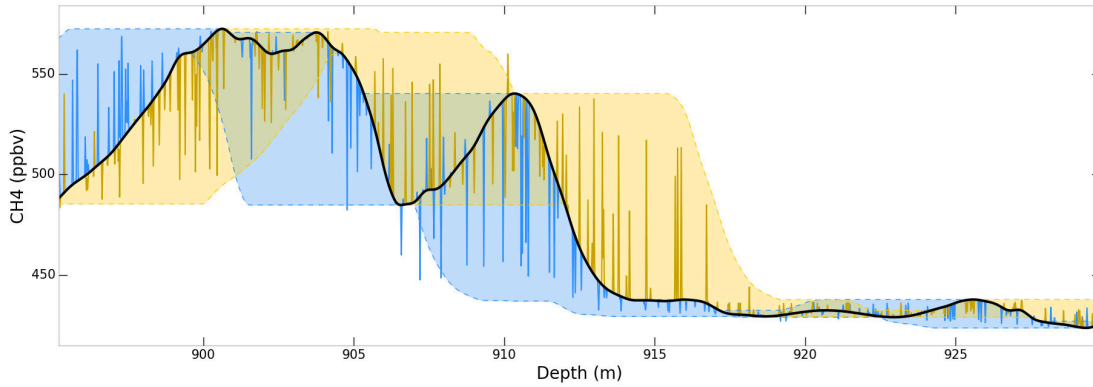


Figure 5.14 – Layered trapping model without limitation for late closure age anomalies. Both shaded areas correspond to the range of concentration anomalies for early and late closure anomalies up to two standard deviations (depth anomaly of 5m corresponding to an age anomaly of 415yr).

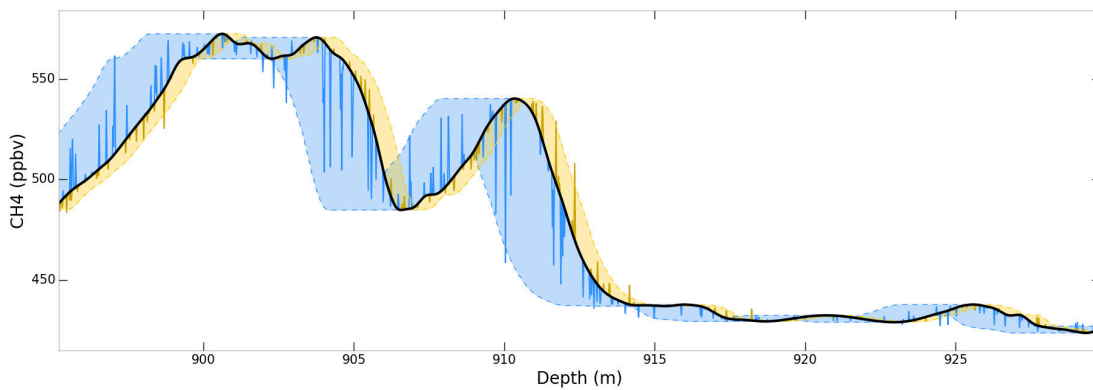


Figure 5.15 – Layered trapping model with density anomalies standard deviation set to $3\text{kg}\cdot\text{m}^{-3}$ and $d\rho/dz$ set to $2.5\text{kg}\cdot\text{m}^{-4}$. Blue shaded areas correspond to the range of concentration anomalies for early closure anomalies up to two standard deviations (depth anomaly of 2.4m corresponding to an age anomaly of 200yr). Yellow shaded areas correspond to late closure anomalies with 25% of the early closure extent (depth anomaly of 0.6m corresponding to an age anomaly of 50yr).

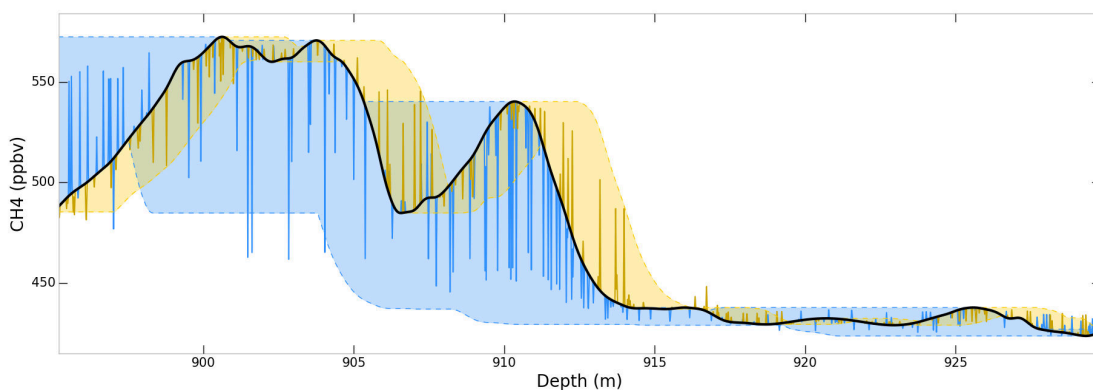


Figure 5.16 – Layered trapping model with density anomalies standard deviation set to $7\text{kg}\cdot\text{m}^{-3}$ and $d\rho/dz$ set to $1.7\text{kg}\cdot\text{m}^{-4}$. Blue shaded areas correspond to the range of concentration anomalies for early closure anomalies up to two standard deviations (depth anomaly of 8.2m corresponding to an age anomaly of 684yr). Yellow shaded areas correspond to late closure anomalies with 25% of the early closure extent (depth anomaly of 2.1m corresponding to an age anomaly of 171yr).

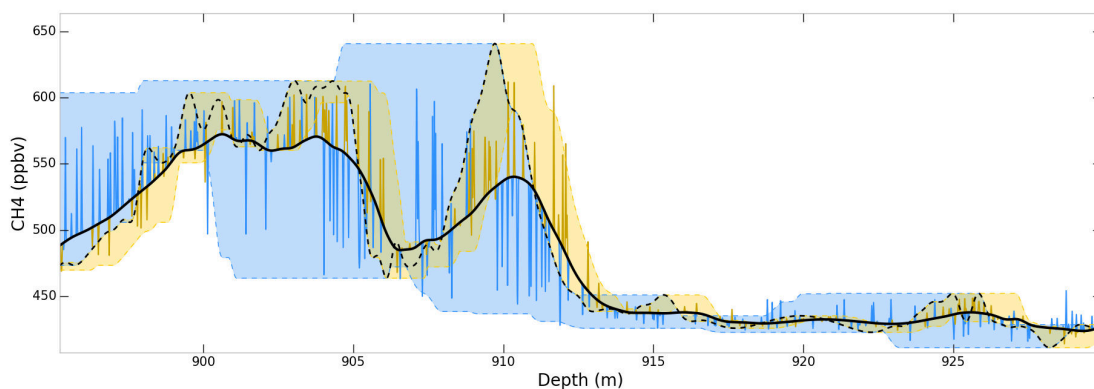


Figure 5.17 – Layered trapping model with anomalous layers undergoing the WDC gas age distribution. The dashed black line corresponds to the WDC signal on the Vostok depth scale. Blue shaded areas correspond to the range of concentration anomalies for early closure anomalies up to two standard deviations (depth anomaly of 5m corresponding to an age anomaly of 415yr. Yellow shaded areas correspond to late closure anomalies with 25% of the early closure extent (depth anomaly of 1.25m corresponding to an age anomaly of 104yr).

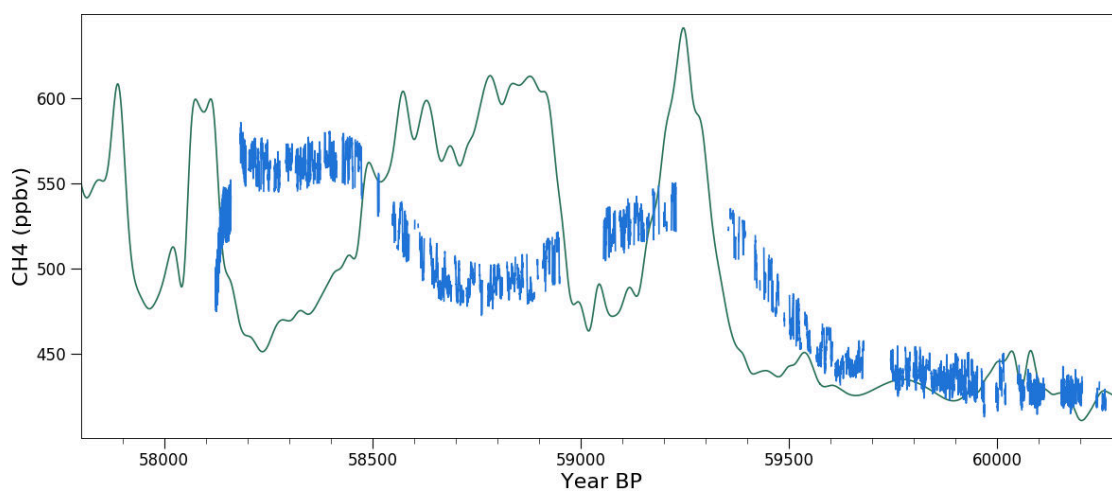


Figure 5.18 – In green: WDC methane record with the WDC2014 gas chronology from Buizert et al. (2015). In blue: Vostok methane record with the AICC2012 gas chronology (Bazin et al., 2013; Veres et al., 2013).

5.3 Estimation of gas record alteration in very low accumulation ice cores

Kévin Fourteau¹, Patricia Martinerie¹, Xavier Faïn¹, Alexey A. Ekaykin², and Jérôme Chappellaz¹, Vladimir Ya. Lipenkov²

[1] Univ. Grenoble Alpes, CNRS, IRD, Grenoble INP, IGE, 38000 Grenoble, France

[2] Climate and Environmental Research Laboratory, Arctic and Antarctic Research Institute, St. Petersburg, 199397, Russia

Abstract

We measured the methane mixing ratios of enclosed air in five ice core sections drilled on the East Antarctic plateau. Our work aims to study two effects that affect the recorded gas concentrations in ice cores: layered gas trapping artifacts and firn smoothing. Layered gas trapping artifacts are due to the heterogeneous nature of polar firn, where some strata might close early and trap abnormally old gases that appear as spurious values during measurements. The smoothing is due to the combined effects of diffusive mixing in the firn and the progressive closure of bubbles at the bottom of the firn. Consequently, the gases trapped in a given ice layer span a distribution of ages that acts similarly to a moving average, removing the fast variability from the record. We focus on the study of East Antarctic plateau ice cores, as these low accumulation ice cores are particularly affected by both layering and smoothing. Our results suggest that presence of layering artifacts in deep ice cores is linked with the chemical content of the ice. We use high resolution methane data to parametrize a simple model reproducing the layered gas trapping artifacts for different accumulation conditions typical of the East Antarctic plateau. We also use the high resolution methane measurements to estimate the gas age distributions of the enclosed air in the five newly measured ice core sections. It appears that for accumulations below 2cm ie yr^{-1} (ice equivalent) the gas records experience nearly the same degree of smoothing. We therefore propose to use a single gas age distribution to represent the firn smoothing observed in the glacial ice cores of the East Antarctic plateau. Finally, we used the layered gas trapping model and the estimation of glacial firn smoothing to estimate their potential impacts on a million-and-a-half years old ice core from the East Antarctic plateau. Our results indicate that layering artifacts are no longer individually resolved in the case of very thinned ice near the bedrock. They nonetheless contribute to slight biases of the measured signal (less than 10ppbv and

0.5ppmv in the case of methane and carbon dioxide). However, these biases are small compared to the dampening experienced by the record due to firn smoothing.

5.3.1 Introduction

The East Antarctic plateau is characterized by low temperatures and low accumulation rates. The low precipitations create the conditions for the presence of very old ice near the domes of the region (Raymond, 1983; Martín and Gudmundsson, 2012). Thanks to this particularity, the ice core retrieved at Dome C, within the EPICA project, has been dated back to 800,000yr in the past (Bazin et al., 2013; Veres et al., 2013). The analysis of the ice, and of the bubbles within, has made possible the reconstruction of the Earth past temperatures and atmospheric concentrations in major greenhouse gases over the last eight glacial cycles (Lüthi et al., 2008; Loulergue et al., 2008). In turn, this knowledge helps us to better understand the Earth climate system and its past and future evolutions (Shakun et al., 2012). Furthermore, there is currently an active search for ice older than one-and-a-half million years with the International Partnership in Ice Core Sciences oldest ice core project. Most of the potential drilling sites for such old ice are located on the East Antarctic plateau (Fischer et al., 2013; Van Liefferinge and Pattyn, 2013; Passalacqua et al., 2018). Within the next decade, we might therefore expect the retrieval of new deep ice cores at low accumulation drilling sites of East Antarctica, with ages reaching back to one-and-a-half million years or more.

However, the gas records in low accumulation ice cores should not be directly interpreted as images of the atmospheric history. Indeed, due to the very process of gas trapping in the ice, two distinct effects might create discrepancies between the actual atmosphere's history and its imprint in the ice. The first one is due to the heterogeneous structure of the firn when transforming into airtight ice. The overall structure of the firn column is characterized by a progressive increase in density with depth, associated with the constriction of the interstitial pore network (Stauffer et al., 1985; Arnaud et al., 2000; Salamatin et al., 2009). At high enough densities, pores in the firn pinch and isolate the interstitial air from the atmosphere (Stauffer et al., 1985). However, firn is a highly stratified medium (Freitag et al., 2004; Fujita et al., 2009; Hörhold et al., 2012; Gregory et al., 2014) and some of the strata might experience early (respectively late) pore closure when compared to the rest of the firn (Etheridge

et al., 1992; Martinerie et al., 1992). Consequently, abnormal strata might enclose older (respectively younger) air than their immediate surroundings, creating age irregularities in the gas record (Mitchell et al., 2015; Rhodes et al., 2016). In turn, the irregularities appear as spurious values in the measured gas record (Rhodes et al., 2016; Fourteau et al., 2017). These anomalies have been referred to as layered gas trapping artifacts and do not reflect actual atmospheric variations. The second effect that creates differences between the atmosphere and its imprint in the ice, is due to the combination of diffusive air mixing in the firn (Schwander, 1989) and the progressive closure of pores in a firn stratum (Schwander et al., 1993; Mitchell et al., 2015). Consequently, the air enclosed in a given ice layer does not originate from a single point in time, but is rather characterized by a continuous age distribution covering tens to hundreds of years (Schwander et al., 1988; Schwander et al., 1993; Rommelaere et al., 1997). Therefore, the concentration measured in an ice stratum is an average of atmospheric concentrations over a period of time. This effect acts as a moving average, removing the variability from the record, and has therefore been referred to as the smoothing effect (Spahni et al., 2003; Joos and Spahni, 2008; Köhler et al., 2011; Ahn et al., 2014; Fourteau et al., 2017). The degree of alteration between the atmosphere and its recording is strongly dependent on the local precipitation rate, with low accumulation ice cores being particularly affected both in terms of gas layered artifacts (Rhodes et al., 2016; Fourteau et al., 2017) and in terms of smoothing (Spahni et al., 2003; Joos and Spahni, 2008; Köhler et al., 2011; Ahn et al., 2014; Fourteau et al., 2017).

In order to properly evaluate the composition of past atmospheres based on the gas records in polar ice cores, it is thus necessary to characterize the specificities of those two effects. For the smoothing, the gas age distributions can be calculated, in the case of modern ice cores, using gas trapping models parameterized by firn pumping and pore closure data (Buizert et al., 2012; Witrant et al., 2012). However, to estimate the gas age distribution in bubbles it is necessary to use a closed porosity profile in firn. Such closed porosity profiles are associated with large uncertainties (Schaller et al., 2017). Moreover, a specific problem arises in the case of glacial ice cores from East Antarctica. They were formed under very low precipitation rates, below $2\text{cm}\cdot\text{ie}\cdot\text{yr}^{-1}$ (ice equivalent, Veres et al., 2013; Bazin et al., 2013), and temperatures that have no known equivalent nowadays. Thus, gas trapping models cannot be constrained and used to estimate the gas age distributions responsible for smoothing during glacial periods. Concerning layered gas trapping, it originates from firn hetero-

geneities and is therefore a stochastic process. Moreover, current gas trapping models do not fully represent the centimeter scale variability of the firn. The proper modelling of layered gas trapping is thus limited by the lack of knowledge of glacial firn heterogeneities and the difficulty to model gas trapping in a layered medium. [Fourteau et al. \(2017\)](#) proposed an empirical model to reproduce the artifacts observed in the Vostok ice core during the Dansgaard-Oeschger event 17. However, this model has only been applied to this particular event and might not be directly applicable for different periods and conditions.

For this work, we analyzed methane concentrations in five ice core sections from the East Antarctic plateau. These sections cover accumulation and temperature conditions representative of East Antarctica for both the glacial and inter-glacial periods. The new data are used to parameterize a revised version of the gas layered trapping model proposed by [Fourteau et al. \(2017\)](#). Our goal is to render this model applicable to a range of accumulation rates characteristic of glacial and inter-glacial conditions on the East Antarctic plateau. Then, the gas age distributions for each of the five records are estimated by comparing the low accumulation records with much higher accumulation records ([Fourteau et al., 2017](#)). Finally, we simulate gas trapping in a hypothetical million-and-a-half years old and thinned ice core, including gas layering artifacts. We then simulate the process of methane measurements using a continuous flow analysis system, and of carbon dioxide measurements using a discrete method. The synthetic signals are finally compared to the original atmospheric reference to quantify the deterioration of atmospheric information.

5.3.2 Methods

5.3.2.1 Choice and description of the studied ice cores

The newly measured ice core sections originate from the East Antarctic sites of Vostok, Dome C, and Lock-In. The three sites are displayed on a map in Figure 5.19. The five measured sections correspond to time periods where high resolution methane measurements from high-accumulation ice cores are also available.

Modern Lock-In ice core:

The first studied ice core section is the upper part of the Lock-In ice core. The site of Lock-In

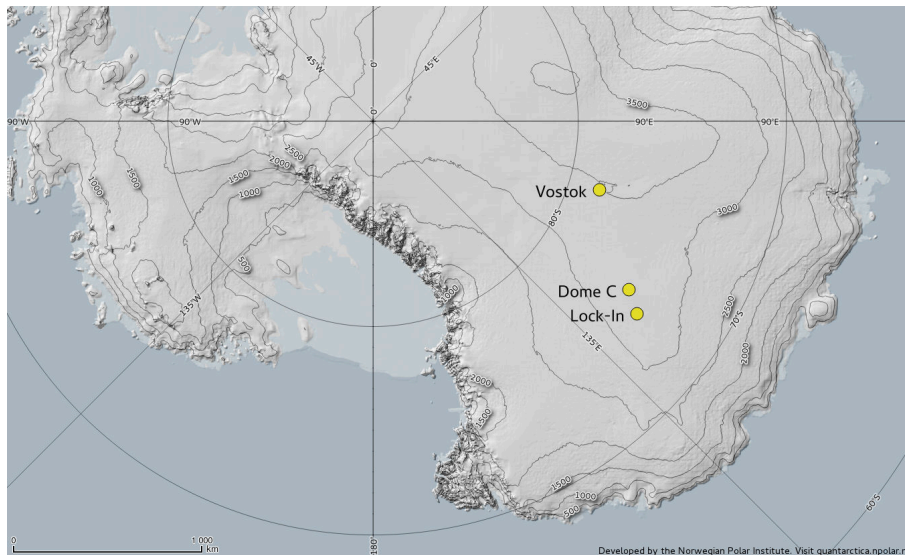


Figure 5.19 – Map of the East Antarctic plateau with the sites of Lock-In, Dome C, and Vostok shown (made with the Quantartica package).

is located 136km away from Dome C, towards the coast (3209m above sea level, coordinates 74°08.310' S, 126°09.510' E). The local accumulation is of 3.9cm.ie.yr⁻¹ (Yeung et al., in press.). About 80m of ice was analyzed for methane, ranging from 116m near the firn-ice transition to 200m depth. The last firn air pumping during drilling operation was conducted at 108.3m depth. The gas record ranges from 500 to 3000yrBP (Before Present, with present defined as 1950 in this article).

Modern Dome C ice core:

A shallow ice core from Dome C was analyzed for depths ranging from 108 to 178m. Similar to Lock-In this section corresponds to ages ranging from 500 to 3000yrBP, but is characterized by a lower accumulation rate of 2.7cm.ie.yr⁻¹ (Gautier et al., 2016).

Holocene Dome C ice core:

Ice from the second drilling of the EPICA Dome C ice core (referred to as EDC99 hereafter) was measured from depth 312 to 338m. According to the AICC2012 chronology, the gas ages range from 7950 to 9000yrBP, with an average accumulation of 3.1cm.ie.yr⁻¹ (Bazin et al., 2013; Veres et al., 2013). This period includes the 8.2ka cold event (Thomas et al., 2007), notably characterized by a sharp decrease in global methane concentrations (Spahni et al., 2003; Ahn et al., 2014).

DO6-9 Dome C ice core:

A section from the first drilling of the EPICA Dome C ice core (referred to as EDC96 hereafter) was analyzed for depths ranging from 690 to 780m. The AICC2012 chronology indicates gas ages covering the period 33000 to 41000yrBP, and an average accumulation rate of $1.5\text{cm}\cdot\text{ie}\cdot\text{yr}^{-1}$ (Bazin et al., 2013; Veres et al., 2013). The Dansgaard-Oeschger (DO) events 6 to 9 are included in this gas record (Huber et al., 2006b; Chappellaz et al., 2013).

DO21 Vostok ice core:

The last analyzed section originates from the Vostok 4G ice core, for depths between 1249 and 1290m. The expected gas ages span from 84000 to 86500yrBP, with an average accumulation of $1.5\text{cm}\cdot\text{ie}\cdot\text{yr}^{-1}$ (Bazin et al., 2013; Veres et al., 2013). This section was chosen as it includes the record of the DO21 event, the fastest methane increase of the last glacial period (Chappellaz et al., 2013).

5.3.2.2 High-resolution methane measurements

The five ice core sections were analyzed for methane concentrations using a Continuous Flow Analysis (CFA) system, including a laser spectrometer based on optical-feedback cavity enhanced absorption spectroscopy (OF-CEAS; Morville et al., 2005), at the Institut des Géosciences de l'Environnement (IGE), Grenoble, France. The IGE's CFA apparatus and data processing procedure are described in greater details in Fourteau et al. (2017). The five ice core sections were melted at an average rate of $3.6\text{cm}\cdot\text{min}^{-1}$, which allows one to access centimeter scale variations in the methane record. However, the measured concentrations are affected by the preferential dissolution of methane in the meltwater (Chappellaz et al., 2013; Rhodes et al., 2013). It is therefore necessary to apply a correction factor to account for this effect. However, this factor is a priori not known and potentially ice core dependent. The methodology for correcting for methane dissolution will be addressed in Section 5.3.3.1 below.

5.3.3 Results and Discussion

5.3.3.1 Correction for methane dissolution

In order to correct the measured mixing ratios for the preferential dissolution of methane in water, a correction factor is applied to the data to raise them to absolute values (Chappellaz

et al., 2013; Rhodes et al., 2013). One way to estimate this correction factor is to compare the dissolution-affected CFA data with records that are already on an absolute scale.

The discrete methane measurements from the high accumulation WAIS Divide (WD) ice core published by Mitchell et al. (2013) cover the period from 500 to 3000yrBP. We therefore use the WD data to estimate the correction factors for the modern sections of Lock-In and Dome C.

Loulergue et al. (2008) performed discrete methane measurements in the Dome C EPICA ice core, that include the 8.2ka, DO6 to 9, and DO21 events. We use these discrete methane data to correct our CFA data for the dissolution, for the Holocene and DO6-9 Dome C ice core sections and for the DO21 event section in Vostok.

Note that in the case where our CFA data and the absolute scale measurements do not originate from the same ice core, the match between the datasets are performed on sections with low methane variability to reduce the influence of firn smoothing. The signals after correction for the dissolution of methane are displayed in light blue in the upper panels of the Figures 5.20 to 5.24. The black superimposed curves in Figures 5.22 to 5.24 correspond to the part of the signal cleaned for layering artifacts, as described in Section 5.3.3.3.

5.3.3.2 Atmospheric references

In the later Sections 5.3.3.3 and 5.3.3.4 of the article, weakly smoothed methane gas records will be used as atmospheric references to study gas trapping in low accumulation ice cores. As it is important that these gas records contain enough fast variability to be used as atmospheric references, we use methane gas records from much higher-accumulation ice cores (Fourteau et al., 2017).

For the modern Lock-In and Dome C sections, we use the discrete measurements from the WD ice core, also used for correcting the methane preferential dissolution (Mitchell et al., 2013). For the Holocene section of EDC99, we used CFA data from an ice core drilled at Fletcher promontory as the atmospheric reference (Xavier Faïn, personal communication). For the DO6-9 events section in the EDC96 ice core, we use high-resolution CFA data from the WD ice core (Rhodes et al., 2015). The WD gas record dating has been made consistent with the AICC2012 and GICC chronologies following Buizert et al. (2015). Finally, the atmospheric reference used for the Vostok DO21 period is the NEEM CFA record published by Chappellaz et al. (2013), whose gaps in the data have been filled with a method similar to the one introduced by Witrant and Martinerie (2013). However, the Vostok and NEEM sites

are in different hemispheres and it is necessary to take into account the inter-hemispheric methane gradient between the two sites. We evaluated this inter-hemispheric gradient to be at 30ppbv for the DO21 period. This value is in line with the work of Dällenbach *et al.* (2000). Yet, it remains possible that the inter-hemispheric gradient is not constant during this period of global methane rise. The use of a high resolution and weakly smoothed Antarctic record as the atmospheric reference would resolve this problem, but such a record is not available. The atmospheric references are displayed as orange dashed lines in the lower panels of Figure 5.20 to 5.24.

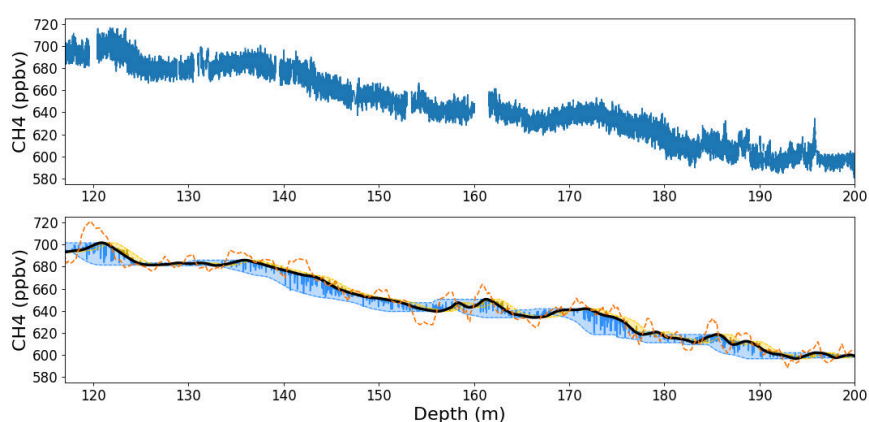


Figure 5.20 – Measured and modeled modern Lock-In methane profile. Upper panel: High resolution methane measurements in light blue. Lower panel: Modeled layering artifacts. The black curve is the expected signal without artifacts. The blue and yellow spikes respectively are randomly distributed early and late closure artifacts. The blue and yellow shaded areas respectively correspond to the range of early and late artifacts with density anomalies up to two standard deviations. The dashed orange curve is the record used as the atmospheric reference.

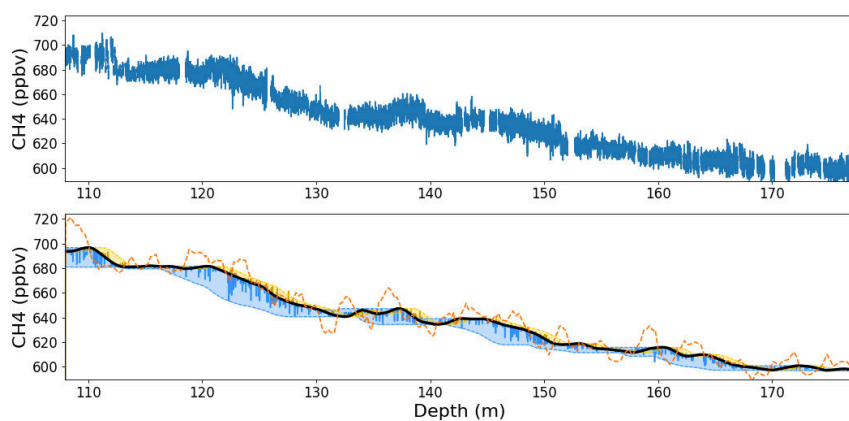


Figure 5.21 – Same as Figure 5.20 for the modern Dome C section.

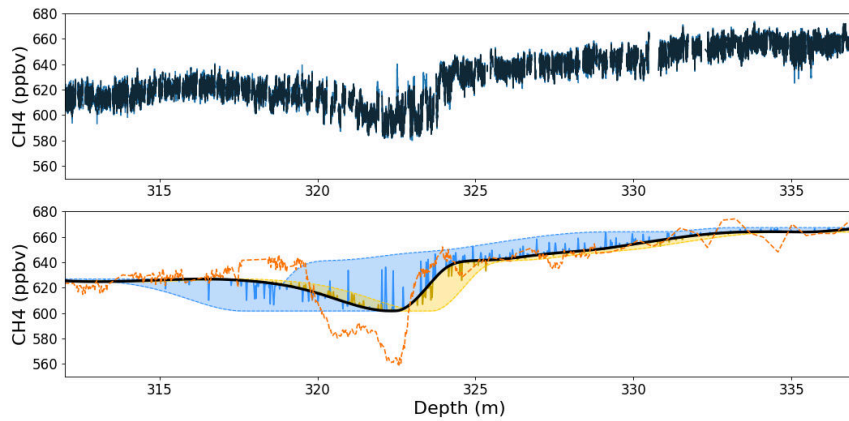


Figure 5.22 – Same as Figure 5.20 for the Holocene EPICA Dome C section. In addition the superimposed black signal in the upper panel shows the data cleaned of layering artifacts

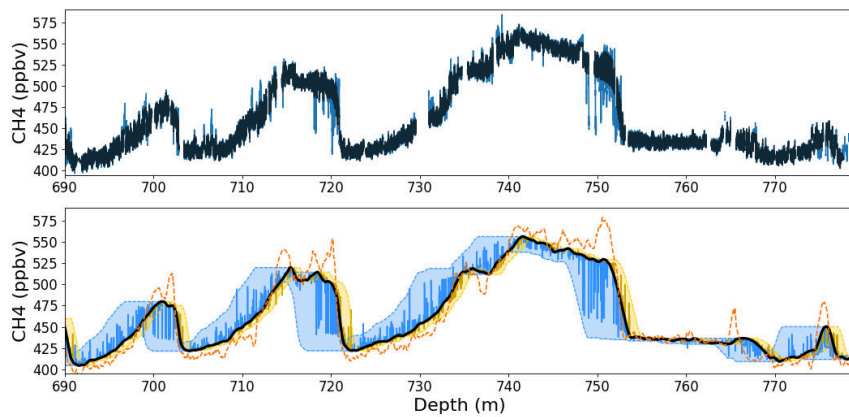


Figure 5.23 – Same as Figure 5.22 for the DO6-9 EPICA Dome C section.

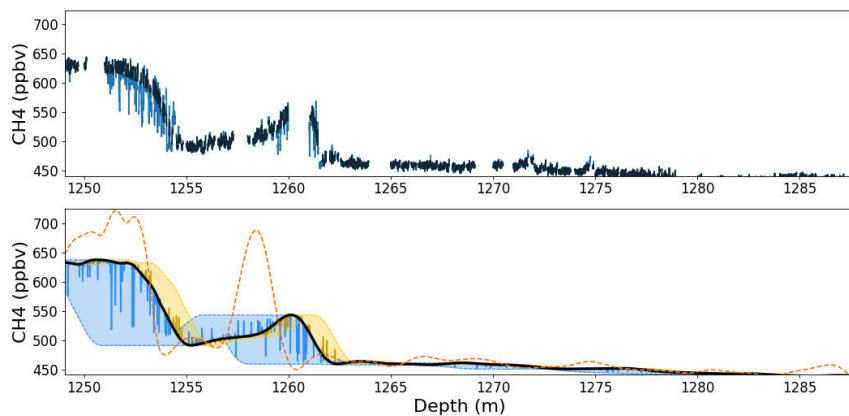


Figure 5.24 – Same as Figure 5.22 for the DO21 Vostok section.

5.3.3.3 Layered trapping artifacts

It has been observed in the high-accumulation firn of DE08 that not all layers close at the same depth (Etheridge et al., 1992), and that the air in summer layers is generally older than in winter layers. Building on this idea, Mitchell et al. (2015) and Rhodes et al. (2016)

proposed that the layering observed at the firn-ice transition induces gas stratigraphic irregularities and age inversions in the record. Rhodes et al. (2016) and Fourteau et al. (2017) used such stratigraphic heterogeneities to explain the observation of sudden variations in high resolution methane records. These abrupt methane variations do not correspond to actual atmospheric variations and have been called layered trapping artifacts, or more simply layering artifacts. The mechanism producing them is that layers closing especially early (or late) contain air older (or younger) than their immediate surroundings. During periods of variations of atmospheric composition, the methane mixing ratios in these layers are thus different than in their surroundings and appear as anomalous values (Rhodes et al., 2016). In accordance with Rhodes et al. (2016) and Fourteau et al. (2017), we observe abrupt variations in the methane records, larger than the analytical noise of ~ 10 ppbv, during periods of variations in atmospheric concentrations. These layering artifacts are notably well marked during the onset of DO events 8 and 21, corresponding to 750 and 1252m depth in the EDC96 and Vostok ice cores, respectively in Figure 5.23 and 5.24. They appear as reduced methane concentration layers near the onset of the DO events, and cannot therefore be explained by contamination issues. The layered trapping artifacts tend to disappear in the absence of marked atmospheric variations. This explains the absence of important layering artifacts in the Lock-In and Dome C modern records (Figures 5.20 and 5.21).

Important late closure artifacts are unusual in methane gas records. These new measurements confirm this observation. Late closure artifacts, that should appear as positive methane anomalies at the onset of the DO events, are almost absent in our measurements. This can be explained by the fact that the surrounding firn layers are already sealed and prevent long distance gas transport, which in turn prevents the late closure layers to enclose young air (Fourteau et al., 2017).

Impact of chemistry on layered gas trapping

The EDC96 methane data suggest a lack of layering artifacts affecting the DO6 event (around the depth 700m in Figure 5.23). We counted only 14 layering artifacts that clearly stand out of the analytical noise on the 20m long section between 695 and 715m. For a comparison, we counted 15 artifacts on the 4m long section from 718 to 722m (DO7 event). These sections are not directly comparable as they are not characterized by the same atmospheric methane variations, but it nonetheless suggests that the upper section of the DO6-9 record shows a lower number of layering artifacts per meter. Previous studies have high-

lighted the role of chemical impurities for the presence of dense strata in polar firn. [Hörhold et al. \(2012\)](#) and [Fujita et al. \(2016\)](#) argue that the presence of ions can soften the firn and facilitate the densification of some strata.

To evaluate the potential impact of ions on layered gas trapping artifacts in the EDC96 methane record, we compared the high resolution methane data with total calcium data measured in the ice phase ([Lambert et al., 2012](#)). We chose to focus on calcium since high resolution data are readily available and [Hörhold et al. \(2012\)](#) observed a correlation between calcium content and the density of firn layers. However, as pointed out by [Hörhold et al. \(2012\)](#) and [Fujita et al. \(2016\)](#), calcium should not be seen as the ion responsible for the preferential densification of firn, but rather as a proxy for the general ionic content. A comparison of the two datasets is shown in Figure 5.25. The depth difference between the EDC96 ice core, in which the methane measurements were performed, and the EDC99 ice core, in which the calcium measurements were performed, was taken into account using volcanic markers ([Parrenin et al., 2012](#)). The calcium data clearly show a transition between two parts: ice below the depth 718m is characterized by relatively high calcium values and a high variability, while ice above 718m is characterized by low calcium values and a low variability. The transition between these two parts corresponds to the high methane plateau of the DO7 event. It also matches with the transition described above between the two regions of large and small numbers of layering artifacts. It therefore appears that the number of significant artifacts (standing out of the analytical noise) is correlated to the variability of calcium concentrations. It is consistent with the mechanisms proposed in the literature: calcium variability is associated with a general ionic concentration variability that creates particularly dense strata in the firn ([Hörhold et al., 2012](#); [Freitag et al., 2013](#); [Fujita et al., 2016](#)). These strata then close in advance and trap young air that appears as layering artifacts ([Rhodes et al., 2016](#); [Fourteau et al., 2017](#)). As the methane and calcium records were measured in two different ice cores, we are not able to quantify the direct link between the presence of layering artifacts and the local calcium concentration.

We then evaluated the calcium levels for the other studied ice core sections. Using the data of [Lambert et al. \(2012\)](#), it appears that the 8.2ka and modern periods of Dome C are characterized by low calcium levels and variability. Similar low calcium levels and variability at Lock-In have been observed by chemistry measurements ([Fourteau et al., 2019](#), submitted to The Cryosphere and presented in Chapter 4). Unfortunately, high resolution chemistry data are not available for Vostok. Assuming that the calcium variability is similar at Dome C and Vostok, the data from [Lambert et al. \(2012\)](#) indicate that the DO21 period displays

low calcium level and variability, while the DO17 period studied by Fourteau et al. (2017) shows high calcium level and variability, similar to the DO7 to 9 period.

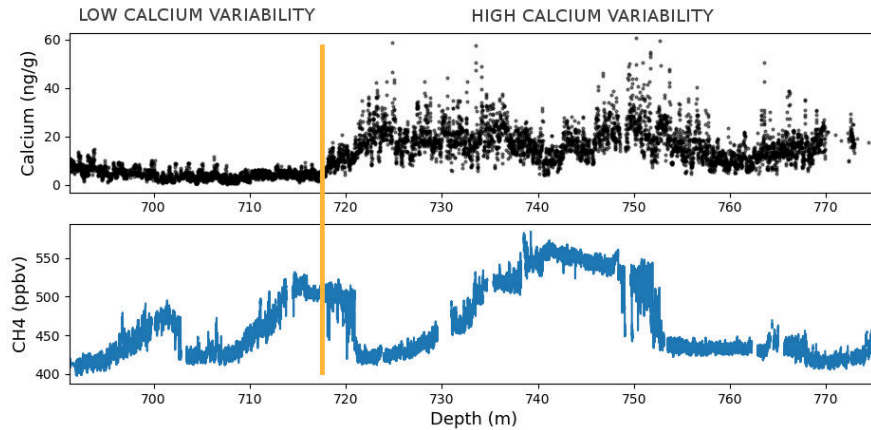


Figure 5.25 – Upper panel: Calcium concentrations measured in the EPICA Dome C ice core section covering the DOs 6 to 9 (Lambert et al., 2012). Lower panel: Methane mixing ratios measured in this study.

Modeling layered trapping artifacts

The ability to model layered gas trapping helps quantifying and predicting its impact on gas records. For this purpose, we revised the simple layered gas trapping model proposed by Fourteau et al. (2017) for the Vostok DO17 section. Our aim is to parametrize the model in order to reproduce the layering artifacts observed in the new five measured sections, as well as in the previously published DO17 section of the Vostok core. This layered trapping model is based on the physical assumption that the density anomaly of a layer (its density difference with the bulk behavior) can directly be converted into a trapping depth anomaly (the difference in closing depth with the bulk behavior). The computation of depth anomalies is given by:

$$\Delta z = \frac{\Delta \rho}{\partial_z \rho} \quad (5.1)$$

where Δz is the depth anomaly of a layer, $\Delta \rho$ the density anomaly, and $\partial_z \rho$ the derivative of the bulk firn density with depth in the trapping zone. For the rest of the article $\partial_z \rho$ will be referred to as the densification rate. The concentration enclosed in an early trapping layer is then simply the concentration trapped by the bulk firn at a depth Δz below. Fourteau et al. (2017) original model is based on the computation of the age anomalies of abnormal layers (the time difference between the closure of the layers and the bulk behavior). However, this age-based formulation is sensitive to the dating of the ice core, and can lead to abnormally strong artifacts where the chronology is poorly constrained. On the other hand, the depth-

based formulation proposed here is not affected by dating uncertainties.

The model requires a densification rate for the firn-ice transition zone. Observations of density profiles in Dome C and Vostok proposed by [Bréant et al. \(2017\)](#) reveal densification rates around $2.2\text{kg}\cdot\text{m}^{-4}$ for both sites. This value also applies the Lock-In firn as inferred from high resolution density measurements. Therefore, the densification rate was set at $2.2\text{kg}\cdot\text{m}^{-4}$ for all sites studied here. Finally, the model requires a typical density anomaly σ_ρ in the closing part of the firn. Based on the linear relationships of density standard deviation with temperature and accumulation proposed by [Hörhold et al. \(2011\)](#), [Fourteau et al. \(2017\)](#) estimated the typical density anomaly to be $5 \pm 2\text{kg}\cdot\text{m}^{-3}$ for the Vostok firn during the glacial DO17 event. Moreover, [Hörhold et al. \(2011\)](#) report a density standard deviation of $4.6\text{kg}\cdot\text{m}^{-3}$ around the firn-ice transition of the Dome C site. As a first guess, we set the density anomalies to obey a zero-centered Gaussian distribution of standard deviation $5\text{kg}\cdot\text{m}^{-3}$. Similarly to [Fourteau et al. \(2017\)](#), the depth anomalies of late closure layers are reduce by 75% in order to replicate their low impact in the measured records.

While this parametrization produces adequate results for most of the gas records studied here, it results in a clear underestimation of the layering artifacts for the DO events 7 and 8 in the EDC96 ice core (Figure 5.34 of the Supplement). Our understanding is that the layering model fails to take into account the impact of high calcium variability during this period. To introduce the influence of calcium in the model, we simply increase the typical density anomaly during period of high calcium variability, by applying an enhancing factor of 1.5. This enhancing factor was empirically chosen to produce visually correct results in the case of the high calcium variability period of the DO7 to 9 (depths below 718m in the EDC96 record). For consistency, we also applied this enhancing factor for the DO17 period in Vostok, as this period displays a calcium variability similar to the DO 7 and 9 period.

The modeled artifacts are displayed below the newly measured signals in Figures 5.20 to 5.24, and the modeled artifacts for the DO17 in Vostok with the new calcium parametrization are displayed in Figure 5.26. The model produces layering artifacts in the expected parts of the records and with the expected signs and amplitudes. However, it is hard to reproduce the precise distribution of layering artifacts. This is due to the fact that the position of layering artifacts is stochastic, and that the observed layering artifacts in an ice core record are one single outcome among many possibilities. The simple parametrization

we derived thus appears to provide reasonable results for accumulation conditions ranging from 3.9 to 1.3 cm. ie. yr⁻¹, encompassing most of the climatic conditions of the East Antarctic plateau for both the glacial and interglacial periods.

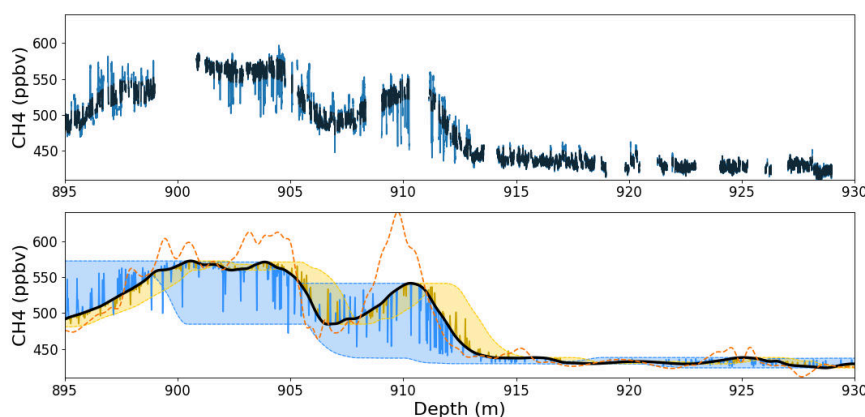


Figure 5.26 – Same as Figure 5.20 for the DO17 Vostok section. The methane data of the upper panel are from [Fourteau et al. \(2017\)](#) and the atmospheric reference of the lower panel is from [Rhodes et al. \(2015\)](#).

Removing layered trapping artifacts

Since layered gas trapping artifacts are not due to chronologically ordered atmospheric variations, a proper interpretation of gas records requires them to be cleaned from the datasets. As pointed out by [Fourteau et al. \(2017\)](#), in some sections of the records these artifacts only exhibit negative or positive methane anomalies. They cannot therefore be removed by applying a running average without introducing bias in the signal.

To clean the new three methane signals presenting layering artifacts (EDC96, EDC99 and Vostok) we use the cleaning procedure described by [Fourteau et al. \(2017\)](#). Briefly, this cleaning algorithm starts by estimating a smooth signal that should represent the measured signal free of layering artifacts and analytical noise. For this purpose, a running median is first computed to remove the layering artifacts while minimizing bias. Then, the signal is smoothed with a binned average, and interpolated back to high resolution using an interpolating spline. Then, the analytical noise is estimated and the data clipped to remove artifacts larger than the analytical noise.

This procedure was successfully applied to the Holocene section of EDC99, that only exhibits a few artifacts. The resulting cleaned signal is displayed in the upper panel of Figure 5.22 as a black curve. However, direct application of this algorithm to the EDC96 DO6-9 and Vostok DO21 records leads to an ineffective removal of layering artifacts in periods of

fast methane rise. After investigation, it appears that the main issue the algorithm is facing is the determination of an artifacts free signal by the rolling median. In some section of the ice cores, the signal displays high concentrations of artifacts with methane anomalies of 50ppbv or more, as seen for instance in the onset of the DO8 in Figure 5.23. In these conditions, the rolling median is influenced by the presence of the artifacts and yields a biased signal. To circumvent this problem, we manually provided a set of values that correspond to the artifact free part of the signal. As it is easy to distinguish the layering artifacts from the rest of the signal, the manual selection of these points is fairly unambiguous and straightforward. The rest of algorithm then proceeds as normal. The cleaned EDC99 Holocene, EDC96 DO6-9 and Vostok DO-21 signals are displayed in the upper panels of Figures 5.23 and 5.24 in black.

5.3.3.4 Smoothing in East Antarctic ice cores

The five ice core sections measured in this article all originate from the East Antarctic plateau. The low temperatures and aridity of this region result in a slow densification of the firn, and a slow bubble closure. Therefore, the gas enclosed in a given ice layer tends to have a broad age distribution. This leads to the important smoothing of atmospheric fast variability observed in East Antarctic ice cores (Spahni et al., 2003; Joos and Spahni, 2008; Köhler et al., 2011; Ahn et al., 2014; Fourteau et al., 2017).

Estimating gas age distributions

Since smoothing in an ice core record is a direct consequence of the gas age distribution (GAD), the knowledge of GADs for various temperature and accumulation conditions is necessary to predict the impact of smoothing on gas signals. We thus apply the GAD extraction method proposed by Fourteau et al. (2017) to the five new high resolution records. This method, designed to estimate the GAD of low accumulation records, is based on the comparison with a weakly smoothed record from a high accumulation ice core, used as an atmospheric reference (see Section 5.3.3.2). An optimal log-normal age distribution is derived to best match the measured signal with the smoothing of the atmospheric reference by the GAD. Using a log-normal law allows one to have a well-defined problem in the mathematical sense. A log-normal distribution is fully defined by two independent parameters. The GAD extraction problem is thus reduced to the recovery of a pair of optimal parameters. Nonetheless, log-normal laws exhibit a large range of shapes that can adequately represent

Table 5.4 – Parameters defining the log-normal gas age distributions derived by comparison with weakly smoothed records. The location and scale parameters correspond to the μ and σ parameters used to define the log-normal laws in Equation 1 of Köhler et al. (2011).

Site and Period	Location	Scale	Mean (yr)	Std Dev (yr)
Lock-In late Holocene	4.063	1.333	141	313
Dome C late Holocene	4.156	1.611	234	823
Dome C early Holocene	4.615	0.821	141	139
Dome C DO6-9	4.765	1.231	250	472
Vostok DO21	4.339	1.988	552	3950

the age distributions (Köhler et al., 2011; Fourteau et al., 2017). The gas age distributions obtained for the five new ice core sections are displayed as solid lines in Figure 5.27, and an uncertainty analysis is available in Section 5.3.6.2 of the Supplement. The parameters defining the different log-normal distributions are listed in Table 5.4. The standard deviation in this table should not be directly interpreted as the broadness of the age distribution and therefore its degree of smoothing. Indeed, some distributions exhibit strong asymmetries that tend to increase the standard deviation values. For instance, the Vostok DO-21 age distribution has a standard deviation value much larger than the other distributions, but does not induce a much larger smoothing.

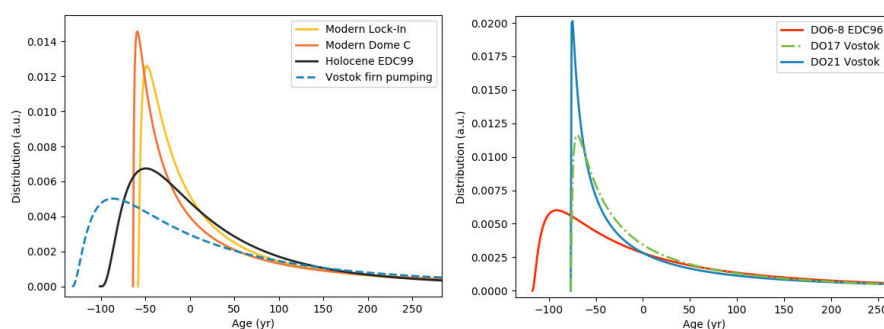


Figure 5.27 – Gas age distributions in various ice cores. The left panel contains Holocene GADs and the right panel glacial period GADs. The DO21 Vostok, DO6-9 EDC96, Holocene EDC99 and modern Lock-In and Dome C age distributions in solid lines were determined in this article. The dashed Vostok DO-17 distribution was determined by comparison with a high-accumulation record (Fourteau et al., 2017). The dashed Vostok firn pumping distribution was obtained with a gas trapping model, constrained with firn air pumping data (Witrant et al., 2012).

Smoothing and accumulation

The degree of smoothing in a gas record is strongly linked to the accumulation rate under which the gases are trapped, with low accumulation sites exhibiting a stronger degree of smoothing (Spahni et al., 2003; Joos and Spahni, 2008; Köhler et al., 2011). First, lower

accumulation is generally associated with low temperatures. Low-temperature ice deforms less easily and the densification process is therefore slower and bubble closure spans a larger time period. Moreover, low accumulation is also associated with a slow mechanical load increase of the ice material, also resulting in a slower densification and a longer bubble closure period.

Two new glacial period gas age distributions were derived in this work (EDC96 DO6-9 and Vostok DO21). This is to be added to the previously published GAD obtained for the Vostok site during the DO17 event (1.3cm.ice.yr^{-1} accumulation rate; [Fourteau et al., 2017](#)). These three age distributions of East Antarctic sites under glacial conditions are displayed in the right panel of Figure 5.27. The smoothing they induce is represented for the DO6 to 9 and DO21 events in Figure 5.28. It appears that the two Vostok distributions lead to similar smoothing. On the other hand the GAD obtained for EDC96 for the DO6-9 events is significantly broader than the Vostok ones and results in a stronger smoothing, especially visible on the onset of the DO21 event. This is surprising as the Vostok DO21 and Dome C DO6-9 records have the same accumulation rate, and should therefore present similar age distributions. However, the distributions obtained for glacial Vostok (DO17 and 21 events) also appear to be suited for the smoothing of DO6 to 9 events in EDC96, as seen in the lower panel of Figure 5.28. Moreover, the uncertainty analysis reveals that the distribution extracted from the EDC96 record is poorly constrained, with a large range of GADs resulting in adequate smoothing (Figure S8 in Section S2 of the supplement). It appears that the three glacial records exhibit similar degree of smoothing, and therefore enclose gases with the same gas age distribution. We propose to use a common gas age distribution to represent the smoothing in ice cores with accumulations below 2cm.ice.yr^{-1} . The distribution proposed by [Fourteau et al. \(2017\)](#) is a good candidate for this common distribution, as it reproduces well the smoothing in the EDC96 DO6-9 record and the Vostok DO17 and 20 records. Moreover, its shape is a compromise between the two other glacial GADs proposed in this article (right panel of Figure 5.27). Finally, the similarity of the smoothing encountered during the DO17 (high calcium variability) and DO21 (low calcium variability) events suggests the absence of significant impurity effect on the GADs.

Comparing the common GAD of the glacial period with the ones obtained for the Holocene and modern periods indicates that the later lead to a slightly smaller degree of smoothing. This is illustrated with the smoothing of the 8.2ka event displayed in Figure 5.29. It is con-

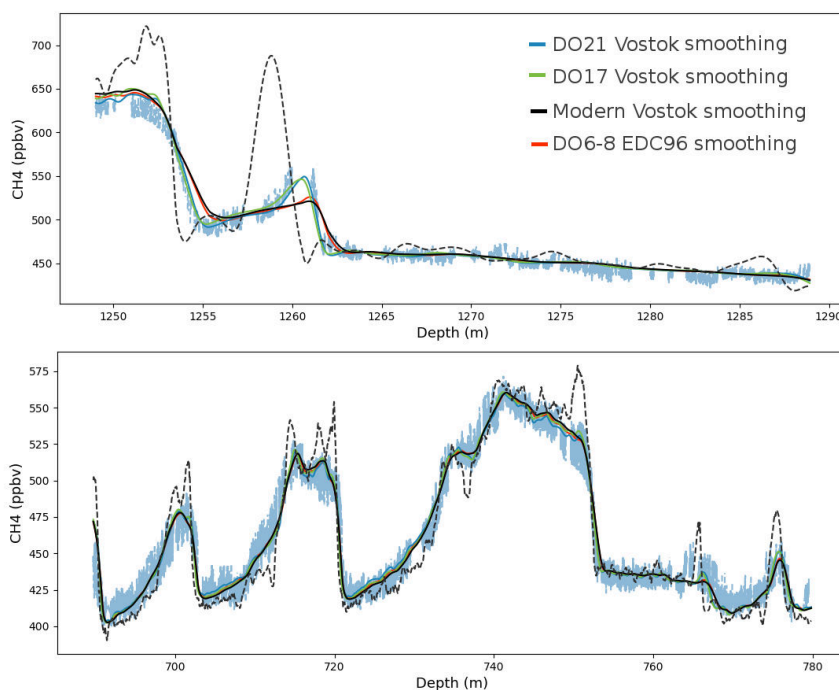


Figure 5.28 – Comparison of smoothing for the three different glacial age distributions, and the modern Vostok GAD constrained with firn air pumping data. Atmospheric references (dashed lines) have been smoothed by the four different GADs and are displayed overlying the measurements (light blue). The upper panel shows the DO21 event as measured in Vostok, and the lower panel shows the DO-6 to 9 as measured in EDC96.

sistent with the expectation that the smoothing during the low-accumulation glacial period should be more important than during the higher-accumulation Holocene period. However, the doubling of accumulation between the DO17 event at Vostok and the 8.2ka event in EDC99 does not result in a drastic diminution of smoothing. It is also noteworthy that for the Dome C site, the transition from 8.2ka conditions ($3.1\text{cm}\cdot\text{ie}\cdot\text{yr}^{-1}$ accumulation rate) to modern conditions ($2.7\text{cm}\cdot\text{ie}\cdot\text{yr}^{-1}$ accumulation rate) does not significantly change the degree of smoothing. It thus appears that for accumulations below $3.9\text{cm}\cdot\text{ie}\cdot\text{yr}^{-1}$ the degree of smoothing only slowly increases with the diminution of the precipitation rate.

Finally, the expected smoothing using the firn pumping GAD estimation for modern Vostok is also displayed in Figure 5.28 in black (Witrant et al., 2012). The smoothing estimated for modern Vostok is stronger than the one measured in the glacial Vostok ice core. This can be seen on the onset of the DO21, where the smoothing induced by the Vostok firn pumping distribution results in a signal with less variability than the CFA measurements. This confirms the observation of Fourteau et al. (2017) that the firn pumping GAD of modern Vostok leads to a stronger smoothing than the one observed during the DO17 event. This stronger smoothing in a modern ice core is in contradiction with the Holocene and modern GADs reported in this article for Dome C and Lock-In. This discrepancy could result from the

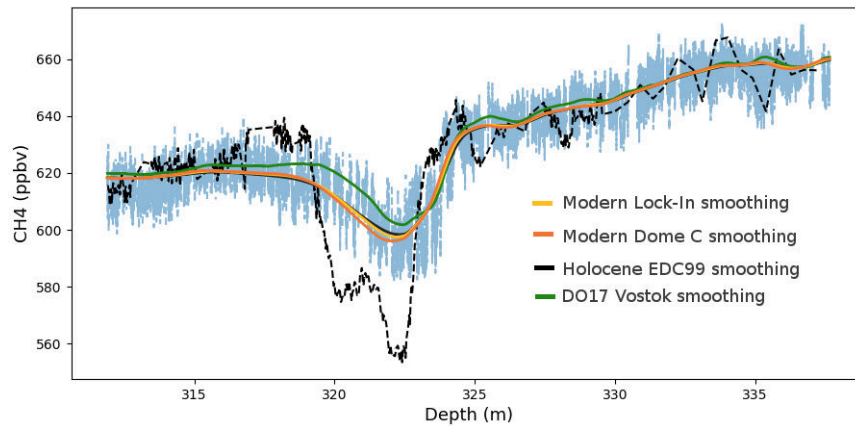


Figure 5.29 – Comparison of the smoothing induced by three different Holocene and a modern age distributions. The atmospheric reference for the 8.2ka event (dashed line) has been smoothed by the four different GADs and displayed over the EDC99 measurements (light blue).

large uncertainties associated with the firn-model-based GAD, which notably arise from the poor constraints on the closed porosity profiles used (Schaller et al., 2017). Unfortunately, high-resolution methane measurements of the late Holocene period in the Vostok ice core are not available to apply the GAD extraction method.

Effect of smoothing on the synchronization of records

Compared to the GADs of the Holocene and modern periods, the GADs of the glacial period exhibits a stronger degree of skewness (see Figure 5.27). This asymmetry of the distributions means that the smoothing not only removes variability, but also induces phase shifts during fast variations (Fourteau et al., 2017). This is especially visible on the variation recorded at depth 1260m in the Vostok DO21 ice core section, displayed in the upper panel of Figure 5.28. The peak of the event is recorded a couple of meters before its position in the absence of smoothing. Studies relying on the synchronization of atmospheric variability between ice cores should be aware of this potential bias (Bazin et al., 2013; Veres et al., 2013). The best synchronization should either be done on signals with similar degree of smoothing, or the phase shifts should be taken into account in the age uncertainty estimates.

5.3.4 Loss of climatic information in a deep and thinned ice core from East Antarctica

East Antarctica is a region of particular interest for the drilling of deep ice cores. Indeed, thanks to low accumulation rates, it likely contains the oldest stratigraphically-undisturbed

ice on earth. There is currently a search for very old ice, with ages potentially dating back one-and-a-half million years (Fischer et al., 2013; Passalacqua et al., 2018). When retrieved, such an ice core will be characterized by the gas trapping of low-accumulation East Antarctic plateau ice cores. Moreover, the old ice will be located close to the bedrock and therefore will be thinned by shear strains.

In this section, we estimate the potential alterations that smoothing and layering would induce between the atmosphere and its measurements in a theoretical one-and-a-half million years old ice core, for methane and carbon dioxide. For this purpose, we consider that the gas trapping occur under an accumulation rate of $2\text{cm}\cdot\text{ie}\cdot\text{yr}^{-1}$. We suppose that the enclosed gases follow the age distribution obtained for Vostok during the DO17 period, established to be representative of East Antarctic glacial smoothing in Section 5.3.3.4. The presence of layered trapping artifacts is simulated using the model parametrized Section 5.3.3.3, with the assumption of high calcium variability. Finally, we assume that the thinning of the ice results in a resolution of $10,000\text{yr}\cdot\text{m}^{-1}$ (Passalacqua et al., 2018). This implies that a given ice layer at the bottom of the core is 200 times thinner than at the firn-ice transition. This has to be taken into account as analytical techniques have limited spatial resolutions below which variations are no longer resolved. In particular, layering artifacts will no longer be visible as singular events in the record. Note that we do not consider the loss of climatic information due to diffusive mixing of trace gases within the ice matrix itself (Bereiter et al., 2014). This effect would further degrade the recorded trace gas signal.

5.3.4.1 Methane alterations

As a first case, we study the alterations of a methane record measured using a CFA system analogous to the one currently used at IGE. For the sake of simplicity, we assume that the atmospheric history recorded in this theoretical one-and-a-half million year-old ice core is similar to the DO17 event of the last glacial period. Hence, we simply use the WD CFA methane measurements as the atmospheric reference (Rhodes et al., 2015). We first determine the initially enclosed signal using the layering artifacts and smoothing models, and apply a 200 times thinning factor. The resulting signal is displayed in blue in the upper panel of Figure 5.30. Then, we simulate the process of CH_4 measurements by applying the smoothing induced by the CFA system. For this, we use the CFA impulse response derived by Fourteau et al. (2017). The end result is displayed in blue in the lower panel of Figure 5.30. The layering artifacts are no longer visible as they have been smoothed out

by the CFA measurement. However, they affect the measured signal due to their asymmetry. This is illustrated by the difference between the blue and green curves in the lower panel of Figure 5.30, that respectively represent the CFA measurements with and without the presence of layering artifacts. However, even during periods of strong methane variations, the bias specifically due to layering artifacts does not exceed 10ppbv. This is of the order of the analytical noise usually observed with the CFA system (Fourteau et al., 2017). It therefore appears that layering artifacts only negligibly affect the measured signal in the case of thinned ice cores. However, the potential impact of layering artifacts is sensitive to the parameters of the layering model. Notably, increasing the number of anomalous layers increases the amplitude of the biases.

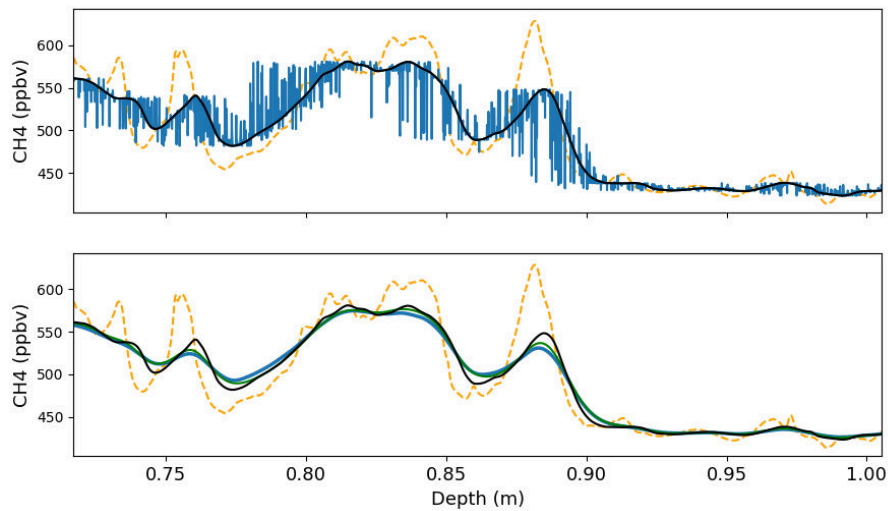


Figure 5.30 – Impacts of layered trapping and smoothing on a synthetic million-and-a-half years old methane record. Upper panel: signal recorded in the ice taking into account smoothing (in black) and layered trapping artifacts (in blue). The atmospheric reference is displayed in orange. The depth scale takes into account the thinning of the ice. Lower panel: CFA measurements with (in blue) and without layering artifacts (in green). The atmospheric reference is displayed orange and the initial recorded signal without layering artifacts is also displayed in black.

The internal smoothing of the CFA system also tends to deteriorate information recorded in the ice core by attenuating fast variability. It is therefore important to determine to what extent CFA smoothing adds to the already present firn smoothing. To study this point, we compare the frequency responses of the CFA system and firn smoothing. These frequency responses represent the attenuation experienced by a sine signal, as a function of the sine period. To achieve this, we first expressed the CFA impulse response (its smoothing function) on a gas age scale, taking into account the thinning of the ice. Then, the frequency responses were deduced using fast Fourier transforms. The gas age distribution and the CFA impulse response are displayed in the left panel of Figure 5.31 with the frequency responses in the

right panel. For sine periods longer than 100yr the firm smoothing is larger than the CFA smoothing. Yet, for a sine period of 500yr the firm induces a smoothing of 50% while the CFA system smooths by about 20%. The CFA smoothing is therefore noticeable and adds to the already present firm smoothing. This is illustrated in the lower panel of Figure 5.30, where the difference between the black and green curves is due to the presence of CFA smoothing. The influence of this analytical smoothing would be even stronger in the case of a narrower gas age distribution, for instance during interglacial periods. This is problematic as it deteriorates climatic information still present in the gas record. It thus appears important to improve current CFA gas systems in order to minimize their internal smoothing, in order to take full advantage of the gas records entrapped in deep ice cores.

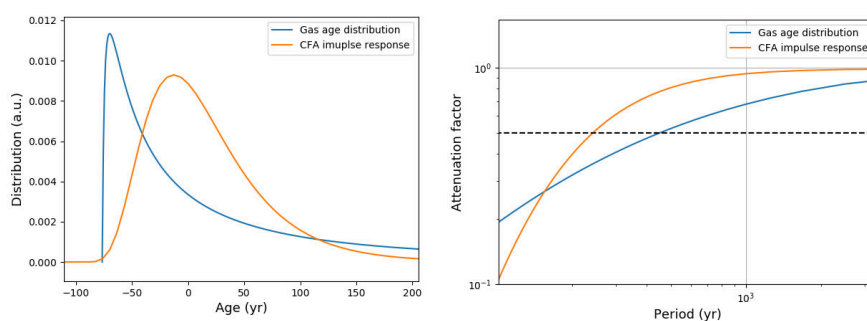


Figure 5.31 – Left panel: gas age distribution in the synthetic million-and-a-half years old ice core in blue, and CFA impulse response on a gas age scale in orange. Right panel: attenuation of a sine signal by the firm and CFA smoothing in blue and orange respectively. The horizontal dashed line indicates the 50% attenuation.

5.3.4.2 Carbon dioxide alterations

So far in this article only methane records have been considered. However, smoothing and layering artifacts also potentially affect other gaseous records, such as carbon dioxide records. Since CO_2 is one of the principal and most studied greenhouse gases, we propose to quantify the potential impacts of gas trapping on the record enclosed in a million-and-a-half years old ice core. Similar to the methane case of the previous section, we used the CO_2 measurements of the high accumulation WD ice core as the atmospheric reference (Marcott et al., 2014). The chosen data points correspond to the last deglaciation, as they constitute a fast atmospheric increase of CO_2 . As for CH_4 , the synthetic ice core signal is determined with the smoothing and layering model and ice layers are thinned 200 times. Finally, we emulate the process of discrete measurements. For that, we assume that the final ice core is continuously discretized into 4cm thick pieces, and that the measured value is the average value of the concentrations enclosed in the ice piece.

The results are displayed in Figure 5.32. The ice core signal is displayed in blue in the left panel of Figure 5.32, with the artifact free record superimposed in black. It can be seen that during enclosure, the layering heterogeneities can produce artifacts reaching up to 10ppmv. The measurements obtained by a discrete method are displayed on the right side of Figure 5.32 with and without the presence of layering artifacts in blue and black respectively. These results show that the impact of layering artifacts on the final measurements does not exceed 0.5ppmv, even during abrupt CO₂ rises. However, as for methane the impact of the layering artifacts is sensitive to the amount of abnormal layers per meter.

We also compared the rate of change of carbon dioxide in the atmospheric reference and in the measured record. For some of the fast variations of atmospheric CO₂, a reduced rate of change is deduced from the ice core record. A specific example (the deeper part of the records in Figure 5.32) is shown in Figure 5.33, where the rates of change of CO₂ in the atmosphere, recorded in the ice, and deduced from discrete measurements are compared. For this event, the atmospheric rate of change peaks at about 0.055ppmv.yr⁻¹, while the corresponding imprint in the ice has only a rate of change of 0.035ppmv.yr⁻¹ due to firn smoothing. The process of discrete measurement further diminishes the measured rate of change to about 0.02ppmv.yr⁻¹, a bit more than a third of the atmospheric value.

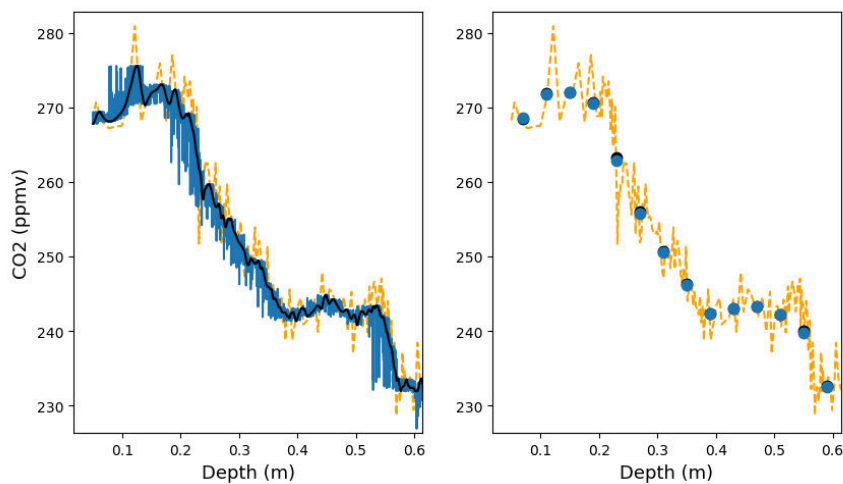


Figure 5.32 – Impacts of layered trapping and smoothing on a synthetic million-and-a-half years old carbon dioxide record. Left panel: Recorded signal in the ice taking into account smoothing (in black) and layered trapping artifacts (in blue). The atmospheric reference is shown in orange. Right panel: Measured signal by a discrete system as blue points. The atmospheric reference (in orange) and the measured signal without layering artifacts (black points) are also displayed.

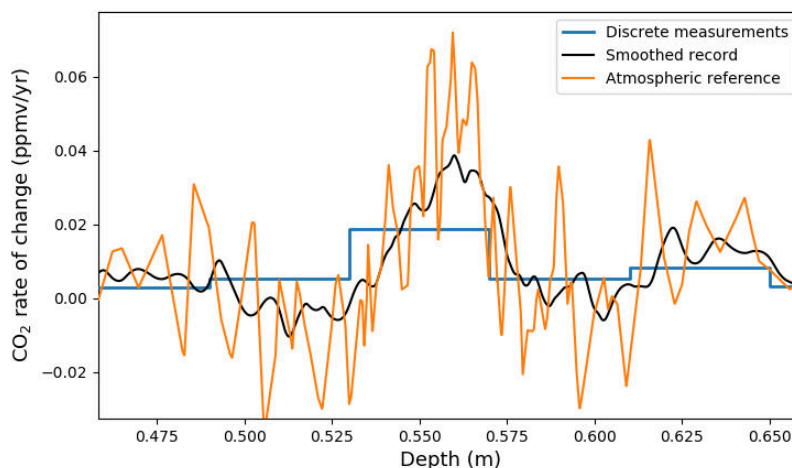


Figure 5.33 – Impact of gas trapping processes and measurements on the CO₂ rate of change. The rate of change of the atmosphere is displayed in orange, while the rate change recorded in the ice is in black, and the measured one is in blue.

5.3.5 Conclusions

This work evaluated two gas trapping effects that affect the recorded atmospheric trace gas history in polar ice cores. The first one is the layered gas trapping, that produces stratigraphic heterogeneities appearing as spurious values in the measured record (Rhodes et al., 2016). The second one is the smoothing effect that removes a part of the variability in the gas records (Spahni et al., 2003; Joos and Spahni, 2008; Köhler et al., 2011). Our work focuses on the arid region of East Antarctica, as this is where the oldest ice cores are retrieved. Five new sections from East Antarctic ice cores have been analyzed at high resolution for methane concentration.

The observation of layering artifacts in these new measurements is consistent with the physical mechanisms already proposed for their existence (Etheridge et al., 1992; Rhodes et al., 2016). In accordance with previous studies (Hörhold et al., 2012; Fujita et al., 2016), the data suggest that chemistry could promote the presence of especially dense layers closing in advance and creating the layering artifacts. We parameterized a simple model to reproduce the observed distribution and characteristics of layering artifacts, and were able to find a common set of parameters to reproduce the measured artifacts in all studied East Antarctic ice cores.

In order to study the smoothing effect, we estimated the enclosed gas age distributions in each of the five ice core sections. For this purpose, we use the method proposed by Fourteau et al. (2017) based on the comparison with higher accumulation methane records. It appears that during the last glacial period, the different methane records in ice cores formed under

accumulation rates below $2\text{cm}\cdot\text{ie}\cdot\text{yr}^{-1}$ all display similar degree of smoothing. We therefore propose to use a common gas age distribution for glacial East Antarctic sites with accumulations below $2\text{cm}\cdot\text{ie}\cdot\text{yr}^{-1}$. The comparison of the glacial and interglacial GADs suggests that smoothing is higher at Dome C during the glacial period than during the interglacial period. Yet, despite a doubling of accumulation during the interglacial period, the resulting smoothing is only slightly lower. Similarly to [Fourteau et al. \(2017\)](#), we observed that the smoothing during the glacial in the Vostok ice core is weaker than the one predicted for modern Vostok by the age distribution estimated by gas trapping models ([Witrant et al., 2012](#)).

Finally, we applied our methodology to the theoretical case of a million-and-a-half years old ice core drilled on the East Antarctic plateau. Our results suggest that due to thinning the layering artifacts will no longer be resolved during measurements. However, it appears that their potential influence on the end result measurements is rather low, with impacts below 10ppbv and 0.5ppmv for methane and carbon dioxide respectively. In the case of methane variations during DO events, most of the record alterations originate from the firn smoothing. Yet, the limited spatial resolution of the CFA system induces a smoothing that is not entirely negligible compared to the one of the firn. For carbon dioxide, firn smoothing appears to significantly diminish the recorded rates of change of abrupt CO_2 increases, compared to their atmospheric values. The estimations of CO_2 rates of change are further altered by the process of discrete measurement, and measured values can be three time lower than the actual atmospheric rate of change.

5.3.6 Supplementary Material

5.3.6.1 Layering artifacts model, without impurity effect

In the main text, a parametrization was included to account for the enhancement of layering due to the presence of high calcium concentrations and variabilities. Here we present the result of the layering model for the DO6 to 9 period in the EDC96 ice core, without taking into account the enhancement due to chemistry. The output of the model is displayed in [Figure 5.34](#). As seen on the figure, the model does not predict enough layering artifacts on the onset of the DO7 and 8. This highlights the necessity to take into account the effect of impurities on layering.

5.3.6.2 Uncertainty on Gas Age Distributions

The extraction method yields an optimal GAD that minimizes the RMSD between the CFA measurements and the smoothed atmospheric reference. To quantify the uncertainties associated with the calculated GADs, we performed a dedicated analysis. For each of the five ice core sections, we studied the impact of choosing slightly modified location and scale parameters.

Practically, we modify the scale and location parameters until the resulting RMSD is 15% larger than its optimal value. The location and scales were modified following straight lines in the {location, scale} space, starting from the optimal values (Figure 5.35). We then obtained a set of 10 GADs meant to represent the limit of acceptable distributions. These GADs and their corresponding smoothed methane records in the ice are displayed in Figures 5.36 to 5.40. In the right panel of these figures, we also represented the set of location and scale values that increase the RMSD by 15%. The regions enclosed by those values can be viewed as the uncertainty ranges of the location and scale parameters.

To better appreciate the uncertainty associated with the EDC96 and Vostok glacial GADs, we plotted their uncertainty ranges on the common Figure 5.41. It confirms that the EDC96 age distribution is less well constrained than Vostok GAD.

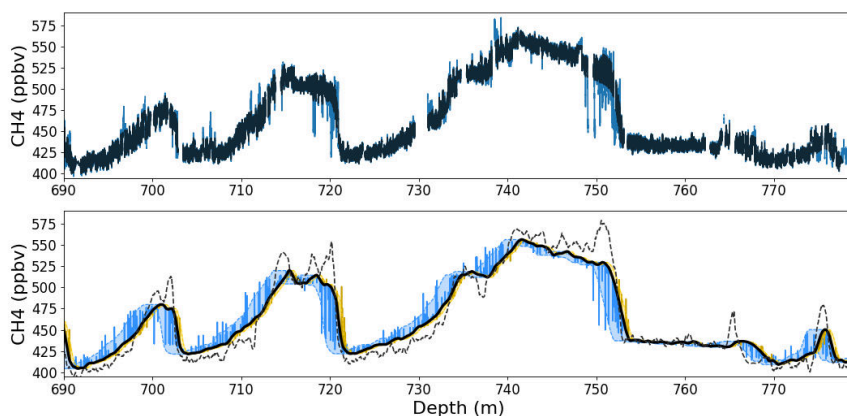


Figure 5.34 – Results of the layering model. This figure is similar to Figure 5 of the main article, but does not include the effect of impurity driven enhancement of layering.

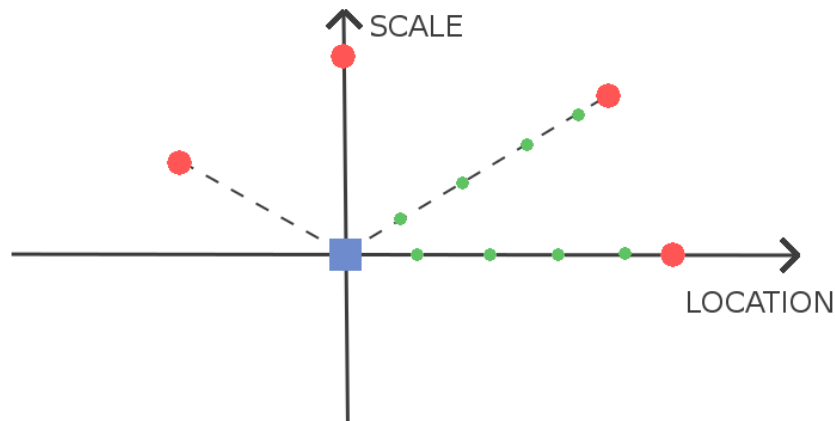


Figure 5.35 – Method used to modify the location and scale parameters for the uncertainty assessment. Starting from the optimal values (blue square), the location and scale parameters are moved away following straight lines (dashed lines). If the new RMSD differs by less than 15% with the optimal value (green dots) the location and scale are further modified, until the 15% are reached (red dots). Then the parameters are modified following a new line. In total 10 different lines are tested.

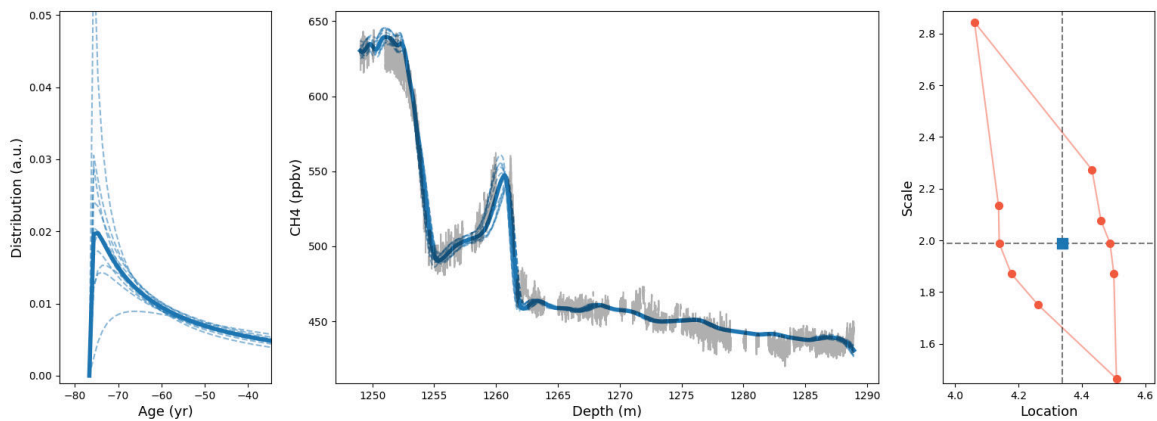


Figure 5.36 – GAD for the DO21 event in Vostok. Left panel: Optimal gas age distribution as a bold solid line. Age distributions resulting in 15% RMSD increases are shown as dashed lines. Middle panel: Methane smoothed record using the optimal GAD as a bold solid line, and methane smoothed records using the 15% higher RMSD distributions are displayed as dashed lines. CFA measurements are displayed in gray. Right panel: Location and scale parameters defining the gas age distributions. The blue square marks the optimal parameters and the red dots represent age distributions resulting in a 15% increase of RMSD.

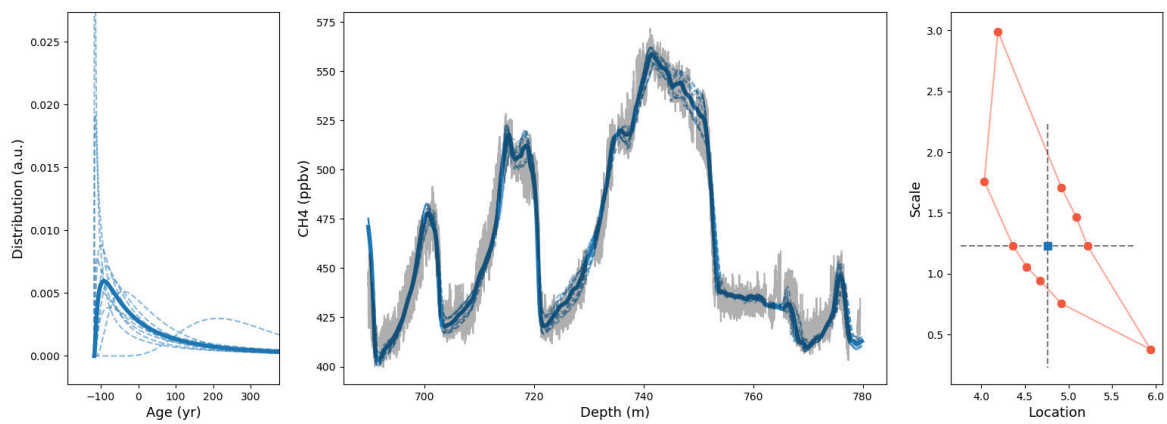


Figure 5.37 – Same as Figure S2 for DO6-8 events in EDC96.

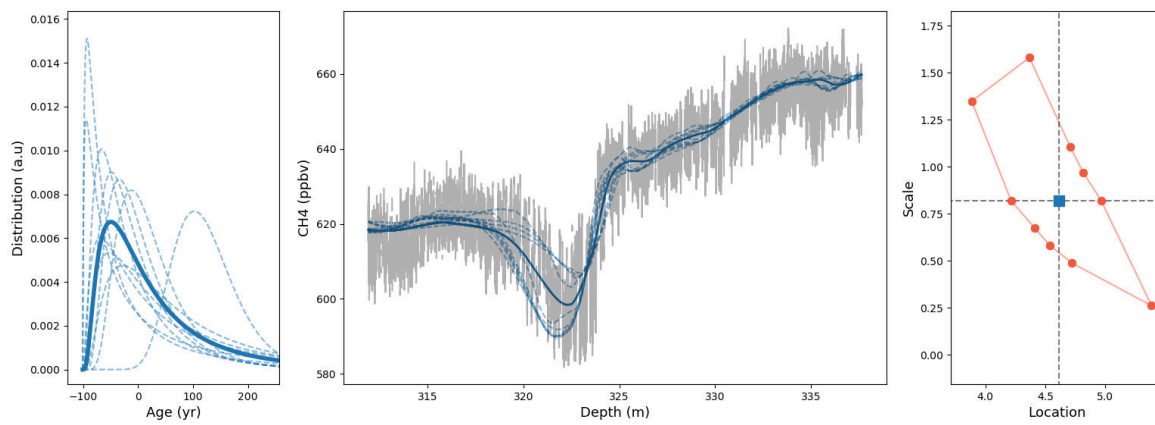


Figure 5.38 – Same as Figure S2 for 8.2ka event in EDC99.

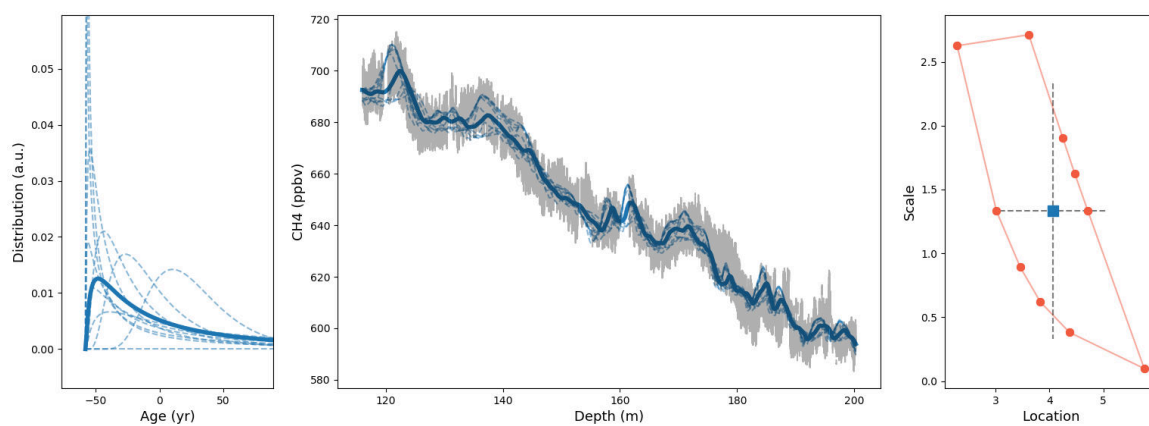


Figure 5.39 – Same as Figure S2 for the modern section of Lock-In.

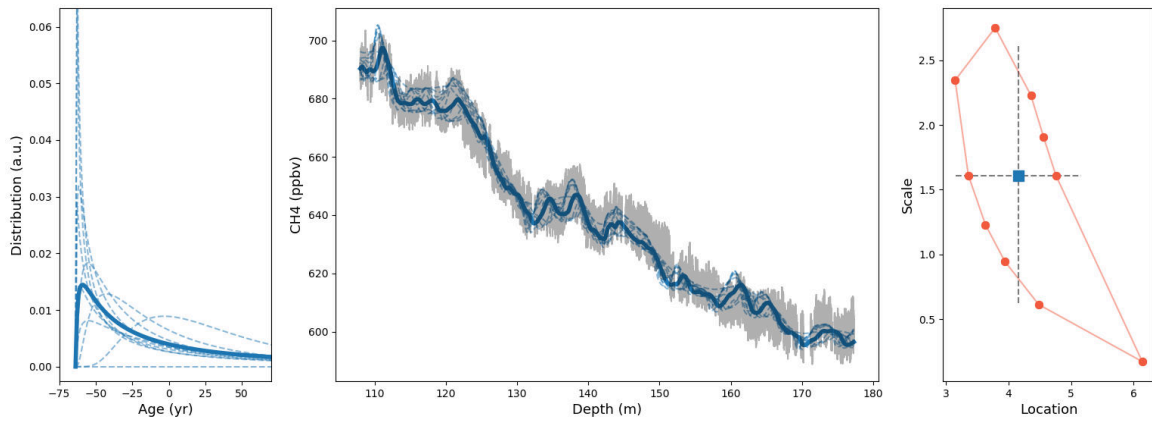


Figure 5.40 – Same as Figure S2 for the modern section of Dome C.

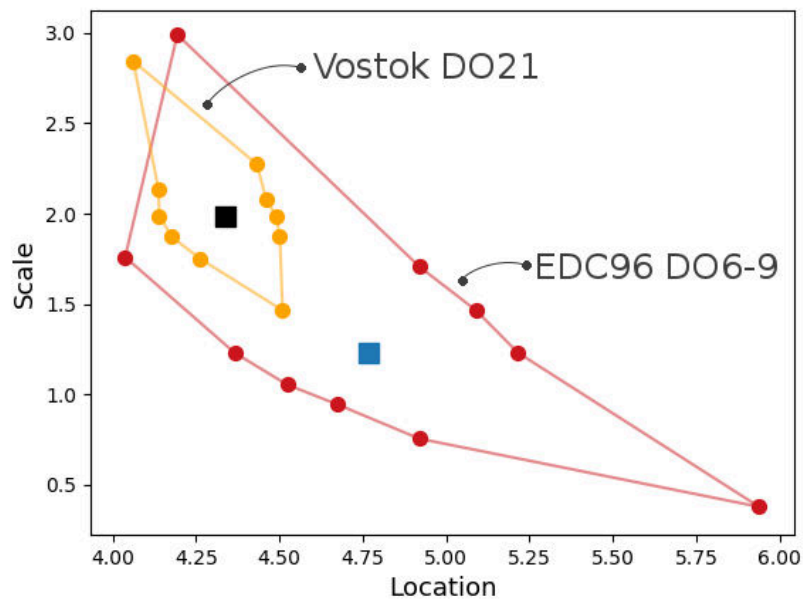


Figure 5.41 – Uncertainty range of the location and scale parameters for the EDC96 DO6-8 and Vostok DO21 GADs. The EDC96 uncertainty range is represented as red dots, and the optimal EDC96 parameters is marked as a blue square. The Vostok DO21 uncertainty range is represented as orange dots, and the optimal Vostok DO21 parameters is marked as a black square.

5.4 Conclusion of the chapter

This chapter presents new insights concerning the impact of layered gas trapping and firn smoothing on gas signals recorded in low-accumulation ice cores. This study was made possible thanks to the acquisition of high-resolution methane data using the CFA system of IGE during my PhD.

In both articles, I first analyze the impact of layered gas trapping. In accordance with [Rhodes et al. \(2016\)](#), layered gas trapping artifacts appear as centimeter scale methane variations during periods of atmospheric methane variations. In the case of low-accumulation ice cores these artifacts' anomalies can reach of up to 100ppbv, equivalent to the methane increases observed during DO events. Moreover, the numbers of artifacts in the EPICA Dome C ice core appears to be linked with the level and variability of calcium in the ice. This is consistent with the description of stratified gas trapping presented in Chapter 4.

I propose a simple model to predict the presence and amplitudes of the layering artifacts in gas signals. This model converts the density anomaly of a firn stratum into a closure depth anomaly, representing the advance or delay of closure of the stratum. The greenhouse gas concentrations of the air enclosed in the stratum is computed according to its time of closure. The model was originally developed for the record of the DO17 event in the Vostok ice core. It was then extended to the all the methane records obtained during this PhD, and was revised to include the influence of ionic content of the ice. After model parameters adjustment, the model can simulate the presence of layering artifacts observed in six ice cores from East Antarctica, for accumulation rates ranging from 3.9 to 1.3cm.ice.yr⁻¹.

I introduce a novel technique to estimate the gas age distribution of gases enclosed in low-accumulation ice cores. It is based on the comparison of the low-accumulation record with a higher-accumulation one. In particular, this method can be applied to the case of glacial ice cores from East Antarctica and climatic conditions with no present-day equivalent. Applying this methodology to six different East Antarctic methane records, I am able to obtain estimations of gas age distributions for accumulation rates between 3.9 to 1.3cm.ice.yr⁻¹. In particular, I estimate three age distributions for glacial conditions over the East Antarctic plateau, for accumulation rates of 1.5 and 1.3cm.ice.yr⁻¹. All the three glacial period records

display a similar degree of smoothing. I thus propose to use a common gas age distribution to represent the smoothing of gas signals recorded in glacial ice cores of the East Antarctic plateau. Moreover, comparing the smoothing observed in glacial and interglacial conditions, it appears that smoothing is only slightly more important during the glacial period. This suggests that the degree of smoothing slowly increases with the decrease of accumulation in the case of ice cores from the East Antarctica plateau.

Finally, I apply the layering model and smoothing methodology to the theoretical case of a million-a-and-half years old and very thinned ice core from East Antarctica. The goal is to estimate the alterations to be expected for the gas signals recorded in the future core of the Oldest-Ice project. For the case of methane measured with a CFA system, the signal will be principally altered by firn smoothing, with also a non-negligible contribution of CFA smoothing, if current setups are applied without further improvements. The layered gas trapping artifacts will no longer be resolved, but only account for a slight bias (< 10 ppbv) of the measurements. In the case of discrete measurements of carbon dioxide, firn smoothing leads to an underestimation of the rate of change recorded in the ice during fast variations. Moreover, the process of discrete measurement also strongly affects the rate of change, and results in a further underestimation of the rates of change in CO_2 concentrations.

Modeling the compression of firm layers

Contents

6.1	Presentation of the chapter	197
6.2	Description of the model	198
6.2.1	General principles	199
6.2.2	Numerical implementation	200
6.3	Numerical experiments	208
6.3.1	Mass conservation	208
6.3.2	Effect of internal pressure on pore compression	210
6.3.3	Evolution of a firm layer	212
6.4	Discussion	215
6.5	Conclusion of the chapter	217

6.1 Presentation of the chapter

One question at the beginning of my PhD was if closed porosity profiles could be estimated for the case of past glacial firns from East Antarctica. Indeed, the amount of smoothing in gas records is directly linked to the progressive closure of bubbles, and knowing the relation between density and closed porosity for past firns would help to better constrain the age distribution of entrapped gases.

Direct observations of past glacial firns of the East Antarctic plateau or of modern equivalents are not possible. A possibility to overcome this issue would be the development of numerical models explicitly able to represent the porous network and its evolution during densification. Such models could be forced with accumulations and temperatures that have no known modern equivalents on the Antarctic continent. Moreover, such a general model could also be used to study the impact of the firn microstructure on the evolution of the density and of the porous network. After discussions with C. Martin from the SIMAP laboratory, Grenoble, I was introduced to the Level-Set method and its application to metallic powder sintering, notably by [Bruchon et al. \(2012\)](#).

I consequently worked on the implementation of a similar method to the case of firn compression, as described in this chapter. For this work, F. Gillet-Chaulet helped me with the Finite Element Method and the Elmer software. The chapter begins with the presentation of the algorithm and the specificities of firn compression. In its current form, the model is not fully operational to estimate closed porosity profiles. Nonetheless, it can simulate the mechanical response of a 3D porous network due compression forces, and its evolution over time. In this chapter, the model is used to study the influence of internal pressure of bubbles on their compression in deep firn. Furthermore, an illustration of firn evolution with the processes of curvature-driven diffusion and ice creep is provided at the end of the chapter. Moreover, while this study is focused on the deep pore-closure zone, the model developed here could be applied to shallower and less dense firn samples.

I intend to publish my work on this firn compression model in the special issue of the *Frontiers in Earth Science* journal: About the Relevance of Snow Microstructure Study in Cryospheric Sciences. This article will be presented as a proof-of-concept of using the Level-Set method to study the evolution of the microstructure of snow, firn, or other bi-phasic media under compression forces.

6.2 Description of the model

Firn layers are composed of two phases, namely the ice matrix and the pores inside. Under the compression forces due to the overlying column, firn layers get compressed over time, and the porous network evolves as a response to this compression (Arzt et al., 1983; Maeno and Ebinuma, 1983). In addition to compression, curvature differences at the surface of the ice material induce molecular diffusion of the water molecules and further modify the porous network (Burr et al., 2019). The overall evolution of the porous network is characterized by a reduction in size, equivalent to an increase in firn density, as well as topological changes such as pore splitting or coalescence (Burr et al., 2019). A numerical model explicitly representing the porous network and its evolution should therefore be able to handle these topological changes. The bi-phasic nature of the firn is replaced by a mono-phasic medium with the addition of a characteristic function retaining the position of the ice-pore interface, the so called Level-Set (LS) function ϕ (Osher and Sethian, 1988; Gibou et al., 2018). A typical choice for the LS function is the signed distance to the interface.

Let's consider a domain D of firn, which for the rest of the chapter will be a rectangular cuboid. The Level-Set function ϕ is given by:

$$\phi(x) = \begin{cases} +\text{dist}(x, \Sigma) & \text{if } x \in \text{ice} \\ -\text{dist}(x, \Sigma) & \text{if } x \in \text{pore} \\ 0 & \text{if } x \in \Sigma \end{cases} \quad (6.1)$$

where x is a point of D , Σ is the interface between the ice and pore phases, and $\text{dist}(x, \Sigma)$ is the distance of point x to the interface. The position of the interface is thus captured by the zero-level of the LS function. In other words, one can retrieve the position of the interface with $\Sigma = \{x \mid \phi(x) = 0\}$. The evolution of the porous network is therefore represented through the evolution of the zero-level of the LS function. This framework naturally handles topological changes (Osher and Sethian, 1988). Furthermore, due to the complex geometries present in firn, the model relies on the Finite Element Method (FEM) to solve the equations involved.

6.2.1 General principles

Assuming that a LS function ϕ is already defined on a tetrahedral mesh \mathcal{M}_D covering the whole domain D , the model simulates the evolution of the porous network by looping over three main stages, summarized in Figure 6.1. During a complete cycle, the time of simulation advances by a time-step Δt .

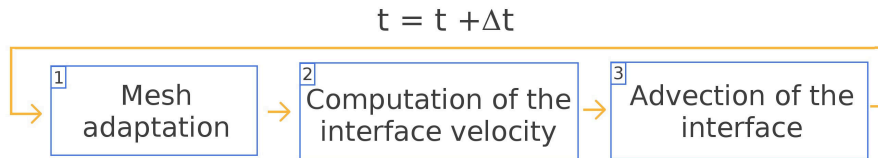


Figure 6.1 – The three stages composing a time-step loop in the firn compression model.

6.2.1.1 Mesh adaptation

The method involves a mesh adaptation step at the beginning of every time-step. It first aims at improving the computational efficiency of the model by keeping a refined mesh near the ice-pore interface and a coarser resolution far from it, where a high density of elements is not needed. The second goal is to produce two sub-meshes. One is meant to cover the ice phase only, while the second one covers the pore phase only. The sub-meshes are referred to as \mathcal{M}_i and \mathcal{M}_p , respectively for the ice and pore phases.

6.2.1.2 Computation of the interface velocity

Once the meshes for a given time-step are ready, they are used to compute the ice-pore interface velocity. This is done by solving the equations governing the mechanisms responsible for the motion of the interface using the FEM. This step encapsulates all the physics of the model. Here, I take into account the motion of the interface due to ice dislocation creep (Arzt et al., 1983; Maeno and Ebinuma, 1983) and curvature driven diffusion (Burr et al., 2019). Thanks to the modular nature of this model, other mechanisms can be added in the future, if necessary.

6.2.1.3 Advection of the interface

Once the total velocity of the ice-pore interface \mathbf{v}_{tot} is calculated, it is used to advect the Level-Set function. This is done by solving the transport equation over a time-step Δt (Ols-

son and Kreiss, 2005; Bernacki et al., 2008):

$$\frac{\partial \phi}{\partial t} + \mathbf{v}_{\text{tot}} \cdot \nabla \phi = 0 \quad (6.2)$$

6.2.2 Numerical implementation

This section describes the specific implementation of the general principles introduced in the previous section. The main FEM framework used in this study is the open-source software Elmer¹, that has been completed with equation solvers specifically developed for this firn layer model.

6.2.2.1 Mesh adaptation

Assuming that at the end of the n^{th} time-step the Level-Set function is defined on a tetrahedral mesh \mathcal{M}_D^n , the mesh adaptation procedure produces three meshes \mathcal{M}_D^{n+1} , \mathcal{M}_i^{n+1} , and \mathcal{M}_p^{n+1} that respectively cover the whole domain, the ice phase and the pore phase. The ice and pore meshes are sub-meshes of \mathcal{M}_D^{n+1} , meaning that the ice mesh is composed of the elements of \mathcal{M}_D^{n+1} that lie in the ice phase region, and similarly for the pore mesh. The vertices of \mathcal{M}_i^{n+1} and \mathcal{M}_p^{n+1} are thus also vertices of \mathcal{M}_D^{n+1} .

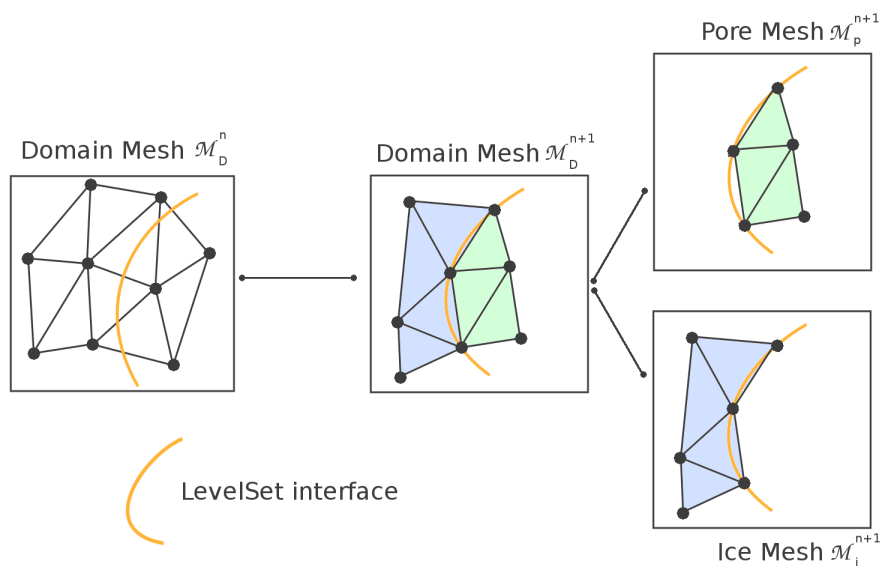


Figure 6.2 – Mesh adaptation of the domain following the LevelSet function. The submeshes of the ice and pore phases \mathcal{M}_i , and \mathcal{M}_p are also produced during mesh adaptation.

¹<https://www.csc.fi/web/elmer/elmer>

To remesh the domain according to the LS function, I use the remeshing library MMG² (based on [Dapogny et al., 2014](#)), that we have interfaced with Elmer. The library yields a tetrahedral mesh that is refined around the pore-ice interface, with tetrahedral elements either in the ice or the pore phase and tagged accordingly. The boundaries between the elements of the ice and pore regions thus lie on the interface defined by the Level-Set function. The MMG library includes parameters to adjust the mesh refinement. The main ones are the h_{grad} and h_{ausd} parameters, that respectively set the gradation of element sizes and the maximal distance between the ideal interface defined by the Level-Set function and the interface captured by the tetrahedral mesh.

The mesh obtained with MMG is then converted into the three meshes \mathcal{M}_D^{n+1} , \mathcal{M}_i^{n+1} , and \mathcal{M}_p^{n+1} . Note that for \mathcal{M}_D^{n+1} , the elements are no longer tagged according their original phase as the LS framework relies on a mono-phasic medium. The different variables defined at the nodes of \mathcal{M}_D^n are finally interpolated on the new nodes of \mathcal{M}_D^{n+1} . This includes the Level-Set function.

In order to facilitate the transfer of variables between the \mathcal{M}_D^{n+1} , \mathcal{M}_i^{n+1} , and \mathcal{M}_p^{n+1} meshes, permutations tables that link a vertex in \mathcal{M}_D^{n+1} to its equivalent in \mathcal{M}_i^{n+1} and/or \mathcal{M}_p^{n+1} are saved under the form of two arrays of integers. For a given node of index i in the domain mesh, the i^{th} value of the permutation table is the index of the corresponding node in the ice mesh (respectively pore mesh) or 0 if the node does not lie in the ice phase (respectively pore phase). This allows one to transfer variables from one mesh to another without interpolation, and with a good numerical efficiency. The complete mesh adaptation step procedure is summarized in Figure 6.2.

6.2.2.2 Ice creep

The first physical mechanism responsible for the deformation of the porous network and therefore the motion of the ice-pore interface is the dislocation creep of the ice phase due to the compression forces of the firn column above ([Maeno and Ebinuma, 1983](#); [Arzt et al., 1983](#)). The creep motion of ice is represented thanks a to viscoplastic motion with a low Reynolds number. The Equation governing the ice motion is the Stokes equation:

$$\nabla \cdot \bar{\sigma} + \rho \mathbf{g} = 0 \quad (6.3)$$

²<https://www.mmgtools.org>

where $\nabla \cdot$ is the divergence operator, $\bar{\sigma}$ is the stress tensor, ρ is the density of ice and \mathbf{g} is the gravity acceleration vector. Several rheological laws relating the stress tensor to the internal velocities can be implemented for the ice material, with or without non-linearities and with or without anisotropy.

The enforced boundary conditions are conditions of non-penetration on all the domain sides ($\mathbf{u} \cdot \mathbf{n} = 0$, where \mathbf{u} and \mathbf{n} respectively are the velocity vector and normal vector to the boundary), except for the top side where a normal stress is enforced, with a free slip condition ($\bar{\sigma} \mathbf{t} = \mathbf{0}$, where \mathbf{t} is tangent to the boundary). In this case, the upper constraint is the pressure of the overlying firn column and of the atmosphere. Finally, the effect of air pressure in the pores is applied at the pore-ice interface. The Stokes equation is solved on the \mathcal{M}_i mesh using the solver readily available in Elmer.

After solving Equation 6.3, the creep velocities are known within the ice material. However, in order to advect the LS function it is necessary for the advection velocity field to be defined on each side of the interface, and thus also inside the pore phase. This is a classical problem of the Level-Set method that can be solved with the aid of velocity extension methods (Adalsteinsson and Sethian, 1999). Here, the ice velocity is extended to the pore phase by solving the Equation:

$$-\alpha \Delta V_{\text{ext}} + V_{\text{ext}} = 0 \quad (6.4)$$

where Δ is the Laplace operator, V_{ext} the extended velocity, and α a smoothing parameter. The equation is solved on the pore mesh \mathcal{M}_p , with the boundary condition setting the extended velocity equal to the dislocation creep velocity on the ice-pore interface.

The creep velocity on the ice mesh, and the extended velocity on the pore mesh are then transferred to the main mesh \mathcal{M}_D . This results in a continuous velocity field defined on the whole domain D , that matches the ice creep in the ice region. An example of ice creep velocity extension is given in Figure 6.3.

In this model, the creep of ice is represented by Glen's law (also referred to as Norton's law

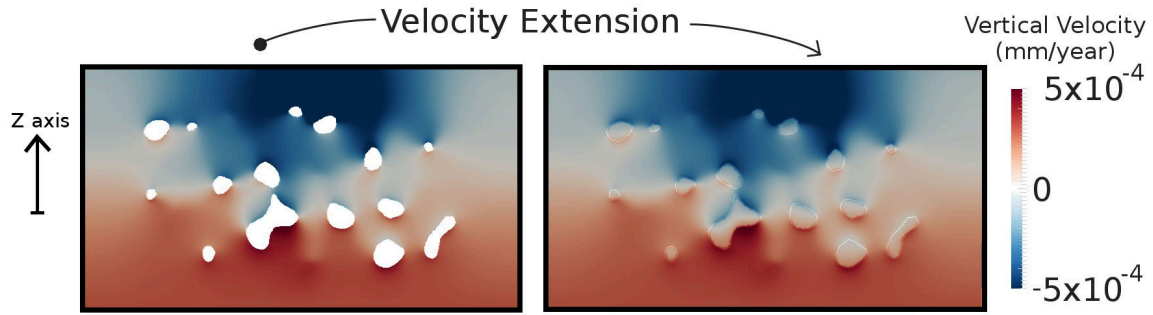


Figure 6.3 – Left panel: Creep velocities computed in the ice phase. Right panel: Creep velocities extended to the whole domain.

Duval et al., 1983; Cuffey and Paterson, 2010; Schulson and Duval, 2009):

$$\dot{\epsilon}_{ij} = A\tau^{n-1}\sigma'_{ij} \quad (6.5)$$

where $\dot{\epsilon}_{ij} = \frac{1}{2}(\frac{\partial u_i}{\partial x_j} + \frac{\partial u_j}{\partial x_i})$ is the strain rate tensor, $\sigma'_{ij} = \sigma_{ij} - 1/3 Tr(\sigma)\delta_{ij}$ is the deviatoric stress tensor component, with $\bar{\sigma}$ the stress tensor and δ_{ij} the Kronecker delta, and $\tau^2 = \frac{1}{2}\sigma'_{ij}\sigma'_{ij}$ is the effective shear stress. The parameter n is set to 3 (Cuffey and Paterson, 2010; Schulson and Duval, 2009). The pre-factor A is assumed to follow an Arrhenius type law (Cuffey and Paterson, 2010; Schulson and Duval, 2009):

$$A = A_0 e^{(-\frac{Q}{RT})} \quad (6.6)$$

where Q is an activation energy equal to $60\text{kJ}\cdot\text{mol}^{-1}$ (Cuffey and Paterson, 2010), T the temperature in K, and R the ideal gas constant. The parameter A_0 is set to $9.13 \times 10^{12} \text{MPa}^{-n}\cdot\text{yr}^{-1}$ (Cuffey and Paterson, 2010).

6.2.2.3 Curvature driven diffusion

The second mechanism involved in the densification of polar firn is the diffusion of ice molecules due to gradients of chemical potential created by local curvature conditions (Ashby, 1974; Maeno and Ebinuma, 1983). There are several mechanisms for the diffusion of water molecules in the ice matrix as a response to curvature effects. It is however not clear what is the dominant mechanism of diffusive mass transport at the temperature considered in this model ($\sim -50^\circ\text{C}$) and for the curvatures encountered in deep firn. Diffusive mechanisms

however tend to reduce the overall curvatures of the ice/pore interface. To achieve this, we implemented the specific mechanism of surface diffusion (Bruchon et al., 2010, 2012). The equation governing the motion of the interface is:

$$\mathbf{v}_d = -C_0(\Delta_s K)\mathbf{n} \quad (6.7)$$

with C_0 being a parameter representing the effectiveness of the diffusive mechanism, K the curvature of the interface, \mathbf{n} the normal vector to the interface and pointing in the ice phase, and Δ_s is the "surface Laplacian" (the Laplace-Beltrami operator). To compute \mathbf{v}_d , this equation requires the curvature K and the normal vector \mathbf{n} . They are calculated using:

$$\mathbf{n} = \frac{\nabla\phi}{\|\nabla\phi\|} \quad (6.8)$$

and

$$K = -\nabla \cdot \mathbf{n} \quad (6.9)$$

Equations 6.7 and 6.9 requires second-order derivatives. To reduce numerical noise, they are stabilized with the introduction of diffusion parameters A_k and A_v :

$$\begin{aligned} K + A_k \Delta K &= -\nabla \cdot \mathbf{n} \\ v_d + A_v \Delta v_d &= C_0(\Delta_s K) \end{aligned} \quad (6.10)$$

In Equation 6.10, v_d is the norm of \mathbf{v}_d . All equations are defined over the all domain, and are thus solved on the mesh \mathcal{M}_D using specifically developed Elmer solvers. This yields a velocity field defined over the whole domain, that matches the diffusion velocity at the ice/pore interface.

We set the physical parameter C_0 of Equation 6.7 so that it would ideally represent the contribution of the different diffusive mechanisms to the overall curvature decrease (Ashby, 1974; Maeno and Ebinuma, 1983). We evaluated that the mechanism of diffusion results in interface velocities similar to ice creep for $C_0 \simeq 10^{-6} \text{ mm}^4 \cdot \text{yr}^{-1}$. Therefore, in the rest of the study the parameter C_0 will be set to the values 10^{-6} or $10^{-7} \text{ mm}^4 \cdot \text{yr}^{-1}$ to respectively

represent the presence of a strong or mild influence of the diffusion process, relatively to ice creep.

6.2.2.4 Advection of the Level-Set function

Once the total velocity of the interface is computed, it is used to modify the porous structure of the firn material by advecting the Level-Set function. However, the sole advection of the Level-Set using the velocity field is not sufficient to ensure a good representation of the evolution of the interface. Indeed, the property of the Level-Set function to be a signed distance function is lost during the advection step, although it is fundamental for the computation of normal vectors and curvatures. That is why the Level-Set is regularly renormalized to remain a signed distance (Osher and Fedkiw, 2001). However, the renormalization of the Level-Set introduces errors and numerical diffusion in the model, that result in unphysical gain or loss of volume (Olsson and Kreiss, 2005). To overcome this issue, Zhao et al. (2014a) introduced the Improved Conservative Level-Set (ICLS) method following the work of Olsson et al. (2007) on the Conservative Level-Set method. To ensure volume conservation, I have implemented a version of the ICLS method for the advection stage.

The ICLS method introduces a new scalar field H , similar to the Level-Set function ϕ , defined as:

$$H = \frac{1}{2} \left(1 + \tanh\left(\frac{\phi}{2\epsilon}\right) \right) \quad (6.11)$$

This new function is a Heaviside function, smeared on a width of the order of ϵ . Similarly to the LS function, H captures the position of the ice-pore interface, that lies where $H = 1/2$. Moreover, H can also be used to compute the normal vector to the interface using Equation 6.8.

The implementation of the ICLS method works as follows. The LS and H functions are both advected on the mesh \mathcal{M}_D using the total interface velocity. The advection is performed using the Advect software³. Then, the LS function is renormalized to remain a signed dis-

³<https://github.com/ISCDtoolbox/Advect>

tance function, using the `mshdist` software ⁴ (based on [Dapogny and Frey, 2012](#)).

Then, the normal vectors to the new interface are computed. Near the interface the normal vector \mathbf{n} is computed using the H function, and far from it is computed using the renormalized LS function. This is done because using the H function to compute the normal vectors yields spurious oscillations far from the interface, a problem that does not arise with the LS function ([Zhao et al., 2014a,b,c](#)). A point of the domain is considered to be in the vicinity of the interface if its distance to the interface is smaller than ϵ . Then the shape and the width of the H function are maintained thanks to a re-initialization step ([Olsson et al., 2007](#); [Zhao et al., 2014a,b,c](#)). It consists in solving the equation:

$$\frac{\partial H}{\partial \tau} + \nabla \cdot [H(1 - H)\mathbf{n}] = \nabla \cdot [\epsilon(\nabla H \cdot \mathbf{n})\mathbf{n}] \quad (6.12)$$

In this equation, τ is a fictional time, distinct from the actual time, that is solely used to relax the equation to equilibrium. The equation should be solved until a steady-state is reached. I solve it for 15 time-steps, which is enough to reach a steady state ([Olsson et al., 2007](#)). Once the H function has been re-initialized, the Level-Set function ϕ is updated in the vicinity of the interface using:

$$\phi = 2\epsilon \tanh^{-1}(2H - 1) \quad (6.13)$$

Then, the advection step is over and the Level-Set function now defines the new interface.

6.2.2.5 Initialization

The model needs to be initialized with an initial LS function, representing either a real firm porous structure or an idealized geometry. The initial porous structure can be derived from 3D voxel models obtained with Xray tomography of firm samples ([Barnola et al., 2004](#); [Gregory et al., 2014](#); [Burr et al., 2018](#)). To simplify the boundary conditions, the tomography models are padded with ice material on all sides, meaning that the pore-ice interface lies away from the boundaries of the domain D .

Starting from a 3D voxel model, the signed distance is computed on a Cartesian grid using

⁴<https://github.com/ISCDtoolbox/Mshdist>

the Fast Marching Method (FMM). It was performed using the `scikit-fmm`⁵ python package. The signed distance is then smoothed using a gaussian filter to remove the jags of the interface. The resulting signed distance defines the initial LS function, and is interpolated on the initial mesh \mathcal{M}_D^0 . Since, one does not know in advance where the pore-ice interface lies in the domain, \mathcal{M}_D^0 is finely resolved over the whole domain to properly capture the initial position of the interface.

Then, the H function is determined using Equation 6.11. In order to further smooth the interface and remove remaining jags, I perform a re-initialization step of H solving Equation 6.12 to equilibrium. Then, the Level-Set function is updated using Equation 6.13. The simulation can then start with a mesh adaptation step.

The overall algorithm, including the initialization, mesh adaptation, computation of velocities, and advection steps, is summarized in Figure 6.4.

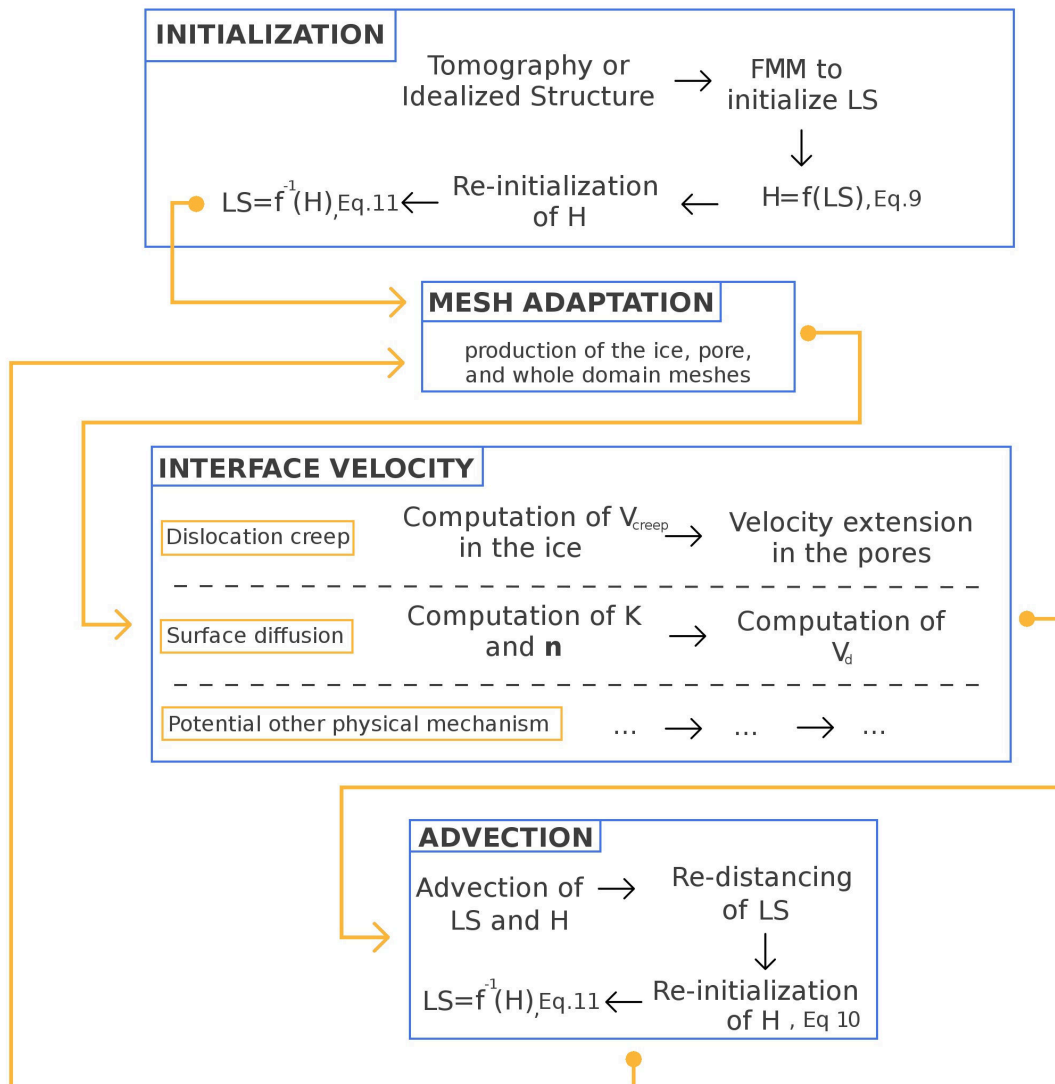


Figure 6.4 – Scheme of the model algorithm. Each blue box represents a stage of the simulation.

⁵<https://pypi.org/project/scikit-fmm/>

6.3 Numerical experiments

As a first application, the ability of the model to conserve mass on an ideal test case is assessed. The model framework is then used to quantify the impact of building pressure in a bubble at the bottom of a firn column. I finally present simulations of the densification of a firn stratum. These simulations illustrate the ability of the model to handle the topological changes happening in the porous network.

6.3.1 Mass conservation

The goal of Equation 6.12 and of the re-initialization step is to ensure mass conservation (Olsson et al., 2007; Zhao et al., 2014a,b,c). I test our implementation of the ICLS on an ideal case.

The domain is composed of a column of ice with dimensions $1\text{mm}\times 1\text{mm}\times 4\text{mm}$. The Level-Set function is initialized to represent a spherical pore of radius 0.25mm at the bottom of the column (see the left panel of Figure 6.5). This sphere is advected upward with a constant velocity of $1\text{mm}\cdot\text{yr}^{-1}$. Pictures of the sphere at the beginning and the end of the simulation are shown in Figure 6.5. The volume of the sphere is computed at the end of each time-step using the volume enclosed by the Level-Set function.

I tested several sets of parameters to find the optimal time-step, h_{grad} , h_{ausd} , and ϵ in terms of mass conservation. It appears that for this specific case, the best parameters are respectively 0.1yr , 1.10 , 0.03mm , and 0.1mm . The error in volume then does not exceed a couple of percent after 20 time-steps and a total advection of 2mm . The evolution of the sphere volume is given in blue in both panels of Figure 6.6.

I also performed a sensitivity analysis of the parameters in order to test their influence on mass conservation. The tested values are reported in Table 6.1, and the corresponding volumes during advection are displayed in the upper panel of Figure 6.6.

Table 6.1 – Parameters used for the sensitivity test of mass conservation.

Time-Step(yr)	h_{grad}	h_{ausd} (mm)	ϵ (mm)	Color in Fig. 6.6
0.1	1.1	0.01	0.1	Blue
0.2	1.1	0.01	0.1	Purple
0.05	1.1	0.01	0.1	Orange
0.1	1.1	0.01	0.2	Green
0.1	1.2	0.01	0.1	Red

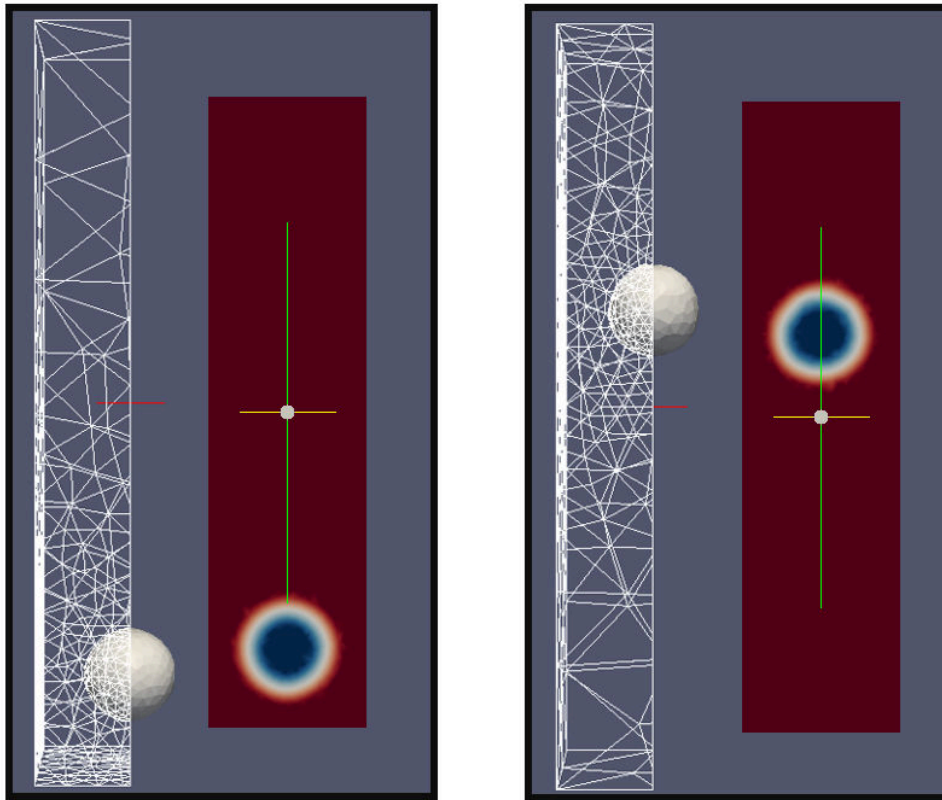


Figure 6.5 – Advection of a sphere using the LevelSet framework. The left and right panels respectively correspond to the start and end the simulation. In each panel: the left part is the side view of the structure with the surface of the sphere in gray and the mesh of the exterior ice in white. The right part is a cross section of the column showing the Level-Set function. Red colors represent the ice phase and blue colors the pore phase.

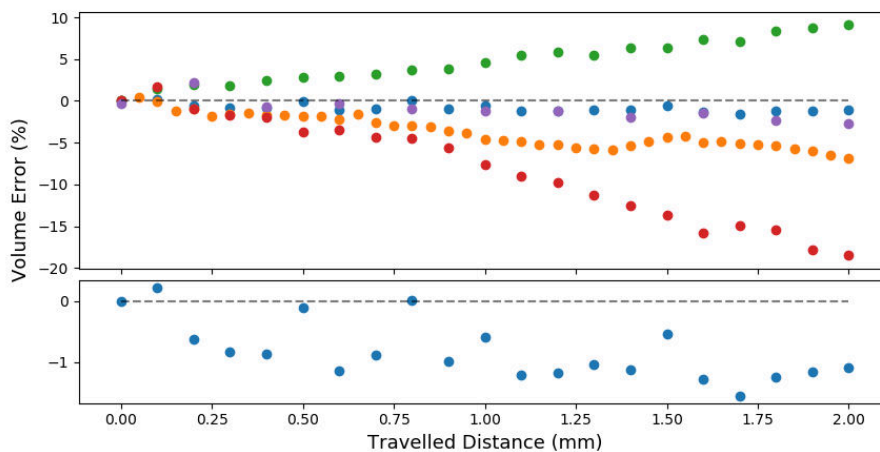


Figure 6.6 – Volume error of the advected sphere, expressed in percent of its initial volume. The blue dots correspond to the optimal parametrization for mass conservation. The specifics parameters of the other simulations are given in Table 6.1. The lower panel is a zoom of the results of the optimal simulation.

The results of the sensitivity analysis show that smaller time-steps do not necessarily imply a better mass conservation. Indeed, comparing the blue ($\Delta t = 0.1\text{yr}$) and orange ($\Delta t = 0.05\text{yr}$) curves in Figure 6.6 indicates a larger error at the end of the total advection in the case of

the smallest time-step. My understanding is that each time-step introduces volume errors during the advection step, and that multiplying time-steps accumulates the errors. Increasing the time-step from 0.1 to 0.2yr (in purple in Figure 6.6) does not increase or reduce the volume error at the end of the total advection.

Moreover, it appears that a poor choice of parameters can lead to a drastic accumulation of errors over time, as seen in green and red in Figure 6.6. The main problem is that it is not straightforward to estimate the ideal parameters for a given simulation, as it depends on the specific geometry and velocity field of the problem. To limit problems of mass conservation, the rest of the simulations of this chapter will not be run for more than 10 time-steps. Following Figure 6.6, this should result in total errors of 5% maximum.

[Zhao et al. \(2014b\)](#) report a similar mass conservation experiment for a 2D case using an advected circle. They manage to maintain a relative error below 2%, for a total advection of about 250 diameters of the circle. Even though the 3D and 2D cases cannot be directly compared, it suggests that the model could be improved in order to ensure a better mass conservation. A better choice of the mesh characteristics (element size and gradation) near the interface could likely improve the mass conservation properties of the method.

6.3.2 Effect of internal pressure on pore compression

Current gas trapping models assume that in deep firn, open and already closed pores compress in a similar fashion ([Rommelaere et al., 1997](#); [Buizert et al., 2012](#); [Wittrant et al., 2012](#)), despite the increased pressure in the already closed bubbles that might slow their compression. However, a lower compression speed in the closed bubbles could explain the discrepancy between measured open to closed porosity ratios in firn and the total amount of air measured in ice in Chapter 4. In this section, we thus propose to test the influence of the internal pressure of bubbles on their compression speed at the bottom of a firn column. For this test, we rely on a firn tomography image obtained in the Lock-In firn core, drilled on the East Antarctic plateau. This site is characterized by an accumulation rate of 3.9cm.yr^{-1} (ice equivalent), a surface temperature of -53°C , and a surface pressure evaluated at 0.0645MPa (645mbar). The chosen sample is $2.5\text{mm}\times 2.5\text{mm}\times 2.5\text{mm}$ wide, and originates from 80m depth, near the start of the pore closure zone.

Two distinct simulations are performed. In the first one, the internal pressure of the pores is set to 0.065MPa (this corresponds to the pressure of open pores found $\sim 100\text{m}$ below surface). In the second case, the internal pressure of the pores increases according to its reduction of volume, following an ideal gas law. In both cases, the compression forces of the overlying column start at 0.62MPa and increase over time due to the surface accumulation rate of 3.9cm of ice equivalent per year. Furthermore, the mechanism of surface-diffusion is removed from the simulations. The time-step is set to 200yr. The volume evolutions for 10 time-steps are displayed in Figure 6.7. It appears that the effect of building pressure does not have a strong impact until more than 500 years have passed. At that point, the building pressure in the closed pores reaches 0.16MPa, more than twice the initial value. The measured thickness of the pore closure zone at Lock-In is of about 20m (see Chapter 4). With an accumulation of 3.9cm per year, a given firn stratum takes about 500yr to cross the pore closure zone. Therefore, this simulation suggests that the effect of building pressure in closed bubbles does not play a major role in the pore closure zone.

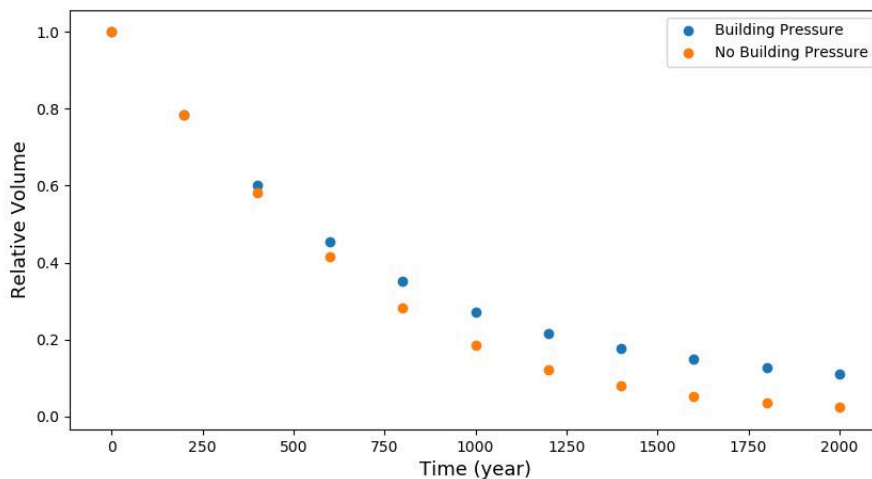


Figure 6.7 – Relative volume as a function of time, with or without building of internal pressure.

To better quantify this effect, we computed the compression speed of the porosity in each case (internal pressure increasing with depth or kept constant). The compression speed is defined here as $\partial_t V/V$, where V is the volume of the porosity and $\partial_t V$ is its temporal derivative. Figure 6.8 shows the ratio of compression speeds with and without building pressure. Within the pore closure zone ($t \leq 500\text{years}$), the compression speed with increasing pressure is on average 90% of the compression speed with constant pressure. We can therefore expect the compression speeds of the open and closed porosity to be similar in the pore closure zone, as assumed in gas trapping models (Rommelaere et al., 1997; Buizert et al., 2012).

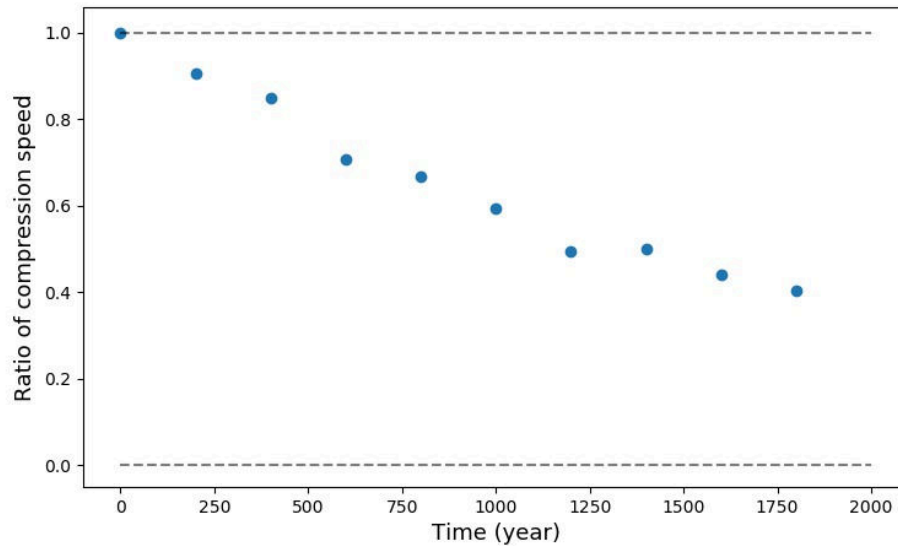


Figure 6.8 – Ratio of compression speeds: with building pressure in the porosity over without building pressure.

6.3.3 Evolution of a firn layer

This section presents the evolution of the porous network of a firn layer, as simulated by the model. Four different experiments are reported to present the contribution of ice creep and curvature-driven diffusion to the morphological changes of the porous network. The simulations are all initialized with the same porous network, extracted from the tomography image of a real firn sample. The firn sample was excavated around the 100m depth in the Lock-In firn core, described in the previous section. A 5.35mm×5.35mm×3.75mm rectangular cuboid was extracted from a tomography image and used for initialization. The external compression starts at 0.66MPa and increases over time according to the 3.9cm of ice per year accumulation rate. The internal pressure of the pores is maintained at 0.065MPa, as we have seen that the building pressure in closed pores is small in the pore closure zone. All simulations are performed with a 100 years time-step, for a maximum of 10 time-steps.

6.3.3.1 Diffusion process only

In the first simulation, the process of ice creep is removed and only the curvature-driven diffusion is taken into account. The parameter C_0 is set to $10^{-6}\text{mm}^4\cdot\text{yr}^{-1}$. A slice of the firn medium is shown in Figure 6.9, and illustrates the evolution of the micro-structure over 700 years. As seen in the figure, the mechanism of surface diffusion leads to a rounding of pores over time. This is consistent with a mass transport occurring from regions of high

curvature towards regions of low curvature, as exemplified in Figure 6.10. While Burr et al. (2019) reports that letting firn samples at rest in a relatively high-temperature environment (-2°C) leads to pore splitting, we did not observe such phenomenon in our simulation. To the contrary, our simulation exhibits pore coalescence, where several small pores merge into a larger one.

As the Level-Set function gives the position of the ice/pore interface, it is possible to convert the output of the simulation into binary images, similar to tomographic images. We performed this conversion for the time-steps $t = 0$ and $t = 700$ years. The binary images can then be analyzed as tomographic images, and the number of individual pores in the medium can be counted (using the ImageJ plug-in Analysis_3D here; Boulos et al., 2012). It reveals that the simulation starts with 39 individual pores in the volume and drops to only 9 individual pores after 700 years. This highlights that pore coalescence happened multiple times during the simulation. Thanks to the Level-Set function, the density of the medium during the simulation can be quantified. The initial relative density to pure ice is 0.902, and drops to 0.884 after 700 years, that is to say a decrease of about 2%. However, the mechanism of surface diffusion should theoretically not modify the density of the medium (Bruchon et al., 2010). The density variation is of the order of the volume error reported in Section 6.3.1. Furthermore, a closer look at the surface diffusion velocity field in Figure 6.10, indicates that despite the stabilization of the equations (introduced in Equations 6.10) the velocity field exhibits a lot of variability that is likely related to numerical noise, rather than physically-relevant variability. We might therefore expect our representation of surface diffusion to introduce some numerical noise in the results, which could also contribute to the decrease in density.

6.3.3.2 Ice creep only

The second simulation is performed with solely the mechanism of ice creep. A slice of the firn medium after compression is displayed in Figure 6.9. As seen in the figure, this simulation leads to a densification of the medium, with a smaller porous network. This observation is confirmed by the analysis of the density, that increased from 0.902 to 0.960 after 700 years. Moreover, the simulation visually exhibits pore splitting. This is again confirmed by counting the number of individual pores before and after the compression. This number increased from 39 to 57 pores, showing the ability of the ice creep mechanism to split and isolate pores from the atmosphere.

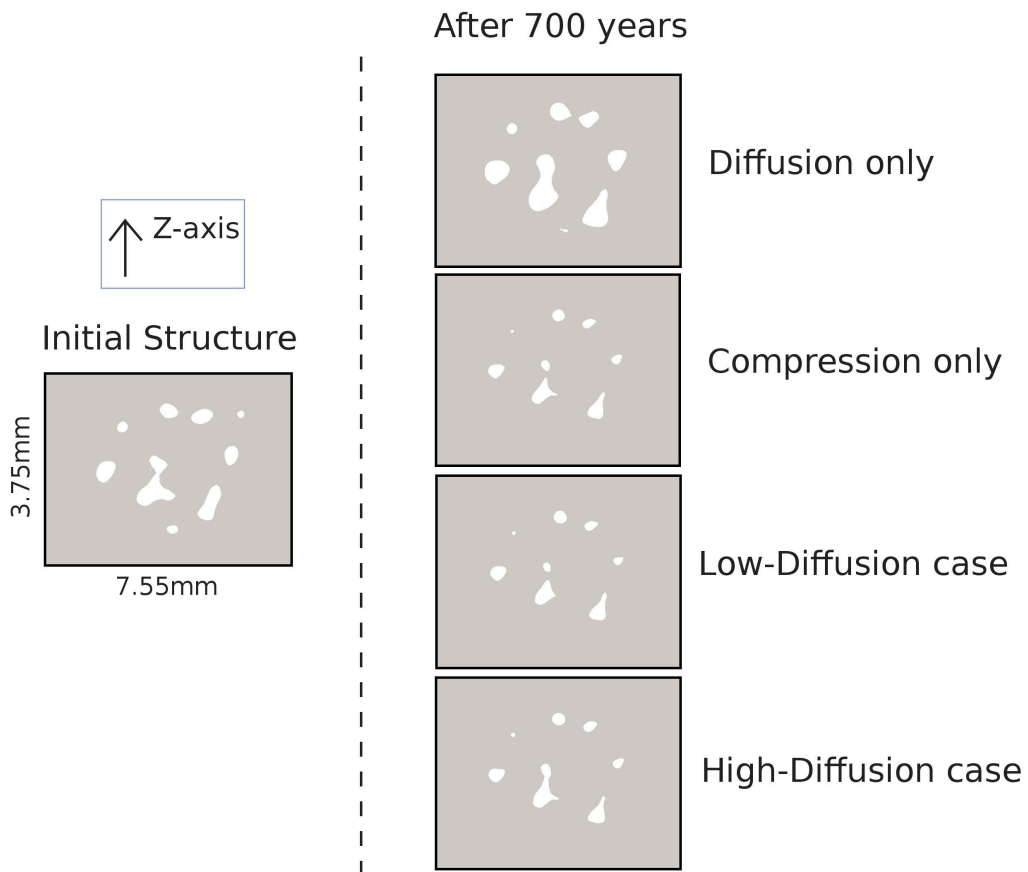


Figure 6.9 – 2D cut-views of the firn material during the simulations. The gray medium is the ice matrix, and the white spaces are the pores. The slice on the left shows the initial porous structure used in all the simulations, and the four slices on the right show the results of the four different simulations after 700 years.

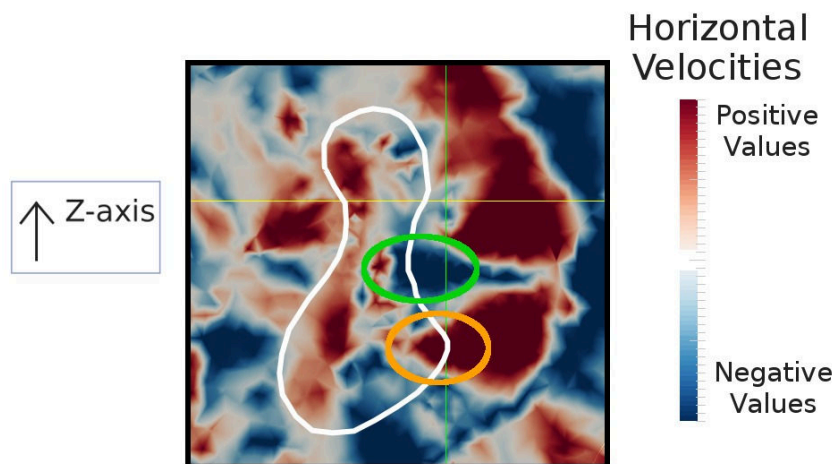


Figure 6.10 – 2D cut-view of the firn material showing the surface-diffusion velocity field in the horizontal direction. Blue colors stand for negative values and red colors for positive values. The interface of a pore is highlighted in white in the middle of the section. The green and orange circles respectively show the regions where the interface is receding in the ice phase and growing in the pore phase. This leads to the rounding of the pore.

6.3.3.3 Ice creep and surface diffusion

The third and fourth simulations take into account the combined effects of curvature-driven diffusion and ice creep. The parameter C_0 is set to values of $10^{-6}\text{mm}^4\cdot\text{yr}^{-1}$ and $10^{-7}\text{mm}^4\cdot\text{yr}^{-1}$, to represent different levels of curvature-driven diffusion, respectively referred to as the low and high-diffusion case for the rest of the section.

2D cut-views of both simulations after 700 years are displayed in Figure 6.9. The results show an increase in relative density from 0.902 to 0.959 for the low-diffusion case, and to 0.953 for the high-diffusion case. Increasing the role of diffusion in the simulation leads to a slightly smaller density. This is consistent with the 0.960 value reported in the absence of surface diffusion. Observation of the Lock-In firn core shows that densities of 0.95 are found around the 130m depth. This is consistent with the 700 years sinking time of the simulation, which corresponds to about 30m of depth increase.

Analysis of the results also shows an increase in the number of individual pores from 39 to 61 and 50 for the low and high-diffusion respectively. It appears that in the high-diffusion case, the mechanism of surface diffusion slows down the splitting of pores. The diffusive mechanism leads to a rounding of the pores, preventing the development of small necks that would eventually lead to pore splitting. Surprisingly, the low-diffusion case displays a little more pore splitting than the case without any surface diffusion, that resulted in 57 individual pores after 700 years. It is not clear if this is related to a specific inter-play between the diffusion and creep mechanisms that would accelerate the splitting of pores, or simply numerical noise.

6.4 Discussion

Combining the Finite Element and Level-Set methods is a promising modeling approach to simulate the topological evolution of firn under compression. Notably, the use of a separate mesh for the ice phase enables to easily compute deformation velocities as response to mechanical compression. This velocity field can then be used to simulate the evolution of the ice/pore interface using the Level-Set function.

Yet, several optimizations of the model are still required before its operational application to study the closure of pores in polar firn. First, the model is currently fully sequential. Run-

ning a ten steps simulation in a $5.35\text{mm}\times 5.35\text{mm}\times 3.75\text{mm}$ firn sample requires roughly a day of computation. The parallelization of the model would curb down this time, to use the model on larger domains. This will allow one to perform simulations of several-centimeter large domains, which have been shown to be more representative of real firn (Schaller et al., 2017). Moreover, as shown in Section 6.3.3.1, the current implementation of the surface diffusion mechanism leads to a noisy velocity field that might deteriorate the robustness of the results. The use of a very fine mesh near the interface could help resolve this problem, but would lead to a sharp increase in the computation time. On the other hand, the use of more sophisticated stabilization techniques (such as in Bruchon et al., 2010) could resolve this issue without an additional computational cost. Another solution could be the use of second-order elements for the computation of the second-derivatives required for the diffusive mechanism. As diffusion appears to play a significant role in the morphology of pores (Burr et al., 2019), it seems important to implement a fast and robust representation of diffusive mechanisms in the model. This would help to decipher the relative contributions of ice creep and diffusion to the evolution of the porous network, and provide insights on the evolution of pores at very-low temperature.

6.5 Conclusion of the chapter

This chapter presents the development, and first few applications of a new model simulating the micro-mechanics of firn. In this model, the ice-pore interface is explicitly taken into account, and its movement is deduced from physical laws. To handle the complex geometries and the topological changes that occur in firn, the model relies on the Level-Set and Finite Element methods.

To capture the evolution of the interface, the model is decomposed in three independent steps, namely the mesh adaptation, computation of velocities and the advection steps. This formulation gives modularity to the model, as physical mechanisms can be added or removed from the computation of the interface's velocity. Moreover, thanks to this modular formulation, the mesh adaptation and advection steps could be modified (for instance to improve mass conservation) without complicating their integration to the rest of the model.

In this chapter, I use the model to first quantify the effect of the building pressure in bubbles in the pore closure zone. Results indicate that the building of pressure does not have a strong impact on the compressibility of bubbles in the pore closure zone, and can therefore be safely neglected in gas trapping models. I also use the model to estimate the impacts of curvature-driven surface diffusion and ice creep on the evolution of the pores in a firn sample. The mechanism of ice creep leads to a densification of the medium, as well as pores splitting. On the other hand, it appears that the mechanism of surface diffusion is responsible for pore coalescence rather than splitting. Moreover, these two examples should be seen as showcases, to demonstrate the ability of the model to compute and capture the movement of the ice-pore interface in response to physical drivers.

Two major issues remain to be improved before an operational use of the model is made possible. First, as shown in the chapter, the Level-Set method does not naturally conserve mass during the simulation. The implementation of the ICLS method greatly improve the mass conservation performance of the model, but improvements remains possible. Notably, more control could be put of the size of the mesh elements near the interface, as [Zhao et al. \(2014a\)](#) showed that its is an important factor for a proper mass conservation. Secondly, the simulations sometimes produce small degenerate elements during the mesh adaptation step. Because of these degenerate elements, the simulations crash before the last time-step.

Again, a better focus should be put on the mesh adaptation step in order to better control the size of the elements near the interface.

Unfortunately, this model cannot represent the crystalline texture of the ice material. Future work should be dedicated to quantify the impact of not explicitly representing the crystal orientations at the pore scale. Such a crystalline texture could be implemented using more than one Level-Set function, each representing a specific crystalline orientation (Bernacki et al., 2008), but is beyond the scope of this study.

Nonetheless, this work exemplifies the possibility to use Level-Set methods to characterize the evolution of porous network in firn. A potential application could be to estimate the impact of different thermodynamical mechanisms on the movement of the interface and the closure of pores (Ashby, 1974; Shieh and Evans, 1991). A second potential application in the future would be to apply it to a large domain (of the order a few centimeters), in order to estimate the progressive closure of the firn porosity. Finally, this type of model could be used to study the development or disappearance of structural anisotropy under metamorphism and compression, and to quantify its impact of the mechanical behavior of the firn material.

Conclusion and Outlooks

Contents

7.1	General conclusion	221
7.2	Perspectives	223
7.3	A few personal words	225

7.1 General conclusion

The goal of this work was to provide a better understanding of the process of gas trapping in polar ice, and notably for the very low accumulation rates typical of the glacial periods on the East Antarctic plateau. By studying the enclosure of gases, we aim to enable a more precise interpretation of the gas signals in ice cores, in order to take full advantage of ice core gas records.

The new insights obtained on the questions introduced in Chapter 2, and that guided my work during these three years of PhD, are summarized below.

What are the physical characteristics of early and late gas trapping layers ? What is the origin of their presence in the firn?

The study of the Lock-In firn core in Chapter 4 confirmed that the firn is a medium with a strong and heterogeneous stratification. This heterogeneous stratification is responsible for the staggered trapping of gases, creating age inversions in the gas records (Mitchell et al., 2015; Rhodes et al., 2016). Using closed porosity data obtained with gas pycnometry, we observed that all firn strata of a given firn have the same relationship between their density and their amount of closed pores. In particular, strata that are especially dense compared to their surroundings contain a higher quantity of closed bubbles than neighboring strata. A similar observation was made concerning the centimeter scale variations of the porous network morphology. Two layers with the same density appears to have porous network with similar shapes, sizes, and gas transport properties, no matter how apart they might be in the firn column. Therefore, early closure layers simply correspond to the dense layers of the firn, and trap gases in a similar fashion as the rest of the firn, simply at shallower depths.

A direct link between the liquid conductivity of firn strata and their density was observed in the pore closure zone. This supports the vision of a deep firn stratification due to the chemical softening of certain firn layers (Hörhold et al., 2012; Fujita et al., 2016). Some layers contain abnormally high amount of ions in their ice phase, leading to a faster densification and a shallower closure in the firn column. This impurity-driven layered gas trapping mechanism is also supported by observations made in deep ice cores. Indeed, we observed that periods with high numbers of important layering artifacts correspond to periods of high levels and variabilities of calcium concentrations in the ice phase.

What is the influence of accumulation on the progressive closure of pores in firn of the East Antarctic plateau? What can be known about the closing of pores under very-low accumulation rate conditions?

Comparing closed porosity data obtained in the Lock-In and Vostok firn cores, we observed that an increase in accumulation rate at constant temperature results in a firn closing at a lower density. This is corroborated by air content data showing that the total porous volume during closure V_i is higher at the higher-accumulation site of Lock-In. This difference in closure density is certainly linked to a difference in the morphology of the two sites' porous networks (e.g. Burr et al., 2018).

The next questions are thus in what sense are the porous networks different, and why would that cause them to seal-off at different densities? The ongoing acquisition of tomography images from different firns of both Greenland and Antarctica (Gregory et al., 2014; Schaller et al., 2017; Burr et al., 2018) could help decipher what are the important characteristics governing the density of closure of firn strata. The compression model that I started to develop during this PhD aims at using tomographic images to simulate the evolution of the firn micro-structure over time, and notably help predicting the characteristics of the porous networks present in past glacial firns of East Antarctica.

What is the degree of smoothing encountered in glacial and interglacial period ice cores from East Antarctica? What is the relationship of smoothing with accumulation?

The gas age distributions of the gases enclosed in ice cores from East Antarctica have been estimated, thanks to a novel technique presented in this work. We are then able to compare the degree of smoothing of gas records for different low-accumulation conditions. The smoothing of gas records in ice cores from East Antarctica dampens out the atmospheric variability that takes place over time scales shorter than a couple of centuries. This notably means that sub-millennial variability can be inferred from the gas records of very low accumulation ice cores, unlike previously thought

We observed that the degree of smoothing increases with the reduction of accumulation from interglacial to glacial conditions. Yet, it is not as drastic as expected. Moreover, the different gas records obtained for the glacial period all appear to have the same degree of smoothing. Thus, smoothing is weakly sensitive to the variations of accumulation for the conditions encountered on the East Antarctic plateau. Therefore, future studies could rely on the usage of a unique age distribution for the study of glacial gas records from East Antarctica.

What is the loss of atmospheric information that one can expect, in the case of low-accumulation and highly thinned deep ice cores drilled on the East Antarctic plateau?

The total loss of information between the atmospheric history and its estimation in ice core gas records, is due to the combined effect of firn smoothing, layering artifacts, and analytical limitations. As discussed above, firn smoothing in ice cores from East Antarctica removes variations that take place over time scales of a couple of hundreds of years and shorter. For layered gas trapping, the thinning of the ice at the bottom of ice sheets implies that the artifacts will no longer be individually resolved. Due to their non-symmetrical distribution, they will add to the total alteration of the gas signal. Yet, results of the layering model, combined with analytical smoothing, indicate that the overall impact will be limited to 10ppbv and 0.5ppmv for the case of methane and carbon dioxide respectively. The influence of analytical resolution cannot be neglected. In the case of methane, even with current CFA systems specifically designed to ensure a good spatial resolution, the act of measurement will remove a part of the record variability and add up to the firn smoothing. For carbon dioxide, estimations of rates of change in the gas records can be significantly underestimated due to the effect of firn smoothing. This underestimation is further aggravated due to the limited spatial resolution of discrete measurements.

7.2 Perspectives

A missing mechanism for gas trapping?

The data obtained for the Lock-in firn and ice core have shown that there is a large discrepancy between the modeled and measured air content values. As explained, this mismatch does not appear to originate from measurement errors, which indicate that the problem lie in the model itself. The inability of models to estimate the right amount of air highlights a potentially missing mechanism in our comprehension of gas trapping in polar ice. To improve our understanding of gas trapping, and to be able to properly model it, this discrepancy needs to be resolved.

In Chapter 4 we proposed a few potential mechanisms to reconcile the data and model. The mechanism of limited compression in the closed bubbles seems unlikely to be the explanation at this stage. Other explanations could be the re-opening of closed bubbles in the firn due to excessive pressure building, or the releasing of air through capillaries not visible

with our experimental methodology. Future work should focus on solving this discrepancy. It will improve the capabilities of models not only to estimate the amount of air in polar ice, but also its composition. Finally, the study of the potential release of gases through capillaries in the pore closure zone could work in synergy with the study of the fractionation of O₂ and N₂ during the trapping process (Huber et al., 2006a; Severinghaus and Battle, 2006).

Parametrizations of pore closure

Another point to improve the ability of gas trapping models to accurately represent the enclosure of gases in polar ice, is the availability of reliable closed porosity profiles. Two major problems hindered this point. First, the measurements of closed porosity data are affected by finite size effects, under the form of cut-bubbles. The acquisition of large firn samples can mitigate this point, but do not totally resolve it. The adaptation of the percolation theory (Enting, 1993) and of finite size analysis (Baglietto and Albano, 2008) from the field of statistical physics could be a way to determine the firn macroscopic properties from smaller scale samples. Moreover, the tools of statistical physics could also help to determine the diffusive properties of firn from centimetric samples.

Then, from the knowledge gained studying various polar sites, new closed porosity parametrizations should be derived. Indeed, such parametrizations are required for firns without direct measurements, such as past firns. Currently, the development of robust closed porosity parametrizations is limited by the inerrant uncertainties due to finite size effects and by the low number of studied sites. It is particularly important to obtain data from sites with similar temperatures but different accumulations (and vice-versa), to independently study the impact of temperature and accumulation on the closure of pores.

Influence of surface metamorphism

A point introduced in Chapter 2, but not further developed in this thesis, is the impact of surface metamorphism. A better comprehension of surface metamorphism and its impact on gas trapping would be of great interest for the dating of ice cores based on air content or O₂/N₂ records (Bender, 2002; Raynaud et al., 2007; Lipenkov et al., 2011). The recent study of Calonne et al. (2017) on the upper surface layering observed at Point Barnola in East Antarctica reports the development of a preferential texture of the ice crystals due to metamorphism. They notably observe, similarly to alpine snow, that dense layers at the surface are characterized by smaller rounded grains and a lesser degree of structural anisotropy.

This appears as inconsistent with the observation of [Fujita et al. \(2009\)](#), that report a positive correlation between density and structural anisotropy. This indicates that the mechanisms at play in the first few meters of the firn column are not yet well understood. The ongoing development of analytical techniques and models focused on the stratification and on the micro-structural properties of snow should bring new insights within the coming years.

Retrieving methane sub-millennial variability

This work provides the gas age distributions of the gas enclosed in East Antarctica ice cores. With this new knowledge, deconvolution techniques could now be used to retrieve as much information as possible from ice core methane records ([Shumway and Der, 1985](#); [Witrant and Martinerie, 2013](#)). Deconvolution methods applied to CFA data from the penultimate glacial period and beyond, would yield new insights on the atmospheric methane variations at the sub-millennial scale.

Such deconvolution could also be applied to the future Oldest-Ice core. In this case, the convolution function to be used in the method should reflect the combined smoothing of the firn and of the analytical system.

7.3 A few personal words

The combination of experimental methods, code development, and general problem solving has been greatly intellectually stimulating during these past few years. This thesis has convinced me of the importance of the interaction between experimental methods and numerical modeling. In my near (and perhaps long) future I intend to continue in the field of scientific research, with a combined approach of experimental and modeling works.

My stay at IGE also introduced me to teaching and science communication. During this three years of PhD I have been teaching at Université Grenoble Alpes, for both undergraduate and graduate students and in the fields of physics, mathematics, computer sciences, and remote sensing. These 192 hours of teaching have been valorized by a Label Recherche et Enseignement Supérieur (Research and Higher Education). Concerning science communication, I have been involved in outreach events outside the institute (Tribulations Savantes, Rencontres Montagnes et Sciences, Pint of Science) and within the institute walls (Cordées

de la réussite and tours of the lab for visitors). I notably keep a particularly good memory of my involvement in the 100 Parrains 100 Classes program, in which I mentored a high school class on the subject of climate change and Antarctic glaciology. These outreach events were the occasion to inform a general audience about the physical mechanisms behind natural phenomena such as glacier flow or the greenhouse effect. I hope that by having a better insight on the underlying material processes, people got a deeper and lasting understanding of the natural phenomena around them.

Appendices

Historical closed porosity data in polar firn

This appendix deals with pycnometry measurements performed by Jean Marc Barnola at IGE in the 1990's. The data have been used to derive a parametrization of the closure of firn porosity, notably used in [Goujon et al. \(2003\)](#), [Buizert et al. \(2012\)](#), or [Witrant et al. \(2012\)](#). Yet, despite their significance for the ice core community, these data have not been published to this day.

To be able to compare the pycnometry data of Lock-In (measured during my PhD) with the ones from Vostok, Antarctica, (measured by JM Barnola), I had to re-process the experimental data of JM Barnola. I reconstructed, with the aid of L Arnaud, X Faïn, and P Martinerie, the processing chain of JM Barnola and was able to apply it to the data obtained for the three polar sites measured in the 1990's: Vostok, Summit (Greenland), and DE08 (Antarctica).

We now intend to publish these data, alongside with the explanation of the processing chain. The goal is to provide the ice core community with these datasets of closed porosity data, to clarify how the parametrization first proposed in [Goujon et al. \(2003\)](#) was derived, and to discuss their limitations. This appendix is thus written as an article draft for a data journal.

Article Draft

Kévin Fourteau¹, Laurent Arnaud¹, Xavier Faïn¹, Patricia Martinerie¹, Jean-Marc Barnola^{1,†}

[1] Univ. Grenoble Alpes, CNRS, IRD, Grenoble INP, IGE, 38000 Grenoble, France

A.1 Introduction

The enclosing of atmospheric air in the ice of polar regions is of great importance for the study of past climates. Indeed, ice cores drilled in the polar regions have the unique characteristics of containing bubbles of air from past atmospheres. These enclosed bubbles have been used to reconstruct the atmosphere history in major greenhouse gas concentrations for the last 800,000 years (Lüthi et al., 2008; Loulergue et al., 2008). However, in order to properly interpret the gas records from ice cores, it is necessary to understand how they are trapped in the ice (Stauffer et al., 1985; Schwander et al., 1993; Rommelaere et al., 1997).

The snow at the surface of polar ice sheets is a porous material, and its interstitial air can freely exchange with the atmosphere (Stauffer et al., 1985). Snow strata are progressively buried under new precipitations and are compressed due to the weight of the younger snow above. This buried and compacted snow is referred to as firn. With time the firn strata are further buried and their interstitial porous networks shrink. Depending on the local temperature and accumulation conditions, some of the pores start to pinch and encapsulate the interstitial air at depths between 50 and 100m below the surface (Witrant et al., 2012). The porous network then continues to pinch until all the interstitial space is isolated from the atmosphere. The firn then becomes airtight ice with enclosed bubbles of atmospheric air.

One way to characterize the closing of the porous network and the trapping of gases is to rely on the closed and the open pore volumes. Closed pores are pores that no longer reach to the atmosphere, and are therefore airtight. On the other hand, open pores reach the atmosphere and the air inside is thus free to escape. Moreover, data of closed and open pore volumes are required for the usage of densification and gas trapping models (Rommelaere et al., 1997; Goujon et al., 2003; Buizert et al., 2012; Witrant et al., 2012). That is why these closed and open volumes have been measured along various firn columns from Greenland

and Antarctica (Schwander et al., 1993; Schaller et al., 2017).

Such measurements were notably performed in the 1990's by JM Barnola on firn cores drilled at the three polar sites of Vostok (Antarctica), Summit (Greenland) and DE08 (Antarctica), using the technique of gas pycnometry on cylindrical samples of approximately 4cm in diameter and height. These data have been used to parametrized closed porosity curves used in gas trapping models (Goujon et al., 2003; Buizert et al., 2012; Witrant et al., 2012). Unfortunately, JM Barnola passed away before publishing the data in the peer-reviewed literature. In an effort of transparency, we propose to make them available. Our goal is to provide an understanding of how the closed porosity parametrization proposed in Goujon et al. (2003) was derived. Moreover, measuring closed porosity is labor intensive and requires large amount of firn material. As a result, this type of data is rather scarce. We hope that making these data available will help the ice core community to better understand the trapping of gases in polar ice.

A.2 The pycnometry method

The technique used by JM Barnola to measure the closed and open porosity volumes in firn samples is the gas pycnometry method (Stauffer et al., 1985). The pycnometry apparatus is composed of two airtight chambers of known volumes V_1 and V_2 with a valve between them allowing one to either connect or isolate the chambers. A pressure gauge is joined to the chamber V_1 to monitor its internal pressure. For the measurements, a firn sample is placed in the first chamber V_1 , while the second one is isolated and vacuum-pumped. Placing a firn sample in the chamber V_1 renders a volume V_s inaccessible to the gases. The pressure P in V_1 is recorded. Then the two chambers are connected, and the gas in chamber V_1 expand in a larger volume. The pressure after dilation P' is then recorded. The volume V_s can be related to the recorded pressure by:

$$V_s = V_1 - \frac{R}{1-R} V_2 \quad (\text{A.1})$$

where $R = P'/P$.

The specific protocol followed by JM Barnola was to first execute a dilation without any sam-

ple in the first chamber, then a second dilation with the sample in. In this case, Equation A.1 can be rearranged as:

$$V_s = V_2 \left(\frac{R_0}{1 - R_0} - \frac{R_1}{1 - R_1} \right) \quad (\text{A.2})$$

where R_0 and R_1 are respectively the pressure ratio in the cases without and with the firm sample in V_1 .

The volume inaccessible to gases is composed of the ice phase and of the closed pores phase. Therefore, one can deduced the closed and open porosity volume:

$$\begin{aligned} V_{cl} &= V_s - V_{ice} \\ V_o &= V_{cyl} - V_s \end{aligned} \quad (\text{A.3})$$

where V_{cl} and V_o are the closed and open porosity volumes, V_{ice} the volume of the ice phase and V_{cyl} the volume of the firm sample. The volume of the ice phase is deduced from the mass M of the sample knowing that $V_{ice} = M/\rho_{ice}$, where ρ_{ice} is the density of pure ice. The density of pure ice is estimated using the temperature relationship $\rho_{ice} = 0.9165(1 - 1.53 \times 10^{-4} T)$, where T is the temperature (Bader, 1964; Goujon et al., 2003). The volume of the firm sample V_{cyl} is measured geometrically.

Note that the pycnometry method assumes that all the pores reaching the edge of the sample are considered as open. This means that some pores that are closed in the firm column (they do not reach the atmosphere) will be considered open during the pycnometry measurement. This is known as the cut-bubble effect and leads to an underestimation of the closed porosity (Martinerie et al., 1990; Schaller et al., 2017).

A.3 Processing of the data

For each of the three sites we retrieved a computer file containing the dilation ratios R_0 and R_1 , the mass of the firm samples, their volumes, and the temperature during the experiment. We also retrieve the source codes of JM Barnola used to process the data. Finally, we also have the experiment notebooks of JM Barnola.

A.3.1 Original data processing

In this section, we aim to reproduce the data processing performed by JM Barnola. This is done for two reasons. First, the data have been used to derive a parametrization of the closed porosity in polar firn (Goujon et al., 2003), and it is therefore important to understand how they were processed. Secondly, the original processing includes corrections for experimental biases that were observed by JM Barnola and that have to be taken into account.

A look at the original source codes indicates that the processing included a correction for a pycnometry system drift and a cut bubbles correction. This correction is based on the idea that the pycnometry method should ideally indicate fully open samples at low density ($\rho < 0.72\text{g.cm}^{-3}$) and fully closed ones at high density ($\rho > 0.86\text{g.cm}^{-3}$). Based on this, a correcting factor α to be applied to the inaccessible volume V_s is computed. In the case of low density firn, α is computed as $1 - V_b/V_{ice}$ and in the case of high density firn one has $\alpha = V_{cyl}/V_s$. JM Barnola observed that this α factor is linearly related to the empty dilation ratio R_0 (Figure A.1). We interpret that this relation is indicative of a drift in the pycnometry apparatus. However, as seen in figure A.1, this linear relationship is not the same for high density and low density firn samples. JM Barnola derived intermediate linear relationships, in black Figure A.1. Using this linear relationship, the correcting factor α can be determined even in the case of not fully closed or open samples. Thus, all the V_s measured in a firn core are corrected by estimating an α factor based on the R_0 of the preceding empty dilation. Finally, in all of the three measurement campaigns the volume V_2 has been estimated to be of 7.2cm^3 (value found directly in JM Barnola's processing codes).

Vostok measurement campaign:

In the case of the Vostok campaign, JM Barnola observed a bias due to the measurements of sample volumes with a caliper, depending of the pressure applied by the caliper. He therefore proposed to apply a volume correction of 0.9% to the firn samples that were measured by applying a too weak pressure with the caliper. JM Barnola also applied a 4°C correction to the recorded temperatures, in order to account for the heat dissipation of heated elements towards the temperature sensor. For the Vostok campaign measurements α is computed

following $\alpha = -40.2145R_0 + 39.22304$, in black in the left panel of Figure A.1. These three corrections were found hard coded in the Vostok processing source code, and have been corroborated by the notebooks.

Summit measurement campaign:

In the case of the Summit campaign the same volume correction of 0.9% was applied to all the samples. Moreover, a weighting bias has been found by JM Barnola and is taken into account by applying a 0.9983 correction factor to the measured mass. Finally, the α correction is given by $\alpha = -45.045045R_0 + 43.820459$, in black in the middle panel of Figure A.1. It is interesting to note that in the case the correction chosen by JM Barnola seems to be based on the low density α only.

DE08 measurement campaign:

For DE08, no volume or mass correction is reported in the original processing code. The α correction is given by $\alpha = -37.2577R_0 + 36.4204$, in black in the right panel of Figure A.1. Again, the correction chosen by JM Barnola appears to be based on the low density α .

Using all these data we can deduce the closed and open porosity volumes. Figure A.2 displays closed porosity and closed porosity ratio values against total porosity. Closed porosity is defined as the volume fraction occupied by the closed pores in the firn sample, total porosity is defined as the volume fraction of all pores and the closed porosity ratio is the ratio of the closed pores volume over the total porous volume. We chose to use volume fractions instead of porous volumes per gram of firn, as the former are not sensitive to temperature and therefore makes the comparison between sites easier. Yet, the volume fraction data can easily be converted to porous volumes per gram of firn using the density of ice.

A.3.2 A new data processing

We identify one major issue in the processing elaborated by JM Barnola. In the case of high density firn samples, the correcting factor α both encapsulates the effect of a system drift

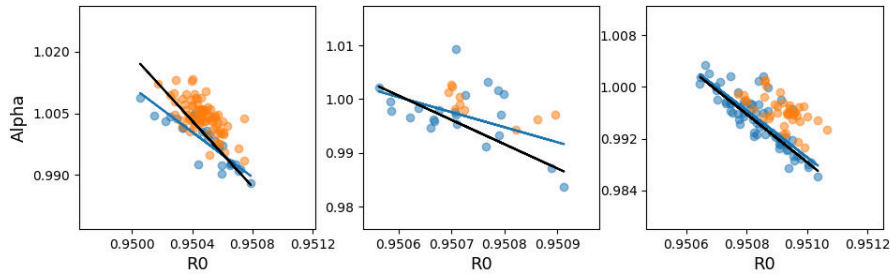


Figure A.1 – In each panel: The blue dots are the correcting factors α computed for low density firn as a function of the preceding R_0 . The orange dots are the correcting factors α computed for high density firn as a function of R_0 . The black line is the linear relation originally derived by JM Barnola. The blue line is the linear regression based solely on the low density α

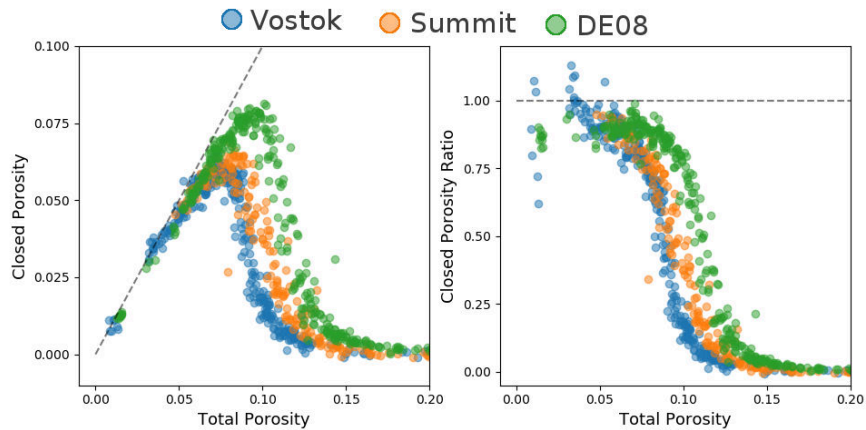


Figure A.2 – Closed porosity data using JM Barnola processing chain. Left panel: Closed porosity against total porosity. The dashed line represents the Closed porosity = Total porosity line. Right panel: Closed porosity ratio against total porosity. The dashed line marks where the closed porosity ratio equals one.

and of cut-bubbles. Indeed, the assumption under which this factor is computed is that the pycnometry experiment should measure a fully closed sample at high density, de facto including a cut-bubble correction. However, the correction to be applied for cut-bubbles is not the same at all densities (Schaller et al., 2017). It thus explains why the high and low density α relationship with R_0 might differ. On the other hand, the low density α does not include any cut-bubble correction, and therefore only accounts for system drifts. We therefore propose to correct the data using only the relationship between low density α and R_0 . These corrections are displayed as blue lines in Figure A.1. As shown in the figure, the new correction mainly differ in the Vostok case. The closed porosity and closed porosity ratio after applying this new correction are displayed in Figure A.3.

It is important to note that these data are not corrected for cut bubbles, and therefore do not directly represent the amount of closed pores in the firn column. We decided not to correct the data for cut bubbles in this article. Indeed, the appropriate corrections are hard

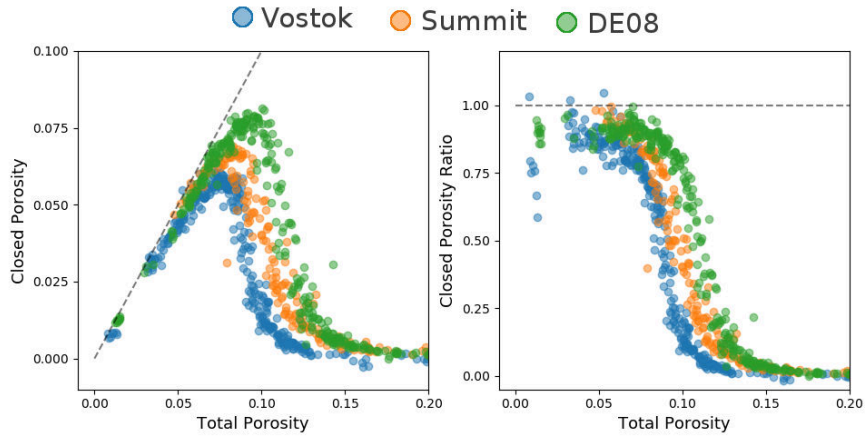


Figure A.3 – Same as Fgire A.2 with the new α correction.

to estimate and potentially site dependent (Schaller et al., 2017). Further research is needed to fully solve this problem.

A.4 The Barnola parametrization for closed porosity

The firn densification and gas trapping model of Goujon et al. (2003) used a parametrization of closed porosity proposed by JM Barnola (Equation 9 of Goujon et al., 2003). This Barnola parametrization relates the closed porosity to the total porosity with:

$$P_{\text{closed}} = \gamma P_{\text{total}} \left(\frac{P_{\text{total}}}{P_{\text{close-off}}} \right)^{-7.6} \quad (\text{A.4})$$

where P_{closed} is the closed porosity, P_{total} the total porosity, $P_{\text{close-off}}$ the close-off porosity that can be estimated using air content measurements or a temperature regression (Martinerie et al., 1994), and γ a factor valued at 0.37.

We are confident to state that the Barnola closed porosity parametrization was deduced from the pycnometry data described in Section A.3.1, with the original processing chain. Indeed, there is a clear linear relationship between the logarithm of the closed porosity ratio and the logarithm of the total porosity normalized by the porosity close-off deduced from air content data. This relation is displayed in Figure A.4, and matches with the Barnola parametrization. The comparison between the experimental closed porosities and the Barnola parametrization is also displayed in Figure A.5. It is therefore important to acknowledge that the Barnola parametrization is based on data that are not fully corrected

for cut-bubbles. Future users of this parametrization should be aware of this limitation. However, since we are not able to properly estimate the corrections to be applied for cut bubbles, we cannot propose a new law replacing the Barnola parametrization.

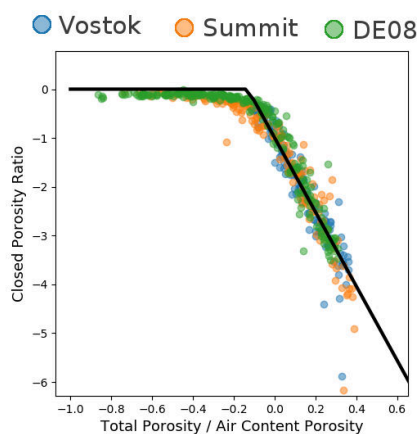


Figure A.4 – Relationship between the logarithm of the closed porosity ratio and the logarithm of the total porosity. The solid black line corresponds to the Barnola parametrization.

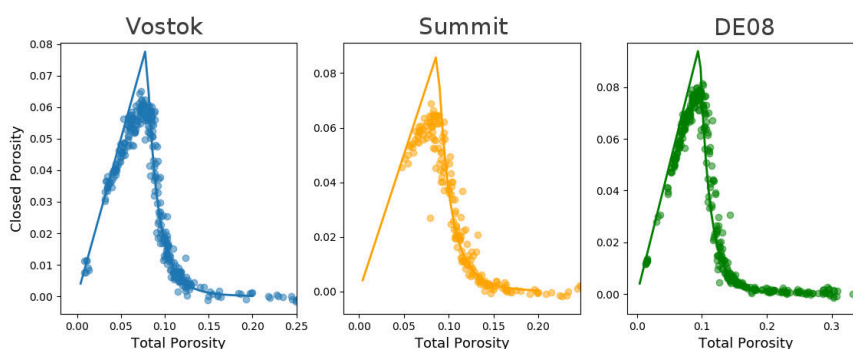


Figure A.5 – Measured closed porosity in the Vostok, Summit and DE08 firns. The corresponding Barnola parametrizations are displayed as solid lines.

A.5 Conclusion

We evaluated pycnometry data from three polar sites obtained in the 1990's by JM Barnola. Based on original computer files, including raw data and processing source codes, we were able to reproduce the processing chain developed by JM Barnola, including experimental bias corrections. We found that these data have not been fully corrected for the cut-bubble effect. We also confirm that the closed porosity data deduced from those pycnometry experiments were used to derive the Barnola closed porosity parametrization, first introduced in Goujon et al. (2003). Consequently, this parametrization suffers from the incomplete cut-bubble correction of the pycnometry data.

Finally, we intend to make these data publicly available. The three sites studied in this article are characterized by a wide range of accumulation rates and temperatures. These data could be useful for future studies focusing on the effect of the climatic conditions on pore closure and gas trapping.

Firn air pumping campaigns at EastGRIP

During my PhD, I participated to two firn air pumping campaigns at the Greenland site of EastGRIP (EGRIP) ¹. EGRIP is located in North-East Greenland, at the surface of the North East Greenland Ice Stream (NEGIS). NEGIS is a large ice stream draining 12% of the Greenland coastal mass flux. A deep drilling campaign is currently taking place, with the main objective of better understanding of the evolution of NEGIS in the past.

Taking advantage of the camp and facilities deployed to host the deep drilling, other scientific projects are conducted at the EGRIP site. Notably, a project of firn air pumping was decided. The main objective of this project is to retrieve a firn core, as well as firn air data from the open porosity of the firn column. This campaign serve three scientific objectives: i) reconstructing past atmospheric concentrations using the air hold in the firn, ii) providing insights on the firn smoothing and layered trapping at a site with no studied equivalent in terms of temperature and accumulation, iii) helping understand the O₂/N₂ signals in ice cores.

My role during this project was to restore and prepare the IGE firn air pumping system, and to participate on its deployment at the EGRIP site.

B.1 General principle of firn air pumping

The method to sample air from the open porosity of the firn is fairly straightforward:

- Drill to the depth of interest.

¹<https://eastgrip.org/>

- Seal the borehole to isolate the bottom of the hole from the upper atmosphere.
- Pump at the bottom of the borehole.

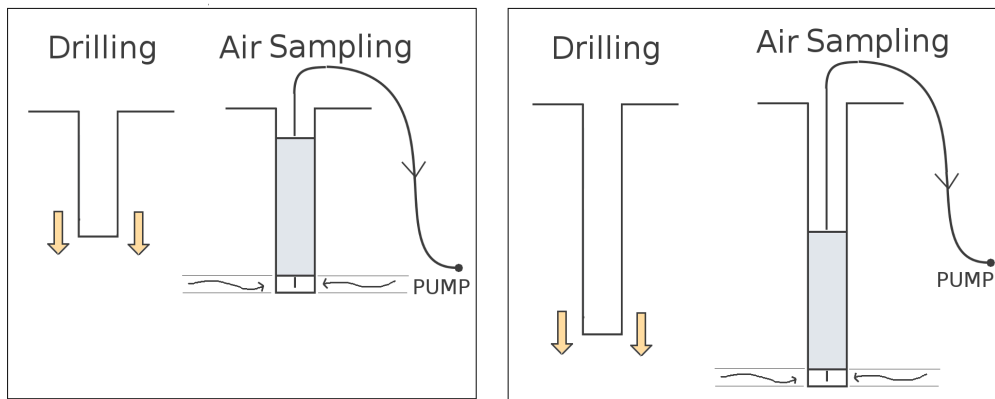


Figure B.1 – Firm pumping methodology. The borehole is drilled until the depth of interest. Then the borehole is sealed (in gray in the Figure) and the air is pumped from the bottom of the firm.

This methodology is summarized in Figure B.1. The borehole is sealed with an inflated rubber bladder, that acts as a plug. The sampled air is then stored either in canisters or in glass bottles.

B.2 Preparing the firm air pumping system

IGE has a firm air pumping system composed of:

- A rubber bladder
- A tripod with a winch fit to lower the bladder into the borehole
- A system of dedicated pumps, tubing, and valves to route the pumped air to containers

This system was restored and assembled at IGE with the help of A. Orsi and X. Faïn. The goal was to ensure that the firm air pumping gear could be deployed in working conditions at the EGRIP site.

B.2.1 Preparing the bladder

A rubber bladder is used to seal the borehole. It ensures that the pumped air originates from the open porosity of the firm, and not from the overlying atmosphere (see Figure B.1). The bladder is composed of a rubber tube, sealed by two aluminum pieces (as shown in

Figures B.2 and B.3). Three separate pieces of dekabon tubing are also connected to the bladder: two that are traversing it (referred to as the Sample and Purge tubings), and one that stops inside the bladder (referred to as the Bladder tubing). The bladder tubing is used to inflate the bladder, and the sample and purge tubings are used to pump firm air.

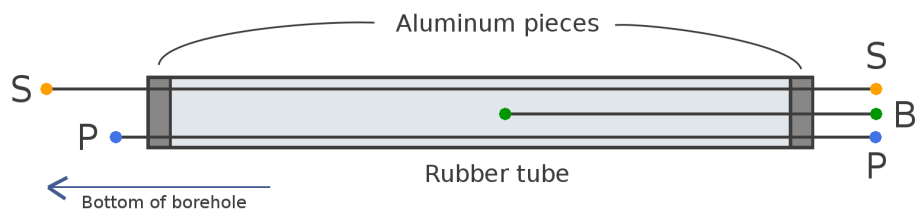


Figure B.2 – Schematics of the bladder with the sealing aluminum pieces. The sample (S), purge (P), and bladder (B) tubings are also displayed.



Figure B.3 – Aluminum piece sealing the rubber tube. The piece is pierced for tubing connections. Three mounted airtight tube fittings are visible.

It is crucial that the bladder does not leak air when inflated in the borehole. Indeed, in the case of a leak two problems arise. First, the bladder might lose its sealing effect and let atmospheric air reach the bottom of the borehole. This would contaminate the sampled firm air. Secondly, the air leaking from the bladder might be released at the bottom of the firm. This would also lead to a contamination of the sample.

The bladder was thus assembled in Grenoble, and checked for potential leaks. To test for leaks, the bladder was inflated with Helium and connected to a pressure gauge. A leak can

be visualized through a decrease in the internal pressure of the bladder. The use of Helium to fill the bladder also allows one to use an Helium detector to spot the precise connection responsible for the leak. The bladder was also tested for leaks in cold rooms, to estimate its airtightness at low temperatures.

From these tests, we decided to use Viton[®] o-rings and PTFE ferrules. Specific care is needed when tightening the PTFE ferrules, as they deform easily and can become leaky. Moreover, with used tube fittings on both sides of the aluminum pieces (therefore inside and outside of the rubber bladder) to increase the airtightness of the system.

B.2.2 Preparing the pumping and tubing system

The pumping system used to collect firm air data can be decomposed in three parts, corresponding to each of the tubings.

Sample tubing

The goal of the sample tubing is to collect firm air from the open porosity and transfer it to the containers at the surface. The air is pumped from the open porosity thanks to a clean pump (Metal Bellows MN151), suitable for carbon monoxide sampling. This air is then dried with a water trap, and routed either to a pre-vacuumed canister or a to glass bottle.

Purge tubing

The goal of the purge tubing is to catch potential leaks before they reach the sample tubing. Indeed, the purge tubing is located above the sample tubing and will thus pump air arriving from the above atmosphere or bladder. The air from the purge tubing is discarded through a vent or used to inflate the bladder.

Bladder tubing

The bladder tubing is simply designed to inflate the bladder in the borehole. It is connected to a pressure gauge to monitor the internal pressure of the bladder. The air sent down the bladder tubing is the air originating from the purge line. This way, it is possible to fill the bladder with firm air and limit the impact of potential bladder leaks.

A specific table was build by X. Faïn and A. Orsi to mount all the necessary valves and

connections. The overall pumping system is summarized in Figure B.4. The table includes a branch to connect spectrometers in order to monitor the sample concentration (e.g. CO₂, CH₄, or CO) in real-time. A pressure regulator is mounted on this branch. A valve used to shunt the table in also included (number 2 in Figure B.4), so other pumping systems can be plugged to the sample line. Before deploying the firm air gear, it is necessary to ensure that the 300m+ of dekabon tubing used to pump gases are not damaged.

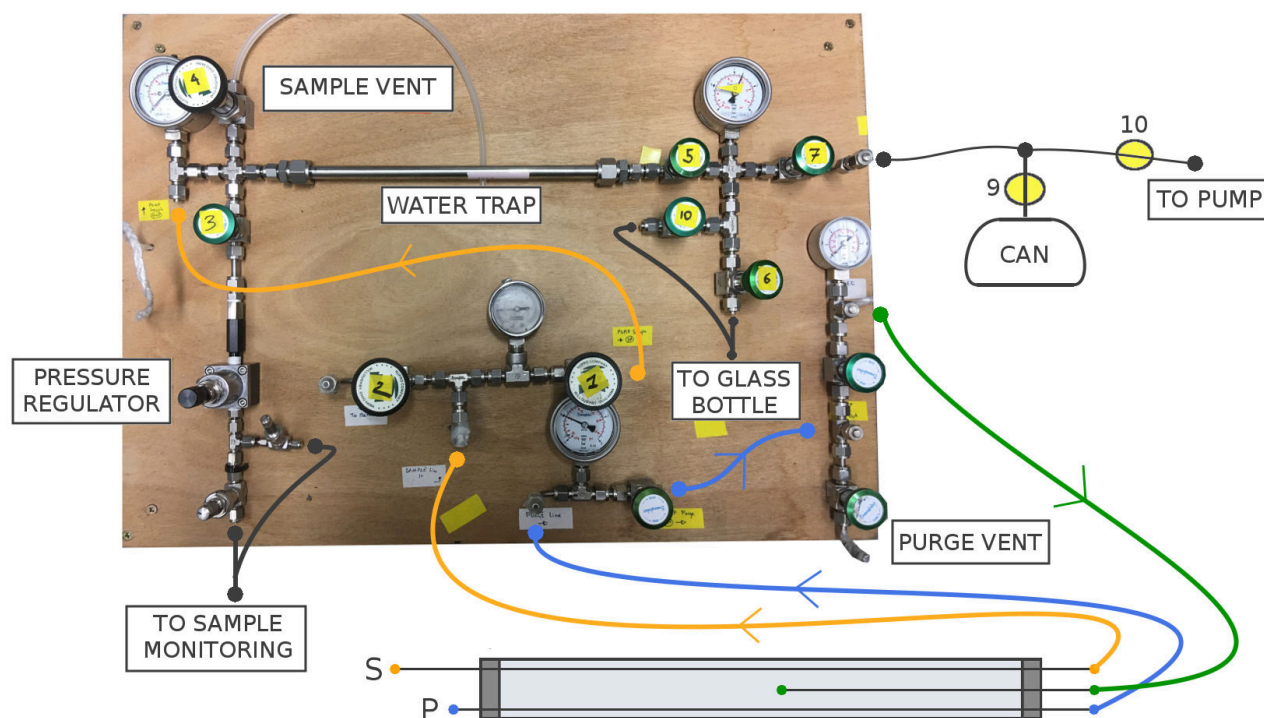


Figure B.4 – Connections table of the IGE system.

B.3 Field work

B.3.1 Protocol of firm air pumping

A specific protocol was written with the help of A. Orsi to sample firm air with the IGE pumping system. It is shown in Figures B.5 and B.6. The number of the valves are the one written on the table in Figure B.4. The valves 9 and 10, which are not directly mounted in the table, are also shown in the figure.

B.4 Tips and tricks

Here are a few feedbacks on my experience doing firn air pumping at EasGRIP.

- Extreme care must be taken to ensure that the bladder fits in the borehole. The first firn air pumping campaign was not successful as the bladder got stuck in the borehole. Moreover, analysis of the collected air samples indicates that the bladder was higher than the bottom of the borehole during the different sample collections. A way to avoid this problem is to ensure that no part of the bladder sticks outside of the rubber tube. In particular, the clamps used to fix the aluminum pieces to the rubber tube might be poorly orientated. Secondly, the borehole should be drilled as straight as possible.

- When the pre-vacuumed canister is abruptly open, a pressure drop will propagate along the sample line. After investigation we discovered that the pressure regulator used to connect measuring instruments to the sample line lets ambient air enter the system, if its input pressure drops below the atmospheric level. To avoid this issue, future users of the IGE system should slowly connect pre-vacuumed canisters to ensure that the pressure at the pressure regulator remains above atmospheric levels at all times.

Installation

1. Lower the bladder :

Do it while pumping, to minimize the modern air pushed into the firm.

Keep valves 1, 3, 4, 20, 21 open ; 2, 5, 22 closed.

Lower the last 10 m very slowly.

2. Inflate bladder : open 22, close 21, until P reaches roughly 0.4 Bar above ambient.
3. Start purge line : when Pbladder ≥ 0.4 Bar, open 21 and close 22 simultaneously. P decreases a bit in the process, so start a bit above 0.4 Bar.
4. Stabilisation : Watch li-cor and Picarro until the concentration stabilizes (can take 30 min)
5. While it is stabilizing, plug the flow meter to the waste line (downstream of valve 4), and write flow rate in the notebook.
6. **Write in notebook:**
 - a. **Sampling depth**
 - b. **Start time, starting values of CH₄ and CO₂**
 - c. **Flow rate through vent valve 4.**
 - d. **Time and stable values of CH₄ and CO₂.**

7. **Evacuate canisters during stabilization or during drill time :**

- a. 5, 6, 7, 10 are closed, 4 is open.
- b. Install canister, start pump C.
- c. Open 8, open 7, wait 15 sec or until you get to "vaccum" on the gage.
- d. Close 8, wait 30 sec to leak check: look at the gauge and see if it is increasing. If it is, you have a leak in the connection you made with the canister, try to tighten it, or take it apart and put it back.
- e. Open 8 again, then open 9 (canister valve) slowly.
- f. Pump at least 15 min.

Glass flask filling procedure :

1. Set up :

- a. Open 4 (vent), close 7, 6 and 10, install the flasks in series and bypass line.
- b. Install the flow meter at the outlet of the bypass.
- c. Open flask valves.
- d. Open 5 and 10 (by pass), close 4
- e. Adjust the pressure release valve to the right setting (1 Bar above ambient, as required by SNU)
- f. Open valve 6.

2. Sample : Close the by pass line (10), flush the flasks for 15 min.

3. Measure flow rate and write in notebook

4. **Note in the notebook:**

- a. **Flask names**
- b. **Start and end time of sampling (flushing)**
- c. **CO₂ and CH₄ of the sampling time**
- d. **Flow rate at the outlet of the line.**

5. Secure sample : when the 15 min are elapsed, open the by pass line, wait for the flow to stabilize again (2 sec), close 6, wait 2 seconds, and close the flask valves, in order, from upstream to downstream (11 then 12).

6. Prepare for the next step :

- a. 6 is closed. Close 10 and open 4.
- b. Start taking out the flasks, when the top one is done, close 4 and open 6, so that valve 6 is our new "vent" valve.

Figure B.5 – Firm air pumping protocol, Part 1.

Canister filling procedure :

7. Hook up canister.
 - 7.A. If canister is not evacuated :
 - close 5 and 6, open 4.
 - Open 8, open 7, wait 15 sec until you get to "vacuum" on the gage.
 - Close 8, wait 30 sec to leak check : look at the gauge and see if it is increasing. If it is, you have a leak in the connection you made with the canister, try to tighten it, or take it apart and put it back.
 - Open 8 again, then open 9 (canister valve) slowly.
 - Set the timer for 15 min evacuation.
 - When 13 min are up, close 7, open 6, open 6 and close 4, flush the water trap for 2 min.
 - 7.B If canister is pre-evacuated:
 - 7 is closed, open 8, wait 5 seconds, open 9, re-evacuate the line and canister for 2 min
 - 5 is open, 6 is open (connected to nothing, as a vent valve) and 4 is closed.
8. Fill-flush 2x canister :
 - a. Close 8 (pump), close 6 and immediately open 7 (slowly), let the pressure increase to 0.2 Bar above ambient
 - b. Close 7, open 6, open 8 to evacuate canister again for 2 min
 - c. Repeat the above 2 steps another time
9. Fill canister : close 8 : close 6 - open 7, let the pressure increase to 2 bars above ambient (max the pump can supply).
 - 3L silco-cans : takes 6 min
 - 6L silco-cans : takes 10 min
10. Write in the notebook:
 - a. Cannister ID
 - b. Start and end time of sampling (step 9)
 - c. CO₂ and CH₄ of the sampling time from Picarro.
11. Prepare a tag to put on the canister with : EGRIP-17; depth; CO₂ value; Pressure (Atm+2bars). For IMAU canisters, there is an additional sheet to fill out.
12. Secure sample: Close 7- open 6, close 9, label the sample can.
13. Open briefly 7 to let air out, close 7. Take out the canister, and put on the next one.
14. Go back to step 7 for the next canister

Disconnect :

15. open 4 (waste), close 5, close 6, 7, 10 to avoid surprises.
16. switch off all pumps.
17. Watch the purge gauge, wait until it reaches Patm.
18. Then, deflate bladder : open 22 slowly until P_bladder reaches Patm.
19. Bring bladder back to the surface.

Figure B.6 – Firm air pumping protocol, Part 2.

Bibliography

- Abe-Ouchi, A., Saito, F., Kawamura, K., Raymo, M. E., Okuno, J., Takahashi, K., and Blatter, H.: Insolation-driven 100,000-year glacial cycles and hysteresis of ice-sheet volume, *Nature*, 500, 190, doi:10.1038/nature12374, 2013.
- Adalsteinsson, D. and Sethian, J.: The Fast Construction of Extension Velocities in Level Set Methods, *J. Comput. Phys.*, 148, 2 – 22, doi:10.1006/jcph.1998.6090, 1999.
- Ahn, J., Brook, E. J., and Buizert, C.: Response of atmospheric CO₂ to the abrupt cooling event 8200 years ago, *Geophys. Res. Lett.*, 41, 604–609, doi:10.1002/2013gl058177, 2014.
- Allan, D. W.: Statistics of atomic frequency standards, *Proc. IEEE*, 54, 221–230, doi:10.1109/proc.1966.4634, 1966.
- Alley, R. B.: Firn densification by grain-boundary sliding: a first model, *J. Phys. Colloques*, 48, C1–249, doi:10.1051/jphyscol:1987135, 1987.
- Anderson, D. L. and Benson, C. S.: The densification and diagenesis of snow, in: *Ice and Snow: Properties, Processes, and Applications*, edited by Kingery, W. D., pp. 391–411, MIT Press, Camb., Mass., 1963.
- Arnaud, L., Barnola, J.-M., and Duval, P.: Physical modeling of the densification of snow/-firn and ice in the upper part of polar ice sheets, *Phys. Ice Core Rec.*, pp. 285–305, URL <http://hdl.handle.net/2115/32472>, 2000.
- Arzt, E.: The influence of an increasing particle coordination on the densification of spherical powders, *Acta Metall.*, 30, 1883–1890, doi:10.1016/0001-6160(82)90028-1, 1982.
- Arzt, E., Ashby, M. F., and Easterling, K. E.: Practical applications of hotisostatic pressing diagrams: four case studies, *Metall. Trans. A*, 14, 211–221, doi:10.1007/BF02651618, 1983.

- Ashby, M.: A first report on sintering diagrams, *Acta Metall.*, 22, 275 – 289, doi:10.1016/0001-6160(74)90167-9, 1974.
- Bader, H.: Density of ice as a function of temperature and stress, Cold Regions Research and Engineering Laboratory, US Army Material Command, 1964.
- Baglietto, G. and Albano, E. V.: Finite-size scaling analysis and dynamic study of the critical behavior of a model for the collective displacement of self-driven individuals, *Phys. Rev. E*, 78, 021 125, doi:10.1103/PhysRevE.78.021125, 2008.
- Barnes, P. R. F., Wolff, E. W., Mader, H. M., Udisti, R., Castellano, E., and Röthlisberger, R.: Evolution of chemical peak shapes in the Dome C, Antarctica, ice core, *J. Geophys. Res. Atmos.*, 108, doi:10.1029/2002JD002538, 2003.
- Barnola, J.-M., Raynaud, D., Korotkevich, Y. S., and Lorius, C.: Vostok ice core provides 160,000-year record of atmospheric CO₂, *Nature*, 329, 408, doi:10.1038/329408a0, 1987.
- Barnola, J. M., Pierritz, R., Goujon, C., Duval, P., and Boller, E.: 3D reconstruction of the Vostok firn structure by X-ray tomography, in: *Data Glaciol. Stud*, vol. 97, pp. 80–84, 2004.
- Battle, M., Bender, M., Sowers, T., Tans, P., Butler, J., Elkins, J., Ellis, J., Conway, T., Zhang, N., Lang, P., et al.: Atmospheric gas concentrations over the past century measured in air from firn at the South Pole, *Nature*, 383, 231, doi:10.1038/383231a0, 1996.
- Bazin, L., Landais, A., Lemieux-Dudon, B., Toyé Mahamadou Kele, H., Veres, D., Parrenin, F., Martinerie, P., Ritz, C., Capron, E., Lipenkov, V. Y., Loutre, M.-F., Raynaud, D., Vinther, B., Svensson, A., Rasmussen, S. O., Severi, M., Blunier, T., Leuenberger, M., Fischer, H., Masson-Delmotte, V., Chappellaz, J., and Wolff, E. W.: An optimized multi-proxy, multi-site Antarctic ice and gas orbital chronology (AICC2012): 120-800 ka, *Clim. Past*, 9, 1715–1731, doi:10.5194/cp-9-1715-2013, 2013.
- Bender, M. L.: Orbital tuning chronology for the Vostok climate record supported by trapped gas composition, *Earth Planet. Sci. Lett.*, 204, 275 – 289, doi:10.1016/S0012-821X(02)00980-9, 2002.
- Bender, M. L., Sowers, T., Barnola, J.-M., and Chappellaz, J.: Changes in the O₂/N₂ ratio of the atmosphere during recent decades reflected in the composition of air in the firn at Vostok Station, Antarctica, *Geophys. Res. Lett.*, 21, 189–192, doi:10.1029/93gl03548, 1994.

- Bereiter, B., Fischer, H., Schwander, J., and Stocker, T. F.: Diffusive equilibration of N₂, O₂ and CO₂ mixing ratios in a 1.5-million-years-old ice core, *Cryosphere*, 8, 245–256, doi:10.5194/tc-8-245-2014, 2014.
- Berger, A.: Milankovitch theory and climate, *Rev. Geophys.*, 26, 624–657, doi:10.1029/RG026i004p00624, 1988.
- Bernacki, M., Chastel, Y., Coupeuz, T., and Logé, R.: Level set framework for the numerical modelling of primary recrystallization in polycrystalline materials, *Scr. Mater.*, 58, 1129–1132, doi:10.1016/j.scriptamat.2008.02.016, 2008.
- Bigler, M., Svensson, A., Kettner, E., Vallelonga, P., Nielsen, M. E., and Steffensen, J. P.: Optimization of high-resolution continuous flow analysis for transient climate signals in ice cores, *Envir. Sci. Tech.*, 45, 4483–4489, doi:10.1021/es200118j, 2011.
- Boers, N., Ghil, M., and Rousseau, D.-D.: Ocean circulation, ice shelf, and sea ice interactions explain Dansgaard–Oeschger cycles, *Proc. Natl. Acad. Sci. USA*, 115, E11 005–E11 014, doi:10.1073/pnas.1802573115, 2018.
- Boulos, V., Fristot, V., Houzet, D., Salvo, L., and Lhuissier, P.: Investigating performance variations of an optimized GPU-ported granulometry algorithm, in: *Proceedings of the 2012 Conference on Design and Architectures for Signal and Image Processing*, pp. 1–6, URL <https://hal.archives-ouvertes.fr/hal-00787861>, 2012.
- Bouxsein, M. L., Boyd, S. K., Christiansen, B. A., Guldberg, R. E., Jepsen, K. J., and Müller, R.: Guidelines for assessment of bone microstructure in rodents using micro-computed tomography, *J. Bone Miner. Res.*, 25, 1468–1486, doi:10.1002/jbmr.141, 2010.
- Bréant, C., Martinerie, P., Orsi, A., Arnaud, L., and Landais, A.: Modelling firn thickness evolution during the last deglaciation: constraints on sensitivity to temperature and impurities, *Clim. Past*, 13, 833–853, doi:10.5194/cp-13-833-2017, 2017.
- Brook, E. J. and Buizert, C.: Antarctic and global climate history viewed from ice cores, *Nature*, 558, 200, doi:10.1038/s41586-018-0172-5, 2018.
- Brook, E. J., Sowers, T., and Orchardo, J.: Rapid variations in atmospheric methane concentration during the past 110,000 years, *Science*, 273, 1087–1091, doi:10.1126/science.273.5278.1087, 1996.
- Brook, E. J., Harder, S., Severinghaus, J., Steig, E. J., and Sucher, C. M.: On the origin and

- timing of rapid changes in atmospheric methane during the Last Glacial Period, *Global Biogeochemical Cycles*, 14, 559–572, doi:10.1029/1999GB001182, 2000.
- Bruchon, J., Drapier, S., and Valdivieso, F.: 3D finite element simulation of the matter flow by surface diffusion using a level set method, *Int. J. Numer. Methods Eng.*, 86, 845–861, doi:10.1002/nme.3079, 2010.
- Bruchon, J., Pino-Muñoz, D., Valdivieso, F., and Drapier, S.: Finite element simulation of mass transport during sintering of a granular packing. Part I. Surface and lattice diffusions, *J. Am. Ceram. Soc.*, 95, 2398–2405, doi:10.1111/j.1551-2916.2012.05073.x, 2012.
- Buizert, C., Martinerie, P., Petrenko, V. V., Severinghaus, J. P., Trudinger, C. M., Witrant, E., Rosen, J. L., Orsi, A. J., Rubino, M., Etheridge, D. M., Steele, L. P., Hogan, C., Laube, J. C., Sturges, W. T., Levchenko, V. A., Smith, A. M., Levin, I., Conway, T. J., Dlugokencky, E. J., Lang, P. M., Kawamura, K., Jenk, T. M., White, J. W. C., Sowers, T., Schwander, J., and Blunier, T.: Gas transport in firn: multiple-tracer characterisation and model intercomparison for NEEM, Northern Greenland, *Atmos. Chem. Phys.*, 12, 4259–4277, doi:10.5194/acp-12-4259-2012, 2012.
- Buizert, C., Cuffey, K. M., Severinghaus, J. P., Baggenstos, D., Fudge, T. J., Steig, E. J., Markle, B. R., Winstrup, M., Rhodes, R. H., Brook, E. J., Sowers, T. A., Clow, G. D., Cheng, H., Edwards, R. L., Sigl, M., McConnell, J. R., and Taylor, K. C.: The WAIS Divide deep ice core WD2014 chronology-Part 1: methane synchronization (68-31 ka BP) and the gas age-ice age difference, *Clim. Past*, 11, 153–173, doi:10.5194/cp-11-153-2015, 2015.
- Burr, A., Ballot, C., Lhuissier, P., Martinerie, P., Martin, C. L., and Philip, A.: Pore morphology of polar firn around closure revealed by X-ray tomography, *Cryosphere*, 12, 2481–2500, doi:10.5194/tc-12-2481-2018, 2018.
- Burr, A., Lhuissier, P., Martin, C. L., and Philip, A.: In situ X-ray tomography densification of firn: The role of mechanics and diffusion processes, *Acta Mater.*, 167, 210 – 220, doi:10.1016/j.actamat.2019.01.053, 2019.
- Caillon, N., Severinghaus, J. P., Jouzel, J., Barnola, J.-M., Kang, J., and Lipenkov, V. Y.: Timing of Atmospheric CO₂ and Antarctic Temperature Changes Across Termination III, *Science*, 299, 1728–1731, doi:10.1126/science.1078758, 2003.
- Calonne, N., Montagnat, M., Matzl, M., and Schneebeli, M.: The layered evolution of fabric

- and microstructure of snow at Point Barnola, Central East Antarctica, *Earth Planet. Sci. Lett.*, 460, 293 – 301, doi:10.1016/j.epsl.2016.11.041, 2017.
- Capron, E., Landais, A., Buiron, D., Cauquoin, A., Chappellaz, J., Debret, M., Jouzel, J., Leuenberger, M., Martinerie, P., Masson-Delmotte, V., Mulvaney, R., Parrenin, F., and Prié, F.: Glacial-interglacial dynamics of Antarctic firn columns: comparison between simulations and ice core air- $\delta^{15}\text{N}$ measurements, *Clim Past*, 9, 983–999, doi:10.5194/cp-9-983-2013, 2013.
- Chappellaz, J., Barnola, J.-M., Raynaud, D., Korotkevich, Y. S., and Lorius, C.: Ice-core record of atmospheric methane over the past 160,000 years, *Nature*, 345, 127–131, doi:10.1038/345127a0, 1990.
- Chappellaz, J., Stowasser, C., Blunier, T., Baslev-Clausen, D., Brook, E. J., Dallmayr, R., Fäin, X., Lee, J. E., Mitchell, L. E., Pascual, O., Romanini, D., Rosen, J., and Schüpbach, S.: High-resolution glacial and deglacial record of atmospheric methane by continuous-flow and laser spectrometer analysis along the NEEM ice core, *Clim. Past*, 9, 2579–2593, doi:10.5194/cp-9-2579-2013, 2013.
- Clark, P. U., Archer, D., Pollard, D., Blum, J. D., Rial, J. A., Brovkin, V., Mix, A. C., Pisias, N. G., and Roy, M.: The middle Pleistocene transition: characteristics, mechanisms, and implications for long-term changes in atmospheric pCO₂, *Quat. Sci. Rev.*, 25, 3150–3184, doi:10.1016/j.quascirev.2006.07.008, 2006.
- Colbeck, S. C.: Air movement in snow due to windpumping, *J. Glaciol.*, 35, 209–213, doi:10.1017/S0022143000004524, 1989.
- Cooper, S. J., Bertei, A., Shearing, P. R., Kilner, J. A., and Brandon, N. P.: TauFactor: An open-source application for calculating tortuosity factors from tomographic data, *SoftwareX*, 5, 203–210, doi:10.1016/j.softx.2016.09.002, 2016.
- Craig, H., Horibe, Y., and Sowers, T.: Gravitational separation of gases and isotopes in polar ice caps, *Science*, 242, 1675–1678, doi:10.1126/science.242.4886.1675, 1988.
- Cuffey, K. and Paterson, W. S. B.: *The Physics of Glaciers*, 4th Edition, Academic Press, 2010.
- Dansgaard, W.: The Abundance of O₁₈ in Atmospheric Water and Water Vapour, *Tellus A, Dyn. Meteorol. Oceanogr.*, 5, 461–469, doi:10.1111/j.2153-3490.1953.tb01076.x, 1953.
- Dansgaard, W., Johnsen, S. J., Clausen, H. B., Dahl-Jensen, D., Gundestrup, N. S., Hammer,

- C. U., Hvidberg, C. S., Steffensen, J. P., Sveinbjornsdottir, A. E., and Jouzel, J.: Evidence for general instability of past climate from a 250-kyr ice-core record, *nature*, 364, 218–220, doi:10.1038/364218a0, 1993.
- Dapogny, C. and Frey, P.: Computation of the signed distance function to a discrete contour on adapted triangulation, *Calcolo*, 49, 193–219, doi:10.1007/s10092-011-0051-z, 2012.
- Dapogny, C., Dobrzynski, C., and Frey, P.: Three-dimensional adaptive domain remeshing, implicit domain meshing, and applications to free and moving boundary problems, *J. Comput. Phys.*, 262, 358–378, doi:10.1016/j.jcp.2014.01.005, 2014.
- Daruka, I. and Ditlevsen, P. D.: A conceptual model for glacial cycles and the middle Pleistocene transition, *Clim. Dyn.*, 46, 29–40, doi:10.1007/s00382-015-2564-7, 2016.
- Delmas, R. J., Ascencio, J.-M., and Legrand, M.: Polar ice evidence that atmospheric CO₂ 20,000 yr BP was 50% of present, *Nature*, 284, 155, doi:10.1038/284155a0, 1980.
- Delmotte, M., Chappellaz, J., Brook, E., Yiou, P., Barnola, J., Goujon, C., Raynaud, D., and Lipenkov, V.: Atmospheric methane during the last four glacial-interglacial cycles: Rapid changes and their link with Antarctic temperature, *J. Geophys. Res. Atmos.*, 109, doi:10.1029/2003JD004417, 2004.
- Dlugokencky, E. J., Myers, R. C., Lang, P. M., Masarie, K. A., Crotwell, A. M., Thoning, K. W., Hall, B. D., Elkins, J. W., and Steele, L. P.: Conversion of NOAA atmospheric dry air CH₄ mole fractions to a gravimetrically prepared standard scale, *J. Geophys. Res. Atmos.*, 110, doi:doi.org/10.1029/2005jd006035, 2005.
- Doube, M., Kłosowski, M. M., Arganda-Carreras, I., Cordelières, F. P., Dougherty, R. P., Jackson, J. S., Schmid, B., Hutchinson, J. R., and Shefelbine, S. J.: BoneJ: free and extensible bone image analysis in ImageJ, *Bone*, 47, 1076–1079, doi:10.1016/j.bone.2010.08.023, 2010.
- Dreyfus, G. B., Jouzel, J., Bender, M. L., Landais, A., Masson-Delmotte, V., and Leuenberger, M.: Firn processes and $\delta^{15}\text{N}$: potential for a gas-phase climate proxy, *Quat. Sci. Rev.*, 29, 28 – 42, doi:10.1016/j.quascirev.2009.10.012, 2010.
- Duval, P., Ashby, M. F., and Anderman, I.: Rate-controlling processes in the creep of polycrystalline ice, *J. Phys. Chem.*, 87, 4066–4074, doi:10.1021/j100244a014, 1983.
- Dällenbach, A., Blunier, T., Flückiger, J., Stauffer, B., Chappellaz, J., and Raynaud, D.:

- Changes in the atmospheric CH₄ gradient between Greenland and Antarctica during the Last Glacial and the transition to the Holocene, *Geophys. Res. Lett.*, 27, 1005–1008, doi:10.1029/1999GL010873, 2000.
- Enting, I. G.: Statistics of firn closure: a simulation study, *Journal of Glaciology*, 39, 133–142, doi:10.3189/S0022143000015781, 1993.
- EPICA community members, Augustin, L., Barbante, C., Barnes, P. R., Barnola, J. M., Bigler, M., Castellano, E., Cattani, O., Chappellaz, J., Dahl-Jensen, D., Delmonte, B., et al.: Eight glacial cycles from an Antarctic ice core, *Nature*, 429, 623–628, doi:10.1038/nature02599, 2004.
- Etheridge, D. M., Pearman, G. I., and Fraser, P. J.: Changes in tropospheric methane between 1841 and 1978 from a high accumulation-rate Antarctic ice core, *Tellus B Chem. Phys. Meteorol.*, 44, 282–294, doi:10.3402/tellusb.v44i4.15456, 1992.
- Fabre, A., Barnola, J.-M., Arnaud, L., and Chappellaz, J.: Determination of gas diffusivity in polar firn: comparison between experimental measurements and inverse modeling, *Geophys. Res. Lett.*, 27, 557–560, doi:10.1029/1999GL010780, 2000.
- Faïn, X., Chappellaz, J., Rhodes, R. H., Stowasser, C., Blunier, T., McConnell, J. R., Brook, E. J., Preunkert, S., Legrand, M., Debois, T., and Romanini, D.: High resolution measurements of carbon monoxide along a late Holocene Greenland ice core: evidence for in situ production, *Clim. Past*, 10, 987–1000, doi:10.5194/cp-10-987-2014, 2014.
- Fischer, H., Severinghaus, J., Brook, E., Wolff, E. W., Albert, M., Alemany, O., Arthern, R., Bentley, C., Blankenship, D., Chappellaz, J., Creyts, T., Dahl-Jensen, D., Dinn, M., Frezzotti, M., Fujita, S., Gallee, H., Hindmarsh, R., Hudspeth, D., Jugie, G., Kawamura, K., Lipenkov, V. Y., Miller, H., Mulvaney, R., Parrenin, F., Pattyn, F., Ritz, C., Schwander, J., Steinhage, D., van Ommen, T., and Wilhelms, F.: Where to find 1.5 million yr old ice for the IPICS "Oldest-Ice" ice core, *Clim. Past*, 9, 2489–2505, doi:10.5194/cp-9-2489-2013, 2013.
- Fourteau, K., Faïn, X., Martinerie, P., Landais, A., Ekaykin, A. A., Lipenkov, V. Y., and Chappellaz, J.: Analytical constraints on layered gas trapping and smoothing of atmospheric variability in ice under low-accumulation conditions, *Clim. Past*, 13, 1815–1830, doi:10.5194/cp-13-1815-2017, 2017.
- Freitag, J., Dobrindt, U., and Kipfstuhl, J.: A new method for predicting transport properties

- of polar firn with respect to gases on the pore-space scale, *Ann. Glaciol.*, 35, 538–544, doi:10.3189/172756402781816582, 2002.
- Freitag, J., Wilhelms, F., and Kipfstuhl, S.: Microstructure-dependent densification of polar firn derived from X-ray microtomography, *J. Glaciol.*, 50, 243–250, doi:10.3189/172756504781830123, 2004.
- Freitag, J., Kipfstuhl, S., Laepple, T., and Wilhelms, F.: Impurity-controlled densification: a new model for stratified polar firn, *J. Glaciol.*, 59, 1163–1169, doi:10.3189/2013JoG13J042, 2013.
- Fujita, S., Okuyama, J., Hori, A., and Hondoh, T.: Metamorphism of stratified firn at Dome Fuji, Antarctica: A mechanism for local insolation modulation of gas transport conditions during bubble close off, *J. Geophys. Res. Earth Surf.*, 114, F03023, doi:10.1029/2008JF001143, 2009.
- Fujita, S., Hirabayashi, M., Goto-Azuma, K., Dallmayr, R., Satow, K., Zheng, J., and Dahl-Jensen, D.: Densification of layered firn of the ice sheet at NEEM, Greenland, *J. Glaciol.*, 60, 905–921, doi:10.3189/2014JoG14J006, 2014.
- Fujita, S., Goto-Azuma, K., Hirabayashi, M., Hori, A., Iizuka, Y., Motizuki, Y., Motoyama, H., and Takahashi, K.: Densification of layered firn in the ice sheet at Dome Fuji, Antarctica, *J. Glaciol.*, 62, 103–123, doi:10.1017/jog.2016.16, 2016.
- Gautier, E., Savarino, J., Erbland, J., Lanciki, A., and Possenti, P.: Variability of sulfate signal in ice core records based on five replicate cores, *Clim. Past*, 12, 103–113, doi:10.5194/cp-12-103-2016, 2016.
- Gedney, N., Cox, P., and Huntingford, C.: Climate feedback from wetland methane emissions, *Geophys. Res. Lett.*, 31, doi:10.1029/2004GL020919, 2004.
- Genthon, G., Barnola, J., Raynaud, D., Lorius, C., Jouzel, J., Barkov, N., Korotkevich, Y., and Kotlyakov, V.: Vostok ice core: climatic response to CO₂ and orbital forcing changes over the last climatic cycle, *Nature*, 329, 414, doi:10.1038/329414a0, 1987.
- Gibou, F., Fedkiw, R., and Osher, S.: A review of level-set methods and some recent applications, *J. Comput. Phys.*, 353, 82 – 109, doi:10.1016/j.jcp.2017.10.006, 2018.
- Goujon, C., Barnola, J.-M., and Ritz, C.: Modeling the densification of polar firn including heat diffusion: application to close-off characteristics and gas isotopic frac-

- tionation for Antarctica and Greenland sites, *J. Geophys. Res. Atmos.*, 108, 4792, doi:10.1029/2002jd003319, 2003.
- Gregory, S. A., Albert, M. R., and Baker, I.: Impact of physical properties and accumulation rate on pore close-off in layered firn, *Cryosphere*, 8, 91–105, doi:10.5194/tc-8-91-2014, 2014.
- Hagemuller, P., Chambon, G., Lesaffre, B., Flin, F., Calonne, N., and Naaim, M.: Energy-based binary segmentation of snow microtomographic images, in: 1st International Conference on Tomography of Materials and Structures (ICTMS), URL <https://hal.archives-ouvertes.fr/hal-00863099>, 2013.
- Hendy, C. and Wilson, A.: Palaeoclimatic data from speleothems, *Nature*, 219, 48, doi:10.1038/219048a0, 1968.
- Herron, M. M. and Langway, C. C.: Firn Densification: An Empirical Model, *J. Glaciol.*, 25, 373–385, doi:10.3189/S0022143000015239, 1980.
- Hildebrand, T. and Rügsegger, P.: Quantification of Bone Microarchitecture with the Structure Model Index, *Comput. Methods Biomech. Biomed. Eng.*, 1, 15–23, doi:10.1080/01495739708936692, 1997.
- Hobbs, P.: *Ice Physics*, Clarendon Press, Oxford, 1974.
- Höhle, J. and Höhle, M.: Accuracy assessment of digital elevation models by means of robust statistical methods, *ISPRS J. Photogramm. Remote Sens.*, 64, 398–406, doi:10.1016/j.isprsjprs.2009.02.003, 2009.
- Hopcroft, P. O., Valdes, P. J., and Beerling, D. J.: Simulating idealized Dansgaard-Oeschger events and their potential impacts on the global methane cycle, *Quat. Sci. Rev.*, 30, 3258–3268, doi:10.1016/j.quascirev.2011.08.012, 2011.
- Hörhold, M. W., Kipfstuhl, S., Wilhelms, F., Freitag, J., and Frenzel, A.: The densification of layered polar firn, *J. Geophys. Res. Earth Surf.*, 116, doi:10.1029/2009jf001630, 2011.
- Hörhold, M. W., Laepple, T., Freitag, J., Bigler, M., Fischer, H., and Kipfstuhl, S.: On the impact of impurities on the densification of polar firn, *Earth Planet. Sci. Lett.*, 325, 93–99, doi:10.1016/j.epsl.2011.12.022, 2012.
- Huber, C., Beyerle, U., Leuenberger, M., Schwander, J., Kipfer, R., Spahni, R., Severinghaus, J., and Weiler, K.: Evidence for molecular size dependent gas fractionation in firn air

- derived from noble gases, oxygen, and nitrogen measurements, *Earth Planet. Sci. Lett.*, 243, 61–73, doi:10.1016/j.epsl.2005.12.036, 2006a.
- Huber, C., Leuenberger, M., Spahni, R., Flückiger, J., Schwander, J., Stocker, T. F., Johnsen, S., Landais, A., and Jouzel, J.: Isotope calibrated Greenland temperature record over Marine Isotope Stage 3 and its relation to CH₄, *Earth Planet. Sci. Lett.*, 243, 504–519, 2006b.
- Hutterli, M. A., Schneebeli, M., Freitag, J., Kipfstuhl, J., and Röthlisberger, R.: Impact of local insolation on snow metamorphism and ice core records, in: *Physics of Ice Core Records II : Papers collected after the 2nd International Workshop on Physics of Ice Core Records*, vol. 68, pp. 223–232, Institute of Low Temperature Science, Hokkaido University, URL <http://hdl.handle.net/2115/45450>, 2009.
- IPCC: *Climate Change 2014: Synthesis Report. Contribution of Working Groups I, II and III to the Fifth Assessment Report of the Intergovernmental Panel on Climate Change*, 2014.
- Johnsen, S. J., Dansgaard, W., and White, J.: The origin of Arctic precipitation under present and glacial conditions, *Tellus B: Chem. Phys. Meteorol.*, 41, 452–468, doi:10.3402/tellusb.v41i4.15100, 1989.
- Jones, S. and Glen, J.: The effect of dissolved impurities on the mechanical properties of ice crystals, *Philos. Mag. J. Theor. Exp. Appl. Phys.*, 19, 13–24, doi:10.1080/14786436908217758, 1969.
- Jones, S. J.: Softening of ice crystals by dissolved fluoride ions, *Phys. Lett.*, 25A, 366–367, doi:10.1016/0375-9601(67)90702-5, 1967.
- Joos, F. and Spahni, R.: Rates of change in natural and anthropogenic radiative forcing over the past 20,000 years, *Proc. Natl. Acad. Sci. USA*, 105, 1425–1430, URL <https://doi.org/10.1073/pnas.0707386105>, 2008.
- Jouzel, J., Masson-Delmotte, V., Cattani, O., Dreyfus, G., Falourd, S., Hoffmann, G., Minster, B., Nouet, J., Barnola, J.-M., Chappellaz, J., Fischer, H., Gallet, J. C., Johnsen, S., Leuenberger, M., Loulergue, L., Lüthi, D., Oerter, H., Parrenin, F., Raisbeck, G., Raynaud, D., Schilt, A., Schwander, J., Selmo, E., Souchez, R., Spahni, R., Stauffer, B., Steffensen, J. P., Stenni, B., Stocker, T. F., Tison, J. L., Werner, M., and Wolff, E. W.: Orbital and millennial antarctic climate variability over the past 800,000 years, *Science*, 317, 793–796, doi:10.1126/science.1141038, 2007.
- Kawamura, K., Parrenin, F., Lisiecki, L., Uemura, R., Vimeux, F., Severinghaus, J. P.,

- Hutterli, M. A., Nakazawa, T., Aoki, S., Jouzel, J., et al.: Northern Hemisphere forcing of climatic cycles in Antarctica over the past 360,000 years, *Nature*, 448, 912, doi:10.1038/nature06015, 2007.
- Köhler, P., Bintanja, R., Fischer, H., Joos, F., Knutti, R., Lohmann, G., and Masson-Delmotte, V.: What caused Earth's temperature variations during the last 800,000 years? Data-based evidence on radiative forcing and constraints on climate sensitivity, *Quat. Sci. Rev.*, 29, 129 – 145, doi:10.1016/j.quascirev.2009.09.026, 2010.
- Köhler, P., Knorr, G., Buiron, D., Lourantou, A., and Chappellaz, J.: Abrupt rise in atmospheric CO₂ at the onset of the Bølling/Allerød: in-situ ice core data versus true atmospheric signal, *Clim. Past*, 7, 473–486, doi:10.5194/cp-7-473-2011, 2011.
- Köhler, P., Völker, C., Knorr, G., and Bard, E.: High latitude impacts on deglacial CO₂: southern ocean westerly winds and northern hemisphere permafrost thawing, *Nova. Act. Lc.*, 121, 135–140, doi:10013/epic.45322.d002, 2015.
- Krol, Q. and Löwe, H.: Relating optical and microwave grain metrics of snow: the relevance of grain shape, *Cryosphere*, 10, 2847–2863, doi:10.5194/tc-10-2847-2016, 2016.
- Lambert, F., Bigler, M., Steffensen, J. P., Hutterli, M., and Fischer, H.: Centennial mineral dust variability in high-resolution ice core data from Dome C, Antarctica, *Clim. Past*, 8, 609–623, doi:10.5194/cp-8-609-2012, 2012.
- Landais, A., Caillon, N., Severinghaus, J., Barnola, J.-M., Goujon, C., Jouzel, J., and Masson-Delmotte, V.: Analyse isotopique de l'air piégé dans la glace pour quantifier les variations de température, *C.R. Geosci.*, 336, 963–970, doi:10.1016/j.crte.2004.03.013, 2004.
- Landais, A., Barnola, J., Kawamura, K., Caillon, N., Delmotte, M., Ommen, T. V., Dreyfus, G., Jouzel, J., Masson-Delmotte, V., Minster, B., Freitag, J., Leuenberger, M., Schwander, J., Huber, C., Etheridge, D., and Morgan, V.: Firn-air $\delta^{15}\text{N}$ in modern polar sites and glacial–interglacial ice: a model-data mismatch during glacial periods in Antarctica?, *Quat. Sci. Rev.*, 25, 49 – 62, doi:10.1016/j.quascirev.2005.06.007, 2006.
- Landais, A., Masson-Delmotte, V., Stenni, B., Selmo, E., Roche, D., Jouzel, J., Lambert, F., Guillevic, M., Bazin, L., Arzel, O., Vinther, B., Gkinis, V., and Popp, T.: A review of the bipolar see-saw from synchronized and high resolution ice core water stable isotope records from Greenland and East Antarctica, *Quat. Sci. Rev.*, 114, 18 – 32, doi:10.1016/j.quascirev.2015.01.031, 2015.

- Lauritzen, S.-E.: High-Resolution Paleotemperature Proxy Record for the Last Interglaciation Based on Norwegian Speleothems, *Quat. Res.*, 43, 133 – 146, doi:10.1006/qres.1995.1015, 1995.
- Legrand, M. and Mayewski, P.: Glaciochemistry of polar ice cores: A review, *Rev. Geophys.*, 35, 219–243, doi:10.1029/96RG03527, 1997.
- Lide, D. R.: *CRC Handbook of Chemistry and Physics*, CRC Press, 2005.
- Lipenkov, V., Candaudap, F., Ravoire, J., Dulac, E., and Raynaud, D.: A new device for the measurement of air content in polar ice, *J. Glaciol.*, 41, 423–429, doi:10.1017/S0022143000016294, 1995.
- Lipenkov, V. Y.: Air bubbles and air-hydrate crystals in the Vostok ice core, in: *Phys. Ice Core Rec.*, pp. 327–358, Hokkaido University Press, 2000.
- Lipenkov, V. Y., Salamatin, A. N., and Duval, P.: Bubbly-ice densification in ice sheets: II. Applications, *J. Glaciol.*, 43, 397–407, doi:10.1017/S0022143000034973, 1997.
- Lipenkov, V. Y., Raynaud, D., Loutre, M., and Duval, P.: On the potential of coupling air content and O₂/N₂ from trapped air for establishing an ice core chronology tuned on local insolation, *Quat. Sci. Rev.*, 30, 3280 – 3289, doi:10.1016/j.quascirev.2011.07.013, 2011.
- Lisiecki, L. and Raymo, M. E.: A Pliocene-Pleistocene stack of 57 globally distributed benthic $\delta^{18}\text{O}$ records, *Paleoceanograph.*, 20, doi:10.1029/2004PA001071, 2005.
- Loulergue, L., Schilt, A., Spahni, R., Masson-Delmotte, V., Blunier, T., Lemieux, B., Barnola, J.-M., Raynaud, D., Stocker, T. F., and Chappellaz, J.: Orbital and millennial-scale features of atmospheric CH₄ over the past 800,000 years, *Nature*, 453, 383–386, doi:10.1038/nature06950, 2008.
- Lundin, J. M., Stevens, C. M., Arthern, R., Buizert, C., Orsi, A., Ligtenberg, S. R., Simonsen, S. B., Cummings, E., Essery, R., Leahy, W., et al.: Firn Model Intercomparison Experiment (FirnMICE), *J. Glaciol.*, 63, 401–422, doi:10.1017/jog.2016.114, 2017.
- Lüthi, D., Floch, M. L., Bereiter, B., Blunier, T., Barnola, J.-M., Siegenthaler, U., Raynaud, D., Jouzel, J., Fischer, H., Kawamura, K., and Stocker, T. F.: High-resolution carbon dioxide concentration record 650,000– 800,000 years before present, *Nature*, 453, 379–382, doi:10.1038/nature06949, 2008.

- Maeno, N. and Ebinuma, T.: Pressure sintering of ice and its implication to the densification of snow at polar glaciers and ice sheets, *J. Phys. Chem.*, 87, 4103 – 4110, doi:10.1021/j100244a023, 1983.
- Marcott, S. A., Bauska, T. K., Buizert, C., Steig, E. J., Rosen, J. L., Cuffey, K. M., Fudge, T. J., Severinghaus, J. P., Ahn, J., Kalk, M. L., McConnell, J. R., Sowers, T., Taylor, K. C., White, J. W. C., and Brook, E. J.: Centennial-scale changes in the global carbon cycle during the last deglaciation, *Nature*, 514, 616–619, doi:10.1038/nature13799, 2014.
- Martín, C. and Gudmundsson, G. H.: Effects of nonlinear rheology, temperature and anisotropy on the relationship between age and depth at ice divides, *Cryosphere*, 6, 1221–1229, doi:10.5194/tc-6-1221-2012, 2012.
- Martinerie, P., Lipenkov, V. Y., and Raynaud, D.: Correction of air-content measurements in polar ice for the effect of cut bubbles at the surface of the sample, *J. Glaciol.*, 36, 299–303, doi:10.3189/002214390793701282, 1990.
- Martinerie, P., Raynaud, D., Etheridge, D. M., Barnola, J.-M., and Mazaudier, D.: Physical and climatic parameters which influence the air content in polar ice, *Earth Planet. Sc. Lett.*, 112, 1–13, doi:10.1016/0012-821x(92)90002-d, 1992.
- Martinerie, P., Lipenkov, V. Y., Raynaud, D., Chappellaz, J., Barkov, N., and Lorius, C.: Air content paleo record in the Vostok ice core (Antarctica): A mixed record of climatic and glaciological parameters, *J. Geophys. Res. Atmos.*, 99, 10 565–10 576, doi:10.1029/93JD03223, 1994.
- Masson-Delmotte, V., M., Schulz, A., Abe-Ouchi, J., Beer, A., Ganopolski, J., González Rouco, E., Jansen, K., Lambeck, J., Luterbacher, T., Naish, T., Osborn, B., Otto-Bliesner, T., Quinn, R., Ramesh, M., Rojas, X. S., and Timmermann, A.: Information from paleoclimate archives, in: *Climate change 2013: the physical science basis. Contribution of working group I to the fifth assessment report of the Intergovernmental Panel on Climate Change*, edited by Stocker, T. F., Qin, D., Plattner, G. K., Tignor, M., Allen, S. K., Boschung, J., Nauels, A., Xia, Y., Bex, V., and Midgley, P. M., pp. 383–464, Cambridge University Press, Cambridge, United Kingdom and New York, NY, USA, 2013.
- Mayer, E. W., Blake, D. R., Tyler, S. C., Makide, Y., Montague, D. C., and Rowland, F. S.: Methane: Interhemispheric concentration gradient and atmospheric residence time, *Proc. Natl. Acad. Sci. USA*, 79, 1366–1370, doi:10.1073/pnas.79.4.1366, 1982.

- McDermott, F.: Palaeo-climate reconstruction from stable isotope variations in speleothems: a review, *Quat. Sci. Rev.*, 23, 901 – 918, doi:10.1016/j.quascirev.2003.06.021, 2004.
- Mees, F., Swennen, R., Geet, M. V., and Jacobs, P.: Applications of X-ray computed tomography in the geosciences, *Geol. Soc. Lond. Special Publ.*, 215, 1–6, doi:10.1144/GSL.SP.2003.215.01.01, 2003.
- Milankovitch, M. M.: *Théorie Mathématique des Phenomenes Thermiques Produits par la Radiation Solaire*, Ph.D. thesis, Académie Yougoslave des Sciences et des Arts de Zagreb, 1920.
- Mitchell, L., Brook, E., Lee, J. E., Buizert, C., and Sowers, T.: Constraints on the Late Holocene Anthropogenic Contribution to the Atmospheric Methane Budget, *Science*, 342, 964–966, doi:10.1126/science.1238920, 2013.
- Mitchell, L. E., Brook, E. J., Sowers, T., McConnell, J. R., and Taylor, K.: Multidecadal variability of atmospheric methane, 1000–1800 C.E., *J. Geophys. Res. Biogeosci.*, 116, 2007, doi:10.1029/2010JG001441, 2011.
- Mitchell, L. E., Buizert, C., Brook, E. J., Breton, D. J., Fegyveresi, J., Baggenstos, D., Orsi, A., Severinghaus, J., Alley, R. B., Albert, M., Rhodes, R. H., McConnell, J. R., Sigl, M., Maselli, O., Gregory, S., and Ahn, J.: Observing and modeling the influence of layering on bubble trapping in polar firn, *J. Geophys. Res. Atmos.*, 120, 2558–2574, doi:10.1002/2014jd022766, 2015.
- Morville, J., Kassi, S., Chenevier, M., and Romanini, D.: Fast, low-noise, mode-by-mode, cavity-enhanced absorption spectroscopy by diode-laser self-locking, *Appl. Phys. B-Lasers O.*, 80, 1027–1038, doi:10.1007/s00340-005-1828-z, 2005.
- Muller, R. A. and MacDonald, G. J.: Glacial cycles and astronomical forcing, *Science*, 277, 215–218, doi:10.1126/science.277.5323.215, 1997.
- Nakamura, T. and Jones, S.: Softening effect of dissolved hydrogen chloride in ice crystals, *Scr. Metall.*, 4, 123–126, doi:10.1016/0036-9748(70)90176-6, 1970.
- Newman, M. and Barkema, G.: *Monte carlo methods in statistical physics chapter 1-4*, Oxford University Press: New York, USA, 1999.
- Olsson, E. and Kreiss, G.: A conservative level set method for two phase flow, *J. Comput. Phys.*, 210, 225 – 246, doi:10.1016/j.jcp.2005.04.007, 2005.

- Olsson, E., Kreiss, G., and Zahedi, S.: A conservative level set method for two phase flow II, *J. Comput. Phys.*, 225, 785–807, doi:10.1016/j.jcp.2005.04.007, 2007.
- Orsi, A. J., Cornuelle, B. D., and Severinghaus, J. P.: Magnitude and temporal evolution of Dansgaard–Oeschger event 8 abrupt temperature change inferred from nitrogen and argon isotopes in GISP2 ice using a new least-squares inversion, *Earth Planet. Sc. Lett.*, 395, 81–90, doi:10.1016/j.epsl.2014.03.030, 2014.
- Osher, S. and Fedkiw, R. P.: *Level Set Methods: An Overview and Some Recent Results*, *J. Comput. Phys.*, 169, 463 – 502, doi:10.1006/jcph.2000.6636, 2001.
- Osher, S. and Sethian, J. A.: Fronts propagating with curvature-dependent speed: Algorithms based on Hamilton-Jacobi formulations, *J. Comput. Phys.*, 79, 12 – 49, doi:10.1016/0021-9991(88)90002-2, 1988.
- Parrenin, F., Petit, J.-R., Masson-Delmotte, V., Wolff, E., Basile-Doelsch, I., Jouzel, J., Lipenkov, V., Rasmussen, S. O., Schwander, J., Severi, M., Udisti, R., Veres, D., and Vinther, B. M.: Volcanic synchronisation between the EPICA Dome C and Vostok ice cores (Antarctica) 0-145 kyr BP, *Clim. Past*, 8, 1031–1045, doi:10.5194/cp-8-1031-2012, 2012.
- Parrenin, F., Masson-Delmotte, V., Köhler, P., Raynaud, D., Paillard, D., Schwander, J., Barbante, C., Landais, A., Wegner, A., and Jouzel, J.: Synchronous Change of Atmospheric CO₂ and Antarctic Temperature During the Last Deglacial Warming, *Science*, 339, 1060–1063, doi:10.1126/science.1226368, 2013.
- Passalacqua, O., Cavitte, M., Gagliardini, O., Gillet-Chaulet, F., Parrenin, F., Ritz, C., and Young, D.: Brief communication: Candidate sites of 1.5 Myr old ice 37 km southwest of the Dome C summit, East Antarctica, *Cryosphere*, 12, 2167–2174, doi:10.5194/tc-12-2167-2018, 2018.
- Peternell, M., Russell-Head, D., and Wilson, C.: A technique for recording polycrystalline structure and orientation during in situ deformation cycles of rock analogues using an automated fabric analyser, *J. Microsc. Oxford*, 242, 181–188, doi:10.1111/j.1365-2818.2010.03456.x, 2010.
- Petit, J. R., Jouzel, J., Raynaud, D., Barkov, N. I., Barnola, J.-M., Basile, I., Bender, M. L., Chappellaz, J., Davis, M., Delaygue, G., Delmotte, M., Kotlyakov, V. M., Legrand, M., Lipenkov, V. Y., Lorius, C., Pépin, L., Ritz, C., Saltzman, E., and Stievenard, M.: Climate

- and atmospheric history of the past 420,000 years from the Vostok ice core, Antarctica, *Nature*, 399, 429–436, doi:10.1038/20859, 1999.
- Petrenko, V. V., Martinerie, P., Novelli, P., Etheridge, D. M., Levin, I., Wang, Z., Blunier, T., Chappellaz, J., Kaiser, J., Lang, P., Steele, L. P., Hammer, S., Mak, J., Langenfelds, R. L., Schwander, J., Severinghaus, J. P., Witrant, E., Petron, G., Battle, M. O., Forster, G., Sturges, W. T., Lamarque, J.-F., Steffen, K., and White, J. W. C.: A 60 yr record of atmospheric carbon monoxide reconstructed from Greenland firn air, *Atmos. Chem. Phys.*, 13, 7567–7585, doi:10.5194/acp-13-7567-2013, 2013.
- Pimienta, P. and Duval, P.: Rate controlling processes in the creep of polar glacier ice, *J. Phys Colloques*, 48, C1–243, doi:10.1051/jphyscol:1987134, 1987.
- Raymond, C. F.: Deformation in the Vicinity of Ice Divides, *J. Glaciol.*, 29, 357–373, doi:10.3189/S0022143000030288, 1983.
- Raynaud, D. and Lebel, B.: Total gas content and surface elevation of polar ice sheets, *Nature*, 281, 289, doi:10.1038/281289a0, 1979.
- Raynaud, D., Delmas, R., Ascencio, J., and Legrand, M.: Gas Extraction From Polar Ice Cores: A Critical Issue For Studying The Evolution of Atmospheric CO₂ and Ice-Sheet Surface Elevation, *Ann. Glaciol.*, 3, 265–268, doi:10.3189/S0260305500002895, 1982.
- Raynaud, D., Chappellaz, J., Barnola, J., Korotkevich, Y. S., and Lorius, C.: Climatic and CH₄ cycle implications of glacial–interglacial CH₄ change in the Vostok ice core, *Nature*, 333, 655, doi:10.1038/3336, 1988.
- Raynaud, D., Lipenkov, V., Lemieux-Dudon, B., Duval, P., Loutre, M.-F., and Lhomme, N.: The local insolation signature of air content in Antarctic ice. A new step toward an absolute dating of ice records, *Earth Planet. Sci. Lett.*, 261, 337–349, doi:10.1016/j.epsl.2007.06.025, 2007.
- Rhodes, R. H., Fain, X., Stowasser, C., Blunier, T., Chappellaz, J., McConnell, J. R., Romanini, D., Mitchell, L. E., and Brook, E. J.: Continuous methane measurements from a late Holocene Greenland ice core: atmospheric and in-situ signals, *Earth Planet. Sc. Lett.*, 368, 9–19, doi:10.1016/j.epsl.2013.02.034, 2013.
- Rhodes, R. H., Brook, E. J., Chiang, J. C. H., Blunier, T., Maselli, O. J., McConnell, J. R., Romanini, D., and Severinghaus, J. P.: Enhanced tropical methane produc-

- tion in response to iceberg discharge in the North Atlantic, *Science*, 348, 1016–1019, doi:10.1126/science.1262005, 2015.
- Rhodes, R. H., Faïn, X., Brook, E. J., McConnell, J. R., Maselli, O. J., Sigl, M., Edwards, J., Buizert, C., Blunier, T., Chappellaz, J., and Freitag, J.: Local artifacts in ice core methane records caused by layered bubble trapping and in situ production: a multi-site investigation, *Clim. Past*, 12, 1061–1077, doi:10.5194/cp-12-1061-2016, 2016.
- Ritman, E. L.: Micro-Computed Tomography—Current Status and Developments, *Annu. Rev. Biomed. Eng.*, 6, 185–208, doi:10.1146/annurev.bioeng.6.040803.140130, 2004.
- Romanini, D., Chenevier, M., Kassi, S., Schmidt, M., Valant, C., Ramonet, M., Lopez, J., and Jost, H.-J.: Optical-feedback cavity-enhanced absorption: a compact spectrometer for real-time measurement of atmospheric methane, *Appl. Phys. B-Lasers O.*, 83, 659–667, doi:10.1007/s00340-006-2177-2, 2006.
- Rommelaere, V., Arnaud, L., and Barnola, J.-M.: Reconstructing recent atmospheric trace gas concentrations from polar firn and bubbly ice data by inverse methods, *J. Geophys. Res. Atmos.*, 102, 30 069–30 083, doi:10.1029/97jd02653, 1997.
- Rothwell, R. G. and Rack, F. R.: New techniques in sediment core analysis: an introduction, *Geol. Soc. Lond. Special Publ.*, 267, 1–29, doi:10.1144/GSL.SP.2006.267.01.01, 2006.
- Rousseeuw, P. J. and Hubert, M.: Robust statistics for outlier detection, *Wires Data Min. Knowl. Discov.*, 1, 73–79, doi:10.1002/widm.2, 2011.
- Salamatin, A. N., Lipenkov, V. Y., Barnola, J. M., Hori, A., Duval, P., and Hondoh, T.: Snow/firn densification in polar ice sheets, *Low Temperature Science*, 68, 195–222, 2009.
- Salmon, P. L., Ohlsson, C., Shefelbine, S. J., and Doube, M.: Structure Model Index Does Not Measure Rods and Plates in Trabecular Bone, *Front. Endocrinol.*, 6, 162, doi:10.3389/fendo.2015.00162, 2015.
- Schaller, C. F., Freitag, J., and Eisen, O.: Critical porosity of gas enclosure in polar firn independent of climate, *Clim. Past*, 13, 1685–1693, doi:10.5194/cp-13-1685-2017, 2017.
- Schmitt, J., Schneider, R., and Fischer, H.: A sublimation technique for high-precision measurements of $\delta^{13}\text{CO}_2$ and mixing ratios of CO_2 and N_2O from air trapped in ice cores, *Atmos. Meas. Tech.*, 4, 1445–1461, doi:10.5194/amt-4-1445-2011, 2011.

- Schulson, E. M. and Duval, P.: Creep and Fracture of Ice, Cambridge University Press, doi:10.1017/CBO9780511581397, 2009.
- Schwander, J.: The transformation of snow to ice and the occlusion of gases, in: The environmental record in glaciers and ice sheets, edited by Oeschger, H. and Langway, C. C. J., pp. 53–67, John Wiley, New York, 1989.
- Schwander, J. and Stauffer, B.: Age difference between polar ice and the air trapped in its bubbles, *Nature*, 311, 45–47, doi:10.1038/311045a0, 1984.
- Schwander, J., Stauffer, B., and Sigg, A.: Air mixing in firn and the age of the air at pore close-off, *Ann. Glaciol.*, 10, 141–145, doi:10.1017/S0260305500004328, 1988.
- Schwander, J., Barnola, J.-M., Andrié, C., Leuenberger, M., Ludin, A., Raynaud, D., and Stauffer, B.: The age of the air in the firn and the ice at Summit, Greenland, *J. Geophys. Res. Atmos.*, 98, 2831–2838, doi:10.1029/92jd02383, 1993.
- Severinghaus, J. P. and Battle, M. O.: Fractionation of gases in polar ice during bubble close-off: New constraints from firn air Ne, Kr and Xe observations, *Earth Planet. Sci. Lett.*, 244, 474–500, doi:10.1016/j.epsl.2006.01.032, 2006.
- Severinghaus, J. P., Albert, M. R., Courville, Z. R., Fahnestock, M. A., Kawamura, K., Montzka, S. A., Mühle, J., Scambos, T. A., Shields, E., Shuman, C. A., Suwa, M., Tans, P., and Weiss, R. F.: Deep air convection in the firn at a zero-accumulation site, central Antarctica, *Earth Planet. Sci. Lett.*, 293, 359 – 367, doi:10.1016/j.epsl.2010.03.003, 2010.
- Shackleton, N. and Opdyke, N.: Investigation of late Quaternary paleoceanography and paleoclimatology, vol. 145, chap. Oxygen-Isotope and Paleomagnetic Stratigraphy of Pacific Core V28-239 Late Pliocene to Latest Pleistocene, p. 449, *Geol. Soc. Am.*, doi:10.1130/MEM145-p449, 1976.
- Shakun, J. D., Clark, P. U., He, F., Marcott, S. A., Mix, A. C., Liu, Z., Otto-Bliesner, B., Schmittner, A., and Bard, E.: Global warming preceded by increasing carbon dioxide concentrations during the last deglaciation, *Nature*, 484, 49–54, doi:10.1038/nature10915, 2012.
- Shieh, S. and Evans, J. W.: The stability of cylindrical voids and of cylinders subject to closure by viscous flow or evaporation/condensation, *J. Appl. Phys.*, 70, 2968–2972, doi:10.1063/1.349323, 1991.

- Shindell, D. T., Walter, B. P., and Faluvegi, G.: Impacts of climate change on methane emissions from wetlands, *Geophys. Res. Lett.*, 31, doi:10.1029/2004GL021009, 2004.
- Shumway, R. H. and Der, Z. A.: Deconvolution of Multiple Time Series, *Technometrics*, 27, 385–393, doi:10.1080/00401706.1985.10488077, 1985.
- Sowers, T., Bender, M., Raynaud, D., and Korotkevich, Y. S.: $\delta^{15}\text{N}$ of N_2 in air trapped in polar ice: A tracer of gas transport in the firn and a possible constraint on ice age-gas age differences, *J. Geophys. Res. Atmos.*, 97, 15 683–15 697, doi:10.1029/92JD01297, 1992.
- Spahni, R., Schwander, J., Flückiger, J., Stauffer, B., Chappellaz, J., and Raynaud, D.: The attenuation of fast atmospheric CH_4 variations recorded in polar ice cores, *Geophys. Res. Lett.*, 30, doi:10.1029/2003gl017093, 2003.
- Stauffer, B., Fischer, G., Neftel, A., and Oeschger, H.: Increase of atmospheric methane recorded in antarctic ice core, *Science*, 229, 1386–1388, doi:10.1126/science.229.4720.1386, 1985.
- Stauffer, B., Schwander, J., and Oeschger, H.: Enclosure of air during metamorphosis of dry firn to ice, *Ann. Glaciol.*, 6, 108–112, doi:10.3189/1985AoG6-1-108-112, 1985.
- Storn, R. and Price, K.: Differential evolution – A simple and efficient heuristic for global optimization over continuous spaces, *J. Global. Optim.*, 11, 341–359, doi:10.1023/a:1008202821328, 1997.
- Stowasser, C., Buizert, C., Gkinis, V., Chappellaz, J., Schüpbach, S., Bigler, M., Fäin, X., Sperlich, P., Baumgartner, M., Schilt, A., and Blunier, T.: Continuous measurements of methane mixing ratios from ice cores, *Atmos. Meas. Tech.*, 5, 999–1013, doi:10.5194/amt-5-999-2012, 2012.
- Sutter, J., Fischer, H., Grosfeld, K., Karlsson, N. B., Kleiner, T., Van Liefferinge, B., and Eisen, O.: Modelling the Antarctic Ice Sheet across the mid-Pleistocene transition – implications for Oldest Ice, *Cryosphere*, 13, 2023–2041, doi:10.5194/tc-13-2023-2019, 2019.
- Svendsen, J. I., Alexanderson, H., Astakhov, V. I., Demidov, I., Dowdeswell, J. A., Funder, S., Gataullin, V., Henriksen, M., Hjort, C., Houmark-Nielsen, M., Hubberten, H. W., Ólafur Ingólfsson, Jakobsson, M., Kjær, K. H., Larsen, E., Lokrantz, H., Lunkka, J. P., Lyså, A., Mangerud, J., Matiouchkov, A., Murray, A., Möller, P., Niessen, F., Nikolskaya, O., Polyak, L., Saarnisto, M., Siegert, C., Siegert, M. J., Spielhagen, R. F., and Stein, R.: Late Quaternary ice sheet history of northern Eurasia, *Quat. Sci. Rev.*, 23, 1229

- 1271, doi:10.1016/j.quascirev.2003.12.008, quaternary Environments of the Eurasian North (QUEEN), 2004.
- Thomas, E. R., Wolff, E. W., Mulvaney, R., Steffensen, J. P., Johnsen, S. J., Arrowsmith, C., White, J. W., Vaughn, B., and Popp, T.: The 8.2 ka event from Greenland ice cores, *Quat. Sci. Rev.*, 26, 70–81, doi:10.1016/j.quascirev.2006.07.017, 2007.
- Trudinger, C. M., Enting, I. G., Etheridge, D. M., Francey, R. J., Levchenko, V. A., Steele, L. P., Raynaud, D., and Arnaud, L.: Modeling air movement and bubble trapping in firn, *J. Geophys. Res. Atmos.*, 102, 6747–6763, doi:10.1029/96jd03382, 1997.
- Ueltzhöffer, K. J., Bendel, V., Freitag, J., Kipfstuhl, S., Wagenbach, D., Faria, S. H., and Garbe, C. S.: Distribution of air bubbles in the EDML and EDC (Antarctica) ice cores, using a new method of automatic image analysis, *J. Glaciol.*, 56, 339–348, doi:10.3189/002214310791968511, 2010.
- Van Liefferinge, B. and Pattyn, F.: Using ice-flow models to evaluate potential sites of million year-old ice in Antarctica, *Clim. Past*, 9, 2335–2345, doi:10.5194/cp-9-2335-2013, 2013.
- Van Liefferinge, B., Pattyn, F., Cavitte, M. G. P., Karlsson, N. B., Young, D. A., Sutter, J., and Eisen, O.: Promising Oldest Ice sites in East Antarctica based on thermodynamical modelling, *Cryosphere*, 12, 2773–2787, doi:10.5194/tc-12-2773-2018, 2018.
- Vasiliev, N., Talalay, P., Bobin, N., Chistyakov, V., Zubkov, V., Krasilev, A., Dmitriev, A., Yankilevich, S., and Lipenkov, V. Y.: Deep drilling at Vostok station, Antarctica: history and recent events, *Ann. Glaciol.*, 47, 10–23, URL 10.3189/172756407786857776, 2007.
- Veres, D., Bazin, L., Landais, A., Toyé Mahamadou Kele, H., Lemieux-Dudon, B., Parrenin, F., Martinerie, P., Blayo, E., Blunier, T., Capron, E., Chappellaz, J., Rasmussen, S. O., Severi, M., Svensson, A., Vinther, B., and Wolff, E. W.: The Antarctic ice core chronology (AICC2012): an optimized multi-parameter and multi-site dating approach for the last 120 thousand years, *Clim. Past*, 9, 1733–1748, doi:10.5194/cp-9-1733-2013, 2013.
- Wilkinson, D. and Ashby, M.: Pressure sintering by power law creep, *Acta Metall.*, 23, 1277–1285, doi:10.1016/0001-6160(75)90136-4, 1975.
- Willeit, M., Ganopolski, A., Calov, R., and Brovkin, V.: Mid-Pleistocene transition in glacial cycles explained by declining CO₂ and regolith removal, *Sci. Adv.*, 5, eaav7337, doi:10.1126/sciadv.aav7337, 2019.

- Wilson, A. T. and Long, A.: New approaches to CO₂ analysis in polar ice cores, *J. Geophys. Res. Oceans*, 102, 26 601–26 606, doi:10.1029/97JC00159, 1997.
- Wilson, C. J. L., Russell-Head, D. S., and Sim, H. M.: The application of an automated fabric analyzer system to the textural evolution of folded ice layers in shear zones, *Ann. Glaciol.*, 37, 7–17, URL 10.3189/172756403781815401, 2003.
- Witrant, E. and Martinerie, P.: Input Estimation from Sparse Measurements in LPV Systems and Isotopic Ratios in Polar Firns, *IFAC Proc. Vol.*, 46, 659 – 664, doi:10.3182/20130204-3-FR-2033.00201, 5th IFAC Symposium on System Structure and Control, 2013.
- Witrant, E., Martinerie, P., Hogan, C., Laube, J. C., Kawamura, K., Capron, E., Montzka, S. A., Dlugokencky, E. J., Etheridge, D., Blunier, T., and Sturges, W. T.: A new multi-gas constrained model of trace gas non-homogeneous transport in firn: evaluation and behaviour at eleven polar sites, *Atmos. Chem. Phys.*, 12, 11 465–11 483, doi:10.5194/acp-12-11465-2012, 2012.
- Yeung, L. Y., Murray, L. T., Martinerie, P., Witrant, E., Hu, H., Banerjee, A., Orsi, A., and Chappellaz, J.: Isotopic constraint on the increase in tropospheric ozone in the twentieth century, *Nature*, in press.
- Zhao, L., Bai, X., Li, T., and Williams, J.: Improved conservative level set method, *Int. J. Numer. Methods Fluids*, 75, 575–590, doi:10.1002/flid.3907, 2014a.
- Zhao, L., Mao, J., Bai, X., Liu, X., Li, T., and Williams, J.: Finite element implementation of an improved conservative level set method for two-phase flow, *Comput. Fluids*, 100, 138 – 154, doi:10.1016/j.compfluid.2014.04.027, 2014b.
- Zhao, L.-h., Mao, J., Liu, X.-q., Bai, X., and Williams, J.: Improved conservative level set method for free surface flow simulation, *J. Hydrodyn.*, 26, 316–325, doi:10.1016/S1001-6058(14)60035-4, 2014c.